



12th Annual BMEI Symposium

The Precision Medicine Imperative:
The Quest to Extend Healthspan

March 20–21, 2024

Venue:
New York Academy of Medicine
1216 Fifth Avenue New York, NY



Icahn School
of Medicine at
Mount
Sinai

*BioMedical Engineering
and Imaging Institute*

12th Annual BMEII Symposium March 20th-21st, 2024

The organizing committee members: Teresa Lotz, Yijuan (Rachel) Zhu, Yun Soung Kim, David O'Connor, Heli Patel, Mirabai Liu, Christopher Cannistraci, Xueyan Mei, Shams Rashid, Audrey Kaufman, Aislinn Diaz, Georgios Soultanidis, Abraham (Bram) Teunissen

The Editors of this program: Georgios Soultanidis, Altynay Narmanova, Shams Rashid, Christopher Cannistraci

This program or parts of it are not to be copied without the direct permission of the authors
New York, 2024

Contents

Timetable	7
Message from the Director	10
About BMEII	11
Human Imaging Core	12
Small Animal Imaging Core	17
BMEII Research Laboratories	21
Bioinformatics and Data Processing	23
Biographies of the Hosts	26
Zahi A. Fayad, PhD, FAHA, FACC, FISMRM	26
Dennis S. Charney, MD	29
Brendan Carr, MD, MA, MS	32
Panelist Profiles	34
1st Panel Session: Wellness, Screening, and Lifespan	34
2nd Panel Session: Accelerating the Clinical Translation of Nanotherapeutics	37
3rd Panel Session: The Importance of Accessible MRI for the World	40
4th Panel Session: Sustainable Futures, Healthier Outcomes: Navigating AI's Impact in Healthcare	42
5th Panel Session: MRI Tesla Wars	45
6th Panel Session: Revolutionizing Healthcare: Pioneering the Future of Digital Medicine	48
Professional Development Panel	51
Moderators	53
Selected for oral presentations	57
Chief Editor	57
Review Committee	57
Visualization of nonfibrillar Dutch mutant Alzheimer's amyloid beta (A β) aggregates (oligomers) associated with aging-related presynaptic dysfunction	58
Advanced diffusion weighted MRI methods detect fibrosis in renal allografts: A preliminary experience	60
VIS-MAE: A Foundation Model for Medical Image Segmentation and Classification	62
Relationship between brain stiffness, microstructural integrity, beta-amyloid accumulation and cognitive decline in beta-amyloid positive individuals	64
Inhibiting tumor growth using nanoparticle-based photodynamic therapy	66
Prediction of pancreatic cancer aggressiveness using CT-base radiomics	68
Selected for poster presentations	70
Characterizing the subcallosal cingulate gray matter in depression: implications for DBS optimization	72

Impact of white matter abnormalities in therapeutic DBS pathways for treatment-resistant depression	74
An AI-Powered Impedance Flow Cytometry with Basis Impedances for Accurate and Accessible Bio-Particle Analysis	76
Enhanced Spatial Comprehension in Cardiac Catheterization using Extended Reality Visualization	78
Microstructure in amygdala and hippocampal subfields is associated with clinical and behavioral measures in patients with psychiatric illness.	80
Microstructure in amygdala and hippocampal subfields is associated with clinical and behavioral measures in patients with psychiatric illness.	82
Validating mood and anxiety symptom capture in the real-world and exploring the influence of physical activity	84
Multi-modal imaging of carotid atherosclerotic risk in substance use disorders . . .	86
The Neurobehavioral Representations of Regret in Depression	88
Assessment of Cardiac Flow Dynamics in Mitral Valve Prolapse Using Direct Numerical Simulation: Proof of Concept	90
Enhancing allograft survival using nanotherapeutics targeting the innate immune system	92
Specific locations of myocardial inflammation and fibrosis are associated with higher risk of events in cardiac sarcoidosis	94
Cortical lesions in early multiple sclerosis are prevalent and associated with cognitive disability	96
Foundational Transformers with Linear Probing for Sleep Stage Classification using Time Series Sleep Study Data	98
Deep brain stimulation promotes white matter remodeling and is accompanied by functional changes to brain-wide networks	100
White Matter and Differential Treatment Outcomes to Cognitive-Behavioral Therapy or Antidepressant Medication in MDD	102
Differences in White Matter Associated with Relapse in Patients with Major Depressive Disorder	104
Characterizing the Constructs of Motivation	106
Long-term reorganization of structural and functional connectivity among World Trade Center responders with post-traumatic stress disorder: a data-driven multimodal approach	108
Dye Enhancement of an Antibody-Conjugated Nanosensor Platform	110
Idiopathic Intracranial Hypertension assessment of Whole Brain, White Matter and Gray Matter Volumes in IIH patients and on 7T MRI	112
Point of Entry? Is the Olfactory Nervus Terminalis the Route for SARS-CoV-2 Anosmia and Intracranial Infections	114
A Structured-Textual Machine Learning Model to Classify Penumbra-Core Mismatch Among Patients Presenting with Acute Ischemic Stroke due to Large-Vessel Occlusion	116
7T MRI-derived Brain Age Exceeds Chronological Age in Both Early and Long-standing Multiple Sclerosis	118
Exploring the VTA Circuitry of Anhedonia in Major Depressive Disorder using Ultra-High Field 7T MRI	120

Characterization of solid renal masses with functional non-contrast MRI in patients undergoing surgical management.	122
Optimized 7-Tesla QSM reconstruction: Clinical feasibility	124
Exploring in vivo T cell imaging in atherosclerosis	126
Short-term Sirolimus Treatment Increases Cerebral Blood Flow in Asymptomatic APOE4 Females Determined by 3T MRI	128
Functional Connectivity of the Locus Coeruleus with Bilateral Insula is associated with increased Anxious Arousal in Anxiety Disorder and PTSD	130
Automated diagnosability review of liver confidence map overlaid elastograms via deep learning	132
Differential contributions of functional and structural connectivity to chronic stress symptoms	134
Design of a Single Walled Carbon Nanotube-Based Nanosensor for the Inflammatory Cytokine TNF-alpha	136
Monitoring lipid nanoparticles' biodistribution	138
Disaggregating the social exposome's role in brain development: A study of environmental and contextual factors influencing adolescents' functional connectivity	140
AI-Enabled Left Atrial Volumetry in Coronary Calcium Scans (AI-CAC) Predicts Atrial Fibrillation as Early as One Year, Improves CHARGE-AF, and Outperforms NT-proBNP: The Multi-Ethnic Study of Atherosclerosis	142
AI-Enabled Cardiac Chambers Volumetry in Coronary Calcium Scans (AI-CAC) Predicts Heart Failure and Outperforms NT-proBNP: The Multi-Ethnic Study of Atherosclerosis	144
Coronary Artery Calcium Scans Powered by Artificial Intelligence (AI-CAC) Predicts Atrial Fibrillation and Stroke Comparably to Cardiac Magnetic Resonance Imaging: The Multi-Ethnic Study of Atherosclerosis (MESA)	146
Automated Left Ventricular Volumetry using Artificial Intelligence in Coronary Calcium Scans (AI-CAC) Predicts Heart Failure Comparably to Cardiac MRI and Outperforms NT-proBNP: The Multi-Ethnic Study of Atherosclerosis (MESA)	148
Opportunistic Artificial Intelligence-based Detection of Osteoporosis and Osteopenia Using Thoracic Vertebral Bone Mineral Density Measurements in Coronary Artery Calcium Scans	150
AI-enabled Automated Cardiac Chambers Volumetry in Non-contrast ECG-gated Cardiac Scans Vs. Non-contrast Non-gated Lung Scans	152
Distribution Of Microvascular Endothelial Function In Different Clinical And Non-clinical Settings In The United States And China	154
Opportunistic AI-enabled Automated Bone Mineral Density Measurements In Lung Cancer Screening And Coronary Calcium Scoring CT Scans Are Equivalent	156
AI-enabled Cardiac Chambers Volumetry in Non-Contrast Cardiac CT scans Detects HFrEF vs. HFpEF	158
Hybrid 18F-FDG PET/MRI Predicts Adverse Clinical Outcomes in Cardiac Sarcoidosis	160
PET/MRI imaging of mitral valve prolapse	162
Multimodal Profiling Of Stress-induced Immune Reprogramming in Cardiovascular Participants	163
Aptamers as Recognition Probes for Detection of Interleukin-6 with Fluorescent Single-Walled Carbon Nanotubes	164

Ex Vivo MRI and Neuropathology for Investigation of Traumatic Brain Injury	166
White Matter Integrity Predicts Recovery Response Time of Deep Brain Stimulation for Depression	168
Exploring ENTPD3 as a target for beta cell mass imaging by PET	170
Characterizing daily physical activity patterns in endometriosis with unsupervised learning via functional mixture models	172
Patient-specific tissue engineering model of an inherited cardiomyopathy: an in vitro platform for personalized medicine.	174
Mesoscale Lipid Nanoparticle Formulation for Targeted Delivery of Nucleic Acids to Renal Proximal Tubule Epithelium	176
Detection and characterization of perivascular spaces using high-resolution T2- weight 7T MRI and automatic segmentation	178
Correlation of cortical gray / white matter ratio and body mass index (BMI) in a cohort of healthy controls and major depression patients scanned with 7T T1- weighted MRI	180
Strategies for motion- and breathing-robust estimation of fMRI intrinsic neural timescales	182
Using sleep quality and 7T MRI to explore structural differences in the Locus Coeruleus in those with PTSD and pathological anxiety	184
Evaluation of a Novel Self-Sealing Dialysis Port	186
Increased Blood-Brain Barrier Permeability in ME/CFS: An MRI Study	188
Functionalized SWCNT-Aptamer Sensors for Selective Dopamine Detection: Ex- ploring Selectivity and Sensitivity.	190
MRAnnotator: A Multi-Anatomy Deep Learning Model for MRI Segmentation	192
Development of a Next Gen 9.4 T Magnetic Resonance System for Translational Neuroscience	194
Selected for Innovation Station	196
mercure - A flexible open-source platform for deploying AI models into clinical practice	198
Creating an open-source low-field MRI scanner in just one week - Experience from the MRI4ALL hackathon	200
Optimizing Remote Vital Sign Alarms in Healthcare at Home: Insights from Alarm Simulations Using Real-world Data.	202
Development of a reversibly detachable modular electronic interface for a thin wire- less health monitoring patch system	204
A Novel Subdural Hematoma Evacuation Device For Subdural Hemorrhage Treat- ment	206
Consumer-mediated RWD generation for Precision Medicine Research	208
Superfusion Device for Pharmacological Testing in Precision Medicine	210
Sponsors	212

Timetable

Wednesday, March 20

- 9–10 am** **Registration, Breakfast, and Networking** | President's Gallery, First Floor
- 10–10:30 am** **Welcome Remarks** | Hosack Hall, First Floor
Zahi A. Fayad, PhD, Director, BioMedical Engineering and Imaging Institute, Icahn School of Medicine at Mount Sinai School
- 10:15–10:30 am** **Welcome Remarks** | Hosack Hall, First Floor
Dennis S. Charney, MD, Anne and Joel Ehrenkrantz Dean, Icahn School of Medicine at Mount Sinai, President for Academic Affairs, Mount Sinai Health System
- 10:30–11:30 am** **Panel Session: Wellness, Screening, and Lifespan** | Hosack Hall, First Floor
Moderator: **David Luu, MD**, CEO of Hearty Longevity Clinics, Founder of Longevity Docs Network
Speakers:
 - **Sarah Pesce**, Chief Operating Officer, Thorne Lab
 - **Nathan Price, PhD**, Chief Scientific Officer, Thorne HealthTech
 - **Sean London, MD**, Lead Radiologist, Prenuvo
 - **Thomas Witzel, PhD**, VP Radiomics, Q Bio
 - **Giuseppe Petralia, MD**, Department of Oncology and Hemato-Oncology, University of Milan, Division of Radiology, Department of Medical Imaging and Radiation Sciences, IEO European Institute of Oncology IRCCS
- 11:30 am–12:30 pm** **Panel Session: Accelerating the Clinical Translation of Nanotherapeutics** | Hosack Hall, First Floor
Moderator: **Abraham J.P. Teunissen, PhD**, Assistant Professor Director of Radiochemistry, BioMedical Engineering and Imaging Institute Icahn School of Medicine at Mount Sinai
Speakers:
 - **Daniel G. Anderson, PhD**, Massachusetts Institute of Technology
 - **Cristianne JF Rijcken, PharmD, PhD**, CSO Cristal Therapeutics and CEO Liberates
 - **Daniel A. Heller, PhD**, Member, Molecular Pharmacology Program, Memorial Sloan Kettering Cancer Center
 - **Juliane Nguyen, PhD**, University of North Carolina at Chapel Hill
- 12:30–2 pm** **Lunch** | Reading Room, Third Floor
- 1–4 pm** **Young Scholar Sessions**
- 1:15–2 pm** **Professional Development Panel** | Hosack Hall
Moderators: **Vivek Yadav and Hannah Kittrell**, BioMedical Engineering and Imaging Institute, Icahn School of Medicine at Mount Sinai
Speakers:
 - **Julia Nanyi Zhao, PhD**, Global Director of Operations at Nucleate Bio
 - **Nathaniel Swinburne, MD**, Director of Radiology Informatics, Memorial Sloan Kettering Cancer Center
 - **Stephen José Hanson, PhD**, Rutgers University, Psychology, RUBIC
- 2–3 pm** **Panel Session: The importance of accessible MRI for the world** | Hosack Hall, First Floor
Moderator: **Akbar Alipour, PhD**, Assistant Professor, Biomedical Engineering in Radiology, Icahn School of Medicine at Mount Sinai
Speakers:
 - **Matthew Rosen, PhD**, MGH/Martinos Center for Biomedical Imaging, Harvard Medical School
 - **Edmond A. Knopp, MD**, Vice President of Medical Affairs, Hyperfine, Inc.
 - **Marc Dubois, PhD**, Multiwave Imaging, Aix-Marseille Université, France
- 3–4 pm** **Innovation Station** | Periodicals Room, Third Floor
- 4–6 pm** **Poster Session and Welcome Reception** | Reading Room, Third Floor

Thursday, March 21

- 9–10 am** **Registration, Breakfast, and Networking** | President's Gallery, First Floor
- 10–10:15 am** **Opening Remarks** | Hosack Hall, First Floor
Zahi A. Fayad, PhD
- 10:15–10:30 am** **Welcome Address** | Hosack Hall, First Floor
Brendan Carr, MD, MA, MS, Chief Executive Officer of the Mount Sinai Health System
- 10:30–11:30 am** **Panel Session: Sustainable Futures, Healthier Outcomes: Navigating AI's Impact in Healthcare**
Hosack Hall, First Floor
Moderators:
Hayit Greenspan, PhD, Professor in the Department of Diagnostic, Molecular, and Interventional Radiology. Affiliated with Windreich Dept. of Artificial Intelligence and Human Health, Co-Director of AIET PhD Program Icahn School of Medicine at Mount Sinai. & co-founder of RADLogics Inc.
Xueyan Mei, PhD, BioMedical Engineering and Imaging Institute, Icahn School of Medicine at Mount Sinai School
Speakers:
 - **Larry Tanenbaum, MD, FACR**, VP and Chief Technology Officer, Radnet
 - **Zichen Wang, PhD**, Amazon Web Services
 - **Rima Arnaout, MD**, Associate Professor, University of California, San Francisco
 - **David C. Rhew, MD**, Global Chief Medical Officer (CMO) and VP of Healthcare, Microsoft
- 11:30 am–12:30 pm** **Panel Session: MRI Tesla Wars** | Hosack Hall, First Floor
Moderator: **Priti Balchandani, PhD**, Director of the Advanced Neuroimaging Research Program, Associate Director of the BioMedical Engineering and Imaging Institute
Speakers:
 - **J. Thomas Vaughan, Jr., PhD**, Professor of BioMedical Engineering and Radiology, Director of Columbia MR Research Center, Mortimer B. Zuckerman Mind Brain Behavior Institute at CUMC
 - **Nicolas Boulant, PhD**, University of Paris-Saclay, CEA, NeuroSpin, France
 - **Bram Stolk, PhD, MBA**, Vice President, Academic Accounts United Imaging
 - **Himanshu Bhat, PhD**, Head of MR R&D Collaborations, North America Siemens Healthineers
- 12:30–1:30 pm** **Lunch and Trivia** | Reading Room, Third Floor
- 1:30–2:30 pm** **Oral Presentations** | Hosack Hall, First Floor
- 2:30–3 pm** **Coffee Break** | President's Gallery, First Floor
- 3–4 pm** **Panel Session: Revolutionizing Healthcare: Pioneering the Future of Digital Medicine** | Hosack Hall, First Floor
Moderator: **Yun Soung Kim, PhD**, Assistant Professor, Department of Radiology, BioMedical Engineering and Imaging Institute at Icahn School of Medicine at Mount Sinai
Speakers:
 - **Jagmeet P. Singh, MD, ScM, DPhil**, Professor of Medicine, Harvard Medical School, Cardiology Division, Massachusetts General Hospital
 - **Lisa Shah, MD**, Chief Medical Officer, Twin Health
 - **Walter Greenleaf, PhD**, Neuroscientist, Stanford University Virtual Human Interaction Lab
 - **Emily Capodilupo**, Senior Vice President, Data Science and Research, WHOOP Inc.
 - **Nicole Zahradka, PhD**, Senior Clinical Research Program Manager, Current Health
- 4–4:15 pm** **Awards Presentation** | Hosack Hall, First Floor
Sara Lewis, MD, Associate Professor, Biomedical Engineering and Imaging Institute, Icahn School of Medicine at Mount Sinai
- 4:15–4:30 pm** **Closing Remarks** | Hosack Hall, First Floor
Zahi A. Fayad, PhD
- 4:30–6 pm** **Auction and Networking Reception** | Reading Room, Third Floor

Message from the Director

The BioMedical Engineering and Imaging Institute (BMEII) along with the Icahn School of Medicine at Mount Sinai, welcomes you to the 12th Annual BMEII Symposium. Building on the impressive foundations laid by our past events, this year's Symposium is set to deliver an even more engaging and enriching experience for all attendees.

For this year's theme, we have selected "The Precision Medicine Imperative: The Quest to Extend Healthspan." This theme underscores our commitment to pushing the boundaries of healthcare by harnessing cutting-edge technologies, including AI in medical imaging, accessible MRI, wearables and mobile health, and novel therapeutics strategies leverage lipid nanoparticles and nanomedicine. Our goal is to delve deep into the capabilities of precision medicine to enhance both the quality and longevity of life.

Spanning two days, the Symposium will offer a rich program featuring expert-led panel discussions, insightful presentations from distinguished faculty and promising trainees, and an interactive poster session. We have chosen six critical topics within Biomedical Engineering as the focus of our panels, aiming to thoroughly address the prevailing challenges and opportunities in the field.

Continuing from last year, we are excited to present the Innovation Station exhibition again, showcasing the most recent innovations in Biomedical Engineering.

Additionally, we are delighted to introduce a medical art exhibit this year. This exhibit, along with an auction (for charity) and entertainment offerings, will be part of our closing reception, celebrating the fusion of art and science and providing a comprehensive Symposium experience.

We eagerly anticipate your participation in what we hope to be a thought-provoking and transformative event. Join us as we venture together into the future of extending healthspan through the lens of precision medicine and breakthrough engineering.

Zahi A. Fayad, PhD

Director, BioMedical Engineering and Imaging Institute



About BMEII

Our mission is centered around development, validation, translation and education of innovative technology in biomedical imaging to address both basic and clinical research problems and therefore improve human health.

The BioMedical Engineering and Imaging Institute (BMEII) is a state-of-the-art research facility housed in 20,000 square feet in the Hess Center of Science and Medicine (CSM). BMEII (Director, Zahi A. Fayad, PhD) is comprised of faculty, staff and trainees responsible for coordinating and executing all research projects performed in these facilities. Currently BMEII has over 65 members with expertise in all aspects of translational imaging research. The faculty consists of Biomedical and Electrical Engineers and Radiologists who are leading experts in neuroimaging, cardiovascular imaging, body/cancer imaging, and nanomedicine. Highly skilled staff provides a full suite of support services for image acquisition, processing and analysis, scheduling and performance of the proposed experiments.

Access to the BMEII facility is based on a fee-for-service schedule (for more info, visit our website). These user fees are calculated to cover the operating and maintenance costs of the instruments and related Core expenses. These rates are determined and periodically reviewed by the Dean's Office and adjusted to reflect the actual costs. User fees include technical support for operation of imaging equipment.

For internal Mount Sinai users, resource usage time is compiled from the web-based scheduling system and charged directly to your account on a monthly basis. Any questions on the charges should be addressed to the BMEII Director.

Human Imaging Core

MR/PET (3T) Siemens mMR

The 3T MR/PET is a fully integrated and capable of simultaneous whole body PET and MRI scanning. This allows more precisely coregistered functional and structural acquisition while reducing the radiation dose in PET imaging by replacing the CT scans with an MRI scan. True simultaneous acquisition of MR and PET data by the hybrid system merges the highly sensitive PET metabolic information with the highly specific MR anatomical and functional information. The 3T MRI system is a whole body imaging system, capable of routine as well as advanced imaging of all body regions. The PET scanner will be fully integrated into the MR, utilizing state of the art solid-state technology for simultaneous PET imaging during MR image or spectrum acquisition. The 3T MR-PET is designed for the purposes of oncological and neurological diagnostic imaging. The highly integrated nature of these systems provides the capability for full spatial and temporal correlation between both modalities. The maximum gradient amplitude will be approximately 40 mT/m per axis, with a maximum gradient slew rate of about 200 T/m/s per axis. The system's magnet has an integrated cooling system and active shielding. The shimming capabilities include: Active (with 3 electric and 5 electric nonlinear linear shim channels) and Passive shims for maintaining very high homogeneity and excellent image quality over a wide range of applications. Online shimming is performed in less than 20 seconds in order to optimize homogeneity. The RF transmit and receive system include: compact, air cooled tube RF amplifier providing 35 kW peak power; integrated electronics with cabinet water cooling; integrated circularly polarized whole body RF coil; up to 32 receive channels. The PET system include: adaptation to a work environment within high magnetic fields including APD and LSO based detector technology; adaptation and optimization of numerous MR components to an integrated PET imaging unit; high-resolution, high-count rate, positron emission tomography (PET) imaging of metabolic and physiologic processes; high quality metabolic and anatomic image registration and fusion for optimal lesion detection and identification within the body; state-of-the-art 3D PET data acquisition and analysis tools; state-of-the-art 3D PET reconstruction, attenuation and scatter correction software. Expected PET performance specifications: spatial resolution: <6.5mm; timing resolution: < 4.5 ns; sensitivity: > 0.5%; axial FOV: > 19 cm ; transaxial FOV: up to 45 cm. The system also supports MR and PET gated scan acquisition; support for list mode acquisition, offline histogramming and reconstruction; special calibration. Alignment and quality control sources including shielding; multimodality workplace; 3D iterative reconstruction.



7T Siemens MR whole body scanner

This is an ultrahigh field 7.0 Tesla actively shielded whole body MRI scanner. The super-conducting magnet is self-shielded, reducing its overall footprint and making it compact and lightweight by 7T standards, weighing 24-tons. The (warm) inner bore of the magnet is 82 cm, which houses the 60 CM inner patient bore. The dimensions of the magnet without covers is approximately 2.5 m in length, 2.6 m in width, and 2.65 m in height. The 5-Gauss line extends slightly further than for a 3T scanner with 5.6 m radial and 7.8 m axial dimension. A whole-body gradient system provides gradient amplitude of up to 70 mT/m per axis, and a maximum slew rate of up to 200 T/m/s. The RF transmit system comes with 8 parallel transmit channels; 8 individually shaped RF pulses can be prescribed simultaneously and independently in amplitude and phase. The multi-nuclei package allows for imaging and spectroscopy at non-proton frequencies, i.e. detection of e.g. ^{19}F , ^{31}P , ^7Li , ^{23}Na , ^{13}C , ^{17}O . Our 7T/820AS is configured to accommodate an 8-channel Tx-array and 48-channel Rx receivers. Several coils are currently available such as the 1-channel Tx and 32-channel Rx head coil and the 8-channel Tx and 8-channel Rx head coil.



3T Siemens MAGNETOM Prisma

The Siemens Prisma 3D MRI represents a significant advancement in magnetic resonance imaging technology. It offers a powerful 3 Tesla magnet, providing exceptional image quality and resolution. The system includes advanced features such as simultaneous multislice (SMS) acquisition, which accelerates scanning times while maintaining high image quality. Additionally, the Prisma is equipped with BioMatrix technology, ensuring consistent patient results with AI-based adjustments to patient variability.



3T Siemens MAGNETOM Skyra

This unique 3T MRI was designed in a collaboration between Siemens and academic research centers to create a system tuned specifically for the highest performance imaging. With high-end XR gradients (80 mT/m @ 200 T/m/s) the scanner is ideally suited for high angular resolution diffusion imaging of white matter, up to 256 directions and higher SNR for applications like angiography. Built on Numaris X software, the XA30 platform provides product sequences to do cardiac flow imaging, 2D and 3D perfusion imaging, simultaneous multislice EPI and much more. Advanced higher order shims allow for greater specificity in multinuclear spectroscopy.

PET/CT Siemens Biograph Vision

Biograph Vision™ is next generation, high-precision combined positron emission tomography (PET) / computed tomography (CT) system developed by Siemens Healthineers. The PET device in the system features 3.2mm lutetium oxyorthosilicate (LSO) crystals and digital silicon photomultiplier (SiPM) sensors making it the fastest time-of-flight system, with temporal resolution of 214 picoseconds and sensitivity 100 counts per second (cps) / kBq. This leads to improved spatial resolution with reduced partial volume effects,



enabling faster scans and/or lowering the administered dose to the patient. The exceptional sensitivity of the detectors gives the necessary range of count rate from ^{90}Y to ^{82}Rb studies. The CT component has features of the SOMATOM Definition line of scanners. The system features Sinogram Affirmed Iterative Reconstruction (SAFIRE) algorithm for iterative reconstruction to improve the image quality and Iterative Metal Artifact Reduction to reduce metal artifacts. The CT can be utilized also as a low dose screening tool of lung cancer in high-risk patients. With its exceptional features and resolution, this system is used for the whole-body examination of patients to diagnose cancer, as well as cardiac and nervous disorders.

Multidetector CT (MDCT) Siemens Somatom Definition Flash

This Dual Source CT, uses two X-ray sources and two detectors simultaneously, to cover the entire thorax in less than a second. A 2 meter scan requires only 5 seconds, enhancing the efficiency of perfusion or dynamic vascular imaging and reduction the dose for all scans, resulting, e.g. in dose down to sub-mSv for cardiac imaging. Dual Energy automatically provides a second contrast for without any extra dose. Advance software efficiently manages the reduction in dose allowing for: limited exposure to radiation-sensitive organs and increases tissue contrast with no sacrifice to image quality.

Two 1.5T Siemens MR MAGNETOM Aera

Short and open appearance (145 cm system length with 70 cm Open Bore Design) can accommodate subjects with larger body compositions compared to the 60 cm bore of a typical clinical 1.5T & 3T. Newly designed RF system and coil architecture integrates with all digital-in/digital-out technology, one system use standard gradients (33 mT/m @ 125 T/m/s) and the second system has advanced gradients (45 mT/m @ 200 T/m/s). Actively shielded water-cooled gradient system with zero helium boil-off. Inline software is specially designed for: neuro, angio, cardiac, body, onco, breast, ortho, pediatric and scientific specialties such as Magnetic Resonance Elastography; a technique that measures the stiffness of tissues by introducing shear waves and imaging their propagation.

Siemens ACUSAN S3000 ARFI Ultrasound

The ultrasound system automatically produces an acoustic 'push' pulse that generates shear-waves, which propagate into the tissue. Using image-based localization and a proprietary implementation of acoustic radiation force impulse (ARFI) technology, shear wave speed

may be quantified, in a precise anatomical region, focused on a region of interest, with a predefined size, provided by the system. Measurement value and depth are also reported, and the results of the elasticity are expressed in m/s. This system provides new method for the evaluation of the elastic properties of tissues is now available in the Cancer/Body Core. Clinical applications of ARFI imaging include: liver fibrosis quantification, breast, colorectal and prostate tumor imaging.

Dual Source-Dual Detector Siemens Force CT

The Force is the third iteration of Siemens' dualsource CT design which features two sets of x-ray tubes and detectors for enhanced imaging of all patients, including young children, patients with renal insufficiency, and those who cannot hold their breath. Due to its low-kV imaging technique, Force broadens CT's application for patients with renal insufficiency and offers an acquisition speed of 737 mm/sec, so an entire adult chest, abdomen, and pelvis study can be done in one second with no breath-holds. In cardiac imaging, Force can obtain an entire study within one-quarter of a heart beat at a temporal resolution of 66 msec, which is the speed required to freeze the fastest-moving anatomy, such as the right coronary artery.



"Mock" MR PSTNet



The MRI simulator allows researchers to acclimatize the subjects to the 'enclosed' and loud MRI environment before they actually go into a real scanner. This is especially important for studies involving children.

fMRI peripherals

All the MRI scanners are equipped with the latest state of the art peripherals for functional imaging including LCD goggles, integrated eyetracking, fiber optic subject response gloves, pneumatic computerized headphones with microphones as well as a full spectrum of physiological recording probes for ECG, GSR, pulse-Ox etc. There is also a specialized MRI compatible computerized olfacto-meter.

Neuro Testing room

A sound proofed and independent temperature-controlled neuro testing room is located near the 3T MRI for physiological testing such as EEG, ERP and other modalities. This room is also equipped with large monitors for paradigm training and testing.



Small Animal Imaging Core

9.4T MRI Bruker

This is a high-resolution MRI scanner used for in-vivo imaging of mice and smaller specimens.

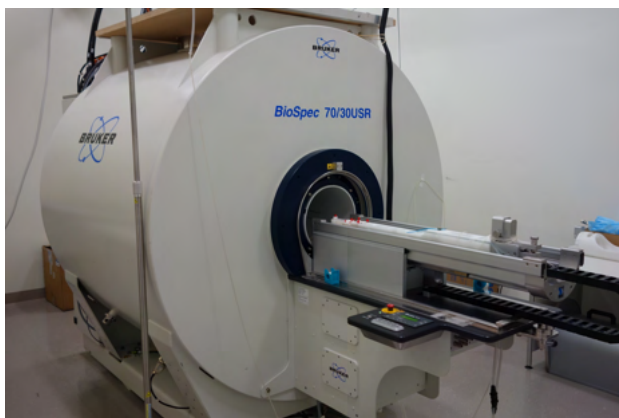


It is 9.4 Tesla 89-mm bore MRI system operating at a proton frequency of 400 MHz (Bruker, Billerica, MA). The 9.4T is equipped with a mouse respiratory and cardiac sensor connected to a monitoring and gating system (SA Instruments, Inc., Stony Brook, NY). Sedation is administered by an Isoflurane/O₂ gas mixture delivered through a nose cone and placed in a 30 mm birdcage coil with an animal handling system. Additionally, a temperature controller is available in the bore of the magnet, to maintain the animal in the RF coil at a selected temperature. Recent upgrades (Bruker Paravision 4) have

enabled the use of navigator pulses to allow for cardiac and/or respiratory gating without the use of electrodes.

7.0T MRI Bruker Biospec 70/30

This is a high-resolution MR scanner for small animals. The maximum bore diameter for



imaging is 15.4cm. This system is equipped with two gradient choices, a large built-in gradient system with up to 200 mT/m and a slew rate of 640 T/m/s. This gradient in combination with a large circular polarized coil will allow imaging of animals up to 15.4cm in diameter. The system is also equipped with a high performance gradient insert with 440mT/m and slew rate of 3,440 T/m/s for high-resolution imaging. The system has 2 transmit and 4 receive channels. There is a 35mm ID circular polarized coil for in-vivo mouse imaging as well as a 4-channel

phased array for mouse brain and a 4-channel phased array for mouse cardiac imaging. There are also 3 other dual tuned 20mm surface coils for ³¹P, ¹³C and ¹⁹F. The 7T Bruker is equipped with the Autopac system, a fully integrated animal handling, laser guided po-

sitioning system. Animal warming holders are available for rats and mice as well as a full spectrum of monitoring peripherals for ECG, triggering and respiratory monitoring etc.

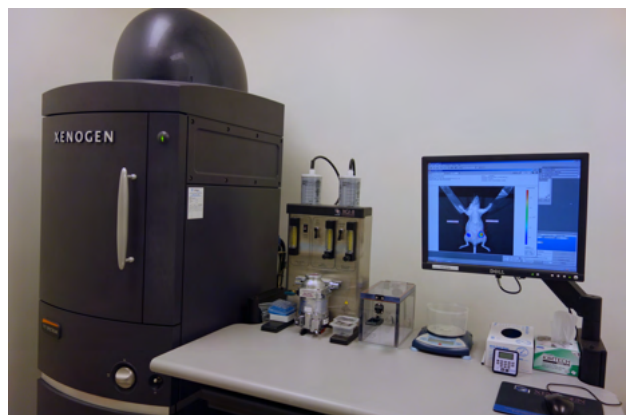
Mediso nanoScan Micro PET/CT

The newest acquisition to the Small Animal Imaging Center, nanoScan Micro PET/CT has the highest PET resolution using the industry's most advanced pixelated modular LYSO detectors. It has an exceptionally high-count rate tolerance supporting high activity studies of multiple animals or short half-life isotopes. The system has easy access to the animal from both the front and the back of the PET/CT gantry and state-of-the-art Tera-Tomo™ 3D PET image reconstruction engine. High imaging throughput can be obtained by large bore size and large field-of-view in both axial and transaxial directions in addition to multiCell imaging chambers for mice, rats and rabbits and a PrepaCell Preparation station.



Biophotonic IVIS-Spectrum

The IVIS Spectrum in vivo imaging system uses a novel patented optical imaging technology to facilitate non-invasive longitudinal monitoring of disease progression, cell trafficking and gene expression patterns in living animals. The IVIS Spectrum is a versatile and advanced in vivo imaging system. An optimized set of high efficiency filters and spectral un-mixing algorithms lets you take full advantage of bioluminescent and fluorescent reporters across the blue to near infrared wavelength region. It also offers single-view 3D tomography for both fluorescent and bioluminescent reporters that can be analyzed in an anatomical context us-



ing our Digital Mouse Atlasor. For advanced fluorescence pre-clinical imaging, the IVIS Spectrum has the capability to use either trans-illumination (from the bottom) or epi-illumination (from the top) to illuminate in vivo fluorescent sources. 3D diffuse fluorescence tomography can be performed to determine source localization and concentration using the combination of structured light and trans illumination fluorescent images. The instrument is equipped with 10 narrow band excitation filters (30nm bandwidth) and 18 narrow band emission filters (20nm bandwidth) that assist in significantly reducing autofluorescence by the spectral scanning of filters and the use of spectral unmixing algorithms. In addition, the spectral unmixing tools allow the researcher to separate signals from multiple fluorescent reporters within the same animal.

Micro Ultrasound Vevo 2100 VisualSonics

This is dedicated Ultrasound system for small animal models (mice to rabbits) of disease.



This scanner is capable of all imaging modes found in clinical US scanners such as color Doppler, M-mode, 3D imaging and volume analysis but at much higher spatial resolution. It allows for rapid animal screening of tumor and other models. The higher resolution of this system will also allow for image-guided injection. B-Mode (2D) imaging for anatomical visualization and quantification, with enhanced temporal resolution with frame rates up to 740 fps (in 2D for a 4x4 mm FOV), and enhanced image uniformity with multiple focal zones. M-Mode is

for visualization and quantification of wall motion in cardiovascular research, single line acquisition allows for the very high-temporal (1000 fps) resolution necessary for analysis of LV function. Anatomical M-Mode is for adjustable anatomical orientation in reconstructed M-Mode imaging; software automatically optimizes field of view for maximum frame rate. Pulsed-Wave Doppler Mode (PW) is for quantification of blood flow. Color Doppler Mode is used for detection of blood vessels including flow directional information and mean velocities; as well as for identification of small vessels not visible in B-Mode. Power Doppler Mode is for detection and quantification of blood flow in small vessels not visible in B-Mode; increased frame rates allow for significantly faster data acquisition. Tissue Doppler Mode for quantification of myocardial tissue movement; for example in assessing diastolic dysfunction. Vevo MicroMarker® Nonlinear Contrast Agent Imaging can be used for quantification of relative perfusion & molecular expression of endothelial cell surface markers; enhanced sensitivity to Vevo MicroMarker contrast agents as linear tissue signal is suppressed. 3D-Mode Imaging is for anatomical and vascular visualization, when combined with either B-Mode, Power Doppler Mode or Nonlinear Contrast Imaging; allows for quantification of volume and vascularity within a defined anatomical structure. Digital RF-Mode is for the acquisition and export

tation of radio frequency (RF) data in digital format for further analysis; full screen acquisition provides a complete data set for more comprehensive analysis and tissue characterization. ECG and Respiration Gating is used to suppress imaging artifacts due to respiration and cardiac movements. Both are important in cardiac and abdominal imaging for both 2D and 3D data sets. Transducers: * MS-200 12.5 or 21 MHz, Depth from 2mm to 36mm *MS-250 16 or 21 MHz, Depth from 2mm to 30mm *MS-400 24 or 30 MHz, Depth from 2mm to 20mm *MS-550D 32 or 40 MHz, Depth from 1mm to 15mm <http://www.visualsonics.com/vevo2100>

Near IR Frangioni imager

This rodent scanner is designed to visualize cellular probes that fluoresce in the Near IR region which provides much better tissue penetration than traditional Green Fluorescent Proteins.

BMEII Research Laboratories

RF Coil Laboratory

The RF Coil Laboratory in BMEII was initially established in 2010. This fully equipped electronics lab is available for RF coil building and troubleshooting. The lab is equipped with vector network analyzers, oscilloscopes, a circuit board printer, 3D printers, a signal generators, DC power supplies, as well as other standard electronics equipment. BMEII core staff, trainees, and faculty have produced numerous custom RF coils and components for basic and translational research projects. These include coils for high resolution imaging at 7T of the human cervical spine cord, brainstem, carotid arteries, and body, as well as a dedicated coil for rabbit cardiac imaging. Recently, a passive wireless RF array for enhancement of RF fields in the central nervous system was designed, prototyped, and tested in the facility. In addition to RF hardware, users have also developed mechanical and electronic accessories that are utilized for specific experiments in the high magnet field environment of the MRI scanners.

Nanomedicine Laboratory

The Nanomedicine laboratory has 2 modules: the synthetic lab and the analytical / biochemistry / biology lab. We are able to synthesize established imaging reagents for supply and distribution. In the synthetic lab, there are 2 large synthetic chemistry hoods that can accommodate 4 synthetic chemists working simultaneously. Each scientist has individual bench space for work-up and for storing samples, reagents, buffers and the like. The analytical/biochemistry/biology lab has 2 smaller hoods for doing wet chemistry work. Both facilities have been equipped with state-of-the-art instruments to support the work. The synthetic lab is well equipped for investigators to perform small-scale syntheses of organic, inorganic and organometallic compounds for use in a multitude of imaging modalities as well as drug delivery nanoparticles. In addition, we are also capable of labeling peptides and antibodies with commercially available optical dyes, CT, or MR contrast agents.

Radiochemistry Laboratory

With the establishment of the BMEII, the nanomedicine program has expanded its facilities to include a radiochemistry suite on SC-1 in the dose preparation room. This has been a long-desired vision and goal for the team and facility, as now nano-platform design, synthesis, radioactive labelling, imaging, and biodistribution studies can all take place within the institute. This greatly reduces reliance on other institutions in the creation of new radioactive tracers and immunotherapeutic nanoscale platforms. Newly purchased equipment, such as an Shimadzu HPLC system (with UV and Radiodetectors), and a radioTLC system, were placed within the newly shielded bio-safety cabinet. Other new additions include vortexes, thermomixers, microfluidics pumps and chips, a microcentrifuge, and a new computer. These additions complement the dose calibration room, which already included two dose calibrators, a large centrifuge, storage for radioactive isotopes, and a computer dedicated for dose tracking, which will soon be the main hub for NMIS. SC-1 continues to be a full-stop

shop for in vivo imaging and biodistribution studies, and with the addition of the radiochemistry suite, our abilities to create novel therapies and diagnostic tools have been significantly bolstered. For more information on the radiochemistry suite, please reach out to a member of the nanomedicine team led by Assistant Professor Mandy Van Leent and Assistant Professor Abraham J. P. Teunissen. The Radiochemistry laboratory is also equipped with gamma counters and a dose calibrator.

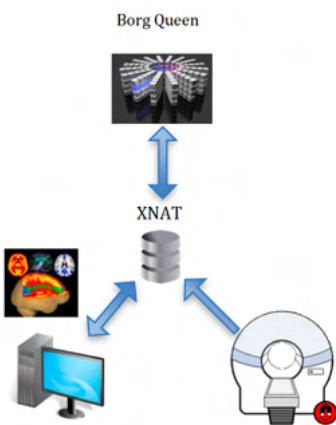
Bioinformatics and Data Processing

One of the main functions of BMEII is to provide the infrastructure for access to research imaging. A comprehensive set of imaging modalities are supported for both human as well as animal work. Scheduling support for access to the different scanners consists of web-based online calendars as well as live telephone scheduling support. BMEII also provides a central hub for image distribution and archival. There are 32TB of online storage where all imaging data is pushed to and distributed from. The capacity will be expanded annually as needed.

Image Analysis Support

BMEII provides image analysis for cardiovascular, body/oncological and neuro imaging. The image analysis for specific projects needs to be discussed directly with the BMEII core (contact BMEII Director Dr. Zahi Fayad.) This core consists of IT personnel, software engineers, imaging physicists, research assistants and other support personnel. Expert consultation for research projects including protocol design, specialized pulse sequences, special image acquisition hardware (coils), custom made functional MRI stimulus hardware are all supported. Comprehensive project based image analysis support is also provided. Modalities supported include PET, MRI, fMRI, DTI and its variants, resting state fMRI. Image analysis training is also supported for those researchers who want to learn more about image analysis in general. Training ranges from regular classroom based graduate course taught by BMEII faculty to hands on training on the use of specific software packages such as FSL, SPM, Brainvoyager and BMEII's own in house developed software packages in all areas (neuro, body, oncology and cardiovascular). The data center has a dedicated servers room which houses a larger Mac Server Cluster with 2 x 16TB of initial online storage with direct connectivity to all the imaging modalities in CSM. In addition, there is also an image analysis room equipped with large viewing display and high performance workstations open for the researcher to learn or perform image analysis.

BMEII XNAT



BMEII XNAT serves as the central point for research data transfer, archive, and sharing. BMEII XNAT is built upon a secure database, supports automated pipelines for processing managed data, and provides tools for exploring the data. Only users authorized by the study investigators can access their data. BMEII XNAT is fully HIPAA compliant. The BMEII XNAT team provides support for data migration between various DICOM repositories, HIPAA de-identification, image preprocessing, image quality control, and other customized services. Currently BMEII XNAT runs on two mirrored Linux servers with 60TB storage space on each. It can host more than 15,000 image sessions with backups. BMEII XNAT user training, documentation, and imaging data management consultations are available by request (<https://BMEII.mssm.edu/xnat>). A yearly service sup-

port contract has been established with the XNAT developer group from Radiologics Inc.

CPU/GPU Servers

BMEII-HPC-1 Server: Available for deep-learning, intensive image and data analysis, the BMEII-HPC-1 server is a NVIDIA DGX-1, comprising of a dual 20 core Intel Xeon 2.2GHz CPU, 512GB of RAM, 7TB of storage, eight NVIDIA Tesla V100 GPUs with a total 256GB of GPU RAM, 5,120 NVIDIA Tensor Cores and 40,960 NVIDIA CUDA Cores. BMEII-HPC-1 provides BMEII with the performance of 1 petaFLOPS. The server runs Ubuntu 18.04 and can support other OS through either Linux containers or virtual machines.

DGX-A100 Server: As BMEII continues to increase their AI and deep-learning capabilities, the NVIDIA DGX-A100 delivering up to 6x the training performance of the DGX-1. Comprising of dual 64 core AMD Rome 7742 2.25GHz CPUs, 1TB of RAM, 15TB of Gen 4 NVME SSD storage, eight NVIDIA A100 GPUs with a total 320GB of GPU RAM, 5,120 NVIDIA Tensor Cores and 40,960 NVIDIA CUDA Cores as of early 2021. DGX-A100 provides BMEII with the performance of 5 petaFLOPS AI and 10 petaFLOPS INT8. The server runs Ubuntu 18.04 and can support other OS through either Linux containers or virtual machines.

DGX-A100-2 Server: As BMEII continues to increase their AI and deep-learning capabilities, the NVIDIA DGX-A100-2 delivering up to 1.25x the training performance of the DGX-A100. Comprising of dual 256 core AMD EPYC 7742 64-Core Processor, 1.97TB of RAM, 28TB of Gen 4 NVME SSD storage, eight NVIDIA A100 GPUs with a total 640GB of GPU RAM, 5,120 NVIDIA Tensor Cores and 40,960 NVIDIA CUDA Cores as of early 2023. DGX-A100-2 provides BMEII with the performance of 9.7 petaFLOPS AI and 624 petaFLOPS INT8. The server runs Ubuntu 20.04 and can support other OS through either Linux containers or virtual machines.

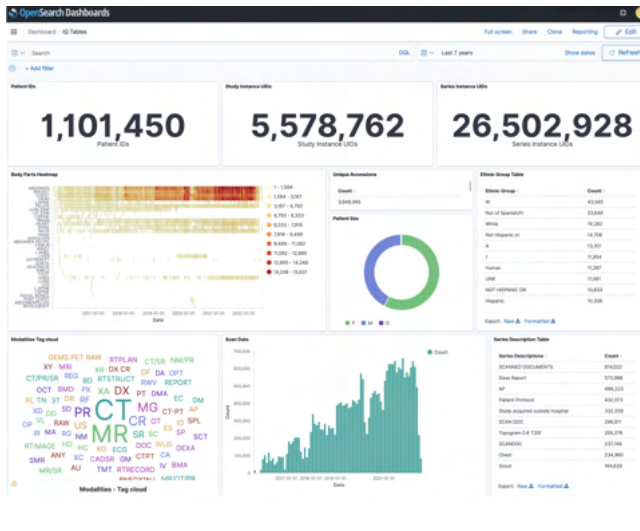
DGX-H100 Server: As BMEII continues to increase their AI and deep-learning capabilities, the NVIDIA DGX-H100 delivering up to 1.5x the training performance of the DGX-A100-2. Comprising of dual 256 core AMD EPYC 7742 64-Core Processor, 1.97TB of RAM, 28TB of Gen 4 NVME SSD storage, eight NVIDIA H100 GPUs with a total 640GB of GPU RAM, 5,120 NVIDIA Tensor Cores and 40,960 NVIDIA CUDA Cores as of early 2024. DGX-H100 provides BMEII with the performance of 10.6 petaFLOPS AI and 11 petaFLOPS INT8. The server runs Ubuntu 20.04 and can support other OS through either Linux containers or virtual machines.

Image reconstruction tools for PET and fast MR imaging

BMEII is equipped with a dedicated workstation for PET images reconstructions, such as the Siemens e7-tools and the open-source package STIR (<http://stir.sourceforge.net/>). The e7-tools are a collection of Microsoft Windows command line programs that allow the processing and reconstruction of Siemens PET emission data both using iterative and analytical algorithms. The software is capable of generating of other correction factors including attenuation, scatter and normalization. The software also allows for listmode histogramming and rebinning. The software is installed on an external computer to reconstruct PET images away from the scanners. STIR software on the other hand is an open source toolbox that offers

the same functionalities as the e7tools, but is not limited to the analysis of Siemens PET emission data. Also available is a dedicated workstation housing PET-SORTEO (Simulation Of Realistic Tridimensional Emitting Objects), a simulation tool that uses Monte Carlo techniques to generate realistic PET data from voxelized descriptions of tracer distributions, in accordance with the scanner geometry and physical characteristics.

Mount Sinai Imaging Research Warehouse (IRW)



The IRW is a platform intended to facilitate research by allowing researchers to gain open access to clinical medical imaging data and tie it to the Mount Sinai Data Warehouse (MSDW). HIPAA compliance is handled by providing a mirror of the Mount Sinai PACS in a de-identified/pseudo-anonymized state. Exams that are archived in Mount Sinai PACS, arising from an ORG that populates other data types to the MSDW, are sent to the IRW. All data in the IRW will use an alternative HIPAA-

compliant identifier that could be cleanly referenced to its associated data in the MSDW. IRW images are house on Minerva, Mount Sinai’s High Performance Computer platform. More information is also available online at <http://BMEII.mssm.edu>

Contact:

Zahi A. Fayad, PhD – Director, BMEII
 Zahi.fayad@mssm.edu
 (212) 824-8452

Christopher J. Cannistraci, MS
 Director, Research Operations
 Christopher.cannistraci@mssm.edu
 (212) 824-8466

Biographies of the Hosts

Zahi A. Fayad, PhD, FAHA, FACC, FISMRM

Director, BioMedical Engineering and Imaging Institute
Director, Cardiovascular Imaging Research
Lucy G. Moses Professor in Medical Imaging and Bioengineering
Vice-Chair for Research, Department of Radiology
Professor of Radiology and Medicine (Cardiology), and AI & Human Health
Icahn School of Medicine at Mount Sinai
New York, NY

Zahi A. Fayad, PhD serves as the Lucy G. Moses Professor of Medical Imaging and Bioengineering at the Icahn School of Medicine at Mount Sinai. He is Professor of Radiology (vice-chair for research) and Professor of Medicine (Cardiology). He is the founding Director of the BioMedical Engineering and Imaging Institute (ranked 15th in 2021 NIH funding in the field of Radiology). Dr. Fayad's research has been dedicated to the detection and prevention of cardiovascular disease with many seminal contributions in the field of multimodality biomedical imaging (MR, CT, PET and PET/MR) and nanomedicine. Recent emphasis of his research has been in: 1) The development of PET/MR methods to study cardiovascular diseases such as mitral valve prolapse and sarcoidosis; 2) the study of psychosocial stress exposure and other lifestyle (diet, exercise, sleep, mental health etc.) exposure effects on the brain, the cardiovascular system and the immune system; 3) the development of a platform to produce nanobiologics for immunotherapy in multiple disease conditions including cardiovascular disease, cancer and organ transplantation; 4) the development of the Mount Sinai Imaging Research Warehouse (de-identified, pseudo-anonymized images and metadata) as a unique repository of radiological imaging/reports for focused imaging and general healthcare research; and 5) the use of mobile health (wearables and apps) and advanced multimodal data acquisition and analysis (AI/ML) for the study of health and disease and the deployment of digital therapies like the Warrior Watch and Warrior Shield programs. Finally, as director of the BioMedical Engineering and Imaging Institute (BMEII) at Mount Sinai and director of Cardiovascular Imaging Research, Dr. Fayad oversees a diverse team of scientists and physicians composed of physicists, engineers, computer scientists, data



scientists, cardiologists, radiologists with combined expertise in MR, PET and CT imaging, AI/ML, digital health, and wearables.

He is Guest Editor for the Journal of the American College of Cardiology Imaging (JACC Imaging), Section Editor for Journal of the American College of Cardiology (JACC), Consulting Editor for Arteriosclerosis Thrombosis and Vascular Biology (ATVB), Guest Editor for the Journal of Cardiovascular Magnetic Resonance (JCMR) and past Associate Editor of Magnetic Resonance in Medicine (MRM). Editorial board member of JNC. From 2013-2017, he served as Charter Member, NIH Center of Scientific Review, Clinical Molecular Imaging and Probe Development Study Section. In 2015, he chaired the Scientific Advisory Board of the Institut National de la Santé et de la Recherche Médicale (INSERM) PARCC program at the HEGP in Paris. Currently, he serves on the NHLBI HLBP study section.

Dr. Fayad has authored more than 400 peer-reviewed publications (h-index of 129 accessed 09/01/2023 on Google Scholar with over 160,000 citations), 50 book chapters, and over 500 meeting presentations. He is currently the Principal Investigator of multiple federal, foundation and industry grants including 4 grants (2 R01s, 2 P01s) funded by the National Institutes of Health's National Heart, Lung and Blood Institute, National Institute of Allergy and Infectious Diseases and National Institute on Drug Abuse. Since 2021, Dr. Fayad ranked in the top 5 in NIH research overall funding in the field of Radiology. Dr. Fayad holds several patents related to his research and some of them have been licensed from Mount Sinai to a startup company (Trained Therapeutix Discovery focused on immunotherapy with nanotechnology and the innate immune system) where he serves on the board of directors.

Dr. Fayad had his engineering trainings at Bradley University (BS, Electrical Engineering '89), the Johns Hopkins University (MS, Biomedical Engineering '91), and at the University of Pennsylvania (PhD Bioengineering '96). From 1996 to 1997 he was junior faculty in the Department of Radiology at the University of Pennsylvania. In 1997 he joined the faculty at the Mount Sinai School of Medicine as Assistant Professor in Radiology and Medicine (Cardiology).

As a teacher and mentor, Dr. Fayad has been also extremely successful. He has trained over 100 postdoctoral fellows, clinical fellows and students. His trainees have received major awards, fellowships, and positions in academia and industry.

Dr. Fayad is the recipient of multiple prestigious awards including, but not limited to Fellow American Heart Association (2001), British Medical Association Book Award (2004), Fellow American College of Cardiology (2005), the John Paul II Medal, Krakow Poland (2007), Outstanding Teacher Award from the International Society of Magnetic Resonance in Medicine (2008), Honorary Professor of Nanomedicine, Aarhus Univ, Denmark (2009), Opening speaker at the 97th Scientific Assembly and Scientific meeting of the Radiological Society of North America (2011), Henry I Russek Lecture at the 45th Anniversary of the ACCF New York Cardiovascular Symposium (2012), Fellow International Society of Magnetic Resonance in Medicine (2013), Academy Radiology Research Distinguished Investigator (2013), Distinguished Reviewer award from Magnetic Resonance in Medicine (2013), Centurion Society Medal from Bradley University (2014), the Editor's Recognition Award, from the journal Radiology (2014), and the Lucy G. Moses Professor of Biogengineering & Medical Imag-

ing (2015), Dr. Joseph Dvorkin Memorial Lecturer at the Cardiac Research Day of the Mazankowski Alberta Heart Institute, University of Alberta, Edmonton, Canada (2015), Heart & Stroke/Richard Lewar lecturer at the Center of Excellence in Cardiovascular Research in Toronto (2016), Dr. Fayad's work on stress, the immune system and cardiovascular disease published in the Lancet was featured in the Altmetric Top 100 (2017), Highly Cited Researchers by Clarivate Analytics (2018, 2019, 2020, 2021,2022, 2023), and the Mount Sinai Jacobi Medallion Award (2019).

He is married to Monique P. Fayad, MBA and is the proud father of Chloé (21 year old) and Christophe (17 year old) and after spending seven years in Manhattan now lives in Larchmont, he runs in Central Park and participates regularly in New York Road Runners races. He also enjoys sailing and stand-up board paddling in Larchmont, New York, Connecticut, Rhode Island, Cape Cod, Martha's Vineyard, Nantucket, the Caribbean Islands and beyond. He follows a daily Crossfit training regimen (while wearing different sensors) and plays Tennis regularly with his wife Monique on the weekend.

Dennis S. Charney, MD

Anne and Joel Ehrenkranz Dean
Icahn School of Medicine at Mount Sinai
Executive Vice President for Academic Affairs
The Mount Sinai Medical Center
New York, NY



Dennis S. Charney is a preeminent expert in neurobiology who has made fundamental contributions to the understanding of human anxiety, fear, depression, and resilience. He has played a key role in the discovery of new treatments for mood and anxiety disorders, and remains a continual champion of rigorous, translational scientific efforts to improve patient care. Dr. Charney is Anne and Joel Ehrenkranz Dean of the Icahn School of Medicine at Mount Sinai and President for Academic Affairs for the Mount Sinai Health System.

Recruited to Icahn Mount Sinai as Dean of Research in 2004. He became the Dean of the School and Executive Vice President for Academic Affairs of the Mount Sinai Medical Center in 2007.

In 2013, Dr. Charney was also named President for Academic Affairs for the newly integrated Mount Sinai Health System, which includes eight hospitals throughout New York City. As the sole medical school partner within the Mount Sinai Health System, Icahn Mount Sinai now has one of the most expansive training and research footprints in the nation.

By recruiting exceptional faculty across the biomedical sciences, as well as in computational biology, genetics, artificial intelligence, information technology, and entrepreneurship, Dr. Charney has cultivated a supercharged, Silicon Valley-style atmosphere at Icahn Mount Sinai. Under his leadership, the School has emerged as a global leader in medical education.

Dr. Charney's commitment to hiring faculty who are innovative and ambitious researchers—as well as dedicated educators—is reflected by the fact that Icahn Mount Sinai is consistently among the nation's top recipients of National Institute of Health funding.

In 2020, to promote diversity and gender equity in medicine, Dr. Charney established the Mount Sinai Institute for Health Equity Research, which aims to advance health and access to care across the nation's demographic divide. The same year, Dr. Charney and Kenneth

L. Davis, MD, President and Chief Executive Officer of the Mount Sinai Health System, convened the Mount Sinai Health System Task Force to Address Racism. The Task Force built a roadmap, currently being implemented, to eliminate structural racism and inequities within Mount Sinai. This roadmap now serves as a national model for dismantling racism and bias in science, medicine, and medical education.

Early in his tenure as Dean, Dr. Charney unveiled a strategic plan that laid the foundation for the dozens of research institutes that Mount Sinai is known for today. Within and across these hubs of scientific and clinical enterprise, renowned scientists and physicians facilitate the development of effective treatments for the most serious medical conditions. By welcoming students into these institutes to work and study with such faculty, Icahn Mount Sinai prepares future researchers and clinicians to continually challenge the limits of science and medicine. This strategic plan is updated every year. Most recently, there have been major investments in genetics, including the Mount Sinai Million project, Immunology, including the establishment of a new department of Immunology and Artificial Intelligence (AI), including the establishment of the first department of AI and Human Health.

In recent years Dr. Charney has placed a particular emphasis in precision medicine. In 2019 Dr. Charney established a partnership with the Hasso Plattner Institute in Potsdam, Germany, to develop digital health products to advance precision medicine. In 2023, alongside Rensselaer Polytechnic Institute, Icahn Mount Sinai opened the Center for Engineering and Precision Medicine, an interdisciplinary partnership aimed at revolutionizing patient care through advances in engineering medicine.

Dr. Charney's career began in 1981 at Yale, where within nine years, he rose from Assistant Professor to Professor of Psychiatry with tenure, a position he held for a decade. While at Yale, he chaired the National Institute of Mental Health's (NIMH) Board of Scientific Counselors, effectively advising the Institute's director on intramural research programs. In 2000, NIMH recruited Dr. Charney to head its Mood and Anxiety Disorder Research Program—one of the largest programs of its kind—as well as the Experimental Therapeutics and Pathophysiology Branch.

Dr. Charney is considered one of the most innovative researchers in psychiatry. His research with colleagues at Yale, the National Institute of Mental Health, and Mount Sinai has led to more rapid treatments for treatment resistant depression (lithium augmentation; ketamine), Post Traumatic Stress Disorder (Ketamine), Rapid treatment for opioid withdrawal (clonidine and naloxone), rapid treatment of panic disorder (clonazepam and sertraline), and the first digital treatment for depression (emotional face memory task). His research on resilience has led to approaches to enhance human resilience to stress and trauma. The work demonstrating that ketamine is a rapidly acting antidepressant has been hailed as one of the most exciting developments in antidepressant therapy in more than half a century.

Dr. Charney is among the most highly cited medical researchers in the world. The 2023 Research.com ranking of the best researchers in all of medicine ranked Dr. Charney 46th in the United States and 64th in the world. Additionally, he was the highest ranked psychiatrist.

Dr. Charney is a member of the National Academy of Medicine since 2000 and has been

honored with every major award in his field for his scientific research.

A prolific author, Dr. Charney has written or co-authored more than 800 publications, including groundbreaking scientific papers, chapters, and books. According to Google Scholar, his publications have been cited over 185,000 times and his H factor is 221. His studies on human resilience, which identified ten key resilience factors for building the strength to bounce back from stress and trauma, are summarized in the celebrated *Resilience: The Science of Mastering Life's Greatest Challenges* (3rd ed.). Co-authored with Steven Southwick and Jonathan DePierro, the newest edition will be published by Cambridge University Press, September 2023.

Dr. Charney's other books include *Charney & Nestler's Neurobiology of Mental Illness* (Oxford University Press, USA, 6th ed., in press); *The Peace of Mind Prescription: An Authoritative Guide to Finding the Most Effective Treatment for Anxiety and Depression* (Houghton Mifflin Harcourt, 2004); *The Physician's Guide to Depression and Bipolar Disorders* (McGraw-Hill Professional, 2006); and *Resilience and Mental Health: Challenges Across the Lifespan* (Cambridge University Press, 2011).

Brendan Carr, MD, MA, MS

Chief Executive Officer of the Mount Sinai Health System
The Mount Sinai Medical Center
New York, NY

Brendan Carr, MD, MA, MS, the Chief Executive Officer of the Mount Sinai Health System, is nationally recognized as a leader in academic medicine and health policy. He is a visionary physician-scientist who will propel Mount Sinai to further success in its mission to provide compassionate patient care through unrivaled education, research, and outreach in the diverse communities it serves.

In partnership with the Boards of Trustees, Dr. Carr will chart a strategy for Mount Sinai and will oversee all critical strategic, operational, and business-building areas of the Health System, including its eight hospitals, the Icahn School of Medicine at Mount Sinai, and more than 400 ambulatory locations and physician practices. Dr. Carr, who has practiced clinical emergency medicine for more than 20 years, is a renowned emergency physician and health policy researcher. He has focused on building regional systems of emergency care, especially for trauma, stroke, cardiac arrest, and sepsis, and developing innovative delivery system solutions to create a more distributed and accessible acute-care delivery system. He has served in an advisory role to domestic and international organizations and is a member of the National Academy of Medicine.



Dr. Carr previously served on the faculty at the Perelman School of Medicine at the University of Pennsylvania and as an Associate Dean of the Sidney Kimmel Medical College at Thomas Jefferson University in Philadelphia. In addition to his academic accomplishments, Dr. Carr also served the U.S. Department of Health and Human Services in a variety of roles focused on improving trauma and emergency care delivery for the nation. Most recently, he was a special adviser on preparedness and response. In that capacity, his principal focus was on understanding how the emergency care infrastructure of the nation's health care system could be strengthened to ensure the ability to respond during large-scale threats to the public's health.

In his research, Dr. Carr initially focused on high-acuity care, but found that the full breadth of emergency care also includes lower-acuity care. As the health care delivery system has evolved, emergency medicine—including urgent care and telemedicine—has emerged as a

In his research, Dr. Carr initially focused on high-acuity care, but found that the full breadth of emergency care also includes lower-acuity care. As the health care delivery system has evolved, emergency medicine—including urgent care and telemedicine—has emerged as a

key home for unscheduled acute care. Integrating emergency care into this broader health care delivery system has launched new research portfolios focused on understanding the association between unscheduled care and population health, how payment and regulatory functions influence care utilization and outcomes, and how delivery system innovations can make health care more timely, efficient, and patient-centered.

Dr. Carr earned his medical degree from Temple University School of Medicine, and completed both his residency in emergency medicine and his fellowship in trauma and surgical critical care at the University of Pennsylvania. He is an alumnus of the Robert Wood Johnson Foundation's Clinical Scholars Program and holds master's degrees in both clinical psychology and health policy research. An accomplished researcher, he has authored more than 175 manuscripts, and has received funding from the National Institutes of Health, the Agency for Healthcare Research and Quality, the Centers for Disease Control and Prevention, and multiple foundations.

Panelist Profiles

1st Panel Session: Wellness, Screening, and Lifespan



Sarah Pesce, MSc
Chief Operations Officer
Thorne Lab

Sarah Pesce is the Chief Operating Officer at Thorne Lab. Thorne HealthTech is a leader in developing innovative solutions for delivering personalized approaches to health and wellness. As a science-driven wellness company that empowers individuals with the support, education, and solutions they need to achieve healthy aging. As a key member of the C-level operations team, Sarah overseeing strategic initiatives and contributing to Thorne's Lab operational excellence. Prior to joining Thorne HealthTech Sarah was COO of Lab100 at Mount Sinai. She is a board-certified Adult Nurse Practitioner, holds a Master of Science degree from Stony Brook University and a master's in healthcare Delivery Leadership from the Icahn School of Medicine. In 2020, Sarah was named by Crain Magazine as one of the Most Notable Women in Healthcare.



Nathan Price, PhD
Chief Scientific Officer
Thorne HealthTech

Dr. Nathan Price is Chief Scientific Officer of Thorne HealthTech and author of *The Age of Scientific Wellness*. Previously he was CEO of Onegevity, an AI health intelligence company that merged with Thorne in 2021. In 2019, he was named as one of the 10 Emerging Leaders in Health and Medicine by the National Academy of Medicine, and in 2021 he was appointed to the Board on Life Sciences of the National Academies of Sciences, Engineering, and Medicine. He spent much of his earlier career as Professor and Associate Director of the Institute for Systems Biology (now on leave), co-director with biotechnology pioneer Lee Hood of the Hood-Price Lab for Systems Biomedicine, and is Affiliate Faculty at the University of Washington in Bioengineering and Computer Science & Engineering. He is a Camille Dreyfus Teacher-Scholar, received the 2016 Grace A. Goldsmith award for his work pioneering 'scientific wellness', was a co-founder of Arivale, and received a Healthy Longevity Catalyst Award from the National Academy of Medicine in 2020. He has co-authored more than 200 peer-reviewed scientific publications and given over 200 talks and keynotes. He also served as Chair of the NIH Study Section on Modeling and Analysis of Biological Sys-

tems (MABS) and is a Fellow of the American Institute for Biological and Medical Engineering. Dr. Price is also the 2023 recipient of the Alexander & Mildred Seelig Award from the American Nutrition Association.



Sean London, MD

Lead Radiologist

Prenuvo

Dr. Sean London is a board certified Diagnostic Radiologist and the Lead Radiologist at Prenuvo with extensive expertise in the practice of whole-body MRI imaging. He earned his medical degree from the Ross University School of Medicine in 2013 graduating with high honors and completed his diagnostic radiology residency at the Medical College of Wisconsin Affiliated Hospital, Inc. Subsequently, he completed a body imaging fellowship at the University of Washington Medical Center. Since joining Prenuvo's Founding Radiology team in 2020, Dr. Lon-

don has been drawn to Prenuvo's comprehensive approach to healthcare, enabling patients to gain a holistic understanding of their health and bodies. He is also a vital contributor to Prenuvo's medical research efforts, co-authoring numerous medical abstracts. Outside of his medical career, Dr. London is an avid sports enthusiast and enjoys outdoor activities such as hiking and skiing alongside his family.



Thomas Witzel, PhD

VP of Radiomics & HW Engineering

Q Bio

Thomas Witzel is the Vice President of Radiomics and Hardware Engineering at Q Bio. He is an MRI scientist with an international reputation for his work in ultra-fast MRI, his work in developing new MRI techniques for detecting small electric currents in the brain directly, and his involvement in the Connector scanner, the most powerful brain imaging MRI scanner in the world today.

At Q Bio, he leads a team of scientist engineers developing image processing, image reconstruction, and novel MR imaging hardware. This team forms a unique group of talent with the sole purpose of recasting MRI into a new, fully vertically-integrated modality by re-approaching many traditional techniques anew from first principles.

Thomas started his career in MRI in 1996 where he started as a student assistant at the Leibniz Institute for Neurobiology in Magdeburg, Germany. In 1998, he moved to Massachusetts General Hospital in Boston, working at the NMR Center that would become the Martinos Center. He assumed the role of Director of the Human MRI core at the Martinos Center in 2011. Thomas also received his Ph.D. at the Harvard-MIT Division of Health Science and Technology for work on 20-fold accelerated echo-volume-imaging, allowing functional

imaging of the whole brain at frame rates below 100ms and the development of a technique capable of detecting electric currents similar to neuronal activations directly with MRI. On the side, he is also the owner and leader of the Open-source Console for Real-time Acquisition (OCRA) project, a low-cost, open-source console (hardware controller) for MRI used by many academic institutions around the world to teach the next generation of MRI scientists.



Giuseppe Petralia MD

Department of Oncology and Hemato-Oncology, University of Milan, Italy

Division of Radiology, Department of Medical Imaging and Radiation Sciences, IEO European Institute of Oncology IRCCS

Giuseppe Petralia is Professor of Radiology at the University of Milan and Director of the Division of Radiology at the European Institute of Oncology, Milan (Italy). The mission of this Division is to deliver the promise of personalized medicine to cancer patients, by using the most advanced imaging techniques in conjunction with clinical parameters and other biomarkers. His main research areas include prostate cancer (multiparametric

MRI, in-bore MRI-targeted biopsy) and whole-body MRI (prostate and breast cancer, multiple myeloma, and cancer screening in high-risk and general populations). He is author of more than 115 articles in peer-reviewed journals, 13 books and several book chapters and he is principal investigator in more than 25 clinical trials, some of them multicentric with international collaborations. Prof. Petralia is president of the MRI working group of the Italian Society of Radiology (SIRM), sits in the executive board of the International Cancer Imaging Society (ICIS) and he is deeply involved in teaching in national and international meetings.

2nd Panel Session: Accelerating the Clinical Translation of Nanotherapeutics



Daniel G. Anderson, PhD

Professor of Chemical Engineering and Institute for Medical Engineering and Science

Massachusetts Institute of Technology

Daniel G. Anderson is the Joseph R. Mares [1924] Professor of Chemical Engineering, and a core member of the Institute for Medical Engineering and Science and the Koch Institute for Integrative Cancer Research at MIT. He is a leading researcher in the fields of nanotherapeutics and biomaterials. Prof. Anderson's work has led to advances in a range of areas, including medical devices, cell therapy, drug delivery, gene therapy and material science, and has resulted in the publication of more

than 500 papers, patents, and patent applications. He has founded several companies, including Living Proof, Olivo Labs, Crispr Therapeutics (CRSP), Sigilon Therapeutics, Verseau Therapeutics, oRNA, and VasoRx. He is a member of National Academy of Medicine, the Harvard-MIT Division of Health Science and Technology, and is an affiliate of the Broad and Ragon Institutes.



Cristianne JF Rijcken, PharmD, PhD

CSO

Cristal Therapeutics and CEO Liberates

Cristianne is a serial life science entrepreneur, as apparent from 16+ years strategic and hands-on experience in various biotech companies. With a relentless and creative mindset, Cristianne spearheads startup's entrepreneurial journeys with primary focus on viable business cases. Hereto, she seamlessly manages the diverse elements from pure R&D to corporate funding, investor relationship, talent acquisition and team growth, intellectual property strategy, business development, strategic assessments and boardroom alignment. She trans-

forms scientific discoveries into commercially successful applications and drives a highly efficient development of innovative drug products to patient evaluation across diverse disease areas. Her core expertise is in nanomedicines in (immune-)oncology; and nowadays also experience with other advanced products in other therapeutic sectors.

As CEO of Liberates, she tackles complex challenges at life science startups with demonstrated ability to articulate long term strategy and focus, propose organizational change, and deliver operational excellence. Cristianne is founder of Cristal Therapeutics, and serves as Chief Scientific Officer of the company. She is inventor of 8 patents, (co-) author of 50 scientific publications, received numerous awards and is invited speaker at various biopharmaceutical conferences. Cristianne is passionate about the human body and how pharmaceutical

compounds can modify (the majority of) its functions, hence beneficially shifting into better health and longevity. She is pharmacist by training, holds a PhD degree in Pharmaceutics from Utrecht University and resides in Maastricht (both The Netherlands).



Daniel A. Heller, PhD

Head, Cancer Nanomedicine Laboratory, Member, Molecular Pharmacology Program, Memorial Sloan Kettering Cancer Center

Dr. Daniel A. Heller, PhD, is Head of the Cancer Nanomedicine Laboratory and Member of the Molecular Pharmacology Program in the Sloan Kettering Institute, and Co-Director of The Pat and Ian Cook Doctoral Program in Cancer Engineering at Memorial Sloan-Kettering Cancer Center. He is also Professor in the Department of Pharmacology at Weill Cornell Medicine. His work focuses on the development of nanoscale technologies for the research, diagnosis, and treatment of cancer. Dr.

Heller obtained his PhD in chemistry from the University of Illinois at Urbana-Champaign in 2010, working in the laboratory of Michael Strano. He completed a Damon Runyon Cancer Research Foundation Postdoctoral Fellowship in the laboratory of Robert Langer at the David H. Koch Institute for Integrative Cancer Research at MIT in 2012. He is a 2012 recipient of the National Institutes of Health Director's New Innovator Award, a 2015 Kavli Fellow, a 2017 recipient of the Pershing Square Sohn Prize for Young Investigators in Cancer Research, a 2018 American Cancer Society Research Scholar, a 2018 recipient of the CRS Nanomedicine and Nanoscale Drug Delivery Focus Group Junior Faculty Award, a 2018 NSF CAREER Awardee, a 2020 awardee of the Weill Cornell Graduate School Pharmacology Teaching and Mentoring Award, a 2021 American Institute for Medical and Biological Engineering (AIMBE) Fellow, and a 2023 awardee of the UM Ventures Life Science Invention of the Year.



Juliane Nguyen, PhD

Professor

University of North Carolina at Chapel Hill

Dr. Juliane Nguyen is Professor, Vice Chair, and Director of Graduate Admissions in the Division of Pharmacoengineering and Molecular Pharmaceutics at UNC at Chapel Hill. She leads an interdisciplinary lab that develops personalized biotherapeutics for cancer, myocardial infarction, colitis, and other diseases by merging cutting-edge molecular engineering with pharmaceutical sciences and bioinformatics. To date, Dr. Nguyen has secured more than \$16.4 million in research funding. She is also a biotech key opinion leader with several of her patents

licensed to biotech. Her work has been recognized with numerous awards including the CMBE Young Innovator Award (Biomedical Engineering Society), the New York STAR Faculty Award, the Emerging Leader Award from AAPS, the Pioneering Pharmaceutical Sciences by Emerging Investigators Award, and the National Science Foundation CAREER

Award. She was also awarded the Guest Professorship at ETH Zuerich by the Galenus Foundation. In 2023, she was elected to the College of Fellows of the Controlled Release Society underscoring her international leadership in the field. Dr. Nguyen received her Ph.D. in Pharmaceutical Sciences from the Philipps-University of Marburg (Germany). She then trained at the University of California, San Francisco (UCSF) under Dr. Frank Szoka as a Deutsche Forschungsgemeinschaft Postdoctoral Fellow. She is a standing member of the National Institutes of Health (NIH) Drug and Biologic Therapeutic Delivery study section. Moreover, Dr. Nguyen serves as the Executive Editor of Advanced Drug Delivery Reviews and holds the role of Associate Editor at Cellular and Molecular Bioengineering, both of which are internationally recognized journals in the field of drug delivery and biomedical engineering.

3rd Panel Session: The Importance of Accessible MRI for the World



Matthew Rosen, PhD

Associate Professor

MGH/Martinos Center for Biomedical Imaging, Harvard Medical School.

Dr. Matt Rosen is a physicist, tool-builder and inventor whose research bridges the spectrum from fundamental physics to applied bioimaging work in the field of MRI. He established the Low-Field MRI and Hyperpolarized Media Laboratory at the Athinoula A. Martinos Center for Biomedical Imaging to focus on the continued development of new hyperpolarization methods and MRI-based tools.

The Rosen Lab focuses on new methods and tools to enable unconventional approaches to MRI scanner construction. This includes the development of new acquisition strategies for robust ultra-low magnetic field implementations of MRI focused on brain imaging. The laboratory also explores opportunities provided by hyperpolarization including in vivo Overhauser DNP, SABRE and spin-exchange optical pumping. The lab creates new quantitative strategies for the acquisition and the reconstruction of highly under-sampled imaging data including neural network deep learning-based approaches such as AUTOMAP that leverage low-cost scalable-compute. Dr. Rosen co-directs the Center for Machine Learning at the Martinos Center. He is a Fellow of the American Physics Society and also the Kiyomi and Ed Baird MGH Research Scholar, and an Associate Professor of Radiology at Harvard Medical School. He is the Founder of five companies including Hyperfine, which has developed the world's first portable MRI scanner which can be used at the patient bedside by virtue of its operation at low magnetic field. He has served on the scientific advisory boards of nine companies since 2014.



Edmond A. Knopp, MD

Vice President

Medical Affairs, Hyperfine, Inc.

Over thirty years of experience in clinical care and research in radiology, neuroradiology, and MR imaging. Faculty at the New York University School of Medicine for over twenty years, including director of neuroradiology and associate chairman for quality, technology, and safety. Senior member of the American Society of Neuroradiology. Currently, the VP of Medical Affairs at Hyperfine, Inc, the manufacturer of the only FDA cleared ultra-low field portable MR brain imaging system. American Board of Radiology examiner. Editorial board member for many leading peer-reviewed publications. Awarded the American Board of Radiology Lifetime Service Award in 2015. Served as an advisor to the International Diagnostic Course

Davos - Neuroradiology, the world's largest medical imaging training course. Author of over eighty publications and speaker for hundreds of presentations worldwide. Emory University BS in Biology. SUNY Downstate Medical Center Doctor of Medicine.



Marc Dubois, PhD

Chief Executive Officer

Multiwave Imaging, Aix-Marseille Université, France

Marc Dubois received his engineering degree from the Ecole Centrale Méditerranée. He received his PhD from the Université Paris Diderot, focusing on waves in complex media and metamaterials at the Institut Langevin. He continued his research on acoustic metamaterial at the University of California Berkeley, joining Professor Xiang Zhang's lab. In 2017, he joined the Institut Fresnel in Marseille to develop novel radiofrequency metamaterial technologies for ultra-high field magnetic resonance imaging. Marc Dubois joined Multiwave Imaging in 2020 as Head of Research. In 2021, he was appointed CEO of the company, leading a team of 15 employees to improve patient throughput and image quality for High field and Ultra-High field MRI scanners with new RF coil technologies. In parallel, he led the development of the ultra-portable low-field MRI scanner MGTNQTM with the ambition to improve access to MRI technologies worldwide. Since 2024, Marc Dubois holds a Chair Professeur Junior with Aix-Marseille Université. He works to strengthen research partnerships between Multiwave Imaging and academic institutions.

4th Panel Session: Sustainable Futures, Healthier Outcomes: Navigating AI's Impact in Healthcare



Lawrence N. Tanenbaum, MD, FACR

VP and Chief Technology Officer

Radnet Inc

Dr. Tanenbaum is the Vice President, Chief Technology Officer and Director of Advanced Imaging at Radnet Inc. (since 2015), having come from Icahn School of Medicine at Mount Sinai in New York where he attended in Neuroradiology and served as an Associate Professor of Radiology, Director of MRI, CT and Outpatient / Advanced Imaging Development since 2008. Prior to that he spent over 20 years in the private practice of Radiology at the JFK Medical Center / New Jersey Neuroscience Institute as Director of MRI, CT and Neuroradiology. Dr. Tanenbaum is a senior member of the American Society of Neuroradiology, and long-term member of the Radiological Society of North America. He is a past President of the Eastern Society of Neuroradiology, and the national Clinical Magnetic Resonance Imaging Society and former Editor in Chief of their Journal Vision. He is a member of the Roster of Distinguished Scientific Advisors of the RSNA as well as several panels and committees of the American College of Radiology including the Expert Panel on Neuroimaging and the CPI / Neuroradiology Expert Review Panel. Dr. Tanenbaum is a member of the editorial boards of several journals and educational organizations and is a columnist and Associate Editor for Artificial Intelligence of Applied Radiology. Dr. Tanenbaum is a long-term collaborator with the medical imaging industry and chairs several advisory boards (OEM, pharma, and AI). He has interests in developing applications of AI and machine learning, contrast agents, MR, CT and advanced rendering. Dr. Tanenbaum is passionate about advancing the clinical practice of medicine focusing on patient centric care, efficiency, radiation dose and physiologic imaging. He is an active educator with interests in advanced imaging and innovative value-adding applications in the spine and brain. He has authored over 100 scholarly and peer reviewed articles which have been cited over 1300 times, continues to chair educational and academic meetings and has delivered close to 2000 invited lectures around the world.



Zichen Wang, Ph.D

Senior Applied Scientist

Amazon Web Services

Zichen Wang is a senior applied scientist at Amazon Web Services (AWS) AI Research and Education. He has been working on various research areas in artificial intelligence including graph machine learning, large language models and multi-modal learning, with a focus on their applications to healthcare and life sciences industries, particularly in structural-based drug discovery. He received his Ph.D. degree in Computational Biology from Icahn School of Medicine at Mount Sinai in New

York, NY in 2016, advised by Professor Avi Ma'ayan. He continued his research in biomedical networks, systems pharmacology, and machine learning for healthcare as a postdoctoral fellow and a research-track assistant professor at Mount Sinai. He then worked as a principal scientist at Sema4 to study the genome-phenotype interactions and health outcomes using large-scale data from the electronic health records. In 2021, he joined AWS to continue his research in machine learning for biomedicine. He has made contributions in many areas of biomedical informatics including bioinformatics software development, drug discovery, functional genomics, clinical informatics, and protein function prediction. He published over 60 peer-reviewed articles in prestigious journals and conferences such as Nature Medicine, Nature Communications, Nucleic Acids Research, and International Conference on Learning Representation.

Rima Arnaout, MD

Associate Professor

University of California, San Francisco



Dr. Rima Arnaout is Associate Professor of Medicine, Radiology and Pediatrics, a Chan Zuckerberg Biohub investigator, and faculty in the Bakar Computational Health Sciences Institute and the Center for Intelligent Imaging at UCSF, as well as the UCSF-UC Berkeley Joint Program in Computational Precision Health. She is investigating whether machine learning can be used to detect standard and novel patterns in biomedical imaging in a scalable fashion, with the goals of decreasing diagnostic error in medical imaging and uncovering new phenotypes for precision medicine research.

She is an American Institute for Medical and Biological Engineering Fellow and an Emerging Leader in Healthcare and Medicine at the National Academy of Medicine. Dr. Arnaout completed her undergraduate degree at MIT, her MD at Harvard Medical School, residency at Massachusetts General Hospital, and cardiology fellowship at UCSF.

David C. Rhew, MD

*Global Chief Medical Officer (CMO) and VP of Healthcare
Microsoft*



David Rhew is Microsoft's Global Chief Medical Officer & VP of Healthcare. He has served as Microsoft's International Coordinator for the Pandemic Response, where he worked with WHO to develop their World Health Data Hub, CDC to standup their vaccine data lake, and U.S. states to roll-out COVID-19 vaccines.

He is Adjunct Professor at Stanford University; holds six U.S. technology patents that enable authoring, mapping, and integration of clinical decision support into electronic health records; and has been recognized as one of the 50 most influential clinician executives by Modern Healthcare.

Dr. Rhew received his Bachelors of Science degrees in computer science and cellular molecular biology from University of Michigan. He received his MD degree from Northwestern University and completed internal medicine residency at Cedars-Sinai Medical Center. He completed fellowships in health services research at Cedars-Sinai and infectious diseases at UCLA.

He has served as CMO and VP for Samsung; and SVP and CMO at Zynx Health. David has served on National Quality Forum's Executive CSAC Board and chaired the Consumer Technology Association's Health Technology Board. He currently sits on AdvaMed's Digital Health Board and the Governing Committee for NESTcc, the medical device advisory group for FDA, CMS, and NIH.

5th Panel Session: MRI Tesla Wars



Thomas Vaughan, Jr., PhD

*Professor of BioMedical Engineering and Radiology,
Director of Columbia MR Research Center, PI in Zuckerman
Mind Brain Behavior Institute, Columbia.*

Thomas Vaughan has dedicated his career to advancing MR technology and applications to higher fields in search of higher SNR for human imaging and spectroscopy. Beginning with building the first home-built 1.8 T system at UT Southwestern in 1984, he has served as lead engineer and later PI on benchmark 4T, 7T, 9.4T and 10.5T first-of prototypes for Philips/UAB, Harvard/MGH and U. Minnesota respectively, sites where he helped to establish, fund and build prominent centers around this technology. He is now Professor and Founding Director of the Columbia MR Research Center and a PI at the Nathan Kline Institute where he is building an NSF sponsored, second generation 9.4T human neuroimager together with GE Global Research. Dr. Vaughan has authored or edited 165 articles, 60 patents and 3 books in his field, and is a fellow of IEEE, ISMRM and AIMBE.



Nicolas Boulant, PhD

*University of Paris-Saclay
CEA, NeuroSpin, France*

Dr. Nicolas Boulant did his PhD in NMR quantum computing at MIT (2000-2005, Cambridge, Massachusetts). After a two-year post-doctoral period at the Atomic Energy Commission (CEA) on solid-state physics (2005-2007), he switched to MRI at NeuroSpin-CEA to first work on data acquisition methods at Ultra-High Field. The focus of his research was for more than 10 years the mitigation of the radiofrequency field inhomogeneity problem with parallel transmission at 7T. He spent 6 months as a visiting scientist at CMRR at the University of Minnesota to work at 10.5T in 2014. Since 2018, he has been the head of the 11.7T human MRI project, and is responsible for solving the scientific, organizational, safety and regulatory issues. In this context he also leads the AROMA European Consortium (<https://aroma-h2020.com/>) aiming at tackling the pillar physics challenges of 11.7T. He is also deputy editor of Magnetic Resonance in Medicine and member of the Skope MRT and Dynamic 14T project scientific advisory boards. He is currently spending a year at the University of California in Berkeley as a visiting scientist. His main research focus now is to optimize data acquisitions at 11.7T to serve neuroscience applications.



Himanshu Bhat, PhD

*Head of MR R&D Collaborations, North America
Siemens Healthineers*

Himanshu is currently Head of the MR R&D Collaborations team for Siemens Healthineers in North America. He earned his Bachelor's and Master's degrees in Electrical Engineering from University of Pune and University of Houston in 2004 and 2006 respectively. He earned his PhD in Biomedical Engineering in 2010 from Northwestern University working with Prof. De-biao Li and coming up with novel MRI sequences and image reconstruction methods for cardiac imaging. Since then he has been at Siemens Healthineers in the MR R&D team in various capacities. His research interests lie in the development of novel MRI sequences and reconstruction methods to solve clinically relevant problems. This requires detailed knowledge of MRI physics, software development, and the underlying anatomy and physiology. As a leader of the Siemens MR R&D Collaboration organization in the US he is in the unique position to bridge the gap between academic research and product development. The overall goal of his team is the development, validation and implementation of new and improved MRI techniques, in collaboration with academic partners. His personal goal is to identify and focus on collaborative projects which have the potential to impact routine clinical care and drive them towards product development. One example of this is his contribution to the Simultaneous Multi Slice project where he was one of the key persons involved from the initial prototyping stage to the final FDA cleared product. Himanshu has over 30 peer reviewed publications and over 25 patents all in the MRI methods development field.



Bram Stolk, PhD MBA

*Vice President, Academic Accounts
United Imaging*

Strategic partnerships are a cornerstone of any company's long term sustainable success. Bram brings almost 30 years of experience in developing medical imaging products, with extensive work in sales management, product development, and collaborations management. He has a passion for developing, nurturing, and leveraging strategic partnerships so that all parties benefit from aligning strategic goals.

Bram started his career in medical imaging at The Johns Hopkins University School of Medicine after receiving an NIH post-doctoral fellowship in Radiological Oncological Imaging. He went on to lead initiatives in MRI development as a Product Manager and Principal Scientist at Otsuka Electronics in Fort Collins. Returning to the academic world, Bram then managed the Small Bore Animal MR Imaging Facility in the department of Radiology at the University of Utah. After attaining his eMBA, Bram spent the next 25 years at Marconi Medical Systems, Siemens Healthineers . and GEHC in various sales, research, and strategic partnership roles. Noteworthy is Bram's role as Sr. Director MR Collaboration in the US at Siemens Healthcare, and as VP and General Manager Global Research and Collaborations at GEHC. Prior to joining United Imaging

Healthcare as VP of Academic Alliances, Bram was Senior VP of Sales for Flywheel Exchange, LLC, exploring the world of data management and aggregation for AI research and development.

Bram holds a Ph.D in Medicinal Chemistry from the University of Utah, Salt Lake City and an Executive MBA from the University of Utah. Bram, who has two children, lives in McAllister, MT with his wife and two dogs and two horses. In his spare time, Bram enjoys riding horses, hiking and reading.

6th Panel Session: Revolutionizing Healthcare: Pioneering the Future of Digital Medicine



Jagmeet P. Singh MD, ScM, DPhil

Professor of Medicine

Harvard Medical School Cardiology Division, Massachusetts General Hospital

Jag Singh is a Professor of Medicine at Harvard Medical School. He is the former Clinical Director of the Cardiology Division and Roman W. DeSanctis Endowed Chair in Cardiology at Mass General Hospital. He is also the Founding Director of the Resynchronization and Advanced Cardiac Therapeutics Program, at the Massachusetts General Hospital Heart Center. Dr. Singh received his medical degree from Pune University, India and completed his internal medicine residency, cardiology and cardiac electrophysiology fellowships at Mass General Hospital. He also earned a doctorate from Oxford University, a Master of science in clinical investigation from MIT-Harvard and a research fellowship at the Framingham Heart Study. Dr. Singh has over 400 peer reviewed publications and has given over 600 invited lectures at national and international conferences. He has served as an International Associate editor for the European Heart Journal, the former Deputy Editor of the Journal of American College of Cardiology: Clinical EP and Editor-in-chief of the Current Treatment Options in Cardiovascular Medicine. Dr. Singh's is the national & global principal investigator on 6 ongoing multi-center clinical trials in device therapy and sensor strategies for heart failure and atrial fibrillation. Much of his current efforts are focused on healthcare redesign, digital health, and medical device innovations.

Jag is a member of the Board of Trustees of the Heart Rhythm Society. He is the author of the recently published book, *Future Care: Sensors, Artificial Intelligence, and the Reinvention of Medicine*.



Emily Capodilupo

*Senior Vice President of Data Science and Research
WHOOP, Inc.*

Emily Capodilupo is the Senior Vice President of Data Science and Research at WHOOP, Inc.

She was the company's first full-time employee and first scientist. Before joining WHOOP in 2013, she studied Neurobiology at Harvard University and studied circadian biology in the Analytical and Modeling Unit of the Division of Sleep Medicine at Harvard's Brigham and Women's Hospital.

As a runner and former gymnast, Capodilupo's work now revolves around creating algorithms to optimize human perfor-

mance using physiological data at WHOOP. She also oversees research that discovered novel findings such as predicting risk for COVID-19 and modulating training according to the menstrual cycle's hormonal fluctuations.

Despite the success of Title IX, female representation in research remains generations behind. According to a study done on sport and exercise science research conducted between 2014 and 2020, just 6% of athletic performance research focuses on females.



Lisa Shah, MD
Chief Medical Officer
Twin Health

Dr. Lisa Shah is the Chief Medical Officer for Twin and a board certified internist and pediatrician. At Twin, she oversees clinical operations, care delivery, and innovation to reverse, improve, and prevent chronic metabolic diseases and significantly impact reductions in healthcare cost while improving experience. Dr. Shah has over a decade of hands-on experience in healthcare and innovation, from designing value-based care models to leading the implementation of new care delivery models in the practice setting. Prior to joining Twin Health, Dr. Shah

served as CMO for Advantia Health, Chief Innovation Officer for Sound Physicians, and SVP of Clinical Operations and Network for Evolent Health. Dr. Shah graduated from Duke University with a BA in English. She completed medical school at the University of Medicine and Dentistry of New Jersey and a residency in Internal Medicine and Pediatrics at the University of Chicago. Subsequently, she completed a health services research fellowship in the prevention and elimination of chronic disease at the University of Chicago. She also holds a Masters in Public Policy from the University of Chicago. Dr. Shah belongs to Women of Impact in Healthcare and has received multiple awards from the Washington Business Journal, including the annual C-Suite award in 2019.



Walter Greenleaf, PhD
Neuroscientist
Stanford University Virtual Human Interaction Lab

Walter Greenleaf, PhD. is a neuroscientist and a medical technology developer working at Stanford University. With over 35 years of work focused on developing clinical applications of medical virtual reality technology, Walter is considered a leading authority. Walter is currently a Visiting Scholar at Stanford University's Virtual Human Interaction Lab.

He also works to develop next-generation wearable sensors as part of the eWear Program at the Stanford School of Engineering.

He previously served as the Director of the Mind Division at the Stanford Center on Longevity,

where his focus was on age-related changes in cognition. Walter was the founding Chief Science Officer for Pear Therapeutics and is the Chief Science Officer for Interaxon. In addition to his academic work, Walter is the technology and neuroscience advisor to several early-stage medical product companies and accelerator/incubator programs.



Nicole Zahradka, PhD

Senior Clinical Research Program Manager

Best Buy Health

Dr Zahradka designs and implements studies to measure the clinical, financial and operational impact of virtual care. She received her PhD in Biomechanics and Movement Science from the University of Delaware and has a background in Mechanical Engineering. Her previous research at Johns Hopkins University focused on wearables, data science, and clinical care. Dr Zahradka has expertise in leading clinical research studies that utilize digital technology to remotely monitor patients and deliver interventions across the care continuum.

Professional Development Panel



Julia Zhao, PhD

Global Director of Operations

Nucleate Bio

Julia Nanyi Zhao serves as the Global Director of Operations at Nucleate Bio, where she propels the nurturing of scientist entrepreneurs and biotech innovation in over 30 international regions. With a Ph.D. in Biomedical Sciences from the Mount Sinai School of Medicine, her extensive background includes healthcare consulting and biotech venture capital positions at Johns Hopkins Medicine International, The Dorenfest China Healthcare Group, and Catalio Capital Management. There, she led key initiatives to enhance global healthcare collaboration, streamline operations, and foster investments in groundbreaking life science startups. Julia's journey from research scientist to strategic leader in a biotech nonprofit is distinguished by her efforts to fortify the biotech community, support its innovators and investors, and bolster Nucleate's mission of empowering the next generation of biotech leaders.



Nathaniel Swinburne, MD

Director of Radiology Informatics

Memorial Sloan Kettering Cancer Center

Dr. Nathaniel Swinburne, MD, is the Director of Radiology Informatics and a clinical neuroradiologist at Memorial Sloan Kettering Cancer Center (MSKCC), bringing a unique blend of expertise in computer science and clinical radiology to his role. After graduating from Tufts University with a bachelor's degree in computer science in 2002, he embarked on a successful career as a systems engineer and business analyst, accumulating six years of invaluable experience in the field.

Motivated by a desire for a career in medicine, Dr. Swinburne completed a premedical post-baccalaureate program in 2005-7 while employed as an engineer. This career change culminated in the completion of a Doctor of Medicine degree from Albert Einstein College of Medicine in 2012. Following a transitional internship at Sound Shore Medical Center, he completed a residency in radiology and a fellowship in neuroradiology at the Icahn School of Medicine at Mount Sinai, joining MSKCC as faculty in 2018.

As the Director of Radiology Informatics for MSKCC, Dr. Swinburne leads the Radiology Informatics Team, focusing on applying technology to improve workflow efficiency and advance artificial intelligence and big data oncology research. In this role he also leads major clinical IT infrastructure projects, including MSKCC's transition from a legacy PACS to a modern cloud based PACS, and provides departmental leadership for MSKCC's transition to the Epic platform. His translational research prioritizes the use of data mining with semi-supervised

learning to accelerate the development and deployment of radiology computer vision models.



Stephen José Hanson

Rutgers University

Psychology, RUBIC

Stephen José Hanson is Full Professor of Psychology at Rutgers University and Director of Rutgers Brain Imaging Center (RUBIC). He has been Department Chair of Psychology and the Department Head of Learning Systems Department at SIEMENS Corporate Research and a research scientist in the Cognitive Science Laboratory at Princeton University. He has held positions at AT&T Bell Laboratories, BELLCORE (AI and Information Sciences Department), SIEMENS Research, Indiana University and Princeton University . He has done modeling in a number of diverse areas including animal learning theory (conditioning theory), human-computer interaction, behavioral genetics, complex skills learning, and neural network learning algorithms. His core research is focused on learning and computational mechanisms of brain functions. He has studied and published over 150+ (7000+ citations) papers and book chapters as well as edited books on learning in humans, animals and machines. He was General Chair (1992) for Neural Information Processing Conference and elected to the NIPS foundation board in 1993 where he is still on the Advisory Board, he was also a founding member of the McDonnell-Pew Cognitive Neuroscience Advisory Board which for over a decade helped launch the fields of Cognitive Neuroscience and Computational Neuroimaging.

Moderators



David Luu, MD

CEO of Hearty Longevity Clinics

Founder of Longevity Docs Network

Dr. David Luu is a longevity-focused cardiac surgeon, entrepreneur, and philanthropist. He is the founder of Hearty, a longevity care platform and clinic; Absolutys, a healthcare venture studio; and Longevity Docs, a global network uniting medical leaders in precision and evidence-based longevity medicine. Dr. Luu is the founding chairman of The Heart Fund, a United Nations ECOSOC accredited non-profit organization democratizing cardiac care in developing countries. He is an

international speaker and educator on longevity, technology, and global health.



Abraham (Bram) Teunissen, PhD

Assistant Professor

BioMedical Engineering and Imaging Institute

Abraham (Bram) Teunissen received M.Sc. and Ph.D. degrees in Molecular Engineering from the Eindhoven University of Technology in 2017. Between 2017 and 2019, Dr. Teunissen was a postdoctoral fellow in the Mulder lab at the Icahn School of Medicine at Mount Sinai. Here, his work focused on developing novel nanotherapeutics and employed these to treat and study various conditions, including atherosclerosis, myocardial infarction, stroke, cancer, and SARS-CoV-2. Afterward, Dr. Teunissen was promoted to Instructor and later to

Assistant Professor (2022) at the same institution. Dr. Teunissen also founded and now directs the radiochemistry facility at Mount Sinai's Biomedical Engineering and Imaging Institute (BMEII). His current work involves developing nanotherapeutics and nuclear imaging strategies for modulating the innate immune system under imaging guidance, with a strong focus on organ transplantation and cancer. Dr. Teunissen also has appointments at Mount Sinai's Cardiovascular Research Institute and Icahn Genomics Institute.



Akbar Alipour, PhD

Assistant Professor

BioMedical Engineering and Imaging Institute

Akbar Alipour is an Assistant Professor of Biomedical Engineering in Radiology at the Icahn School of Medicine at Mount Sinai. He received his PhD degree in Electrical and Electronics Engineering from Bilkent University in 2017, with a focus on implantable medical devices. After completing his PhD, he worked as a postdoctoral fellow at Johns Hopkins University School of Medicine and Biomedical Engineering, where he developed devices for interventional MRI applications. In 2019, he joined the Icahn School of Medicine at Mount Sinai, BioMedical Engineering and Imaging Institute, where he specializes in ultra-high field (UHF) MRI techniques.



Hayit Greenspan , PhD

Professor in the Department of Diagnostic, Molecular, and Interventional Radiology

BioMedical Engineering and Imaging Institute

Dr. Greenspan received the B.S. and M.S. degrees in Electrical Engineering (EE) from the Technion, and the Ph.D. degree in EE from CALTECH – California Institute of Technology. She was a Postdoc with the CS Division at U.C. Berkeley following which, in 2000, she joined Tel-Aviv University. From 2008 until 2011, she was a visiting Professor at Stanford University, Department of Radiology, Faculty of Medicine. She was also a visiting researcher at IBM Research in the Multi-modal Mining for Healthcare group, in Almaden CA. In 2021 she joined the Department of Radiology at the Biomedical Engineering and Imaging Institute (BMEII), Icahn School of Medicine at Mount Sinai. She is a Co-Director of AIET PhD Program. Dr. Greenspan has over 200 publications in leading international journals and conferences and has received several awards and patents. She is member of several journal and conference program committees, including SPIE medical imaging, IEEE-ISBI and MICCAI.



Xueyan Mei, PhD

Instructor

BioMedical Engineering and Imaging Institute

Dr. Mei received a Ph.D. degree in Biomedical Sciences from the Icahn School of Medicine at Mount Sinai (ISMMS) in 2021. She was a Postdoctoral fellow at the BioMedical Engineering and Imaging Institute at ISMMS and supported by an NIH NRSA grant from CTSA at ISMMS during her training. In 2023, she joined the Department of Radiology at ISMMS as an Instructor. She has published in leading professional journals, including Nature Medicine, Nature Communications, and Radiology: Artificial Intelligence. She is on the Trainee Reviewer

Board of the journal Radiology: Artificial Intelligence from 2022.



Priti Balchandani, PhD

Professor

BioMedical Engineering and Imaging Institute

Priti Balchandani, PhD, is a Professor of Diagnostic, Molecular and Interventional Radiology, Neuroscience and Psychiatry. She is the Director of the Advanced Neuroimaging Research Program (ANRP) and Associate Director of the BioMedical Engineering and Imaging Institute (BMEII). She is also the Co-Director of the Center for Engineering and Precision Medicine (CEPM), the first joint center between Icahn School of Medicine at Mount Sinai and Rensselaer Polytechnic Institute. Her research has been focused on bridging gap between advanced electrical engineering techniques and medical imaging applications. Dr. Balchandani received her BASc in computer engineering at the University of Waterloo in Canada and her PhD in electrical engineering at Stanford University.



Yun Soung Kim, Ph.D

Assistant Professor Department of Radiology

BioMedical Engineering and Imaging Institute

Dr. Kim is an Assistant Professor of Radiology in the BioMedical Engineering and Imaging Institute at the Icahn School of Medicine at Mount Sinai. His research is centered on the development of compliant, low-profile, and wireless sensors designed for seamless integration with the skin, enabling continuous monitoring of various health parameters. He earned his BS and MS degrees in Materials Science and Engineering from the University of Illinois at Urbana-Champaign in 2009 and 2012, respectively, followed by a PhD in Bioengineering from the University of California San Diego in 2017. In 2021, Dr. Kim completed his postdoctoral training at Georgia Institute of Technology, where he served as a research faculty until 2022. Utilizing a broad spectrum of emerging manufacturing technologies—including MEMS, printing, laser micromachining, and electronic chip integration—Dr. Kim is dedicated to transforming the concepts of smart medicine and human-machine interfaces into practical devices for use in both clinical and home environments.



Vivek Yadav

Ph.D. Student

Icahn School of Medicine at Mount Sinai

Vivek Yadav is a 1st year PhD Student in Artificial Intelligence and Emerging Medical Technologies at the Icahn School of Medicine at Mount Sinai. His research interests lie in the applications of novel Deep Learning Technologies in the field of Multimodal Medical imaging. Leveraging his background in Computer Science, research focuses on applications of supervised, unsupervised, and reinforcement learning methods to a diverse range of domains and problems involving disease diagnosis

and prognosis.

Vivek has a BE(Hons) in Computer Science from BITS Pilani, India, an MS in Computer Science from Courant Institute of Mathematical Sciences, New York University. Prior to enrolling in the Ph.D. program, he conducted research at Memorial Sloan Kettering Cancer Center (MSKCC), in collaboration with Dr. Nathaniel Swinburne addressed the creation of automated tumor detection and segmentation models which bypass the need for de novo image labeling. He also did research under Dr. Stephen Hanson at the Rutgers Brain Imaging Center focusing on trying to understand the Dynamics of Deep Learning.



Hannah Kittrell

Ph.D. Candidate

Icahn School of Medicine at Mount Sinai

Hannah Kittrell is a Registered Dietitian, ACSM-certified Exercise Physiologist, and in her 3rd year of the Ph.D. program in Artificial Intelligence and Emerging Medical Technologies at the Icahn School of Medicine at Mount Sinai. Her research interests are at the intersection of nutrition, genetics, and machine learning. Integrating her nutrition and exercise physiology background into the framework of precision medicine, her dissertation utilizes unsupervised learning to identify data-driven phenotypes of dietary intake and exercise patterns and

model their association with cardiometabolic disease. The goal of her work is to develop personalized primary prevention strategies by taking an individuals' genetics, inherent physiology, and environment into consideration when prescribing diet and/or exercise.

Hannah has a BS in Integrative Neuroscience from Binghamton University, an MS in Nutrition and Exercise Physiology from Teachers College, Columbia University, and completed her dietetic internship at The Ohio State University. Prior to enrolling in the Ph.D. program, she worked as a research dietitian for the Charles Bronfman Institute for Personalized Medicine where she performed in vivo metabolic deep phenotyping to assess body composition, defects in functional substrate selectivity, and whole-body metabolism and their role in type 2 diabetes and obesity.

Selected for oral presentations

Chief Editor



Shams Rashid, PhD.

Instructor

BioMedical Engineering and Imaging Institute

Shams Rashid, PhD, is an Instructor of Radiology at BMEII in the Icahn School of Medicine at Mount Sinai. He completed his undergraduate studies in Electrical Engineering at the City College of New York (CCNY) and received his PhD in Biomedical Engineering from Stony Brook University. He trained as a postdoctoral scholar at the University of California Los Angeles, specializing in Cardiac MRI. He received an Early Career Award from the Society of Cardiovascular Magnetic Resonance (SCMR) and a Postdoctoral Fellowship award from the

American Heart Association (AHA) for developing the Wideband LGE technique for artifact-free scar imaging of patients with implanted cardiac devices. His research interests include COVID-19, Alzheimer's disease and epilepsy. At BMEII, he focuses on MRI pulse programming and RF pulse design in Translational Neuroimaging with 7T MRI, pertaining to COVID-19, Alzheimer's disease and epilepsy. He also contributes collaboratively to Cardiovascular MRI. He spends his free time designing space pirate treasure maps for his toddler daughters and attempting to brew the perfect coffee.

Review Committee

Octavia Bane, PhD	Philip Robson, PhD
Ashok Chhetry, PhD	Sara Lewis, MD
Valentin Fauveau, MS	Claudia Kirsch, MD
Xiang Xu, PhD	Xueyan Mei, PhD, MS
Georgios (George) Soultanidis, PhD	David O'Connor, PhD
Mandy van Leent, MD, PhD	

Visualization of nonfibrillar Dutch mutant Alzheimer's amyloid beta (A β) aggregates (oligomers) associated with aging-related presynaptic dysfunction

Sam Gandy, MD, PhD¹, Emilie L. Castranio, PhD¹, Merina Varghese, PhD¹, Elentina K Argyrousi, PhD², Kuldeep Tripathi, PhD³, Linda Söderberg, PhD⁴, Erin Bresnahan, PhD⁵, David Lerner, PhD⁵, Francesca Garretti, PhD⁶, Hong Zhang, PhD², Jonathan Van de Loo, PhD², Ronan Talty, PhD⁷, Charles G Glabe, PhD⁸, Efrat Levy, PhD^{9,10}, Minghui Wang, PhD^{1,11,12}, Bin Zhang, PhD^{1,11,12,13}, Lars Lannfelt¹⁴, William D Lubell, PhD¹⁵, Brigitte Guerin, PhD¹⁶, Shai Rahimipour, PhD¹⁷, Dara Dickstein, PhD^{1,18}, Ottavio Arancio, MD PhD², and Michelle E. Ehrlich, MD¹

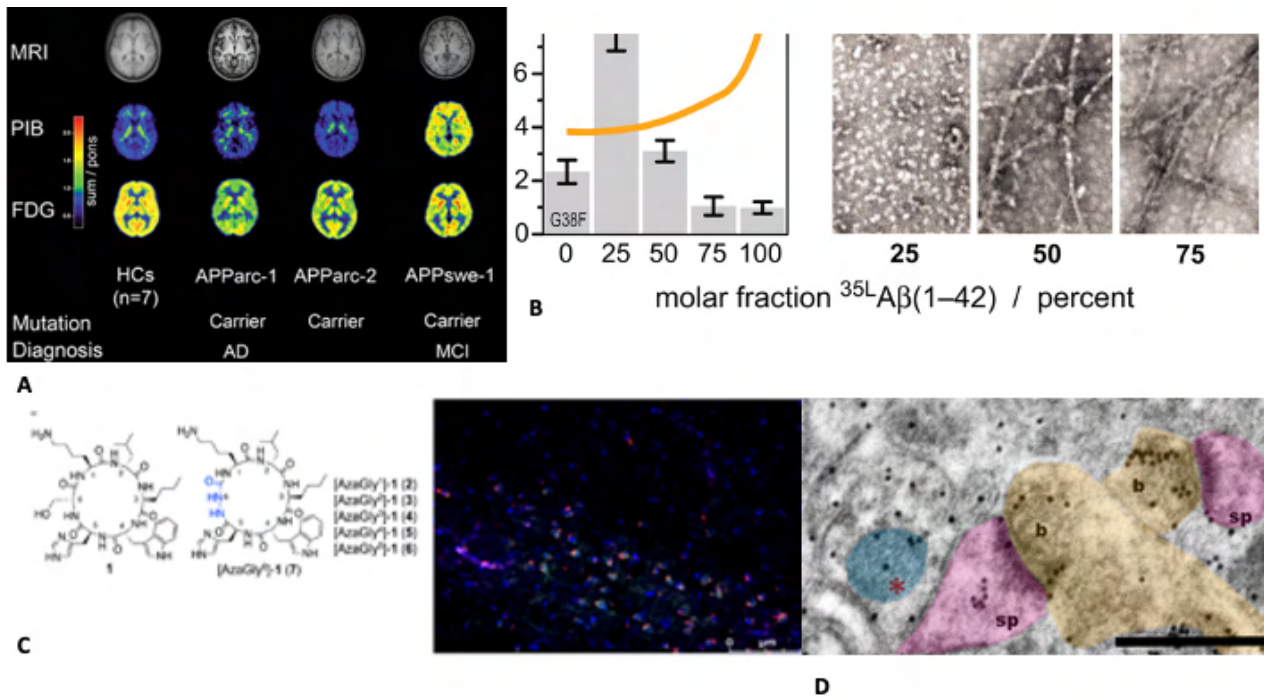
¹Icahn School of Medicine at Mount Sinai, New York, NY, USA, ²Columbia University, New York, NY, USA, ³Bar-Ilan University, Ramat Gan, Israel, ⁴BioArctic AB, Stockholm, Sweden, ⁵Icahn School of Medicine at Mount Sinai, New York, NY, USA, ⁶Icahn School of Medicine at Mount Sinai, New York, NY, USA, ⁷Yale University, New Haven, CT, USA, ⁸University of California Irvine, Irvine, CA, USA, ⁹Nathan S. Kline Institute for Psychiatric Research, Orangeburg, NY, USA, ¹⁰New York University Grossman School of Medicine, New York, NY, USA, ¹¹Icahn Institute for Data Science and Genomic Technology, New York, NY, USA, ¹²Mount Sinai Center for Transformative Disease Modeling, New York, NY, USA, ¹³Ronald M. Loeb Center for Alzheimer's Disease, New York, NY, USA, ¹⁴BioArctic, Stockholm, Sweden, ¹⁵University of Montreal, Montreal, QC, Canada, ¹⁶University of Sherbrooke, Sherbrooke, QC, Canada, ¹⁷Bar Ilan University, Ramat Gan, Israel, ¹⁸Uniformed Services University of Health Science, Bethesda, MD, USA

Background: Clinicopathological studies of Alzheimer's disease (AD) have demonstrated that synaptic or neuronal loss and clinical cognitive decline do not reliably correlate with fibrillar amyloid burden. We created a transgenic mouse model overexpressing Dutch (E693Q; TgAPPE693Q) mutant human amyloid precursor protein (APP) driven by the pan-neuronal Thy1 promoter. TgAPPE693Q mice developed a learning phenotype with severity proportional to brain oA β levels.

Method: Male and female TgAPPE693Q mice and wildtype controls were compared using learning behavioral studies, immunocytochemistry, transmission electron microscopy, immunoelectron microscopy, electrophysiology, protofibril-specific assays, and single cell RNA sequencing.

Results: Brain levels of nonfibrillar oA β in Dutch mice were shown to increase as a function of aging using A11 immunocytochemistry and FITC-cyclic peptide (FITC-CP-2) microscopy. Two assays excluded the presence of protofibrils. Electrophysiological characterization of hippocampal synapses in Dutch and wildtype mice at ~7 and ~11 months revealed no change in basal excitatory transmission, consistent with normal density and morphology of mGluR2/3+ synapses in hippocampal CA1 of the same mice. One exception was increased postsynaptic density in non-perforated mGluR-2/3+ synapses in the Dutch mice. Functional characterization of the presynaptic terminal showed abnormalities in post-tetanic potentiation, synaptic fatigue, and synaptic replenishment after depletion in Dutch mice. Immunoelectron microscopy with A11 confirmed the presynaptic concentration of nonfibrillar oA β . Single cell RNA-seq to elucidate cell-type specific transcriptional responses to oA β revealed altered transcriptional profiles in multiple cell types. Unexpectedly, no obvious differences existed between omics profiles of microglia from Dutch compared to those from wildtype mice. Excitatory neurons showed the most altered profile which was associated with 'protein translation' and 'oxidative phosphorylation'. Ultrastructural analysis of presynaptic mitochondria at excitatory synapses revealed fewer mitochondria in the presynaptic terminals of Dutch mice.

Conclusion: The profound learning behavior deficits in Dutch mice are associated with presynaptic functional deficits and mitochondrial abnormalities in excitatory neurons of the hippocampus. Nonfibrillar oA β deposits were revealed by co-localization of A11 immunoreactivity with FITC-CP-2 microscopy. Ultrastructural localization was revealed by A11 immunoelectron microscopy. Mice accumulating only oA β may be especially useful for further characterization of the oligomer-specific cyclic azaglycine PET tracer Lys (64Cu/NOTA)1]-CP-2 that shows robust PET signal from 44-day-old presymptomatic 5xFAD mice [Habashi, M. et al. Proc. Natl. Acad. Sci. U.S.A. 2022].



(A) oA β Arctic are invisible on amyloid PET; (b) toxicity and structure of oA β and fibrillar A β visualized by TEM; (C) endogenously generated Dutch oA β detected by FITC-CP-2 tracer (C) and by A11 immunoEM (D)

Advanced diffusion weighted MRI methods detect fibrosis in renal allografts: A preliminary experience

Mira Liu PhD¹, Jonathan Dyke PhD², Sergio Calle MS⁽¹⁾, Surya Seshan MD³, Steven Salvatore MD³, Isaac Stillman MD⁴, Thangamani Muthukumar MD⁵, Bachir Taouli MD^{1,6}, Samira Farouk MD⁷, Sara Lewis MD^{1,6} & Octavia Bane PhD^{1,6}

¹BioMedical Engineering and Imaging Institute, Icahn School of Medicine at Mount Sinai, New York, NY, USA. ²Department of Radiology/Citigroup Biomedical Imaging Center, Weill Cornell Medicine, New York, NY, USA. ³Department of Pathology, Weill Cornell Medicine, New York, NY, USA. ⁴Department of Pathology, Icahn School of Medicine at Mount Sinai, Mount Sinai Hospital, New York, NY, USA. ⁵Department of Nephrology and Kidney Transplantation Medicine, Weill Cornell Medicine. ⁶Department of Diagnostic, Molecular and Interventional Radiology, Icahn School of Medicine at Mount Sinai, Mount Sinai Hospital, New York, NY, USA. ⁷Transplant Nephrology, Icahn School of Medicine at Mount Sinai, Mount Sinai Hospital, New York, NY, USA.

Introduction: Renal allograft interstitial fibrosis and tubular atrophy (IFTA) is known to predict allograft failure and increased patient mortality. Multi-compartment advanced diffusion weighted MRI of renal allografts is a potential non-invasive method of measuring abnormal interstitial tubules for continual patient monitoring or studies of novel therapy outcome without invasive biopsy.

Materials and Methods: In a prospective, IRB-approved two-center study, 49 patients (20F/29M, 49.8±10.6y) with either acute or chronic allograft injury and clinically indicative biopsy underwent 3T MRI (Skyra, Siemens Healthcare). Protocol included advanced DWI (9 b-values: 10-800 s/mm²). Advanced-DWI was post-processed with 1) mono-exponential (ADC), 2) Bayesian fixed bi-exponential (IVIM), 3) Bayesian fixed tri-exponential (tri-exp), and 4) model-free spectral diffusion (spectral) as shown in Table 1. Interstitial fibrosis and tubular atrophy (IFTA=ci+ct) were scored clinically by pathologists from 0 to 6, according to the Banff 2017 classification. Cortical regions-of-interest were drawn on allografts by one radiologist, and MRI-parameter histogram characteristics were compared between IFTA thresholds from 1 to 5, and in terms of severity groupings (none=0, low=[1,2,3], high=[4,5,6]). Clinical diagnostic performance was compared via ROC analysis of supervised machine learning logistic regression models built with statistically significant histogram features.

Results: ADC and bi-exponential IVIM returned no statistically significant features for any comparisons (Table 2). Tri-exponential and model-free spectral diffusion return significant parameters and significant AUC values between no fibrosis and fibrosis (IFTA ≥ 2; Table 2). Only tri-exponential returned a significant feature at a threshold of IFTA ≥ 3 (Table 2). Both tri-exponential and model-free spectral diffusion was significant between no fibrosis and low fibrosis, while only model-free spectral diffusion was significant between no fibrosis and high fibrosis. Spectral diffusion returned a greater number of significant features, and higher mean AUCs than tri-exponential, though the 95% CIs overlap. Spectral diffusion between no IFTA and low IFTA returned the highest AUC=0.82[0.67,0.97] of all categorical divisions and post-processing models.

Conclusions: Comparison of mathematical models in advanced diffusion weighted images show benefit of a model-free analysis for the assessment of renal allograft IFTA. Further work is needed on parameter stability, test-retest analysis, and interobserver reliability. Spectral analysis of an optimized advanced DWI sequence could measure IFTA and renal function non-invasively through reduction in interstitial and tubular signal fraction and flow. This may potentially improve multiparametric MRI models for measurement of IFTA, concomitant inflammation, and prediction of clinical outcome, and allow longitudinal and novel therapeutic studies of fibrosis without invasive biopsy.

Post-processing method	Equation Model
ADC	Ae^{-bADC}
Rigid Bi-exponential	$e^{-bD^*} + (1 - f)e^{-bD}$,
Rigid Tri-exponential	$f_{fast}e^{-bD_{fast}} + f_{medium}e^{-bD_{medium}} + f_{slow}e^{-bD_{slow}}$
Spectral (model-free, but max up to these four components)	$f_{blood}e^{-bD_{blood}} + f_{tubule}e^{-bD_{tubule}} + f_{tissue}e^{-bD_{tissue}} + f_{fibrosis}e^{-bD_{fibrosis}}$

Table 1. Four advanced diffusion weighted MRI post-processing methods and the equation models used.

Sequence type	Parameter	IFTA < 2 (20) $\mu \pm \sigma$	IFTA ≥ 2 (29) $\mu \pm \sigma$	p-val	AUC [95%CI]	SN	SP
Spectral	cortical kurtosis f blood	4.53± 5.02	7.34± 8.34	0.044	0.74[0.60, 0.89]	0.70	0.62
	cortical skew f blood	1.21± 0.92	1.75± 1.28	0.042			
	cortical mean D blood	91.04± 28.54	68.48± 38.77	0.027			
	cortical median D blood	85.14± 64.41	52.28± 64.90	0.033			
	cortical mean D tubule	4.78± 2.22	3.65± 3.48	0.036			
	cortical std D tubule	8.66± 4.49	5.63± 4.25	0.014			
	Tri-exp	cortical skew f fast	0.99± 0.57	1.43± 0.77			
cortical mean D fast		0.18± 0.04	0.15± 0.06	0.038			
cortical median D fast		0.21± 0.08	0.15± 0.12	0.027			
cortical skew D fast		-0.363± 0.624	0.17± 1.52	0.042			
		IFTA < 3 (31)	IFTA ≥ 3(18)				
Tri-exp	cortical std D fast	0.114± 0.016	0.10± 0.03	0.03	0.69[0.51, 0.86]	0.63	0.78
Sequence type	Parameter	No IFTA (20)	Low IFTA (12)				
Spectral	cortical median f blood	0.05± 0.04	0.03± 0.05	0.047	0.82[0.67, 0.97]	0.55	1.0
	cortical kurtosis f blood	4.57± 5.02	10.75± 11.61	0.016			
	cortical skew f blood	1.21± 0.92	2.26± 1.60	0.008			
	cortical std f tubule	0.25± 0.08	0.31± 0.05	0.018			
	cortical std f tissue	0.25± 0.06	0.30± 0.041	0.02			
	cortical mean D blood	91.04± 28.54	59.03± 35.98	0.011			
	cortical median D blood	85.14± 64.41	31.74± 52.37	0.01			
	cortical skew D blood	-0.11± 0.84	1.11± 1.72	0.014			
	cortical mean D tubule	4.78± 2.22	3.70± 4.05	0.043			
	cortical std D tubule	8.66± 4.49	5.73± 4.41	0.043			
Tri-exp	cortical mean D fast	0.18± 0.04	0.137± 0.06	0.027	0.72[0.52, 0.92]	0.75	0.67
	cortical median D fast	0.21± 0.08	0.14± 0.10	0.027			
	cortical skew D fast	-0.36± 0.62	0.53± 1.28	0.043			
		No IFTA (20)	High IFTA (17)				
Spectral	cortical std D tubule	8.66± 4.49	5.57± 4.14	0.035	0.70[0.53, 0.88]	0.60	0.76

Table 2. Statistically significant Mann-Whitney U test histogram features with mean ± stdev, p-value, and logistic regression AUC with sensitivity and specificity of Youden's J statistic threshold. Numbers of cases per category are shown in corresponding parentheses by each group.

Table 1 and Table 2

VIS-MAE: A Foundation Model for Medical Image Segmentation and Classification

Zelong Liu¹, Andrew Tieu¹, Nikhil Patel¹, Alexander Zhou¹, George Soultanidis¹, Louisa Deyer², Zahi A. Fayad^{1,3}, Timothy Deyer^{4,5}, Xueyan Mei^{1,3}

¹BioMedical Engineering and Imaging Institute, Icahn School of Medicine at Mount Sinai, New York, NY ²Dwight School, New York, NY ³Department of Diagnostic, Molecular, and Interventional Radiology, Icahn School of Medicine at Mount Sinai, New York, NY ⁴East River Medical Imaging, New York, NY ⁵Department of Radiology, Cornell Medicine, New York, NY

Introduction: Artificial intelligence (AI) has the potential to revolutionize disease diagnosis and segmentation in medical imaging, but it faces multiple challenges including limited data availability and lack of generalizability. A foundation model, which is a large-scale pre-trained AI model, offers a versatile base that can be adapted to a variety of specific tasks and contexts. Here, we present Visualization and Segmentation Masked AutoEncoder (VIS-MAE), a novel foundation model specifically designed for medical imaging shown in Figure 1A.

Materials and Methods: The upstream data, collected from an outpatient radiology practice in New York City between 2005 and 2022, comprises 2,486,425 images including five imaging modalities: MR, CT, PET/CT, X-rays, and ultrasound. We evaluated the VIS-MAE pretrained weights on 9 segmentation datasets and 5 classification datasets. Dice score and AUC were used as evaluation metrics for segmentation and classification tasks, respectively. Paired t-test and DeLong's test were used to find significant differences between VIS-MAE and other benchmark models in segmentation and classification tasks.

Results: Shown in Figure 1B, VIS-MAE showed strong performance in all segmentation tasks compared to nnU-Net and TransUNet. VIS-MAE achieved dice scores of 0.850, 0.711, 0.879, 0.891, 0.883, 0.902, 0.720, 0.780, and 0.923 in BTCV, stroke, ACDC, AMOS, glioma, prostate, thyroid, breast, and ISIC 2016 segmentation tasks, respectively. In segmentation of the BTCV, stroke, AMOS, prostate, and ISIC 2016 datasets, nnU-Net showed significantly decreased performance compared to VIS-MAE, with dice scores of 0.842 ($p < 0.001$), 0.696 ($p < 0.05$), 0.877 ($p < 0.001$), 0.833 ($p < 0.001$) and 0.904 ($p < 0.001$). TransUNet showed similar performance to VIS-MAE in BTCV (0.854, $p = 0.309$) and stroke (0.700, $p = 0.130$), while underperforming in other tasks. In addition, VIS-MAE achieved AUC scores of 0.764, 0.872, 0.665, 0.946, and 0.932 in NIH chest, COVID-19, sarcoidosis, ACL tear, and knee osteoarthritis classification tasks respectively. RadImageNet underperformed only in knee osteoarthritis with an AUC score of 0.903 ($p < 0.001$) and achieved similar performance in other tasks compared to VIS-MAE. ImageNet underperformed in the sarcoidosis and knee osteoarthritis datasets with AUC scores of 0.616 ($p < 0.05$) and 0.921 ($p < 0.001$) and achieved similar performance in other tasks compared to VIS-MAE.

Conclusions: VIS-MAE demonstrates remarkable effectiveness and adaptability across a range of downstream applications. The model exhibits superior performance and generalizability in both segmentation and classification tasks to other state-of-the-art methods within the medical imaging domain. VIS-MAE marks a significant advance in medical imaging, facilitating a more efficient and precise approach that could enhance diagnostic processes in healthcare.

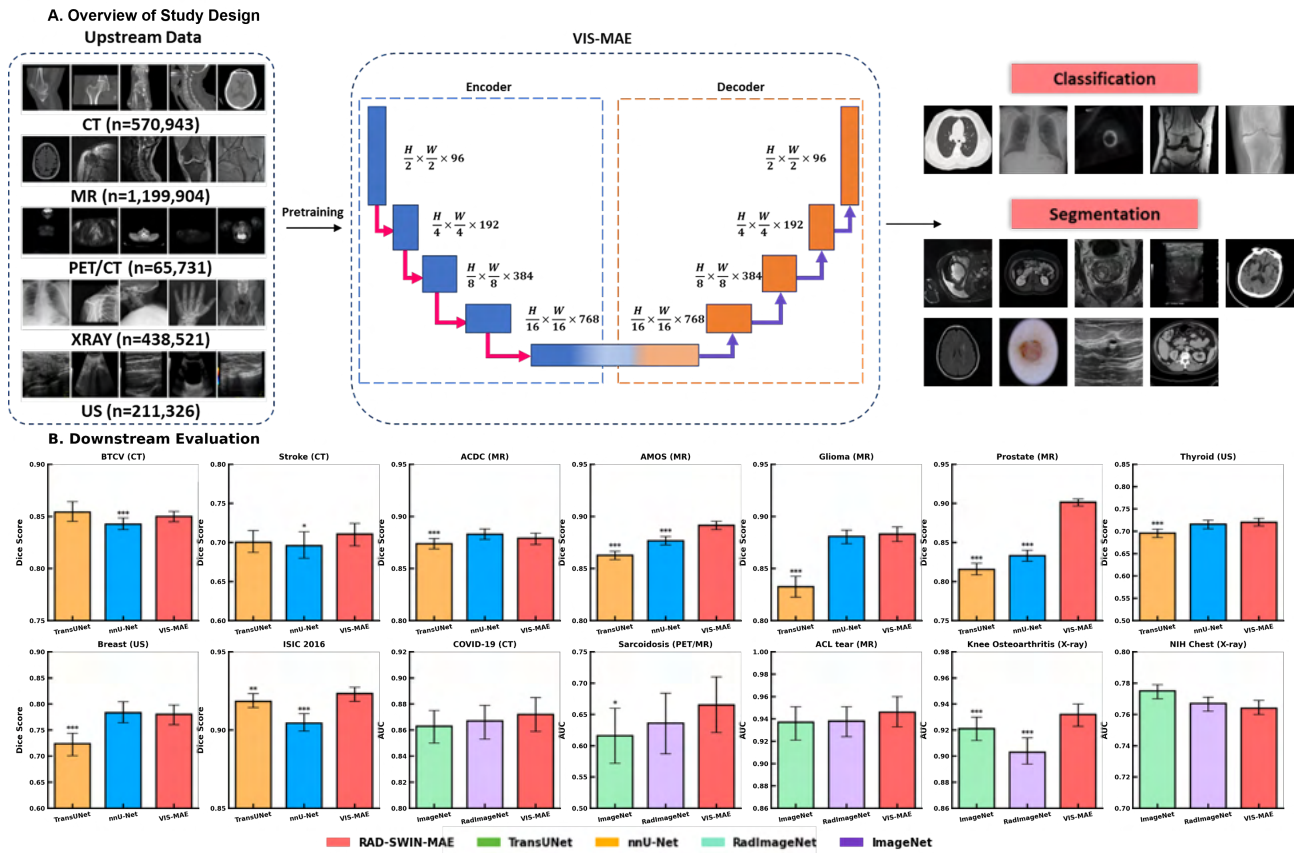


Figure 1. A) Overview of the study design. First, we collected a substantial upstream cohort for developing the self-supervised learning foundation model, VIS-MAE, using a masking-based SSL strategy. Second, we utilized the pretrained weights from VIS-MAE for two types of medical imaging applications: classification and segmentation. For classification tasks, the model's backbone was fine-tuned using the pretrained encoder weights from VIS-MAE. In segmentation tasks, both the encoder and decoder weights were fine-tuned on downstream applications. This approach leverages the learned features from VIS-MAE to enhance performance in specific medical imaging tasks. B) Performance on nine segmentation tasks in terms of dice score and five classification tasks in terms of AUC score. On segmentation task, VIS-MAE was finetuned and evaluated on BTCV abdomen (CT), stroke (CT), ACDC (MR), AMOS (MR), glioma (MR), prostate (MR), thyroid (US), breast (US), and ISIC 2016. Except in the stroke (CT) and thyroid (US) datasets, we performed 5-fold cross validation for each dataset. Each color bar indicates the dice score of the respective model on a specific task. In each task, the dice scores between VIS-MAE and other models were compared by a two-sided t-test. The error bar indicates the 95% CI of the average dice score on five-fold cross validation. On classification task, the encoder of VIS-MAE was finetuned and evaluated on COVID-19 (CT), sarcoidosis (PET/MR), ACL tear (MR), knee osteoarthritis (X-ray), and NIH Chest (X-ray). Except in the NIH Chest (X-ray) dataset, we performed 5-fold cross validation for each dataset. Each color bar indicates the AUC score of the respective model on a specific task. For COVID-19, sarcoidosis, ACL tear, and knee osteoarthritis classification, DeLong's test was applied to compare the AUC scores between VIS-MAE and other models. The error bar indicates the 95% CI of the corresponding AUC score. The p value for statistical significance was listed as the following: * for p value <0.05, ** for p value <0.01, and *** for p value <0.001.

Relationship between brain stiffness, microstructural integrity, beta-amyloid accumulation and cognitive decline in beta-amyloid positive individuals

E. Triolo ¹, M. Langan ², O. Khegai ², A. Diaz ², S. Binder ³, T. Hedden ³, P. Balchandani ², M. Kurt ^{1,2}

¹ Department of Mechanical Engineering, University of Washington, Seattle, WA, USA

² The Biomedical Engineering and Imaging Institute, Icahn School of Medicine at Mount Sinai, New York City, NY, USA

³ Department of Neurology, Icahn School of Medicine at Mount Sinai, New York City, NY, USA

Background: Leveraging non-invasive ultra-high field, 7 Tesla (7T) MRI, with increased signal-to-noise ratio and improved soft tissue contrast afforded by 7T allows us to accurately map tissue microstructure. We aim to use 7T MR Elastography (MRE), 7T Diffusion Tensor Imaging (DTI), 3T amyloid-PET, and Preclinical Alzheimer Cognitive Composite (PACC) score to determine the relationships between these metrics in a cohort of older individuals with either normal cognition (CN), mild cognitive impairment (MCI), or Alzheimer's Disease (AD).

Methods: 7T MRE, 7T DTI, 3T PET (Fig 1A), and PACC test were performed on CN 14 subjects (Avg. age 70.3±5.2 years), and 6 subjects (Avg. age 70.0±9.4 years) with MCI/AD (Clinical Dementia Rating >4.0 in the Clinical Dementia Rating Scale Sum of Boxes). We performed multiple Shapley Regressions in subjects with amyloidosis (average SUVR above the region threshold, described in Bullich, et al.) in five PET-relevant cortical regions with the imaging metrics acquired and PACC score.

Results: We found significant differences ($p < 0.05$) between the CN and AD/MCI groups in complex shear stiffness ($|G^*|$) of the hippocampus and frontal lobe, and SUVR of all brain regions investigated. A significant negative correlation was found between average SUVR and $|G^*|$ in multiple brain regions (Fig 1B). We also found significant correlations between SUVR and mean diffusivity (MD), and $|G^*|$ and MD in the temporal cortex (Fig 1C). There was a significant negative correlation between SUVR and PACC, and positive correlation between $|G^*|$ and PACC, in all regions. Excluding PACC, $|G^*|$ was the best predictor of SUVR in subjects with amyloidosis, apart from in the temporal and parietal cortexes, where MD was a better predictor (Fig 1 D,E). Again, excluding PACC, SUVR was the best predictor of $|G^*|$, apart from the temporal cortex.

Conclusions: The Shapley regression analyses demonstrated that SUVR and $|G^*|$ were the most interrelated imaging covariates for multiple brain regions, which is promising for finding correlates of PET through MRE. Additionally, correlations between SUVR or $|G^*|$ and MD, but not SUVR and $|G^*|$ in the temporal cortex may be indicative of cascades which contribute to $A\beta$ deposition, microstructural damage, and tissue softening and degradation.

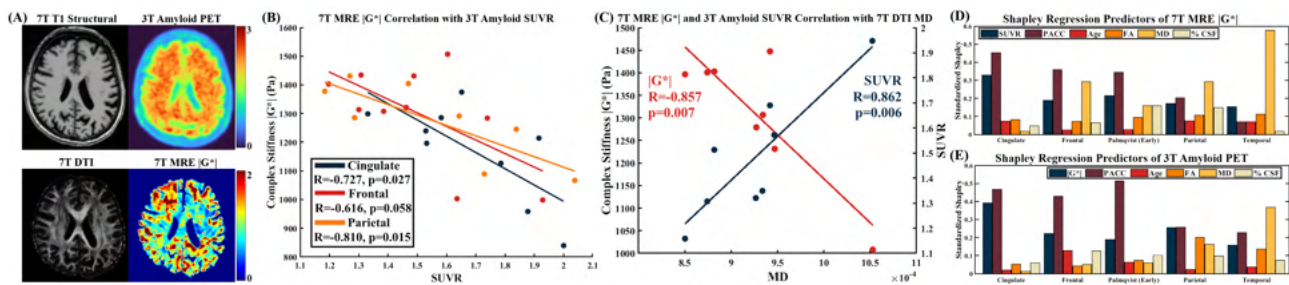


Figure 1: (A) Top: T1 (left), PET (right), Bottom: FA (left), and $|G^*|$ (right) maps for one subject with MCI, (B) Linear correlations between $|G^*|$ and SUVR in three cortical brain regions, and (C) The linear correlations between $|G^*|$ and MD, and SUVR and MD in the temporal cortex; (D,E) Results of the Shapley Regressions, calculating the importance of (D) SUVR, Age, FA, RD, % CSF, and PACC in the results of MRE, and (E) the importance of Age, FA, RD, % CFS, and $|G^*|$ from MRE in the results of SUVR in multiple brain regions.

Inhibiting tumor growth using nanoparticle-based photodynamic therapy

William Wang^{1,2}, Judit Morla-Folch^{1,2}, Jingxing Shao³, Jianhong Wang³, Bram Priem^{1,2}, Jessica Chimene^{1,2}, Tomas Post^{1,4}, Willem Mulder^{1,4,5}, Jan van Hest³, Abraham J. P. Teunissen^{1,2}

¹. BioMedical Engineering and Imaging Institute, Icahn School of Medicine at Mount Sinai, NY, USA ². Cardiovascular Research Institute, Icahn School of Medicine at Mount Sinai, NY, USA ³. Bio-Organic Chemistry, Institute for Complex Molecular Systems, Eindhoven University of Technology, Eindhoven, The Netherlands. Laboratory of Chemical Biology, Department of Biochemical Engineering, Eindhoven University of Technology, Eindhoven, The Netherlands ⁴. Department of Internal Medicine and Radboud Institute for Molecular Life Sciences, Radboud University Medical Center, 6525 GA Nijmegen, Netherlands ⁵. Department of Chemical Biology, Eindhoven University of Technology, 5612 AZ Eindhoven, Netherlands.

Introduction: The ideal therapy for cancer should be able to selectively destroy tumor cells at the primary site and simultaneously trigger the immune system to recognize any remaining or recurring cancer cells. Compared to other unspecific and/or immunosuppressive cancer therapies such as chemotherapy, ionizing radiation and surgery, Photodynamic Therapy (PDT) have these desirable properties. PDT is a traditional cancer treatment¹ which combines a photosensitizer (PS), light, and molecular oxygen to destroy cancer cells via the production of various reactive oxygen species (ROS). In addition to local tumor ablation by PDT-generated ROS, PDT induces inflammation evoking strong immunological response, reducing the risk of distant metastasis.²

Materials and Methods: We designed photosensitizer-loaded nanoparticles that can be efficiently delivered to tumors. Specifically, we have prepared poly(N-vinylcaprolactam) nanogels through precipitation polymerization, loaded with chlorin 6 (Ce6), a porphyrin-derived photosensitizer. BALB/c mice were inoculated with breast cancer cells (4T1 cell line), then administered with Ce6-loaded nanoparticles (p.t. at 1.5 mg Ce6/kg) seven days later. After two hours, tumors were irradiated with the laser at 660 nm, 100 mW for 10 minutes. We similarly inoculated mice, and then treated them seven days later using either PBS, laser w/o nanoparticles, or Ce6-loaded nanoparticles w/o laser, as controls, n=10. Therapeutic performance was assessed by monitoring tumor growth with daily caliper measurements. At day 10, tumors were excised, sliced, and stained for apoptosis and immune cell population markers.

Results: Our in vivo imaging data strongly suggests that Ce6-loaded nanoparticles display high accumulation and long-term retention in the tumor, with two hours post-injection as the optimal timepoint for PDT (Figure 1A). Interestingly, the Ce6-loaded nanoparticle in the presence of the laser provide a noticeable tumor suppression effect over control groups (Figure 1B). Moreover, H&E, and caspase-3 staining also revealed that PDT treated-tumors displayed higher necrosis and apoptosis ratio than non-treated (Figure 1C). Similarly, myeloid cell population is increased in PDT-treated tumors responding to inflammation resulting from PDT-generated ROS.

Conclusions: Ce6-loaded nanoparticles represents a promising platform for PDT treatments, exhibiting dramatic tumor growth inhibition. In addition, the increment of myeloid cells in PDT-treated tumors indicates the potential of such therapy to be combined with immunotherapy (e.g., checkpoint inhibitors), thus increasing their response rates. In this line, we are currently working on the combination of this nanoparticle-based PDT with checkpoint blockade therapy and other types of immunotherapies to potentiate antitumor therapeutic efficacy.

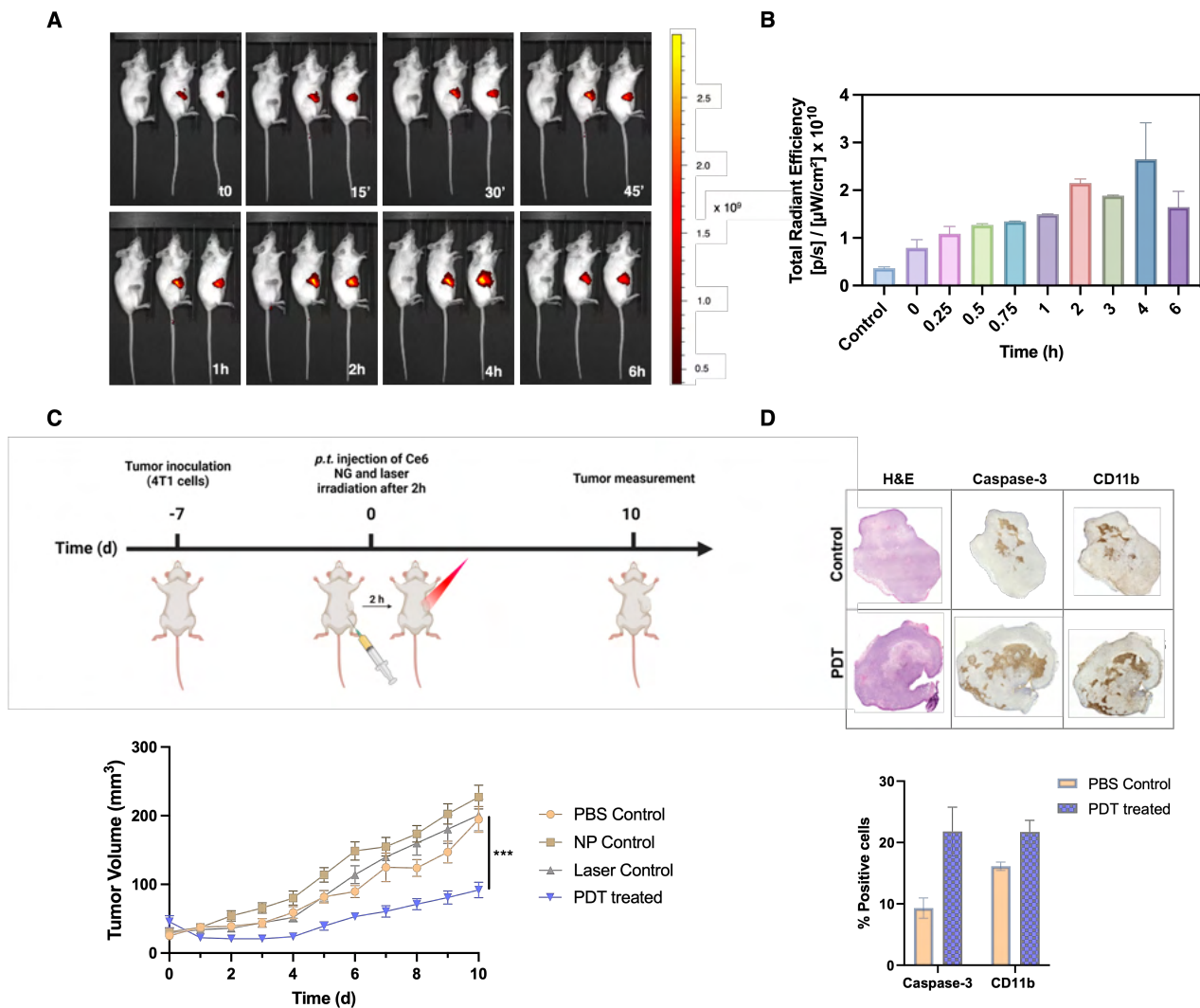


Figure 1. A) Fluorescence imaging of tumor-bearing mice at varying timepoints after p.t. injection of Ce6 PVCL nanoparticles (first mouse from the left side was injected with PBS as a control). **B)** Bar plot of the total radiant efficiency at the area of the tumor (λ_{exc} , 640nm). **C) Top.** Schedule for PDT treatment in 4T1 tumor bearing mice. **Bottom.** Mice tumor sizes after the different treatment (n=10). ***, P < 0.001 **D)** H&E, caspase-3 (apoptosis and necrosis) and CD11b (myeloid cells) staining of tumor slices taken on day 10 after treatment, n=5 (grey, live cells; brown, necrotic and apoptotic cells; brown, CD11b+ cells).

Figure 1. A) Right. Fluorescence imaging of tumor-bearing mice at varying timepoints after p.t. injection of Ce6 PVCL nanoparticles (mouse num. 1 was injected with PBS as a control). Left. Bar plot of the total radiant efficiency at the area of the tumor (λ_{exc} , 640nm). B) Top. Schedule for PDT treatment in 4T1 tumor bearing mice. Bottom. Tumor growth curves after the different treatment (n=10). C) H&E, caspase-3 (apoptosis and necrosis) and CD11b (myeloid cells) staining of tumor slices taken on day 10 after treatment (grey, live cells; brown, necrotic and apoptotic cells; brown, CD11b+ cells).

Prediction of pancreatic cancer aggressiveness using CT-base radiomics

Kazuya Yasokawa^{1,2}, Amine Geahchan^{1,2}, Judy Li³, Elad Sarfaty³, Rebecca Zhou¹, Alexander Zhou¹, Octavia Bane^{1,2}, Camilo Correa³, Noah Cohen³, Bachir Taouli^{1,2}

¹Department of Diagnostic, Molecular and Interventional Radiology, Icahn School of Medicine at Mount Sinai, New York, NY USA

²BioMedical Engineering and Imaging Institute (BMEII), Icahn School of Medicine at Mount Sinai, New York, NY USA

³Department of Surgical Oncology, Icahn School of Medicine at Mount Sinai, New York, NY USA

Purpose: To assess the role of CT-based radiomics for prediction of aggressiveness of resectable and borderline resectable (BR) pancreatic adenocarcinoma.

Materials and Methods: This is a single center retrospective study in which an initial cohort of 49 patients (M/F: 25/24, mean age: 67.9y) with resectable and BR pancreatic ductal adenocarcinoma (PDAC) who had pre-treatment CT were analyzed. 3D segmentation of the tumors was performed on post-contrast CT (portal venous phase). Radiomics features (shape, histogram and texture features) were extracted from a volume of interest encompassing the tumor, using software. The aggressiveness of PDAC was classified using histopathologic tumor grade (grade 0: well, 1: moderately, 2: poorly differentiated), lymphovascular invasion and AJCC stage. The diagnostic performance of radiomic features to identify poorly differentiated tumors, stage 3 tumors, and tumors with lymphovascular invasion was assessed with ROC analysis.

Results: 16 radiomics features were significant for classifying tumor grade (0-1 vs 2), 9 for lymphovascular invasion and 1 for AJCC stage (I-II vs III). The top performing features for classifying tumor grade (0-1 vs 2), were Gray Level Co-occurrence Matrix Joint Entropy (AUC= 0.89, P<0.05), Gray Level Dependence Matrix Dependence Entropy (AUC= 0.87, P<0.05) and Gray Level Run Length Matrix Run Entropy (AUC= 0.82, P<0.05). For lymphovascular invasion and AJCC stage, there were no radiomic features with high diagnostic performance (AUC>0.7).

Conclusion: Our initial results demonstrated useful radiomics features for predicting tumor grade of PDAC. Additional cases will be analyzed for validation, and radiomics features will also be correlated against outcomes.

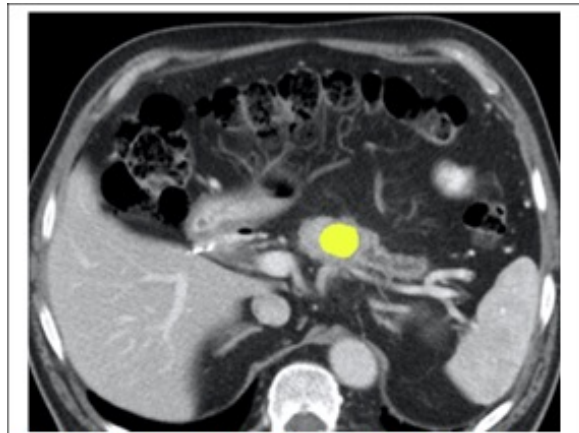


Fig. 1: Example of ROI placement for radiomics feature extraction on CT in a patient with pancreatic adenocarcinoma.

Example of ROI placement for radiomics feature extraction on CT in a patient with pancreatic adenocarcinoma

Selected for poster presentations

Characterizing the subcallosal cingulate gray matter in depression: implications for DBS optimization

Carlos Alcocer^{1,2}, Helen S. Mayberg², Jungho Cha², Ha Neul Song², Martijn Figee², Brian H. Kopell², Ki Sueng Choi²

¹ Weill Cornell Medical College, New York, NY, USA

² Nash Family Center for Advanced Circuit Therapeutics, Icahn School of Medicine at Mount Sinai, New York, NY, USA

Introduction: Variation of neuroanatomy in the subcallosal cingulate cortex (SCC), including structural asymmetry, may moderate differences in response to SCC deep brain stimulation (DBS) in patients with treatment-resistant depression (TRD). We aim to characterize pathological structural abnormality of SCC in TRD subjects versus healthy controls (HC), explore the effects of structural asymmetry on the lateralized behavioral response to DBS, and explore whether SCC gray matter (GM) modulates DBS response.

Methods: Participants included 47 subjects with TRD who underwent bilateral SCC DBS along with 16 HC. Segmentation of SCC was performed with FreeSurfer. Volume and laterality index (LI) were extracted for all subjects. The volume of tissue activated (VTA) was generated with patient-specific stimulation parameters at 6 months. The volume of overlap between VTA and SCC GM (including the upper and lower banks) and the distance between VTA center of mass (COM) and SCC GM was also calculated for TRD subjects. ANCOVA was conducted to compare the above variables between TRD subjects and HC and between DBS responders (>50% decrease of HDRS-17 at 2 years) and non-responders. Lastly, multivariate linear regression was performed using these extract features and the following clinical measures: HDRS-17 baseline, HDRS-17 changes at 2 years, and time to stable response (TSR2, more than 50% HDRS-17 decrease for two consecutive weeks).

Results: There was no significant GM volume reduction of left, right, or mean SCC volumes of TRD subjects versus HC nor between DBS non-responders and responders. Left SCC volume was significantly greater than right across TRD subjects ($p < 0.0001$) and HC ($p = 0.003$). There was no difference between responders and non-responders in VTA and SCC overlap volumes. However, an increased overlap, particularly of the right ($p = 0.026$), mean lower ($p = 0.031$) and lower right bank of SCC ($p = 0.014$), predicted an increase in TSR2. Finally, non-responders demonstrated a greater Euclidian ($p = 0.004$) and horizontal distance ($p = 0.028$) between the right VTA COM and SCC.

Conclusions: Left-sided SCC volume laterality likely represents normal anatomical asymmetry. Placing the DBS lead too medial and inferior may slow the DBS response while positioning the lead too lateral can prevent DBS response, likely due to missing critical white matter tracts. Therefore, optimal DBS response requires not only consideration of targeting WM tracts but also of the location of SCC gray matter in relation to the DBS leads.

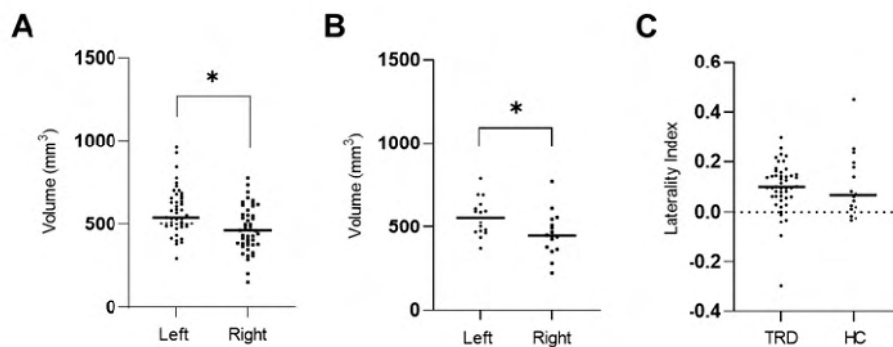


Figure 1. SCC volume laterality of TRD and HC. (A) Left versus right SCC volume in TRD subjects. (B) Left versus right SCC volume in HC. (C) LI in TRD subjects vs HC. * $p < 0.05$, ANCOVA.

Figure 1. SCC volume laterality of TRD and HC. (A) Left versus right SCC volume in TRD subjects. (B) Left versus right SCC volume in HC. (C) LI in TRD subjects vs HC. * $p < 0.05$, ANCOVA.

Impact of white matter abnormalities in therapeutic DBS pathways for treatment-resistant depression

Carlos Alcocer^{1,2}, Helen S. Mayberg², Jungho Cha², Ha Neul Song², Martijn Figee², Brian H. Kopell², Ki Sueng Choi²

¹ Weill Cornell Medical College, New York, NY, USA

² Nash Family Center for Advanced Circuit Therapeutics, Icahn School of Medicine at Mount Sinai, New York, NY, USA

Introduction: Whole-brain diffusion tractography analysis has demonstrated that deep brain stimulation (DBS) responders share unique bilateral pathways from their subcallosal cingulate cortex (SCC) stimulation volumes which include forceps minor (FMi), uncinate fasciculus (UF), cingulum bundle (CB) and subcortical junction (SJ) tracts. DBS non-responders do not activate these pathways. We aim to characterize white matter (WM) abnormalities in these SCC DBS-activated brain networks and explore the effects of WM integrity asymmetry on lateralized behavioral response in subjects with treatment-resistant depression (TRD).

Methods: Participants included 46 subjects with TRD who underwent bilateral SCC DBS and 40 healthy controls (HC). Diffusion-weighted imaging preprocessing was performed using FSL (FMRIB Software Library, <http://www.fmrib.ox.ac.uk/fsl>). A voxel-wise, permutation-based analysis was carried out using tract-based spatial statistics (TBSS) to detect significant differences in fractional anisotropy (FA) and FA laterality index (LI) between TRD subjects and HC and between DBS responders (>50% decrease of HDRS-17 at 6 months) and non-responders. Voxel-wise correlations were performed between FA and clinical measures, including HDRS-17 baseline, HDRS-17 percent change at 2 years, and time to stable response (TSR2, more than 50% HDRS-17 decrease for two consecutive weeks). Second, mean FA was extracted from pre-determined WM regions of interest (ROI), particularly the FMi, UF, CB, and SJ tracts. Differences in FA and laterality between groups were analyzed using a student's t-test and correlated to clinical measures using Spearman correlation.

Results: Voxel-wise TBSS analysis demonstrated significant decreases in FA in TRD subjects versus HC in various WM tracts including CB, FMi and UF (corrected $p < 0.05$). TSR2 was significantly negatively correlated to FA of various tracts, again including CB, FMi, and UF (corrected $p < 0.05$). ROI analysis confirmed these findings as mean FA was significantly decreased in CB ($p = 0.020$), UF ($p = 0.041$), FMi ($p = 0.0005$), and SJ tracts ($p = 0.012$) in TRD subjects versus HC. Lastly, SJ FA LI was negatively correlated with HDRS-17 percent change at 2 years ($r_s = -0.327$, $p = 0.042$).

Conclusions: Compared to HC, TRD patients have decreased WM integrity in critical WM tracts necessary for DBS response, including CB, UF, SJ, and FMi. Notably, more damaged WM in therapeutic pathways took longer for a stable response. Increased left-sided SJ FA laterality may be a biomarker for reduced clinical response. It remains to be determined to what extent changes in FA in these tracts can serve as a biomarker to differentiate DBS responders and non-responders.

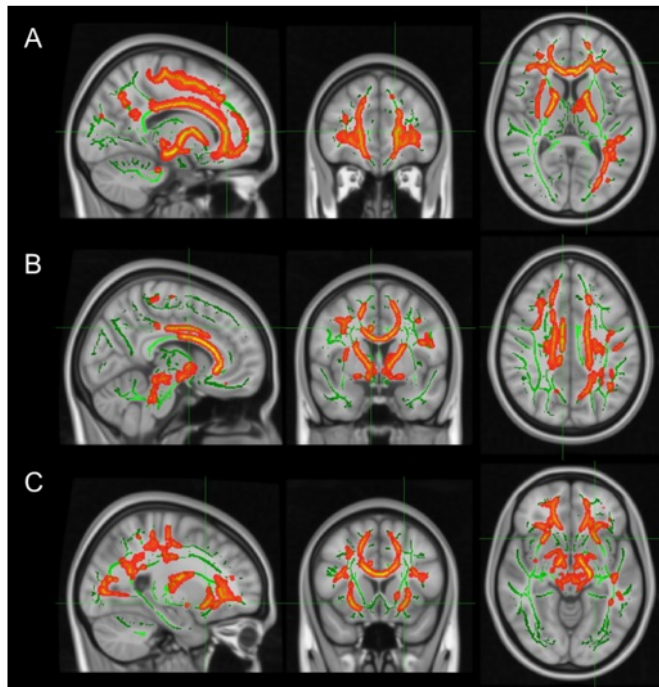


Figure 1. Red-yellow: regions where FA is significantly decreased in TRD patients versus HC. Green: mean FA skeleton projected onto standard MNI template. (A) Forceps minor (B) Cingulum bundle (C) Uncinate fasciculus.

Figure 1. Red-yellow: regions where FA is significantly decreased in TRD patients versus HC. Green: mean FA skeleton projected onto standard MNI template. (A) Forceps minor (B) Cingulum bundle (C) Uncinate fasciculus.

An AI-Powered Impedance Flow Cytometry with Basis Impedances for Accurate and Accessible Bio-Particle Analysis

Zahra Meskar¹, Pouria Esmaeili-Dokht², Mehdi Fardmanesh¹, and Mohsen Annabestani³

¹: Faculty of Electrical Engineering, Sharif University of Technology, Tehran, Iran

²: Max-Planck-Institut für Intelligente Systeme, Stuttgart, Germany

³: Department of Radiology, Weill Cornell Medicine, New York, USA

Introduction: Flow cytometry serves as an indispensable pillar of modern precision medicine, supporting critical advancements in immunology, oncology, and numerous other fields. However, realizing the full potential of Optical Flow Cytometry (OFC) faces substantial roadblocks - conventional systems remain prohibitively expensive, and complex, and require extensive sample preparation. This study proposes an AI-powered Impedance Flow Cytometry (IFC) integrating microfluidics, impedance spectroscopy, and machine learning (ML) to achieve accurate, accessible, and low-cost bio particle analysis. This method promises to unleash the transformative powers of flow cytometry for precision digital medicine, personalized medicine, and point-of-care tests (POCTs).

Materials and Methods: An IFC containing a microfluidic channel with multi-directional electrode pairs was modeled in COMSOL Multiphysics. To facilitate the swift simulation of particle flow, an innovative surrogate ML model equipped with a nonlinear autoregressive with exogenous inputs (NARX) was developed based on a concept called "basis impedances." Basis impedances represent the fundamental impedance responses of individual particles at different positions, serving as basis functions for the multiparticle ML model. Inputting these basis impedances allows the ML model to rapidly predict multiparticle impedance, presenting a disruptive approach to simulating complex particle interactions. The model underwent training using a vast dataset comprising over 80,000 simulated multiparticle signals spanning varying particle sizes, counts, and positions within the channel. Multi-dimensional time series classification was conducted using the sktime ML framework, incorporating 5-fold cross-validation and majority voting strategies to enhance accuracy.

Results: The microchip achieved remarkable accuracy in classifying impedance signals to determine particle counts, with outstanding average accuracies of 99.26-88.2% for particle sizes of 30-5 μ m across rigorous cross-validation. The basis impedances concept enabled the efficient generation of a robust training dataset and precise modeling of complex multiparticle systems.

Conclusions: This AI-powered IFC integrates microfluidics, machine learning, and the novel basis impedance concept to overcome key limitations of conventional OFCs. The system demonstrates accessible, low-cost, and highly accurate particle detection capabilities to drive the ubiquitous adoption of flow cytometry. This could catalyze transformative point-of-care diagnostic and treatment monitoring applications, helping democratize precision data-driven medicine. Additionally, the basis impedance modeling paradigm represents a disruptive framework for simulating complex multiparticle IFC interactions using AI. By bridging microfluidics, electrical engineering, and machine learning, this study lays the groundwork for trailblazing innovations to unleash the full disruptive potential of AI-driven flow cytometry.

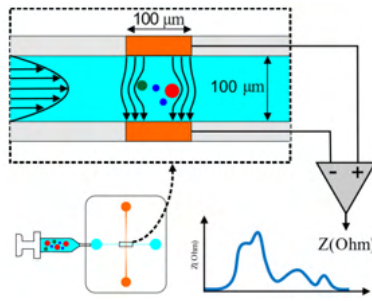


Fig. 1. Proposed Impedance flow cytometer

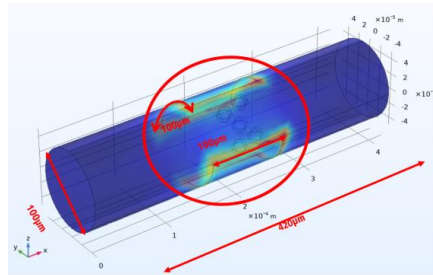


Fig2.The sizes of the channel and the electrodes

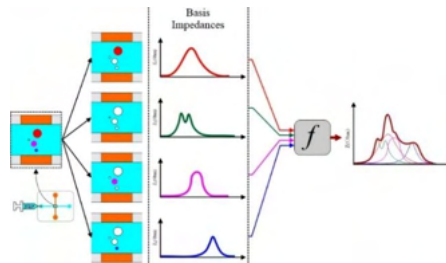


Fig3.Basis Impedance extraction

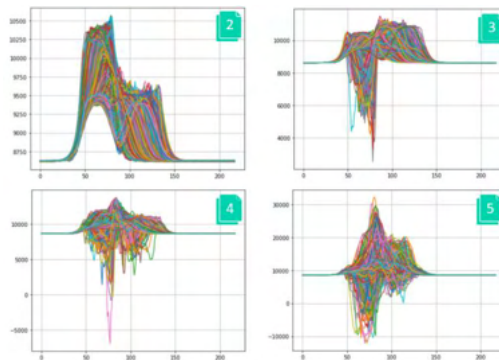


Fig4. Extracted Basis Impedance by COMSOL

Fig. 1. Proposed Impedance flow cytometer Fig2.The sizes of the channel and the electrodes Fig3.Basis Impedance extraction Fig4. Extracted Basis Impedance by COMSOL

Enhanced Spatial Comprehension in Cardiac Catheterization using Extended Reality Visualization

Mohsen Annabestani¹, Sandhya Sriram², Sepehr Janghorbani¹, Alexandre Caprio¹, S. Chiu Wong³, Alexandros Sigras², Bobak Mosadegh¹,

¹,Dalio Institute of Cardiovascular Imaging, Department of Radiology, Weill Cornell Medicine, New York, NY 10021, USA

²,Institute for Computational Biomedicine, Department of Physiology and Biophysics, Weill Cornell, Medicine of Cornell, University, New York, NY, USA

³,Division of Cardiology, Department of Medicine, Weill Cornell Medicine, New York, NY 10021, USA

Introduction: Cardiac catheterization is a complex procedure requiring precise manipulation of catheters through blood vessels for diagnostic and therapeutic access to the heart. Traditional fluoroscopic imaging provides only limited two-dimensional visualization for guiding catheter navigation. This necessitates significant mental reconstruction of the 3D anatomical context by the clinician. To address this challenge, this study presents a novel Extended Reality (XR) platform combining enhanced 3D visualization and immersive interactions to transform and improve cardiac catheterization training. Trainees will directly benefit from this system through improved spatial comprehension of the dynamic catheter position in relation to patient-specific cardiac anatomy as well as the ability to rehearse procedural skills in an interactive virtual environment.

Methods: A customized 3D-printed cubic setup, designed with mounted camera positions, enables real-time biplane orthogonal imaging of a catheter as it is manipulated within the central workspace. A computer vision algorithm processes the synchronized footage from both camera perspectives to accurately reconstruct the full 3D trajectory of the catheter, represented by K tracking points along its length. This real-time catheter tracking data is then seamlessly integrated into an interactive Unity-based scene rendered with high fidelity on the Meta Quest 3 virtual reality headset. The Unity visualization dynamically combines a reconstructed 3D patient-specific heart model with the catheter tracking data, creating an immersive XR training simulation. To assess the technical capabilities of this system, comprehensive experiments using both a commercial catheter and customized 3D-printed catheter phantoms were performed. Quantitative validation evaluates the precision of tip localization as well as the accuracy of reconstructing diverse catheter configurations including angled and curved trajectories.

Results: The proposed XR visualization system can achieve highly precise catheter tip localization within a 1 mm error. Furthermore, thorough experiments confirm the ability to reliably reconstruct arbitrary catheter angles and curves with a high degree of shape-matching fidelity. Augmented by the Meta Quest 3 headset, qualitative XR visualizations showcase the seamless integration of the dynamically tracked catheter within the 3D cardiac scene, enabling an interactive and intuitive training experience.

Conclusions: This work demonstrates the technical feasibility of real-time 3D catheter tracking and immersive Extended Reality visualization for simulated catheterization procedures. By transforming conventional 2D fluoroscopic perspectives into a dynamic 3D experience grounded by patient-specific anatomy, this innovative XR platform aims to significantly enhance catheterization training curricula. Moreover, clinical integration within actual hospital catheterization labs would enable the deployment of this XR training system for real-world training scenarios.

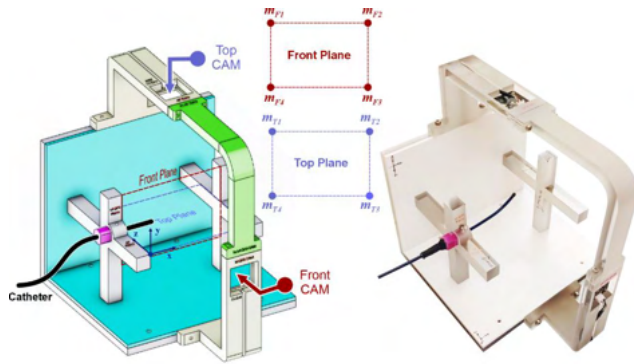


Fig.1 : Cubic 3D setup. Left: 3D Designed version. Right: 3D Printed Version.

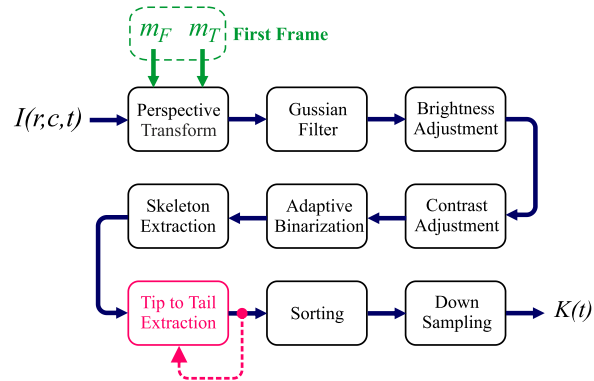


Fig.2: Block diagram of proposed vision algorithm.

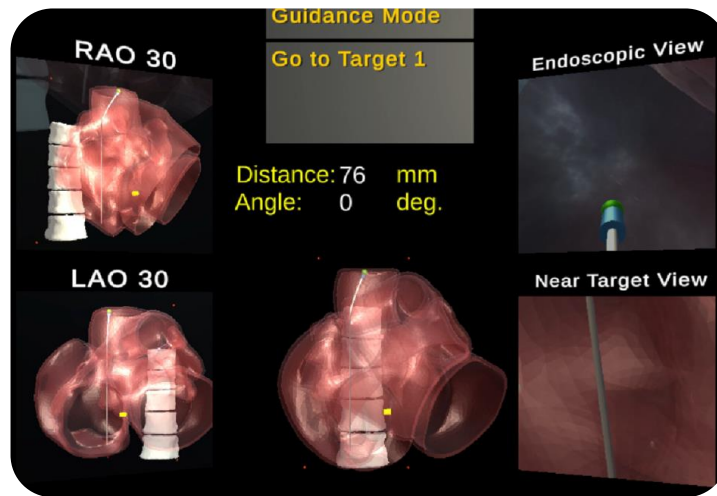


Fig. 3. A sample scene of the proposed XR-based catheter tracking system.

Fig.1 : Cubic 3D setup. Left: 3D Designed version. Right: 3D Printed Version. Fig.2: Block diagram of proposed vision algorithm. Fig. 3. A sample scene of the proposed XR-based catheter tracking system.

Microstructure in amygdala and hippocampal subfields is associated with clinical and behavioral measures in patients with psychiatric illness.

Stuti Bansa¹, Sarah Boukezzi¹, Philipp Neukam¹, Priti Balchandani¹, James Murrough¹,
Laurel Morris¹ * and Yael Jacob¹ *. * - Co-last authors

¹Icahn School of Medicine at Mount Sinai

Introduction: Structural abnormalities in the hippocampus and amygdala have been repeatedly shown in patients with psychiatric illnesses. High-resolution MRI makes it possible to segment individual subfields of each structure, and microstructural data can be captured by NODDI, an MRI model that provides estimates of neurite density (ICVF) and angular complexity (ODI). By using NODDI in combination with segmentation of hippocampus and amygdala subfields, this study provides a unique look at the associations between microanatomical data and clinical and behavioral measures.

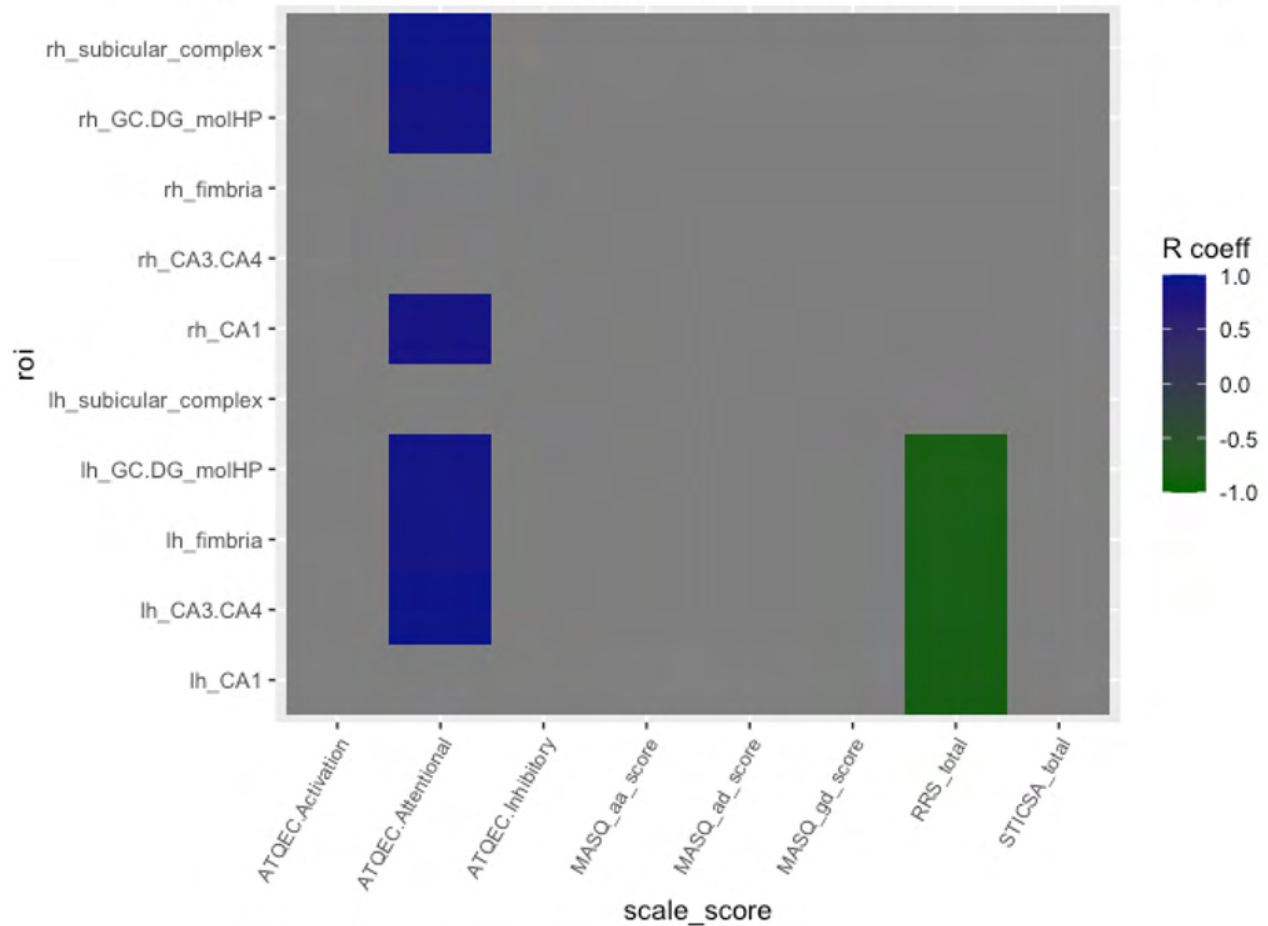
Materials and Methods: 7T MRI scans (T1-weighted structural scan, multi-shell diffusion-weighted scan) were collected in 92 subjects. Freesurfer segmentation, diffusion pre-processing, and NODDI model fitting were run. Individualized ROIs were created of whole hippocampus, whole amygdala, and subfields. Clinical and behavioral data was also collected: the Mood and Anxiety Symptom Questionnaire (MASQ), the Rumination Response Scale (RRS), and the Adult Temperament Questionnaire of Effortful Control (ATQEC). GLMs were run in R: scale measures vs. mean ODI/ICVF in amygdala/hippocampus subfields, controlling for age, sex, medication, and volume of amygdala/hippocampus. Results were thresholded at $p < 0.05$, FDR-corrected.

Results: MASQ: In healthy controls ($n=42$), mean ICVF in the right hippocampus and the left central nucleus (amygdala) positively correlated with MASQ anxious arousal. In patients with PTSD ($n=13$), mean ICVF in the right subicular complex (hippocampus) negatively correlated with MASQ general distress. RRS: In a combined sample of all patients ($n=50$), mean ICVF in right hippocampus (whole and various subfields) positively correlate with the total RRS score. In patients with PTSD ($n=13$), mean ODI in the left accessory basal nucleus (amygdala), and mean ODI in left hippocampus subfields all negatively correlated with total RRS score. ATQEC: In patients with PTSD ($n=13$), mean ODI in bilateral hippocampus and right hippocampus subfields positively correlate with the Attentional Control sub-score of the ATQEC. In patients with MDD ($n=17$), mean ICVF in the left cortical nucleus (amygdala) negatively correlated with Attentional Control. In patients with anxiety disorders ($n=20$), mean ODI in the whole left amygdala negatively correlated with the Activation Control sub-score of the ATQEC, while mean ODI in left amygdala subfields positively correlated with the Inhibitory Control sub-score of the ATQEC.

Conclusions: In patients with psychiatric illnesses, microstructural data in hippocampus and amygdala subfields predicts behavioral measures in ways that healthy controls do not exhibit. Further understanding of the microstructural anatomy of patients with psychiatric disorders may illuminate the complex interactions between brain structure and clinical phenomena.

PTSD: ODI Hippocampus vs. Scale subscore

Controlling for: Age, Sex, Medications, Hippocampus Volume. $p < 0.05$, FDR-corrected



Orientation Dispersion Index (ODI) in hippocampus subfields vs. Clinical and Behavioral Measures, in patients with PTSD (n=13). Controlling for age, sex, medication, and hippocampus volume.

Microstructure in amygdala and hippocampal subfields is associated with clinical and behavioral measures in patients with psychiatric illness.

Stuti Bansal¹, Sarah Boukezzi¹, Philipp Neukam¹, Priti Balchandani¹, James Murrrough¹, Yael Jacob¹ * and Laurel Morris¹ *. * - Co-last authors

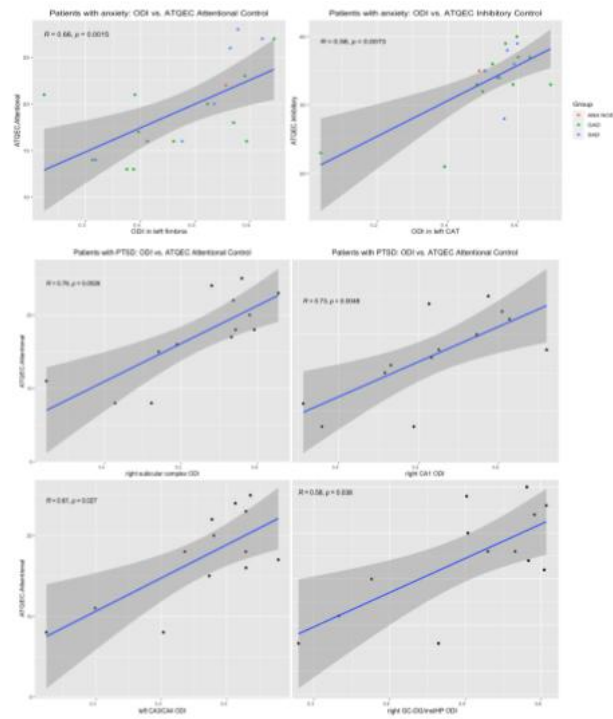
¹Icahn School of Medicine at Mount Sinai

Introduction: Patients with mood and anxiety disorders show structural abnormalities in the hippocampus and amygdala. Using in vivo high-resolution MRI and the neurite orientation dispersion and density imaging (NODDI) model, this study investigates how microstructural properties (neurite density/NDI, orientation dispersion index/ODI) in hippocampus and amygdala subfields are associated with behavioral measures in patients with mood and anxiety disorders.

Materials and Methods: 7T MRI scans (T1-weighted anatomical; multi-shell diffusion-weighted) were collected in 50 patients, preprocessed, segmented in Freesurfer, and fitted to NODDI. Using individualized ROIs, mean NDI and ODI were extracted from hippocampus and amygdala subfields. Mood and Anxiety Symptom Questionnaire (MASQ), Rumination Response Scale (RRS), and Adult Temperament Questionnaire (ATQ) were collected. GLMs: scale measures vs. mean subfield ODI or NDI, controlling for age, sex, medication, and volume of hippocampus or amygdala. Results were reported at $p < 0.05$, FDR-corrected.

Results: In all patients, NDI in right Dentate Gyrus, CA1, CA3/4 were positively associated with the RRS total score. In patients with PTSD ($n=13$), ODI in left Fimbria, Dentate Gyrus, CA1, CA3/4 (hippocampus) and left Accessory Basal Nucleus (amygdala) were negatively associated with RRS; ODI in right Subicular Complex, Dentate Gyrus, CA1, and left Fimbria, Dentate Gyrus, CA3/4 (hippocampus) were positively associated with ATQ Attentional Control; and NDI in the right Subicular Complex (hippocampus) negatively correlated with MASQ general distress. In patients with anxiety disorders ($n=33$), ODI in the left Fimbria (hippocampus) was positively associated with Attentional Control, while ODI in left Cortical Nucleus, Accessory Basal Nucleus, Cortico-Amygdaloid Transition (amygdala) were negatively associated with ATQ Inhibitory Control.

Conclusions: In patients with psychiatric disorders, microstructural properties of hippocampus and amygdala subfields are associated with clinical and behavioral measures like general distress, rumination, attentional control, and inhibitory control. Further understanding of the microstructural anatomy of patients with psychiatric disorders may illuminate the complex interactions between brain structure and clinical phenomena.



Orientation Dispersion Index (ODI) in hippocampus and amygdala subfields vs. ATQ Attentional and Inhibitory Control scores, in patient with anxiety (n=33) and patients with PTSD (n=13). Controlling for age, sex, medication, and volume.

Validating mood and anxiety symptom capture in the real-world and exploring the influence of physical activity

Jacqueline M. Beltran¹, Tasnim Hossain², Marishka M. Mehta³, Abigail A. Adams¹, Andrew Delgado¹, James W. Murrough¹, Laurel S. Morris¹

¹The Icahn School of Medicine at Mount Sinai

²Tufts University

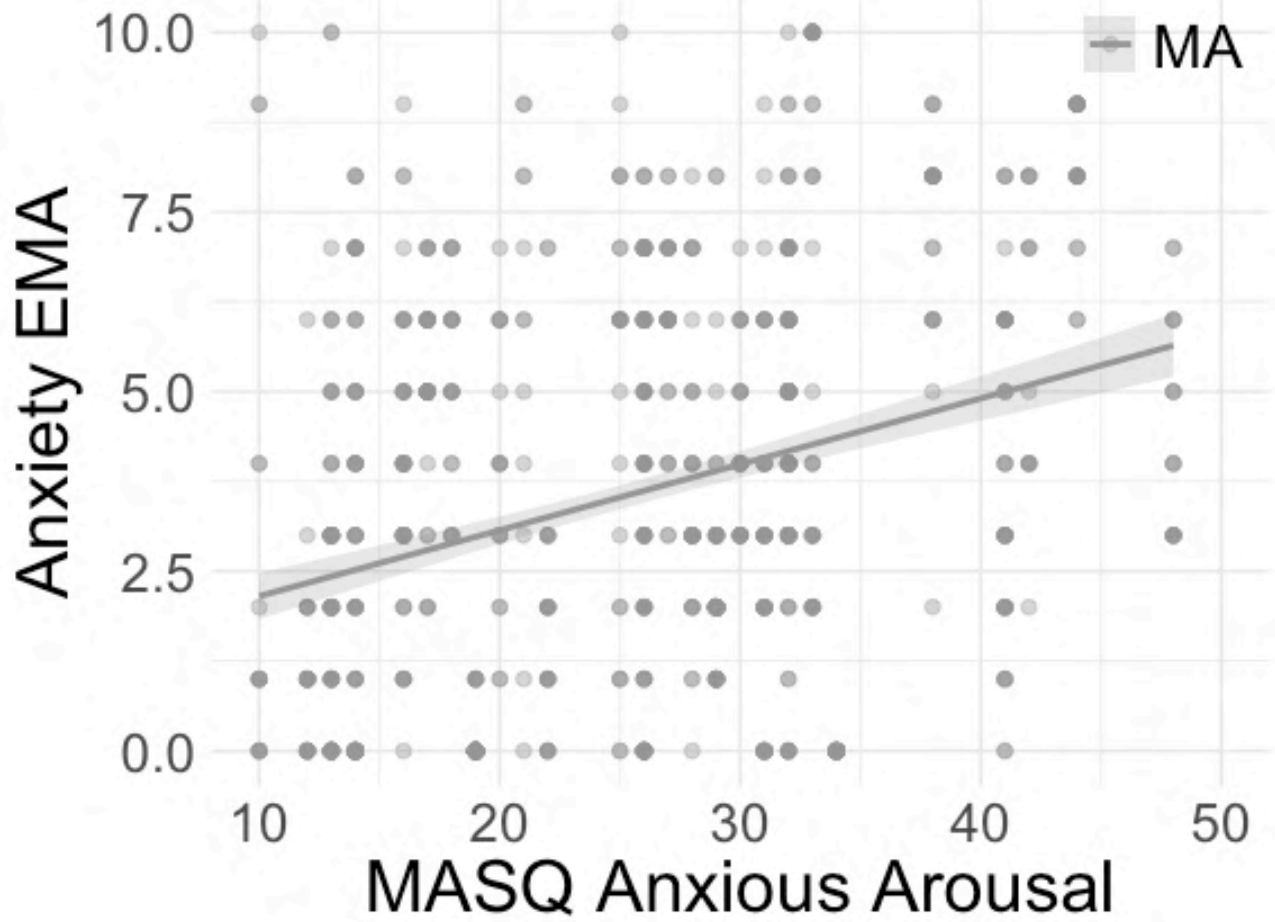
³The Laureate Institute for Brain Research

Introduction: Mood and anxiety disorders are highly prevalent, yet poorly understood. Understanding the lived experience and temporal dynamics of symptoms as they relate to 'gold-standard' in-lab measures is critical.

Materials and methods: To monitor psychiatric symptoms in the real-world, we deployed a smart-phone application to N=106 individuals with mood/anxiety disorders (MA) and healthy controls (HC). The app captured novel single-item measures of depression, anxiety and distress along with daily steps data for N=70 after preprocessing (N=34 MA, N=36 HC). Subjects also completed the Mood and Anxiety Symptom Questionnaire (MASQ) in-lab. Mixed-effects models adjusted for time and individual tested the association between daily self-reported symptoms and gold-standard in-lab measures, while Zero-inflated Poisson (ZIP) mixture models adjusted for time, group, and individual tested the association between self-reported symptoms and steps.

Results: After preprocessing, N=101 participant data were available for analysis (N=52 MA, N=49 HC). There was overall moderate adherence over 30-days (MA=69.9%, HC=71.3% completion), with no group difference in adherence ($t(96.8) = 0.36, p = 0.72$). Daily real-world single-item measures of anxiety/distress/depression were associated with corresponding in-lab measures within our MA group (MASQ anxious-arousal/distress/depression: $t(46.9)=2.33, p=0.024/t(46.4)=4.65, p<0.001/t(46.9)=2.73, p=0.009$). ZIP models revealed that step counts were negatively associated with real-world distress and depression (IRR = 0.95, CI = (0.91 - 1.00), $p = 0.037$ /IRR = 0.93, CI = (0.89 - 0.97), $p = 0.002$).

Conclusions: Preliminary findings suggest the utility of digital phenotyping for accurately monitoring psychiatric symptoms and environmental contingencies that impact mood in a patient population. All updated results will be presented.



Validation of in-lab measures of anxious arousal and real-world longitudinal self-reports of anxiety within individuals with mood/anxiety disorders.

Multi-modal imaging of carotid atherosclerotic risk in substance use disorders

Huang Y¹, Butelman ER¹, McClain N¹, Hao Q², Dhamoon M², Robson P³, Kaufman A³, Goldstein RZ¹, Fayad Z³, Alia-Klein N¹

¹ Neuropsychomaging of Addictions and Related Conditions, Dept. of Psychiatry, ISMMS,

² Department of Neurology, ISMMS,

³ BMEII at ISMMS

Introduction: Multi-modal imaging of carotid atherosclerotic risk in substance use disorders Introduction: Many individuals with cocaine or heroin use disorders (iCUD and iHUD) are reaching older ages in the lifespan, and personalized risk evaluation is crucial. A history of chronic drug use can affect central nervous system structure and function, including increased incidence of carotid atherosclerosis. The underlying mechanisms of this disease in iCUD and iHUD are unknown. Evaluation of carotid atherosclerosis with state-of-the-art multimodal imaging could clarify potential mechanisms underlying increased morbidity risk.

Materials and Methods: Fifteen inpatient and outpatient iCUD and iHUD (aged 50.97 ± 9.41 ; 4 women; with no recorded history of atherosclerotic or cerebrovascular disease) underwent a neurological and carotid duplex exam. Participants were scanned with 18FDG PET/MR (Siemens Biograph mMR) at BMEII. Atherosclerotic plaque was examined with MRI and PET techniques, based on clinically validated cutoffs for thickness (from MR) or target/background ratios (TBR; from PET). Common carotid artery (CCA) thickness was examined for correlation with demographic features. Carotid ultrasound Doppler was performed, the carotid intima-media thickness (IMT, surrogate marker for atherosclerosis), wall thickening, and flow velocities were recorded.

Results: Fifteen iCUD and iHUD in total were scanned. Of the 9 individuals with data available in the left CCA, 8 exhibited $TBR > \text{cutoff}$ associated with increased atherothrombotic events (Fig. 1). Correlations between drug use variables and the PET/MR measures will be explored further with larger samples in the future. Preliminary results reveal a trend of positive correlation between left CCA IMT and age (Pearson $r=0.55$, $p=0.065$). Figure 1: A: 18FDG-PET evaluation with Target/Background Ratio (TBR). B-D Examples of multimodal imaging of a participant in the study. B: Left carotid bulb ultrasound. Intima-media thickness (IMT; measured from the "+" markers)=0.15 cm (i.e., 1.5 mm); cutoff value indicative of plaque. C: 18FDG PET image from left CCA with the region of interest. D: 3D MRI image from the same area as the PET image.

Conclusions: This initial cohort demonstrates the feasibility of multi-modal imaging for carotid atherosclerosis in iHUD and iCUD, together with clinically used ultrasound techniques. Initial results point to elevated carotid atherothrombotic risk in these iCUD or iHUD across the lifespan. Future studies will compare carotid atherosclerotic profiles and risk in persons with these diseases, compared to age-matched controls. Funding: NIH-NIDA 5R01DA049547-02 (MPI Alia-Klein, Goldstein, Fayad).

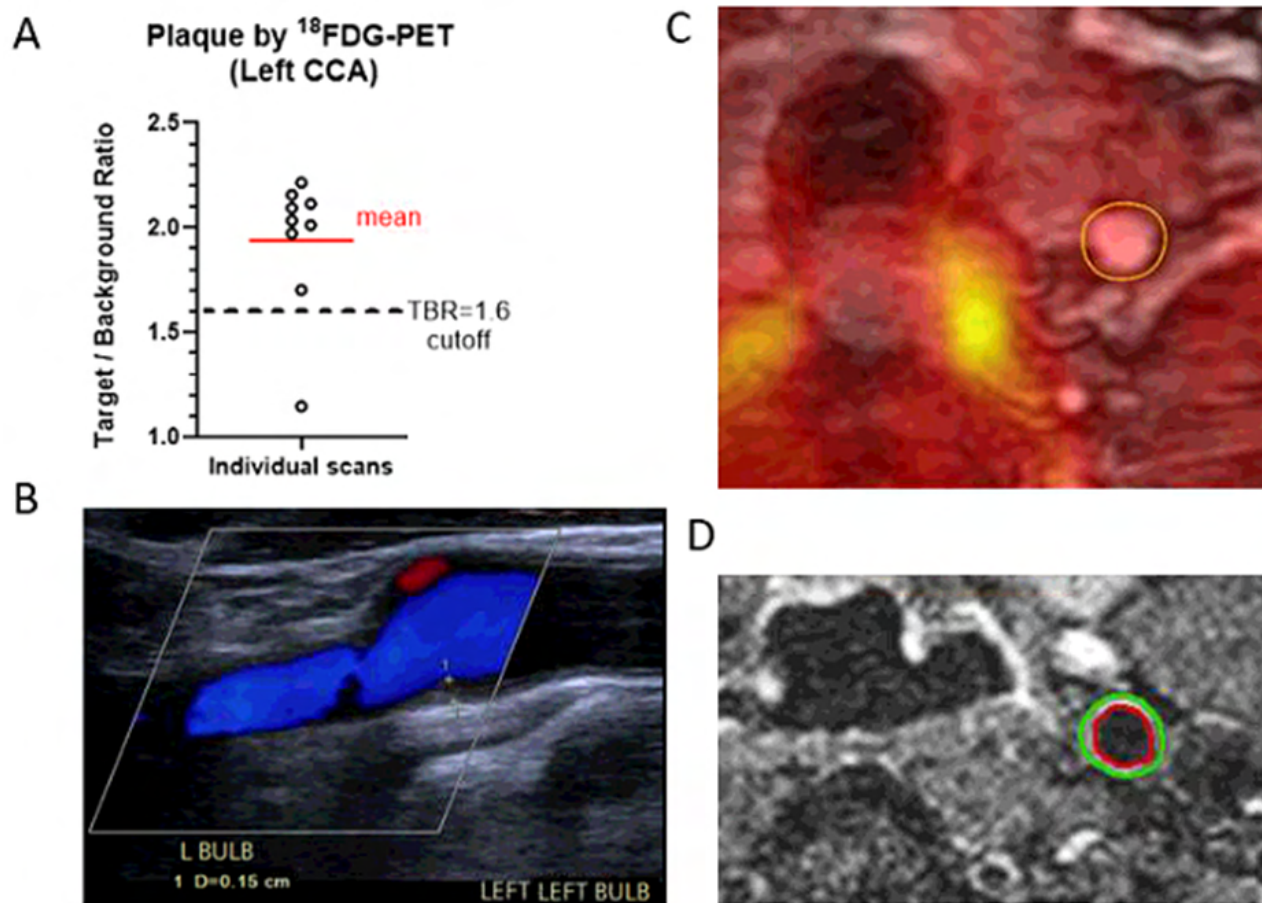


Figure 1: A: ^{18}F FDG-PET evaluation with Target/Background Ratio (TBR). B-D Examples of multimodal imaging of a participant in the study. B: Left carotid bulb ultrasound. Intima-media thickness (IMT; measured from the "+" markers)=0.15 cm (i.e., 1.5 mm); cutoff value indicative of plaque. C: ^{18}F FDG PET image from left CCA with the region of interest. D: 3D MRI image from the same area as the PET image.

The Neurobehavioral Representations of Regret in Depression

Avijit Chowdhury, Philipp Neukam, Laurel Morris, James Murrough, Xiaosi Gu

Icahn School of Medicine at Mount Sinai

Depression is a disorder of the expression and regulation of emotions. Specifying the neurobiological mechanisms of atypical emotional and cognitive processing early during depression is crucial, as it may help in the more effective treatment of depression. Cognitively, depression is characterized by a mood-congruent negativity bias - the tendency to appraise events, the self, and the world negatively. Depression is also associated with anhedonia, which is a blunted or reduced sensitivity to pleasure from usually rewarding activities. However, the association between depression and positive and negative emotions that arise from counterfactual processing - such as regret and relief - needs further investigation. Here, we used functional neuroimaging (fMRI) and a simulated stock market task in which both healthy control and individuals with major depressive disorder participants decided how much to invest (i.e. positive bet) or short-sell (i.e. negative bet) depending on their predictions of the prices. Depending on the participant's investment and market - participants either won or lost money - resulting in a (counterfactual) regret and relief signal. In a sample of non-expert participants (HC=64, MDD=40), we found that following a non-optimal win-outcome, individuals with MDD were more sensitive to regret - they made larger next bets, possibly to compensate for the "missed opportunity". In a subsample of participants (HC=20, MDD=23) who completed fMRI during the stock market task, the magnitude of regret following wins modulated increased activity across participants in the bilateral ventral striatum (VS). Examination by groups revealed this VS activation to only survive cluster correction in the HC but not the MDD sample. Additionally, MDD participants also showed increased activation in the middle/inferior frontal gyri in response to regret, which positively correlated with self-reported depression and anxiety scales (DASS) Our findings may explain potential mechanisms by which regret-related cognition may be differentially modulated in MDD versus HC. Specifically, increased activation in the middle/inferior frontal gyri may be related to efforts to regulate negative emotions.

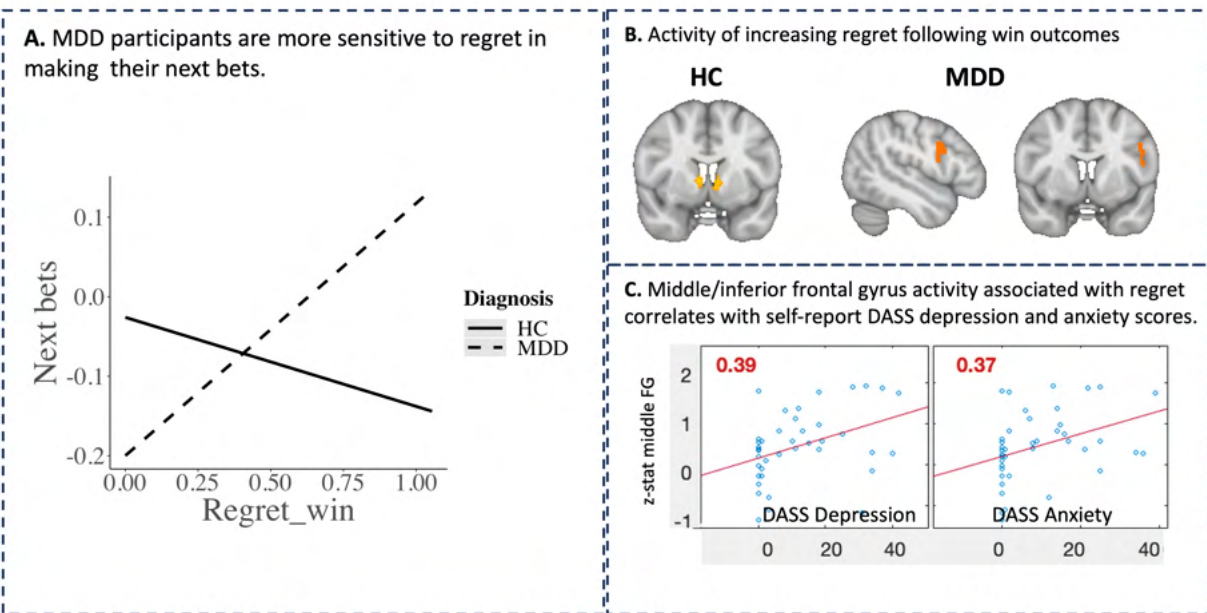


Figure. Differences in behavioral and fMRI responses to regret following wins in individuals with major depressive disorder (MDD) versus healthy controls (HC). **A.** Following a regret-inducing outcome, MDD participants made larger next bets compared to HC. **B.** Ventral striatum activation in response to regret survived correction only in the HC but not in the MDD group. MDD group showed an increased activity in the middle/inferior frontal gyrus in response to regret, which positively correlated (**C**) with depression and anxiety scores.

Differences in behavioral and fMRI responses to regret following wins in individuals with major depressive disorder (MDD) versus healthy controls (HC)

Assessment of Cardiac Flow Dynamics in Mitral Valve Prolapse Using Direct Numerical Simulation: Proof of Concept

Dario Colli^{1,2}, Navindra David³, Maria G. Trivieri⁴, Marc A. Miller⁵, Philip M. Robson⁴, Zahi A. Fayad⁴, Gianni Pedrizzetti², David H. Adams¹, Dimosthenis Pandis¹

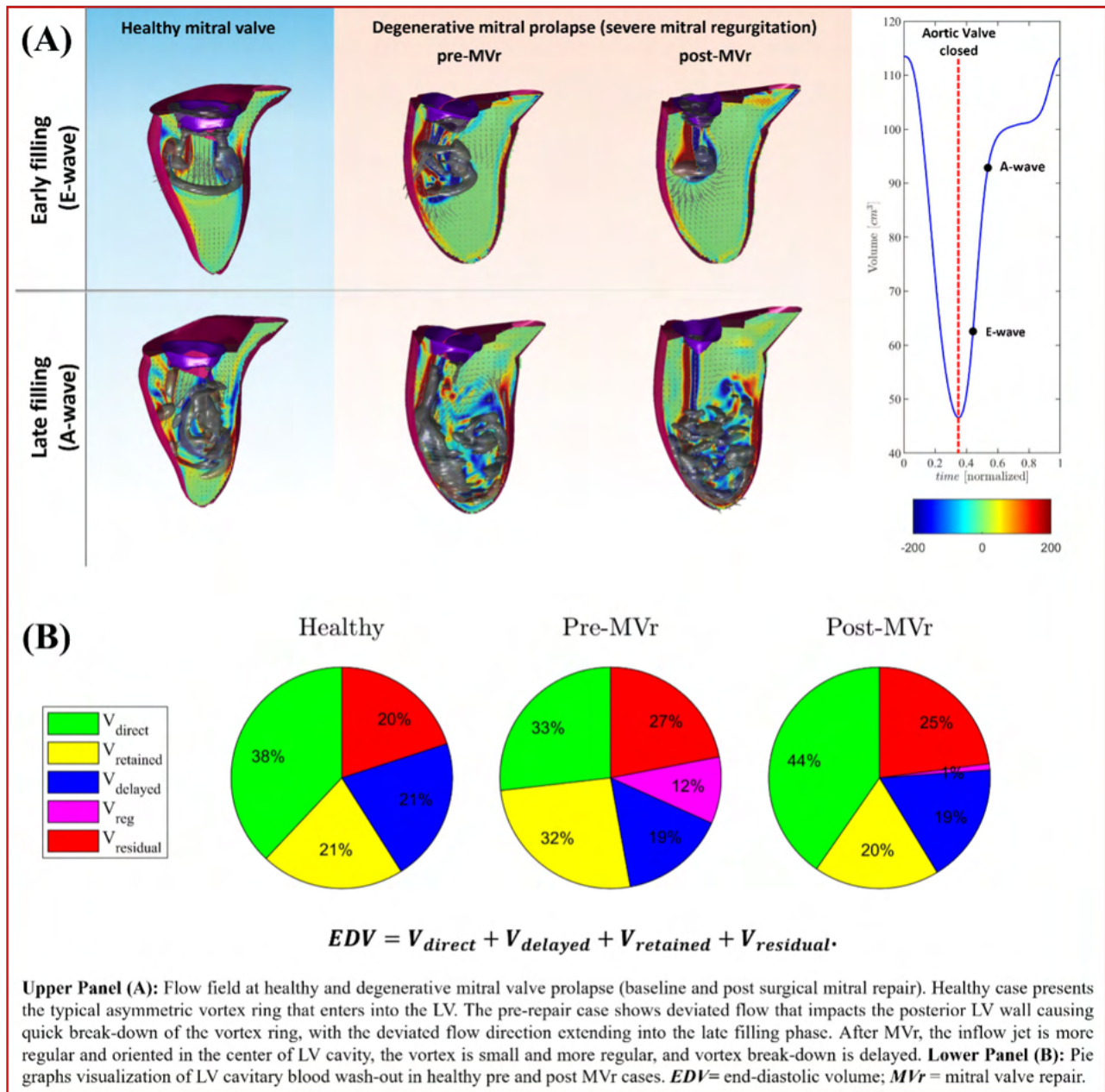
¹Department of Cardiovascular Surgery, Icahn School of Medicine at Mount Sinai, New York, NY, USA, ²Department of Engineering and Architecture, University of Trieste, Trieste, Italy, ³The Icahn School of Medicine at Mount Sinai, New York, NY, USA, ⁴The BioMedical Engineering and Imaging Institute (BMEII), Icahn School of Medicine at Mount Sinai, New York, NY, USA, ⁵ Helmsley Electrophysiology Center, Icahn School of Medicine at Mount Sinai, New York, NY, USA

Introduction: Fluid dynamics are associated with cardiovascular development and adaptation to flow alterations during physiologic stress and cardiovascular disease, including surgical interventions. The aim of this study is to evaluate blood flow (cavitary volumes, energy dissipation, vorticity) in degenerative mitral valve prolapse (MVP).

Methods: In this proof-of-concept study we evaluated flow dynamics in 5 patients with degenerative MVP and severe mitral regurgitation at baseline and following surgical mitral repair (MVR), compared with 5 healthy controls. Mitral valve and left ventricular (LV) geometries were extracted from 4D-transesophageal echocardiography acquisitions. Flow dynamics are reproduced by direct numerical simulation (DNS).

Results: Systolic LV function was similar between healthy controls (n=5) and operative patients (n=5) at baseline (median EF 61% vs. 59%; P=0.4). Notably, mitral prolapse was associated with early breakdown of inflow vortex (median vortex formation time [VFT] 2.3 vs. 4.1; P= 0.04). However, while vorticity was improved following mitral repair ([VFT]: 3.7 vs. 2.3; P=0.13; Fig 1A) it remained abnormal compared to healthy controls. Based on the sub-volume components of the end-diastolic LV volume ($EDV = V_{direct} + V_{delayed} + V_{retained} + V_{residual}$) blood flow residence (wash-out) was also improved following corrective mitral surgery (Fig 1B).

Conclusions: This proof-of-concept study provides important insight on the role of hemodynamics in the evaluation of mitral prolapse. Our results show subclinical alterations in the mechanics of blood flow as it interacts with the prolapsed mitral valve and LV cavity compared to healthy controls. Remarkably, these alterations may only be partially restored following corrective mitral surgery despite abatement of mitral regurgitation, which warrants further work to validate our findings in a larger clinical model.



Enhancing allograft survival using nanotherapeutics targeting the innate immune system

Maria Giulia Davighi¹, William Wang¹, Anna Ranzenigo¹, Judit Morlà-Folch¹, Sufian Mohammad¹, Rianne Maas¹, Abraham Teunissen¹

BioMedical Engineering and Imaging Institute, Icahn School of Medicine at Mount Sinai, 1470 Madison Ave, New York, 10029 New York, USA

When innate immune cells are exposed to certain stimuli, they manifest a long-term enhanced response upon restimulation. This functional reprogramming of innate immune cells is termed trained immunity (Fig.1). Therapeutic modulation of trained immunity by targeting specific metabolic or epigenetic processes in myeloid cells is a promising strategy to treat inflammatory conditions, including allograft rejection. We have previously reported on apolipoprotein A1-based (apoA-I) nanobiologics with high myeloid cell avidity. Furthermore, we developed a modular approach to incorporate drugs in these nanocarriers. The drugs were derivatized with biocleavable lipophilic promoieties to ensure efficient incorporation in nanobiologics without modifying the nanocarrier. The nanobiologics apoA-I constituent was then functionalized with the chelator deferoxamine, allowing their radiolabeling with ⁸⁹Zr and assessing their pharmacokinetics and biodistribution by PET imaging and ex vivo gamma counting. Flow cytometry similarly demonstrated nanobiologics' high uptake and affinity for myeloid cells. Our therapeutic studies initially focused on rapamycin, which inhibits the mammalian target of rapamycin (mTOR), one of the main pathways implicated in trained immunity. We tested rapamycin prodrug-loaded nanobiologics (mTORi-NBs) in a murine model of heart allograft transplantation which resulted to prolong allograft survival without requiring chronic immunosuppression. To better understand which trained immunity pathway play a central role in determining graft survival, we here synthesized a nanotherapeutics library aimed at inhibiting other metabolic and epigenetic targets involved in trained immunity (Fig.2) The small molecule drugs were esterified with 1-octadecanol, stearic acid or stearyl chloride to achieve prodrugs featuring a long apolar pro-moiety to enhance the therapeutic payload's lipophilicity. Some substrates required an enzymatic esterification to achieve a site-specific functionalization. The nanobiologics were formulated with phospholipids, cholesterol, and apolipoprotein-A1 using a microfluid formulation process. Prodrug incorporation was quantified by ¹H NMR or HPLC. Fifteen different prodrugs were successfully synthesized starting from small molecule inhibitors targeting regulators of trained immunity. The prodrugs were incorporated into the nanobiologics with recoveries of 6-91%. Nanobiologics evaluation will occur in vitro using mouse BMDM and human PBMCs and in vivo in a heart allograft mouse model. Previously reported rapamycin prodrug-loaded nanobiologics exhibited high affinity for myeloid cells, enabling targeted drug delivery to the innate immune system. To further understand the impact of our newly synthesized nanobiologics on the immune system, our upcoming experiments will concentrate on assessing their behavior upon in vivo injection in a heart allograft mouse model.

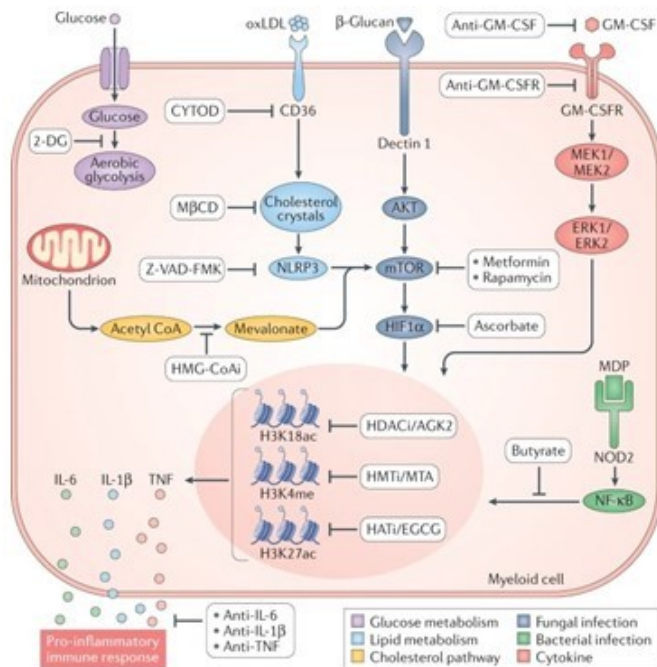
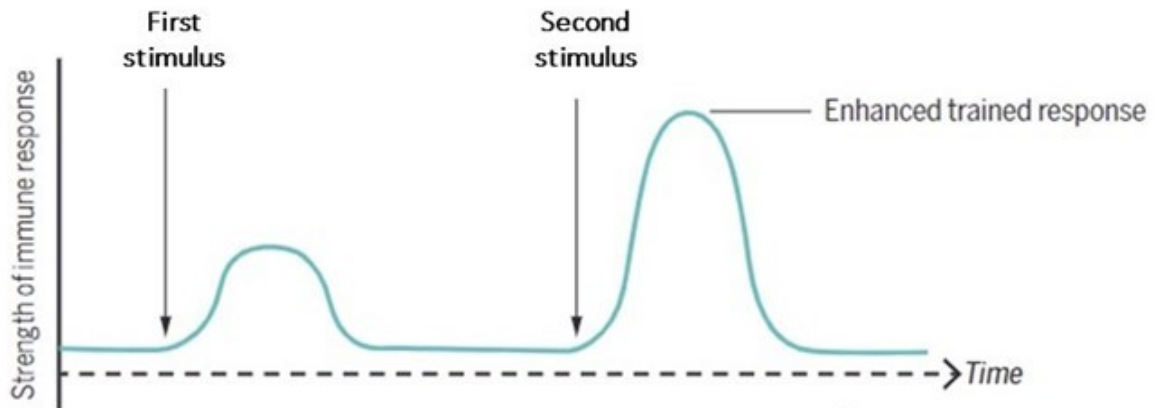


Fig. 1: Adaptive behavior of innate immune cells in trained immunity Fig.2: Intracellular mechanisms mediating trained immunity

Specific locations of myocardial inflammation and fibrosis are associated with higher risk of events in cardiac sarcoidosis

Ana Devesa, MD, PhD^{1,2,3}; Philip M. Robson, PhD¹; Vittoria Vergani MD⁴; Gina LaRocca MD³; Angelica M. Romero-Daza MD⁵, Steve Liao, MD³; Lévi-Dan Azoulay, MD¹; Renata Pyzik, BS¹; Rima A. Fayad MPH¹; Adam Jacobi, MD⁶; Ronan Abgral, MD, PhD⁷; Adam S. Morgenthau, MD⁸; Marc A. Miller, MD⁹; Zahi A. Fayad, PhD¹; Maria Giovanna Trivieri, MD, PhD^{*1,3}.

¹BioMedical Engineering and Imaging Institute, Icahn School of Medicine at Mount Sinai, New York, NY. ²Centro Nacional de Investigaciones Cardiovasculares (CNIC), Madrid, Spain. ³Mount Sinai Heart, Icahn School of Medicine at Mount Sinai, New York, NY. ⁴School of Biomedical Engineering and Imaging Sciences, King's College London, London, UK ⁵Department of Cardiology, Hospital La Luz - Quirón Salud, Madrid, Spain ⁶Department of Radiology, Icahn School of Medicine at Mount Sinai, New York, NY. ⁷Department of Nuclear Medicine, UMR Inserm 1304 GETBO, University Hospital of Brest, France. ⁸Division of Pulmonary, Critical Care and Sleep Medicine, Icahn School of Medicine at Mount Sinai, New York, NY. ⁹Helmsley Electrophysiology Center, Icahn School of Medicine at Mount Sinai, New York, NY.

Introduction: 18F-FDG-PET/MR can identify inflammation and fibrosis, high-risk features in cardiac sarcoidosis. **Objectives:** To evaluate whether the involvement of certain myocardial segments is associated with higher risk compared to others.

Methods: 124 patients with suspected clinical sarcoidosis underwent 18F-FDG-PET/MR. Late gadolinium enhancement (LGE) and focal 18F-FDG uptake were evaluated globally and in the 16 myocardial segments. Presence of LGE was defined when the percentage of LGE exceeded 5.7% globally (relative to myocardial volume) and in each myocardial segment. Patients were followed up for 5.5 years. Events were defined as ventricular arrhythmia (VA, including sustained ventricular tachycardia, ventricular fibrillation, and appropriate ICD discharge), heart failure hospitalization, or all-cause death.

Results: Mean age was 57.1±8.9 years, and 39.5% were female; 22 patients (17.6%) had an event at follow-up, and 9 (7.2%) presented VA. LGE and 18F-FDG uptake were more frequent in patients with than without events (36.4% vs 7.8%, p=0.001). Presence of LGE or 18F-FDG in the basal anterior segment were independent predictors for events after adjustment by left ventricular ejection fraction and relative enhanced volume (LGE: OR 10.5[1.2-92.4]; p=0.034; 18F-FDG: OR 5.5[1.1-27.5], p=0.038) (Figures 1). LGE presence in basal to mid anterior, mid anteroseptal, and basal to mid inferoseptal segments was an independent predictor for VA. Presence of 18F-FDG in basal to mid anterior, mid inferoseptal and mid inferior segments was an independent predictor for VA.

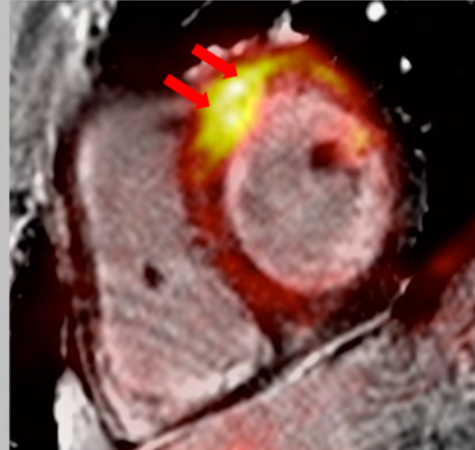
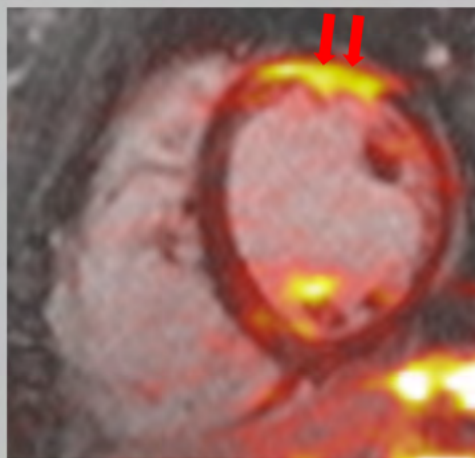
Conclusions: Involvement of specific myocardial segments, particularly basal to mid anterior and mid septal segments, is associated with higher rates of events in patients with suspected cardiac sarcoidosis (Figure 2).

↑ risk of events

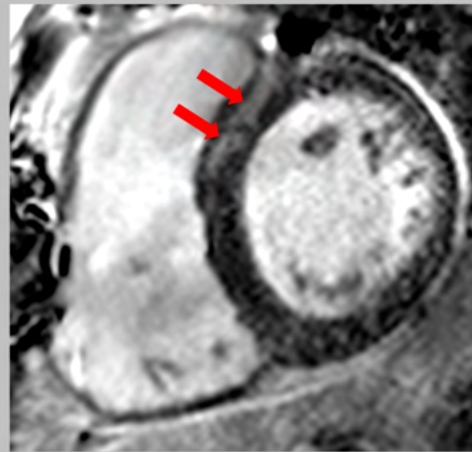
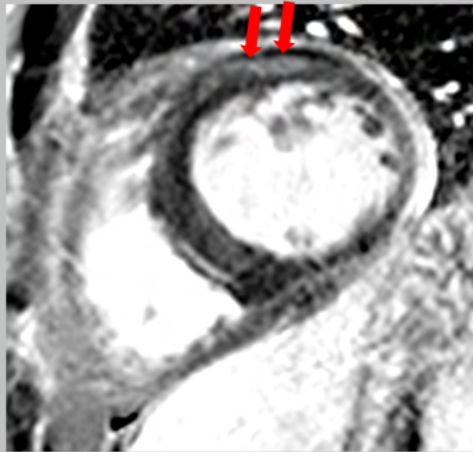
Basal to mid anterior

Mid septum

Inflammation



Fibrosis



Location of inflammation and fibrosis predicts the risk of events in patients with suspected cardiac sarcoidosis. The upper panel shows a representative example of fused 18F-FDG PET/MR images: a short axis view with increased 18F-FDG uptake in the mid anterior wall (red arrows, left upper panel) and in the mid anteroseptum (red arrows, right upper panel). The lower panel shows representative CMR image including a short axis view showing LGE in the mid anterior segment (red arrows, left lower panel) with an intramyocardial pattern; and a short axis view with LGE in the mid anteroseptum (red arrows, right lower panel).

Cortical lesions in early multiple sclerosis are prevalent and associated with cognitive disability

Jonadab dos Santos Silva¹, Francesco La Rosa¹, Julia Galasso¹, Faye Bourie¹, William A Mullins², Govind Nair², James Sumowski¹, Erin S Beck^{1,2}

¹ Department of Neurology, Icahn School of Medicine at Mount Sinai, New York, NY, USA

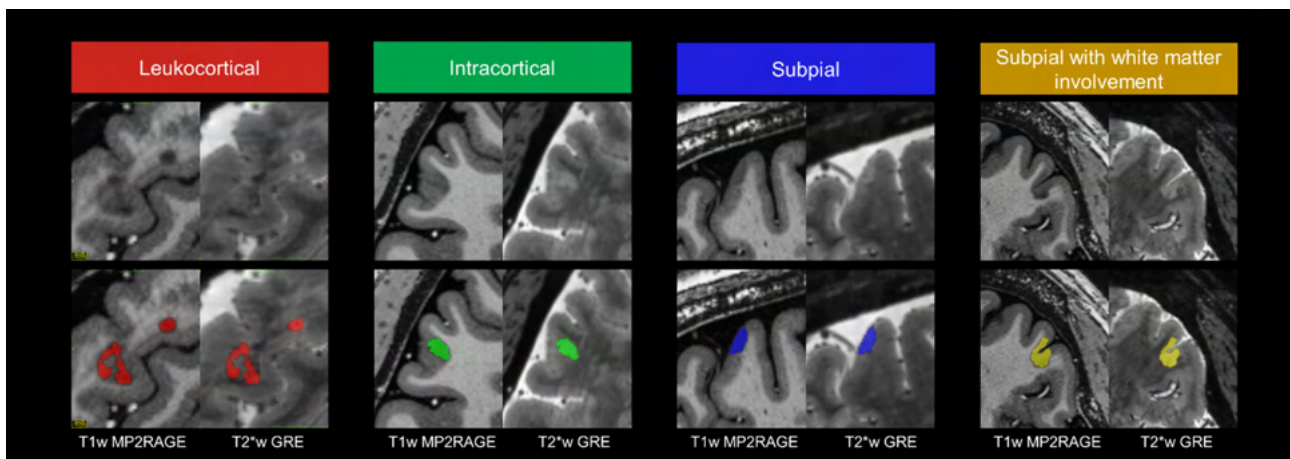
² National Institute of Neurological Disorders and Stroke, National Institutes of Health, Bethesda, MD, USA

Introduction: Cortical lesions are common, extensive, and linked to physical and cognitive disability in multiple sclerosis (MS). Ultra-high-field MRI has substantially enhanced cortical lesion detection. However, the natural history of cortical lesions, including their prevalence and role in early MS is unclear. Therefore, we aimed to assess cortical lesion prevalence and its impact on physical and cognitive performance in adults with newly diagnosed MS.

Methods: Sixteen adults diagnosed with MS in the last year (mean age 33 ± 5 years, 81% female) and eight healthy volunteers (mean age 30 ± 8 years, 63% female) underwent physical and neuropsychological assessment and 7T brain MRI (0.5mm³ MP2RAGE [median of 3 acquisitions], 0.7mm³ MP2RAGE, and 0.5mm³ motion and B0-corrected T2*w-GRE). Normalized brain volume (NBV) estimation and semiautomated white matter lesion (WML) segmentation were performed with FreeSurfer and PLAN, respectively, using 0.7mm³ T1w-MP2RAGE images. Cortical lesions were segmented manually by two blinded raters using median 0.5mm³ T1w-MP2RAGE and T2*w-GRE images. Cortical lesions were subcategorized as: 1) subpial: touching the pial surface, 2) intracortical: contained entirely within the cortex but not reaching the pial surface, and 3) leukocortical: involving both the cortex and white matter.

Results: Cortical lesions were present in 93% of individuals with MS, with a median of 19 lesions (interquartile range [IQR] 26, range 0-63). Subpial lesions were the most common type (median 67%, IQR 48, range 0-100%), and 80% of MS participants had at least one cortical lesion. No cortical lesion was found in any of the healthy volunteers. Cortical lesion volume (1350 mm³, IQR 241, range 32-3877 mm³) was similar to WML volume (842 mm³ [IQR 2522, range 227-15005 mm³], $Z=-0.47$, $P=0.638$). Despite this similarity, age and sex-adjusted cortical lesion, but not WML, burden was associated with lower NBV ($r=-0.64$, $P=0.02$) and worse processing speed performance on the Symbol Digit Modalities Test ($r=-0.70$, $P=0.006$). There was also a negative correlation between the Hopkins Verbal Learning Test-Revised score and leukocortical lesion volume ($r=-0.61$, $P=0.02$), adjusted for age and sex.

Discussion: Cortical lesions are present in most adults with newly diagnosed MS and are linked to cognitive disability and brain atrophy. Unlike in longstanding disease, when WML volume is often 10-100 times greater than cortical lesion volume, in early MS, cortical lesion volume is comparable to WML, suggesting that most cortical lesions form early in disease. Therefore, early detection and monitoring of cortical lesions is important to potentially guide therapeutic strategies to mitigate cognitive decline in MS.



Cortical lesions in people with newly diagnosed Multiple Sclerosis . Cortical lesion subtypes, including leukocortical lesions, which involve both the cortex and white matter, intracortical lesions, which are contained entirely within the cortex, and subpial lesions, which touch the pial surface, are detected in adults with newly diagnosed MS using 7T MRI. T1w MP2RAGE images are the median of three acquisitions (0.5mm³), and navigator guided motion- and B₀-corrected T2*w GRE (0.5mm³).

Foundational Transformers with Linear Probing for Sleep Stage Classification using Time Series Sleep Study Data

Benjamin Fox^{1,3}, Sajila Wickramaratne³, Girish Nadkarni^{1,2}, Ankit Parekh³

¹ The Charles Bronfman Institute for Personalized Medicine, Icahn School of Medicine at Mount Sinai, New York, NY, USA

² Division of Digital and Data Driven Medicine, Icahn School of Medicine at Mount Sinai, New York, New York, USA

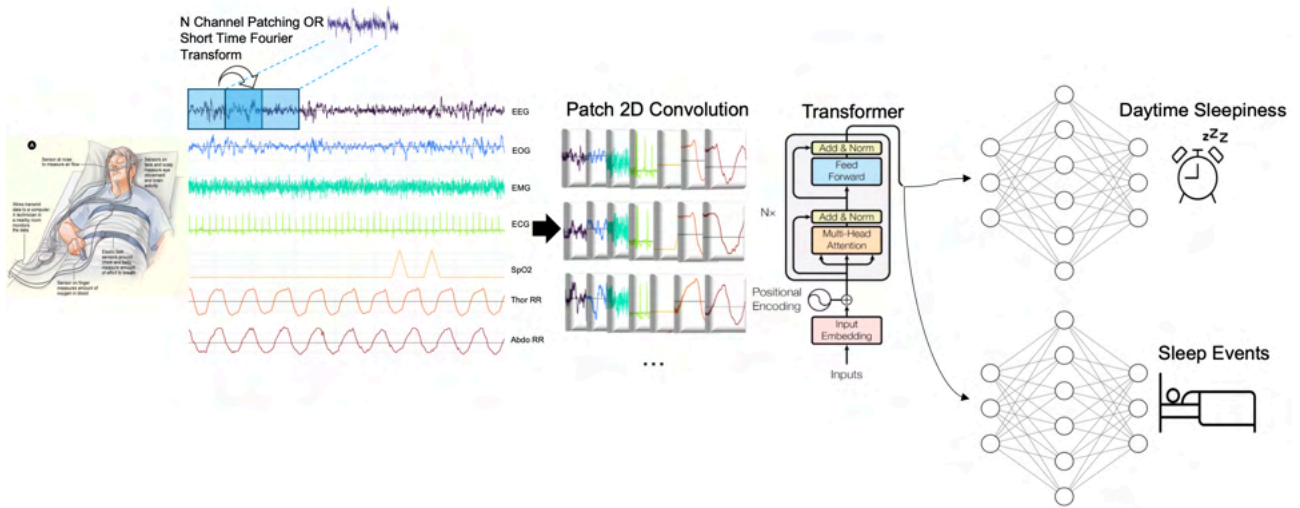
³ Division of Pulmonary, Critical Care and Sleep Medicine, Department of Medicine, Icahn School of Medicine at Mount Sinai, New York

Introduction: Sleep disorders and deprivation disrupt people's daily activities, mental health, and longevity and are related to widespread conditions. Currently, sleep disorders are diagnosed via polysomnography (PSG), where electrophysiological data is collected and manually annotated by a clinician. State of the art machine learning (ML) models, such as the transformer, are particularly well-suited for modeling timeseries PSG data. Specifically, self-supervised models with linear probing could assist with any relevant sleep predictive task including automating sleep stage classification, which would save clinicians time, reduce variability in manual scoring, and help scale to treat more people.

Materials and Methods: Using a self-supervised learning approach and the transformer architecture, we trained a self-supervised ML model that inputs seven PSG channels of length three hours including electroencephalogram, electrooculogram, electromyography, electrocardiography, oxygen saturation, and thoracic and abdomen respiratory rate using the Sleep Heart Health Study database (1995-1998). The model architecture uses the transformer's attention mechanism to learn long range dependencies between intervals of sleep and a convolutional layer to learn relationships among channels. The model learns representations of PSG data through masked reconstruction with a mean squared error loss function. The representations are used as input into a deep neural network that is trained via linear probing (without adjusting the weights of the transformer model) to classify sleep stages.

Results: 5,794 sleep studies from the Sleep Heart Health Study with at least three hours of relevant PSG sleep channel and hypnogram data are included in training the self-supervised and linear probing models. Area under the receiver operator characters curve for sleep stage classification are 0.960 [0.960-0.961], 0.848 [0.846-0.849], 0.906 [0.906-0.907], 0.968 [0.967-0.968], and 0.931 [0.930-0.932] for wake, stage 1, stage 2, stage 3, and REM, respectively. Hyperparameter tuning, class weighting, and dataset cleaning will be performed to increase classification results.

Conclusion: A self-supervised training approach using the transformer architecture with linear probing was utilized to learn multichannel PSG data representations. These representations were used as input into a downstream model to classify sleep stages accurately. Future work should be done to examine the capabilities of the self-supervised model representations for other predictive sleep tasks.



Foundational Transformer Encoder Model and Linear Probing Architecture

Deep brain stimulation promotes white matter remodeling and is accompanied by functional changes to brain-wide networks

Satoka H. Fujimoto^{1,2}, Atsushi Fujimoto^{1,2}, Catherine Elorette^{1,2}, Davide Folloni^{1,2}, Gaurav Verma^{3,6}, William GM Janssen¹, Lazar Fleysheer⁶, Ki Sueng Choi^{3,6}, Brian E. Russ^{1,4,5}, Helen S. Mayberg^{1,3}, Peter H. Rudebeck^{1,2}

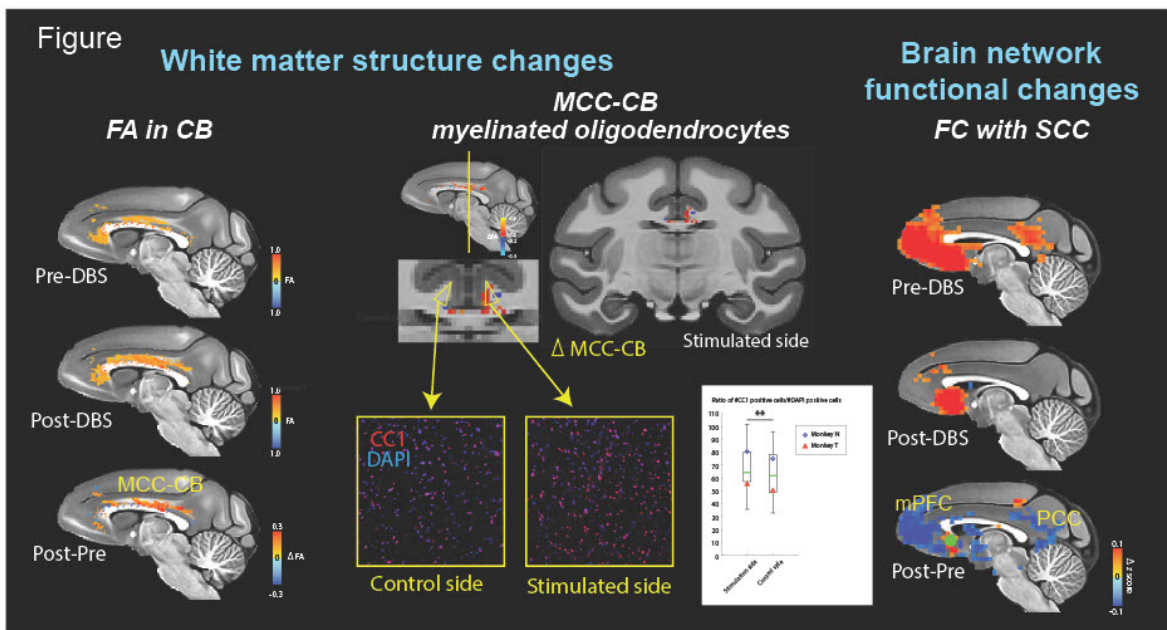
¹Nash Family Department of Neuroscience and Friedman Brain Institute, Icahn School of Medicine at Mount Sinai, One Gustave L. Levy Place, New York, NY 10029 ²Lipschultz Center for Cognitive Neuroscience, Icahn School of Medicine at Mount Sinai, New York, NY, 10029 ³Nash Family Center for Advanced Circuit Therapeutics, Mount Sinai West Hospital, 1000 10th Ave, New York, NY 10019 ⁴Center for Biomedical Imaging and Neuromodulation, Nathan Kline Institute, 140 Old Orangeburg Road, Orangeburg, NY 10962 ⁵Department of Psychiatry, New York University at Langone, One, 8, Park Ave, New York, NY 10016 ⁶BioMedical Engineering and Imaging Institute, Icahn School of Medicine at Mount Sinai, One Gustave L. Levy Place, New York, NY 10029

Introduction: Deep brain stimulation targeting subcallosal anterior cingulate cortex and adjacent white matter (SCC-DBS) is a promising therapy for treatment resistant depression. Indeed, SCC-DBS protocols report a 60 to 70% response rate even for the patients who do not respond to electroconvulsive treatment. However, it remains unclear how DBS stimulation of white matter functionally and anatomically alters brain-wide circuits to promote recovery from depression. Lacking this understanding impedes further optimization of this treatment which is essential to improve clinical outcomes. Thus, the aim of this study was to establish how SCC-DBS works in healthy brains, focusing on determining the brain-wide network-level anatomical and functional effects of white matter stimulation.

Methods: Modeling the approach used to successfully treat TRD patients, we implanted SCC-DBS electrodes in two rhesus macaques. Specifically, we identified the confluence of the cingulum bundle, forceps minor, and uncinata fasciculus using diffusion tractography imaging (DTI). We then implanted a DBS lead unilaterally in this location, the other hemisphere serving as a control. One month after electrode implantation, stimulation (5mA, 130Hz, 90 μ sec) began and was maintained for 6 weeks. DTI and whole brain resting-state functional MRIs (rs-fMRIs) were acquired before electrode implantation and following 6 weeks of SCC-DBS stimulation to reveal the anatomical and functional effects of SCC-DBS. Functional data were analyzed using a seed-based comparative-connectome approach where SCC-DBS stimulation induced changes in functional connectivity (FC) were determined. Fractional anisotropy (FA) was calculated from DTI data to investigate the anatomical white matter changes. Additionally, we investigated the histological changes using immunofluorescence staining of oligodendrocytes using the CC-1 antibody.

Results: Compared to before stimulation, we found that six weeks of chronic SCC-DBS enhanced white matter integrity in midcingulate portion of cingulum bundle (Figure 1). This white matter tract connects the stimulated SCC and posterior cingulate cortex, and we found a significant increases in FA and corroborated this effect by finding a significant increase in the numbers of oligodendrocytes in the mid-cingulum bundle. Additionally, we also demonstrated that SCC-DBS significantly changed the FC between stimulated SCC and multiple brain networks' hubs, mainly in the default mode network and the limbic network hubs which are connected by cingulum bundle projections.

Conclusion: Our data unveiled the specific effects of SCC-DBS on myelin remodeling and brain network level functional changes providing insight into the neural mechanisms of DBS targeted to white matter, as well as the biological bases of depression pathology.



Structural and functional changes induced by SCC-DBS in non-human primates.

White Matter and Differential Treatment Outcomes to Cognitive-Behavioral Therapy or Antidepressant Medication in MDD

Jack Gomberg¹, Jungho Cha¹, Juna Khang¹, Boadie Dunlop¹, Edward Craighead^{2,3}, Helen Mayberg¹, Ki Sueng Choi¹

¹. Department of Neurology and Neurosurgery, Icahn School of Medicine at Mount Sinai, New York

². Department of Psychiatry and Behavioral Sciences, Emory University School of Medicine, Atlanta

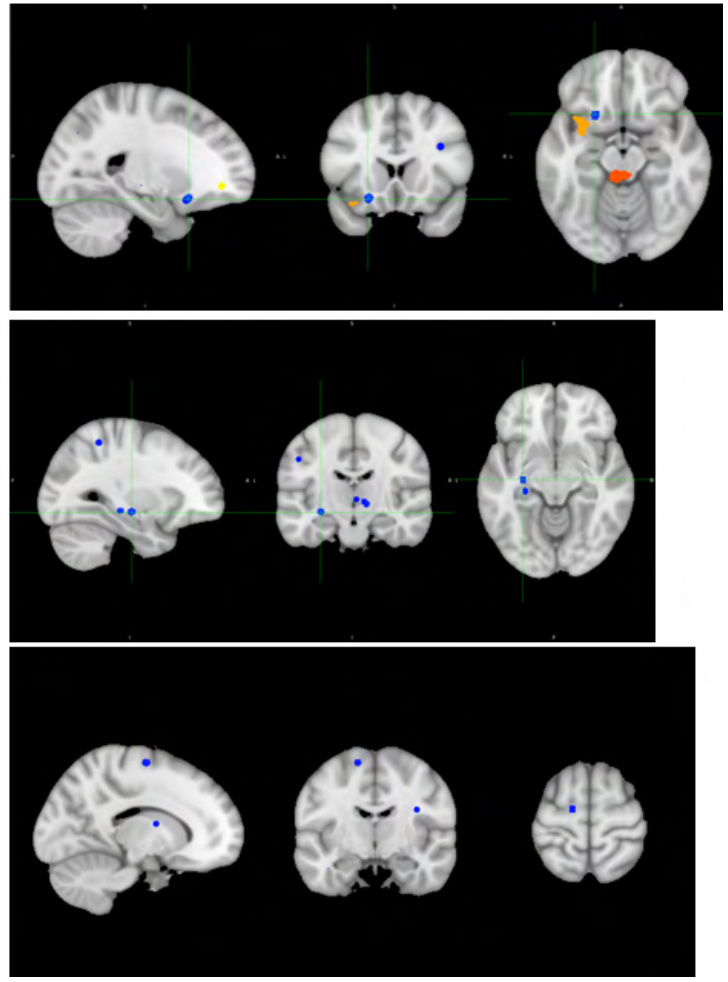
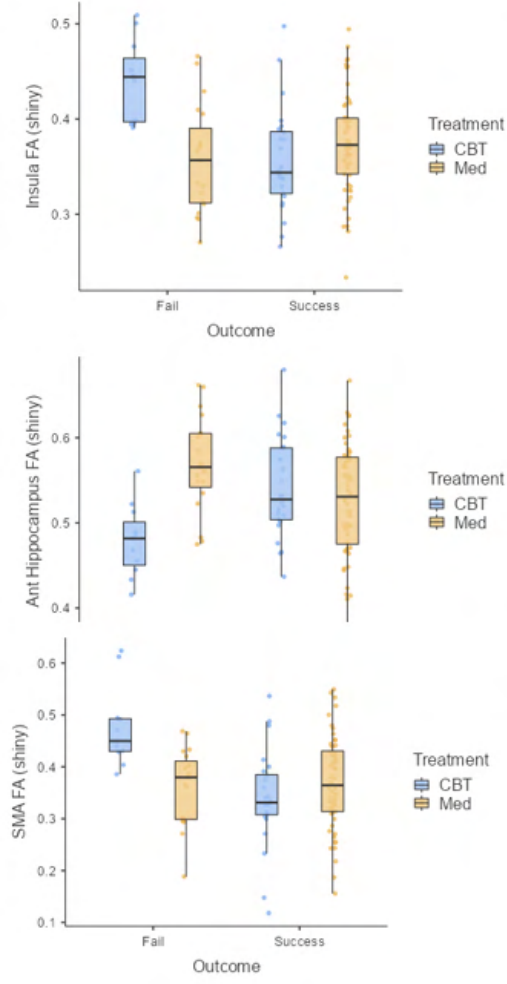
³. Department of Psychology, Emory University, Atlanta

Background: First-line treatment for major depressive disorder (MDD) includes cognitive behavioral therapy (CBT) and/or antidepressant medications (ADM). However, treatment effectiveness varies among patients with similar presentations. Previous studies using rsfMRI suggest distinct functional connectivity (FC) patterns from the subcallosal cingulate to the left anterior insula, ventromedial prefrontal, and periaqueductal gray in CBT and ADM remitters. Structural connectivity changes might mediate these functional connectivity patterns. Therefore, we assessed pretreatment WM integrity preceding 3-months of CBT or ADM monotherapy.

Materials and Methods: 167 treatment-naive MDD patients randomized to 12 weeks of CBT or ADM. Subjects were categorized into remitters (HDRS17 score <7 at 10 and 12 weeks) and treatment failures (HDRS17 score change <30%). Whole-brain fractional anisotropy (FA) maps were generated from diffusion weighted imaging (DWI) via Fdt toolbox in FMRIB and statistically compared using Tract-Based Spatial Statistics. Voxel-wise 2x2 ANOVA (CBT/ADM by remitter/failure) was performed using AFNI 3dMVM, and FA values from significant regions were analyzed post hoc for correlations with HDRS17 scores and previously reported FC biomarkers.

Results: Significant treatment by outcome interactions were identified affecting WM tracts in the left anterior insula, supplementary motor area, and anterior/posterior hippocampus ($p < 0.001$). ADM remitters and CBT failures show higher FA values in the left insula and SMA. In contrast, ADM remitters and CBT failures show lower FA in the left anterior and posterior hippocampus compared to ADM nonresponders and CBT remitters. Post hoc analysis showed the left anterior insula FA anticorrelates with HDRS17 score improvement ($r = -0.364$, $p = 0.008$) in the CBT treatment group only. Hippocampal FA showed significant anticorrelation for HDRS17 score improvement in the ADM group both anteriorly ($r = -0.244$, $p = 0.009$) and posteriorly ($r = -0.202$, $p = 0.031$). The SMA revealed no group correlations. Finally, the insula and anterior hippocampus showed no significant correlation with FC biomarkers. The posterior hippocampus FA significantly correlated with SCC FC to the PAG ($r = 0.311$, $p = 0.002$), insula ($r = 0.294$, $p = 0.003$), and ventromedial prefrontal cortex ($r = 0.241$, $p = 0.016$). The SMA significantly anticorrelated with the insula FC finding ($r = -0.253$, $p = 0.011$).

Conclusion: These findings highlight distinct WM integrity in the insula, SMA, and hippocampus in CBT and ADM remitters and failures. They suggest that structural connectivity patterns may delineate imaging biotypes influencing response to MDD treatment. Differences in white matter HDRS17 correlation between treatment groups suggest varied mechanisms within MDD circuit pathophysiology. Notably, the correlation of posterior hippocampal and SMA FA findings with past functional connectivity biomarkers suggests an intriguing interplay between structural and functional findings in MDD.



ANOVA 2x2 Analysis Treatment Selection White Matter Biomarker

Differences in White Matter Associated with Relapse in Patients with Major Depressive Disorder

Jack Gomberg¹, Jungho Cha¹, Boadie Dunlop², Edward Craighead^{2,3}, Helen Mayberg¹, Ki Sueng Choi¹

¹. Department of Neurology and Neurosurgery, Icahn School of Medicine at Mount Sinai, New York

². Department of Psychiatry and Behavioral Sciences, Emory University School of Medicine, Atlanta

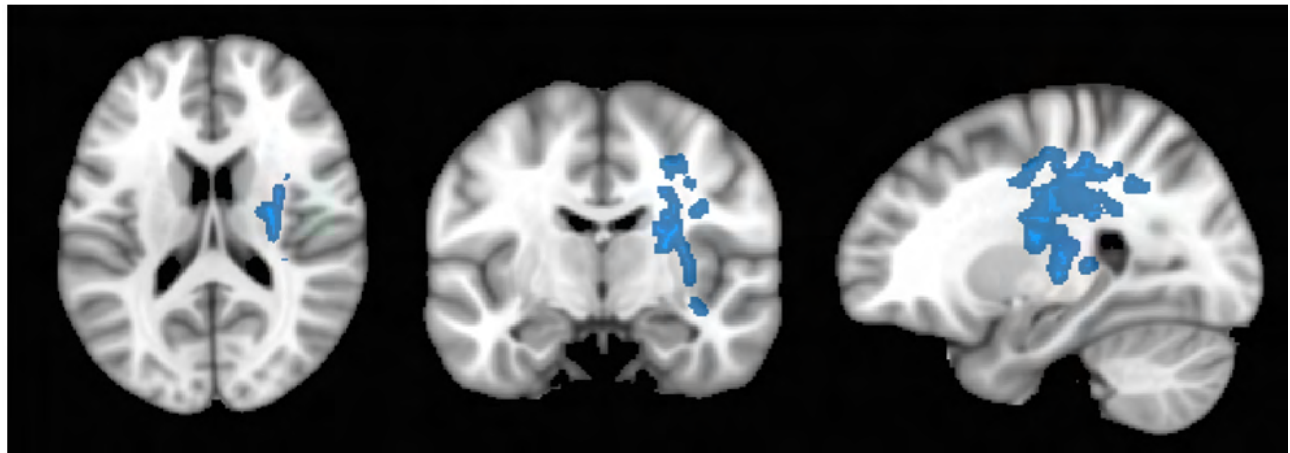
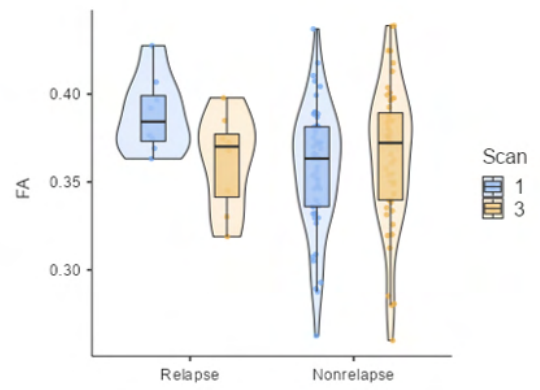
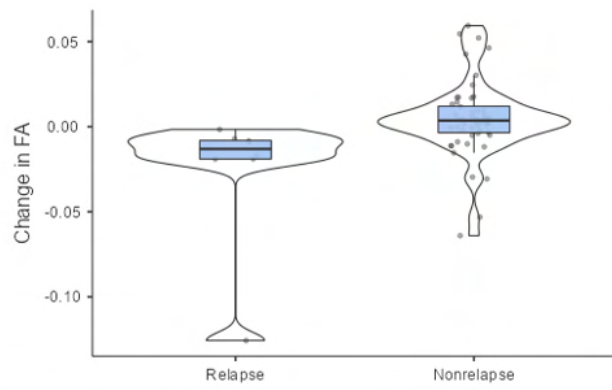
³. Department of Psychology, Emory University, Atlanta

Background: Episodes of recurrence in major depressive disorder (MDD) are common, however predictors of recurrence are not well established. Previous studies have found that differential functional connectivity (FC) in the salience and affective networks show promise for predicting symptom recurrence in previously remitted MDD patients. Structural changes underlying these functional differences are unknown and may offer further biomarkers. Using diffusion weighted imaging (DWI) and clinical data from the 21-month follow-up phase for remitters in the Predictors of Remission in Depression to Individual and Combined Treatments (PReDICT) trial, we evaluated if differences in white matter could predict patient recurrence. We hypothesized potential differences in white matter tracts between the right SCC and insula.

Methods: Of the 344 patients randomized to 12 weeks of CBT, SSRI, or SNRI in PReDICT, 60 patients had usable DWI imaging and achieved remission. Of these 60 patients, 8 experienced recurrence during the follow up phase 24 months from study baseline. MRI scans were obtained the week prior to treatment and 1-5 days prior to the week 12 visit. A whole brain fractional anisotropy (FA) map was calculated for each subject using Fdt toolbox in FMRIB and Tract-Based Spatial Statistics (TBSS) generated for statistical comparison across outcome groups. A two-sample t-test with 5000 permutations was performed using the FA map at the end of treatment as well as the difference between the FA map at the beginning and end of 12 weeks of treatment. We used a significance threshold of family wise error (FWE) corrected $\alpha < 0.05$.

Results: In the FWE corrected t-test, there was a significant difference in the change in FA in regions along the right corticospinal tract, superior longitudinal fasciculus, and fronto-occipital fasciculus. The region of interest showed limited FA change from week 0 to 12 in remitters who stayed well (mean=0.00454, SE 0.00310), whereas in remitters who relapsed this region showed negative changes in FA (mean=-0.0259, SE 0.0144). There was no significant difference in the t-tests of FA at week 12 alone.

Conclusions: These findings show that differences in white matter could serve as a prospective risk factor associated with MDD recurrence. Furthermore, these findings suggest that changes in the white matter during treatment are important in predicting whether remission will last, rather than just endpoint white matter integrity. Finally, the similarities between FA and FC findings in location hint at a relationship between the two in MDD treatment and recurrence.



FA Change Lower in MDD Relapse vs Nonrelapse Remitters

Characterizing the Constructs of Motivation

Natalie Hackman¹, Mu Li, Phillip Neukam¹, James Murrough¹, and Laurel S. Morris¹

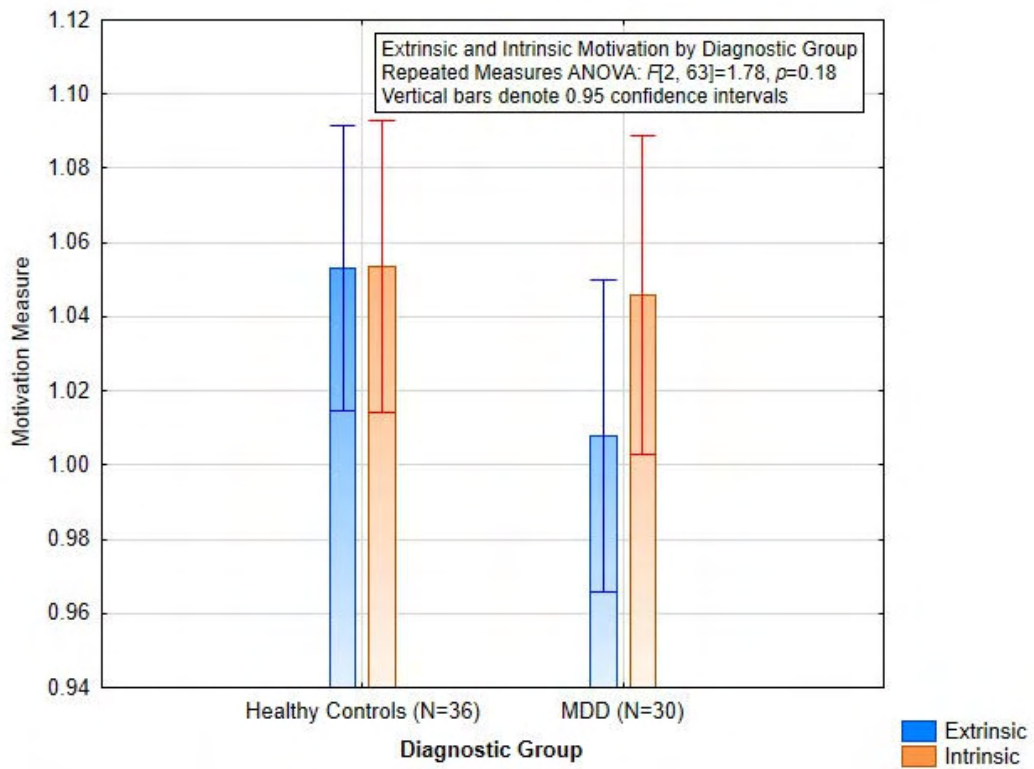
¹Icahn School of Medicine at Mount Sinai

Background: Motivated behavior is commonly differentiated into extrinsic and intrinsic motivation. Extrinsic motivation describes behavior prompted in response to external reinforcers while intrinsic motivation is the manifestation of internally generated incentive. Although there is computational similarity between extrinsic and intrinsic motivation, delineation of internal value functions has proven more difficult. Motivational deficits are a signature attribute of major depressive disorder (MDD). The manifestation of motivational deficit is classified in the DSM-5 as anhedonia. However, established measures of motivation do not address internally generated motivation. Hence, the understanding of the neurocognitive mechanisms which underlie intrinsically motivated behavior, and its deficits are restricted.

Methods: We have developed a multi-modal ultra-high field 7T MRI protocol which provides a significant improvement in the signal to noise ratio. We have also created the Internal Motivation Task (IMT) which serves as a novel measure of internally generated motivation. The IMT involves a choice cue followed by a decision in which participants utilize either extrinsic or intrinsic motivation to attain a reward.

Results: MDD individuals exhibit a statistically significant reduction in extrinsic motivation, but do not exhibit a statistically significant reduction in internally generated motivation compared to healthy individuals. In N=15 healthy controls who completed the task so far, we found differential activation in the occipital cortex ($Z=4.9$) and bilateral anterior insula ($Z=4.3$) during extrinsic control relative to intrinsic control (voxelwise $p<0.005$, $K>350$, $\alpha<0.05$). All updated neuroimaging results in both groups will be presented.

Conclusions: There does not appear to be a dimensional association between lower intrinsic motivation and anhedonia. Perhaps there is a higher sense of agency with intrinsic motivation than extrinsic motivation which accounts for there being less of a difference between healthy and MDD individuals.



Extrinsic and Intrinsic Motivation by Diagnostic Group

Long-term reorganization of structural and functional connectivity among World Trade Center responders with post-traumatic stress disorder: a data-driven multimodal approach

Azzurra Invernizzi¹, Davide Folloni^{2,3}, Elza Rechtman¹, Paul Curtin⁴, Maryam Jalees¹, Stephanie Santiago-Michels⁵, Evelyn J. Bromet⁶, Roberto G. Lucchini^{7,8}, Benjamin J. Luft⁹, Sean A. P. Clouston¹⁰, Cheuk Y. Tang¹¹, Megan K. Horton¹

¹Department of Environmental Medicine and Public Health, Icahn School of Medicine at Mount Sinai, New York, NY, USA ²Nash Family Department of Neuroscience and Friedman Brain Institute, Icahn School of Medicine at Mount Sinai, New York, NY, USA ³Lipschultz Center for Cognitive Neuroscience, Icahn School of Medicine at Mount Sinai, New York, NY, USA ⁴Linus Biotechnology Inc., New York, NY, USA ⁵The Graduate Center and Queens College, City University of New York, New York, NY, USA ⁶Department of Psychiatry, Renaissance School of Medicine at Stony Brook University, Stony Brook, NY, USA ⁷Department of Environmental Health Sciences, Robert Stempel School of Public Health, Florida International University, Miami, Florida, USA ⁸University of Modena and Reggio Emilia, Italy ⁹World Trade Center Health and Wellness Program, Renaissance School of Medicine at Stony Brook University, Stony Brook, NY, USA ¹⁰Program in Public Health and Department of Family, Population, and Preventive Medicine, Renaissance School of Medicine at Stony Brook University, Stony Brook, NY, USA ¹¹Department of Radiology and Psychiatry, Icahn School of Medicine at Mount Sinai, New York, NY, USA

Background: World Trade Center (WTC) responders have a high prevalence (23%) of persistent, clinically significant WTC-related post-traumatic stress disorder (PTSD). Recent structural and functional magnetic resonance imaging (MRI) studies demonstrate neural differences between WTC responders with and without PTSD. Here, we propose a novel multi-modal approach (i.e., Anatomical Connectivity Fingerprint (ACF)) combining functional and structural imaging to better describe the neurobiological underpinnings of PTSD, a crucial step for the progression of treatments and interventions still lacking for this disorder.

Methods: Using graph theory analysis of resting-state (rs-fMRI) data, we calculated eigenvector centrality (EC) in 111 brain areas in WTC responders with PTSD (WTC-PTSD, $n = 45$) and age/sex matched responders without PTSD (non-PTSD, $n = 51$). Partial least squares discriminant analysis (PLS-DA) modeled divergence in EC values between functional hubs. Using diffusion tensor imaging (DTI), we reconstructed five anatomical tracts in the temporal lobes. ACF quantifies the anatomical connectivity features in each functional hub to estimate tract-specific anatomical changes. To account for potential confounding from exposure, we examined associations between WTC-exposure duration (months on site) and ACF after adjusting for PTSD using general linear model (GLM) regression, while also adjusting for medication usage and comorbid depression.

Results: PLS-DA discriminated EC values between WTC-PTSD and non-PTSD (AUC: 0.749 (0.651-0.847)) in nine regions (right/left anterior inferior temporal gyrus, right superior parietal lobule, right anterior parahippocampal gyrus, right anterior/posterior superior temporal gyrus (STG), right caudate nucleus, left amygdala and brainstem) were significantly different and contributed the most to differentiate functional neuro-profiles between groups. Connectivity patterns in four white matter tracts (hippocampus, parahippocampus, inferior and superior temporal gyri (STG)) differed significantly between groups. ACF differences were identified in the inferior fronto-occipital fasciculus (IFOF), medial (ILFmed) and lateral (ILFlat) components of the inferior longitudinal fascicle and in the middle longitudinal fascicle (MdLF). Interestingly, the association between WTC exposure duration and ACF differed significantly between WTC-PTSD and non-PTSD in the IFLmed, right posterior STG ($p = 0.035$).

Conclusions: Using our novel ACF, we found congruent alterations in functional and anatomical connectivity of responders with PTSD versus without PTSD. This study expands our understanding of the neural and neurobiological mechanisms underpinning PTSD in WTC responders.

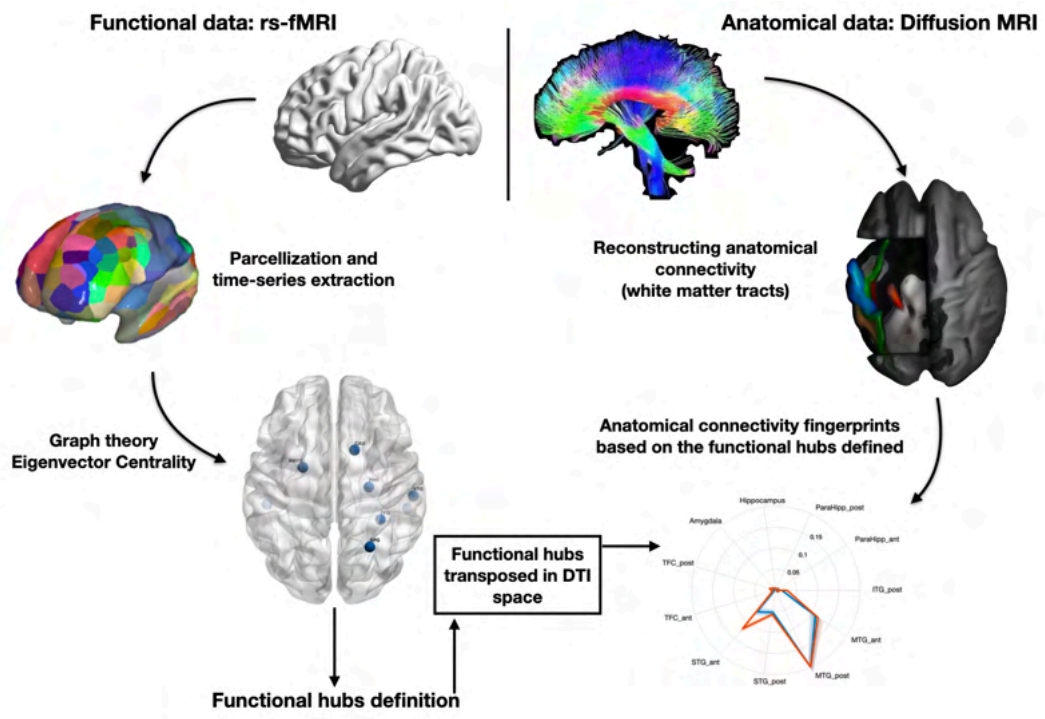


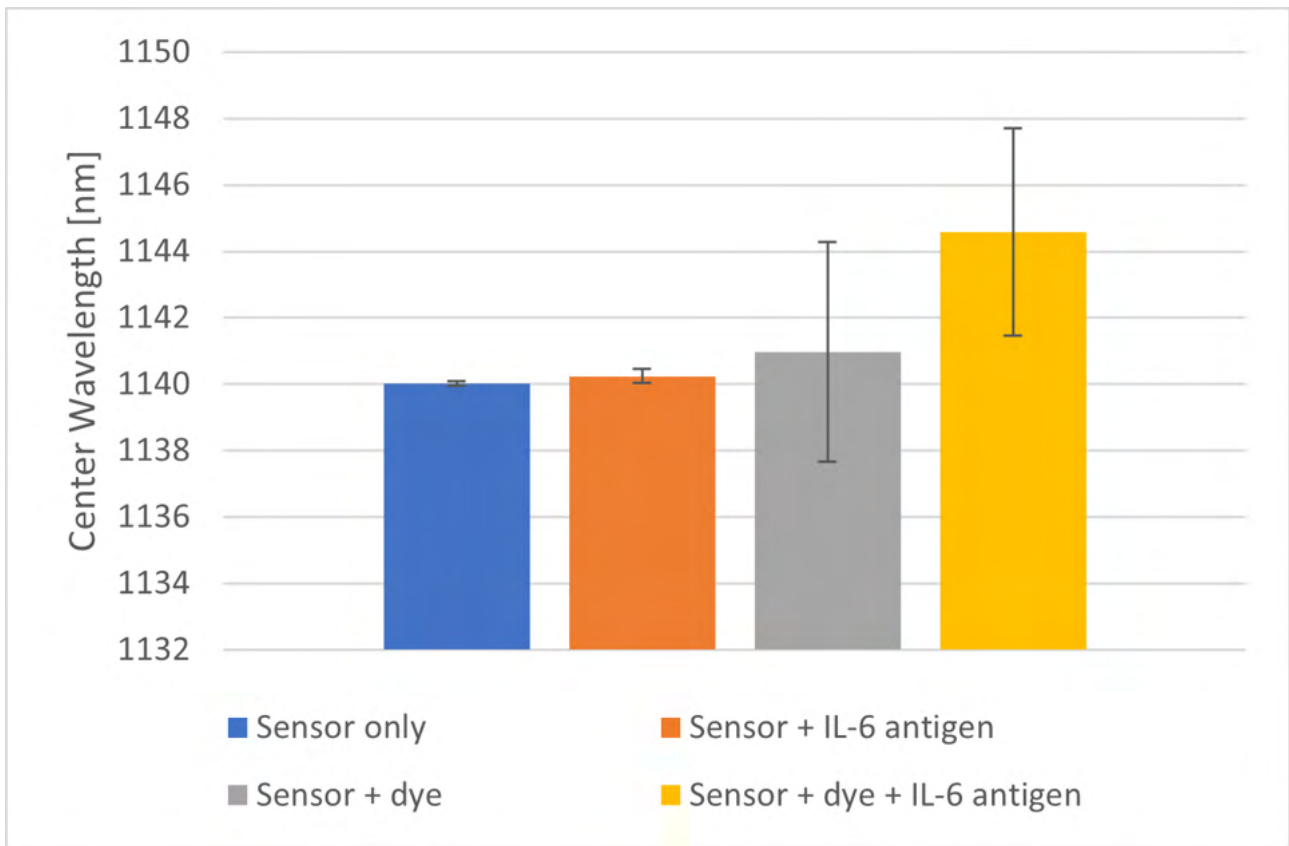
Figure 1

Dye Enhancement of an Antibody-Conjugated Nanosensor Platform

Atara R. Israel¹, Ryan M. Williams, PhD¹

¹ The City College of New York, CUNY

Single-walled carbon nanotubes (SWCNTs) have the unique ability to fluoresce in the near-infrared region (known as the "biological tissue transparency window"), making them useful for applications in imaging and as an in vivo diagnostic tool for early disease detection. Interleukin 6 (IL-6) is a pro-inflammatory cytokine that is found at elevated levels in diseased states, cancers, cardiovascular diseases, and COVID-19. We are working to create a nanosensor platform specific for the detection of IL-6 by analyzing changes in optical band gap fluorescence in response to the nanosensor encountering its complimentary antigen. We implemented organic aromatic dyes to enhance the fluorescence signal, as they are known to interact with the valence electrons on the SWCNT's surface, resulting in center wavelength shifting and/or intensity changes. To accomplish this, combinations of 8 different dyes and 12 ssDNA sequences were initially tested to determine a pairing that would elicit a large change in fluorescence modulation. SsDNA-functionalized SWCNTs at a concentration of 1mg/L were mixed with 1uM of dye in triplicate. Fluorescence was measured using a high-throughput NIR plate reader spectrophotometer over long- and short-time intervals. Once compatible combinations were determined, aminated versions of the selected ssDNA sequence were used to create the nanosensor platform by covalently conjugating an IL-6 antibody to the ssDNA-wrapped SWCNT by activating the carboxylic ends of the antibody. The nanosensor was then left to dialyze for 48 hours, followed by dye and IL-6 antigen addition. Fluorescence measurements were taken with evaluation of their intensity changes and wavelength shifting. A paired t-test was used to analyze the data. Results of the initial dye-ssDNA screening showed some combinations exhibiting wavelength shifts up to 12 nm and intensity either greatly increasing or completely quenched. Using a spectral probe, this interaction was found to happen instantaneously and remains stable. Using the selected ssDNA combinations we saw promising results with, we noted unsuccessful conjugation of the antibody to the functionalized SWCNT. Revision with a ssDNA sequence known to conjugate well to the IL-6 antibody of choice, center wavelength changes were noted upon addition of IL-6 antigen as seen in the figure below, but was not statistically significant. Dyes prove to be a beneficial tool in enhancing SWCNT fluorescence modulation and could assist in protein detection in biological environments, where other metabolites could compete for surface interaction with SWCNTs. Future directions include in vivo implementation and investigation of optimal ssDNA-antibody pairings to result in successful conjugation.



Center wavelength 5 minutes after addition of IL-6 antigen to nanosensor

Idiopathic Intracranial Hypertension assessment of Whole Brain, White Matter and Gray Matter Volumes in IIH patients and on 7T MRI

Authors: Claudia Kirsch MD^{1,2,4}, Gaurav Verma PhD⁴, Laura Couvreur³, Shams Rashid PhD⁴, Mackenzie Langan MS⁴, Akbar Alipour PhD⁴, Daniel Lambert PhD², Syed Ali Khurram PhD², Priti Balchandani PhD²

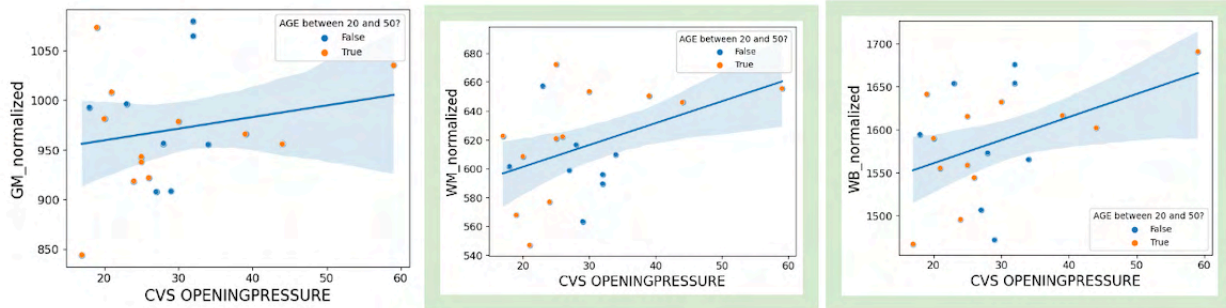
¹Yale Department of Radiology and Biomedical Imaging, Yale School of Medicine, New Haven, CT, 06520, USA

²The School of Clinical Dentistry, University of Sheffield, Sheffield, S10 2TA, United Kingdom

³Spaarne Gasthuis, University of Antwerp

⁴Biomedical Engineering and Imaging Institute, Icahn School of Medicine at Mount Sinai, New York, NY, 10029, USA

Idiopathic intracranial hypertension (IIH) predominately affects obese woman of childbearing age, suffering from increased intracranial pressure (ICP) >250 mm cerebrospinal fluid (CSF) on lumbar puncture LP. IIH patients experience headaches, papilledema, vision loss, double vision from cranial VI palsy, pulsatile tinnitus, and aberrant arachnoid granulation formation with potential for CSF leaks or brain herniation with resultant morbidity and mortality. In the past decades, IIH's incidence has more than doubled and appears to correspond with increasing rates of obesity worldwide. Imaging excludes structural etiologies such as venous sinus thrombosis and assists in diagnosis, with findings, such as a partially empty sella, optic nerve sheath tortuosity and enlargement >6 mm, papilledema, flattening of lateral transverse sinuses, aberrant arachnoid granulations, and skull base erosions. The pathophysiology of IIH is unknown, this research studies assessing whether brain volumes correlate to body mass index (BMI). First, a retrospective analysis of 55 IIH MRIs utilizing artificial intelligence (Icobrain AI), whole brain (WB), gray matter (GM), and white matter (WM) volumes, correlated with BMI and opening LP. In the second, 44 brains scanned on 7T MRI with T1-weighted images were retrospectively segmented using FreeSurfer 6.0 algorithm, parcellating the cortex into regions of interest. Three whole-brain ratios were obtained consisting of total gray matter / white matter ratio (G/W), white matter / supratentorial volume (W/ST) and gray matter / brain segmentation volume (G/BS). Pearson partial correlation was performed between BMI and each 68 cortical ROIs and three whole-brain metrics. Both complete correlations and partial correlations adjusting for age as a covariate were performed. In the first study, AI analysis demonstrated a significant correlation between increased white matter volumes, elevated BMI and opening pressures, between all patients age 20-50. Fig 1. In the second study, BMI was significantly negatively correlated with G/W and G/BS ratios, and significantly positively correlated with W/ST ratio. Table 1 shows rho and p-values for the three whole-brain comparisons. All three whole-brain metrics tested showed significant correlation with age with and without covariation for age. Correlation between age and BMI showed a $r = 0.17$ with $p = 0.11$. CORR Gray/White White/ST Gray/BS Rho -0.28 0.30 -0.26 P-Value 0.0065 0.0042 0.014 PCORR (Age) Gray/White White/ST Gray/BS Rho -0.24 0.25 -0.21 P-Value 0.024 0.017 0.049 IIH pathophysiology was reviewed utilizing a PubMed-MEDLINE, EMBASE, SCOPUS two concept search literature review. These results are presented with a discussion of potential pathophysiologic mechanisms between obesity and IIH.



AI analysis demonstrated a significant correlation between increased white matter volumes, elevated BMI and opening pressures, between all patients age 20-50

Point of Entry? Is the Olfactory Nervus Terminalis the Route for SARS-CoV-2 Anosmia and Intracranial Infections

Claudia Kirsch MD^{1,2,4}, Puneet Belani MD⁴, Shams Rashid PhD⁴, Mackenzie Langan MS⁴, Akbar Alipour PhD⁴, Gaurav Verma PhD⁴, Daniel Lambert PhD⁵, Syed Ali Khurram PhD⁶, Harpreet Hyare MD, PhD³, Priti Balchandani PhD⁴

¹Yale Department of Radiology and Biomedical Imaging, Yale School of Medicine, New Haven, CT, 06520, USA

²The School of Clinical Dentistry, University of Sheffield, Sheffield, S10 2TA, United Kingdom

³University of College London, London, UK

⁴Biomedical Engineering and Imaging Institute, Icahn School of Medicine at Mount Sinai, New York, NY, 10029, USA

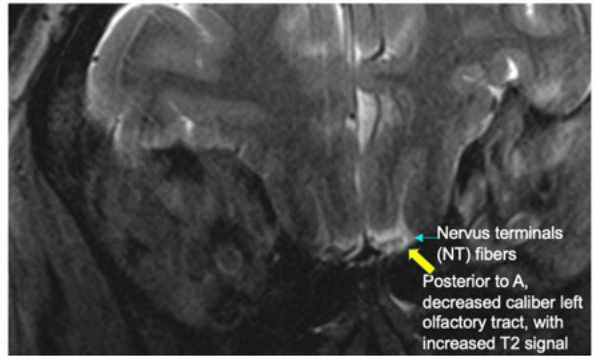
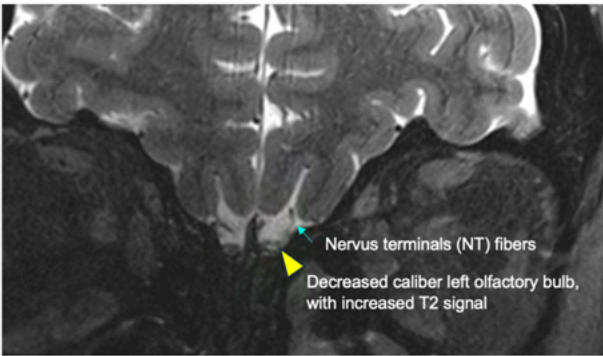
Introduction: The nasal cavity is an important entryway for SARS-CoV-2, with potential for anosmia. SARS-CoV-2 however requires angiotensin-converting enzyme 2 (ACE2) receptors for entry. How SARS-CoV-2 affects olfactory tracts is poorly elucidated because olfactory tracts do not express ACE2. The nervus terminalis (NT), adjacent to olfactory tracts, has extensive ACE2 expression in rat models and may be a SARS-CoV-2 entry site in humans.¹ The NT are often overlooked due to lack of awareness. Objectives: This 7T MRI study in COVID patients with anosmia and controls, sought to determine if NTs are visible on MRI, and if affected and a potential site for SARS-CoV-2 viral invasion.

Materials and Methods: After IRB approval, prospective and retrospective review, was performed on MRIs of controls, and COVID anosmia patients at Icahn School of Medicine Biomedical Engineering and Imaging Institute with Siemens 7T Magnetom system scanner with SC72CD gradient coil, 32-channel head coil, images were evaluated for presence of the NT, olfactory tracts, bulbs, T2 signal change and volume loss.

Results: On 7T MRI, NT were identified as linear neural bundles in subarachnoid spaces adjacent to olfactory tracts, in controls and COVID anosmia. In COVID anosmia, olfactory tracts had volume loss, both tracts and NT demonstrated increase T2 signal, mean = 171, controls, mean =153.

Conclusions: NT ACE-2 receptors are a SARS-CoV-2 entry site in rat models¹. On 7T, NT are identifiable in humans and may be an entry site for SARS-CoV-2. In this study, NT were identifiable on 7T, in controls and in COVID anosmia. Further research may determine if NT are point of entry and potentially quantitative biomarker.

1. Bilinska K, et al. Expression of the ACE2 Virus Entry Protein in the Nervus Terminalis Reveals the Potential for an Alternative Route to Brain Infection in COVID-19. *Front Cell Neurosci.* 2021 Jul 5;15:674123.



Yellow arrowhead in COVID patient with decreased volume left olfactory bulb, light blue arrow pointing to adjacent linear fibers presumed to be the Nervus Terminalis

A Structured-Textual Machine Learning Model to Classify Penumbra-Core Mismatch Among Patients Presenting with Acute Ischemic Stroke due to Large-Vessel Occlusion

Shaun Kohli ¹, Benjamin R. Kummer ^{2,3,4}

¹Icahn School of Medicine at Mount Sinai, New York, NY,

²Department of Neurology, Icahn School of Medicine at Mount Sinai, New York, NY,

³Clinical Neuro-informatics Program, Department of Neurology, Icahn School of Medicine at Mount Sinai, New York, NY,

⁴⁴Windreich Department of Artificial Intelligence and Human Health, Icahn School of Medicine at Mount Sinai, New York, NY

Background: Endovascular thrombectomy is the standard of care for treating acute ischemic stroke (AIS) from large-vessel occlusion (LVO). Patient selection for thrombectomy in extended (6-24h after last known well) time window often relies on the ratio of penumbra-to-core (P:C) volumes determined by perfusion (CTP) imaging. However, CTP remains inaccessible to many hospital centers worldwide and often results in uninterpretable imaging findings, both of which may delay treatment decisions and result in patient harm. To circumvent these shortcomings, we sought to develop a machine learning (ML) algorithm to predict the P:C ratio in AIS using non-imaging data, including both structured and free-text elements, available at the time of hospital presentation.

Methods: We conducted a retrospective analysis on AIS patients from the Mount Sinai Health System, who underwent acute CTP imaging within 30 minutes of hyperacute CTH or CTA imaging for suspected acute stroke between May 14th, 2019, and June 15th, 2021. After excluding cases with uninterpretable CTP images and other specified criteria, we collected P:C ratios, demographic details, medical comorbidities, and all clinical notes prior to CTP. Notes were processed to create "minicorpora" based on three character thresholds (500, 1,000, and 5,000 characters) to reduce noise and emphasize clinically relevant data. We vectorized the clinical notes using BioWordVec word embeddings and TF-IDF weightings, combined with structured data encoded via one-hot vectors and Elixhauser scores. The dataset was divided into a 70%-30% training-testing split. We employed an XGBoost model to predict P:C ratios as a binary outcome (≥ 1.8 or < 1.8), evaluating performance with AUROC and additional metrics such as sensitivity, specificity, precision, and F1 score over multiple decision thresholds. We also conducted ablative analyses to assess the impact of different data features on model performance.

Results: We identified 129 patients meeting our inclusion criteria, with a median age of 69.3 years and a gender distribution of 45.7% female; among them, 115 (89.1%) exhibited a P:C ratio above 1.8. The optimal machine learning model, informed by free-text data with a 500-character minimum threshold, demonstrated a predictive AUROC of 0.79 (95% CI: 0.59-0.92), positive predictive value 0.96 (95% CI:0.92-1.00), and F1 score 0.86 (95% CI:0.64-0.96).

Conclusions: We developed an ML model from non-imaging EHR data to classify key CTP findings with good discriminatory performance. However, further studies in larger patient cohorts are needed to validate our findings.

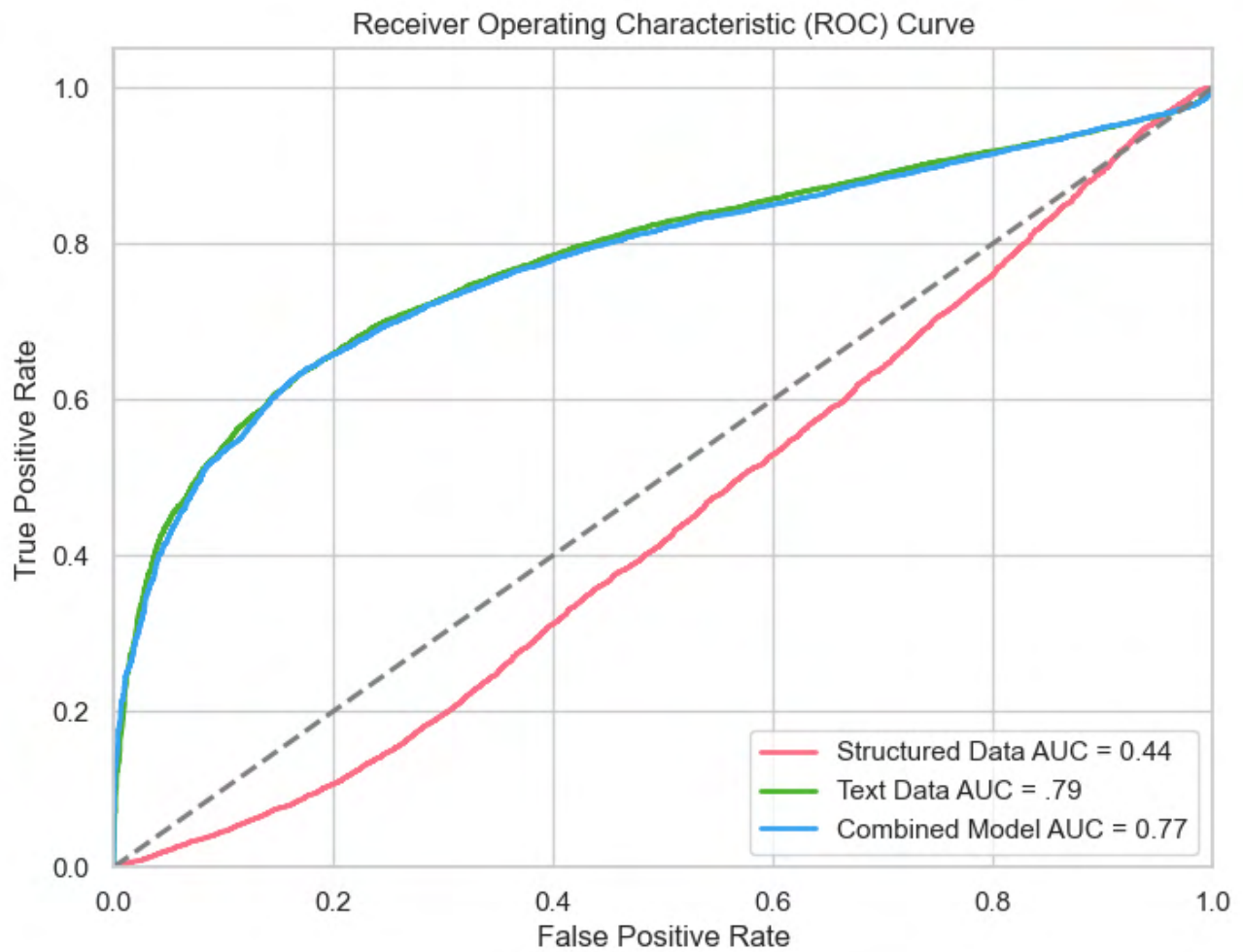


Figure 1. ROC curve and resulting AUC for a model trained with structured features only (red), document embeddings only (green), and one with both structured features and document embeddings (blue). Dashed line represents ROC curve of a model performing at chance.

7T MRI-derived Brain Age Exceeds Chronological Age in Both Early and Longstanding Multiple Sclerosis

Francesco La Rosa¹, Jonadab Dos Santos Silva¹, Gaurav Verma², Julia Galasso¹, Priti Balchandan², Daniel S. Reich³, Hayit Greenspan², Erin S. Beck^{1,3}

¹Department of Neurology, Icahn School of Medicine at Mount Sinai, New York, NY, 10029, USA.

²BioMedical Engineering and Imaging Institute, Icahn School of Medicine at Mount Sinai, New York, NY, USA.

³Translational Neuroradiology Section, National Institute of Neurological Disorders and Stroke, National Institutes of Health, Bethesda, MD, USA.

Introduction: Brain age (BA) is estimated with machine learning methods from brain magnetic resonance imaging (MRI). The gap between chronological age (CA) and estimated BA, known as BA difference (BAD), is a marker of disability in neurological diseases, including multiple sclerosis (MS). Traditional BA models have relied on 1.5/3T MRI, but high-resolution 7T MRI may be more sensitive to accelerated aging. We have developed a BA model utilizing 7T T1-weighted (T1w) Magnetization-Prepared 2 Rapid Acquisition Gradient Echo (MP2RAGE) images and evaluate BAD in subjects with both early and longstanding MS.

Material and Methods: A convolutional neural network (DenseNet) was trained on ~5500 publicly available T1-w MRI scans of HV acquired at 1.5 or 3T at 72 sites to predict BA. We fine-tuned the model on 351 HV 7T T1w MP2RAGE images (median age 32 years, range 19- 75 years; 52% female participants). Pre-processing included skull-stripping, registration to MNI space, and resampling to 0.7mm³ resolution. DenseNet was evaluated on 7T MP2RAGE images from 28 previously unseen HV imaged at Mount Sinai. DenseNet was then applied to 7T MP2RAGE images from 50 people with longstanding MS scanned at the NIH and 26 subjects diagnosed with MS within the previous year scanned at Mount Sinai. All subjects underwent physical and cognitive assessments, including expanded disability status scale (EDSS), symbol digit modalities test (SDMT), and nine-hole peg test (9HPT).

Results: The median BAD in the HV testing set (median age 31 years, range 26 - 53 years; 16 [57%] female participants) was 2.6 years (range -6 - 7; not different from 0, $P = 0.4$). In the early MS cohort (median age 36 years, range 24 - 55 years; 14 [54%] female participants, years since diagnosis 14 ± 7), the median BAD was 9.9 years (range -9 - 32, interquartile range [IQR] 17), greater than 0 ($P = 0.008$), and correlated with 9HPT ($r=0.44$, $P=0.02$) but not EDSS or SDMT. In the longstanding MS cohort (median age 47, range 30 - 77 years; 32 [64%] females; years since diagnosis 14 ± 9), the median BAD was 10.3 years (range -17 - 28, IQR 13), greater than 0 ($P = 0.002$), and correlated with SDMT ($r=-0.41$, $P=0.02$) but not EDSS or 9HPT.

Conclusions: Our 7T-enhanced ML model accurately predicts BA in HV and reveals increased BA in MS, even at the time of diagnosis. By estimating neurodegeneration by means of accelerated aging, BA holds promises as an MS prognostic marker.

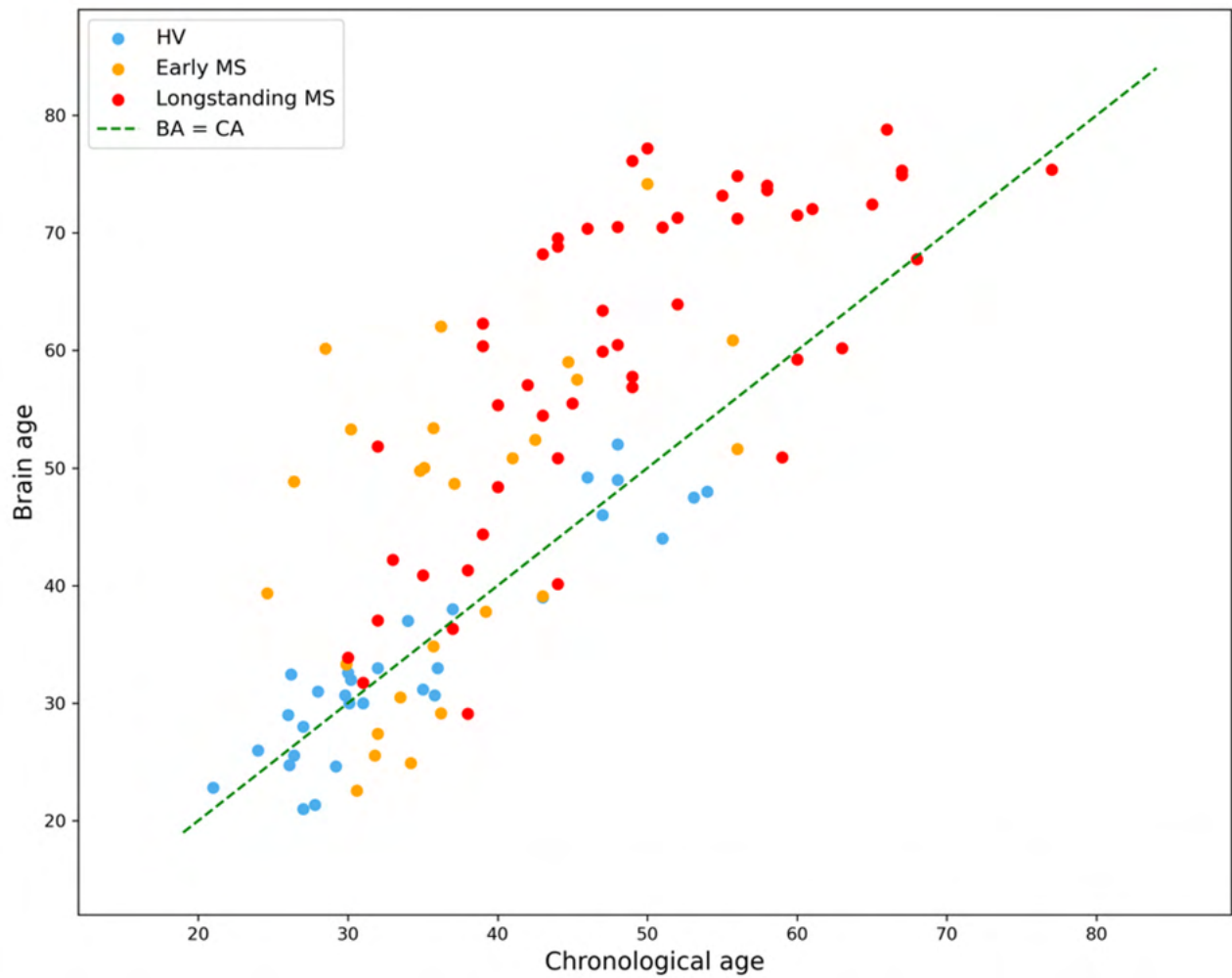


Figure 1: scatter plot showing the predicted brain age for healthy volunteers (blue), participants with early MS (orange), and participants with longstanding MS (red).

Exploring the VTA Circuitry of Anhedonia in Major Depressive Disorder using Ultra-High Field 7T MRI

Mu Li ¹, Laurel S. Morris ¹

¹ Department of Psychiatry, Icahn School of Medicine at Mount Sinai, New York, USA

Introduction: A primary symptom and diagnostic criterion of major depressive disorder (MDD) is a loss of interest and motivation, known as anhedonia. Animal models of depression suggest that ventral tegmental area (VTA) hyperactivity underlies depressive symptoms and anhedonia. However, due to the limited resolution of 3-Tesla (3T) MRI, the VTA circuitry related to motivation in human patients with MDD has not been adequately studied. Fortunately, ultra-high field 7-Tesla (7T) MRI is more sensitive, therefore, we used 7T resting-state MRI to explore the correlation between different levels of anhedonia and VTA with whole-brain functional connectivity across MDD patients and healthy controls, in order to investigate the relevant VTA circuitry.

Materials and Methods: We scanned MDD (n=31) and healthy subjects (n=26) using ultra-high field 7T resting-state MRI and assessed the level of anhedonia using two dimensions of the Temporal Experience of Pleasure Scale (TEPS): TEPS Anticipatory Subscale (TEPSA) and TEPS Consummatory Subscale (TEPSC). We analyzed VTA-whole brain functional connectivity across both groups, with TEPSA and TEPSC scores as covariates. We performed a voxel-wise analysis with a threshold of $p < 0.005$, and cluster-level family-wise error correction was applied.

Results: Across MDD and healthy controls, higher anticipatory anhedonia was associated with higher VTA connectivity with the left thalamus, right inferior frontal gyrus and medial prefrontal cortex. Higher consummatory anhedonia was associated with higher VTA connectivity with the left inferior frontal gyrus, right medial frontal gyrus, and right thalamus.

Conclusions: Higher anhedonia was associated with higher functional connectivity between VTA and various clusters in the brain. This aligns with animal studies showing hyper-connectivity in the VTA circuit in depressive phenotypes. Additionally, the findings suggest that higher levels of anticipatory anhedonia are associated with stronger functional connectivity between VTA and mPFC, replicating our previous findings. Our study is ongoing and will involve more subjects.

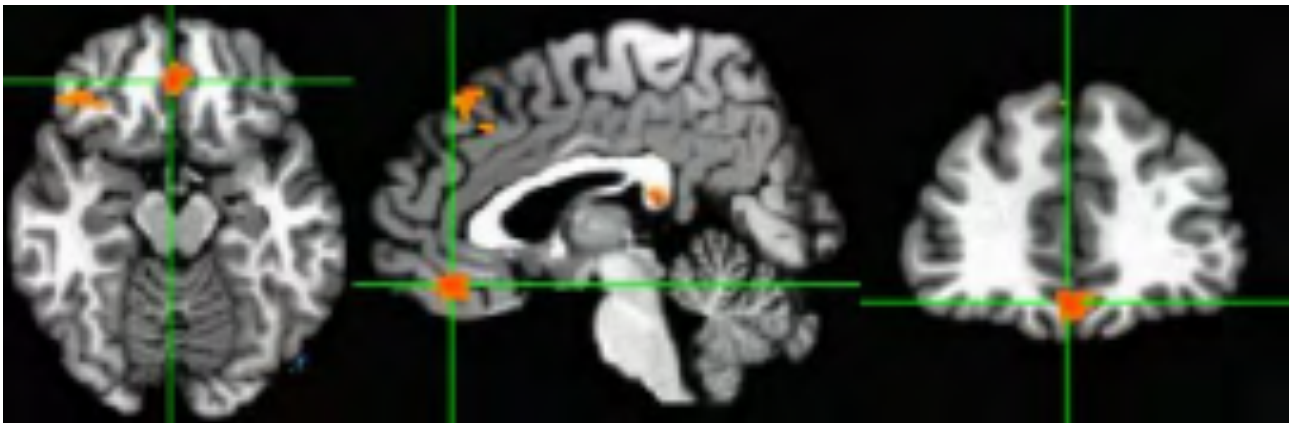


Fig 1. Functional connectivity of the VTA-mPFC with 7T resting-state MRI.

Characterization of solid renal masses with functional non-contrast MRI in patients undergoing surgical management.

Mira Liu PhD¹, Octavia Bane PhD^{1,2}, Haitham Al-Mubarak PhD¹, Arthi Reddy MD², Paul Kennedy, PhD^{1,2}, Philip Robson PhD^{1,2}, Jordan Cuevas BA¹, Kirolos Meilika MD³, Amir Horowitz PhD⁴, Bernd Kuhn PhD⁵, Ketan Badani MD³, Bachir Taouli MD^{1,2}, Sara Lewis MD^{1,2}.

¹BioMedical Engineering and Imaging Institute, Icahn School of Medicine at Mount Sinai, New York, NY, USA.

²Department of Diagnostic, Molecular and Interventional Radiology, Icahn School of Medicine at Mount Sinai, Mount Sinai Hospital, New York, NY, USA.

³Department of Urology, Icahn School of Medicine at Mount Sinai, New York, NY.

⁴Precision Immunology Institute / Tisch Cancer Institute, Icahn School of Medicine at Mount Sinai, New York, NY.

⁵Siemens Healthcare, Erlangen, Germany

Introduction: To compare the diagnostic performance of non-contrast functional MRI sequences - diffusion-weighted imaging (DWI) [apparent diffusion coefficient (ADC), intravoxel incoherent motion (IVIM)], Arterial Spin Labeling renal blood flow (ASL RBF), blood-oxygen level dependent (BOLD)/R2*, and T1 - for solid renal mass (SRM) classification.

Materials and Methods: In a prospective, IRB-approved, single-center study, 41 patients (12F/29M, 60.3±10.8y) with SRMs underwent pre-operative 1.5T MRI (Aera, Siemens Healthcare). MRI protocol included advanced DWI (9 b-values: 10-800 s/mm²), volumetric ASL (pseudo-continuous labeling), R2* (12 TEs: 2-79ms), and T1 (VFAs: 2, 10). Advanced-DWI was post-processed with a mono-exponential (ADC) and a Bayesian bi-exponential (IVIM). R2* and T1 were calculated in-house, and ASL renal blood flow (RBF) maps generated on-scanner. Volumes-of-interest were placed encompassing the entire renal mass by one radiologist; a subset (n=27) was analyzed by a 2nd radiologist. Interobserver reliability was calculated with intraclass correlation (ICC). Voxel-wise MRI-parameter histogram characteristics were compared among SRM subtype and grade with Mann-Whitney U-test. Diagnostic performance of logistic regression models of MRI histogram parameters was evaluated through ROC analysis of significant features.

Results: The 41 SRMs [mean(range)=32(8-68) mm] had the following clinicopathologic diagnoses: 22 clear cell (cc)-RCC, 10 non-ccRCC, 9 benign lesions. Mann-Whitney U test significant features are shown in Table 1 along with the logistic regression AUC for each independent significant feature and multiparametric ROC analysis from logistic regression of all statistically significant features for each classification. ICC was excellent (>0.90) for all IVIM and 3 of 5 R2* parameters. ICC's of ASL and T1 parameters were moderate-to-excellent (0.61-0.96).

Conclusions: IVIM was the only sequence with significant parameters for all subtype classifications, and individual IVIM parameters outperformed ADC and T1. Multiparametric MRI with combination of significant features returned higher AUCs than ROC analysis from independent significant features. ASL RBF and R2* parameters were not significant (p-values>0.05) for classification. The combination of features from a given sequence returned comparable AUCs to previously reported studies and independent features returned statistical significance that supports previous works. Classification of SRM and tumor biology with non-contrast MRI could improve cross-sectional imaging in pre-operative tumor characterization.

Significant sequences	Significant features	Class 1 Mean±std	Class 2 Mean±std	p-val	AUC [95% CI]	SN	SP
Malignant vs Benign		Malignant(27)	Benign(9)				
IVIM	skew D*	2.3±0.9	1.60±0.60	0.043	0.70[0.45,0.94]	0.81	0.57
ADC	std ADC	0.34±0.12	0.25±0.99	0.034	0.71[0.54,0.89]	0.52	1.0
T1	kurtosis T1	345±1157	7.20±7.10	0.027	0.69[0.42,0.96]	0.70	0.71
Multiparametric					0.77[0.60,0.95]	0.59	0.86
ccRCC vs non-ccRCC		CC(19)	Non-CC(8)				
IVIM	mean D	1.88±0.38	1.46±0.43	0.015	0.80[0.58,1.0]	0.79	0.88
	median D	1.89±0.41	1.44±0.40	0.019	0.79[0.59,1.0]	0.79	0.75
	kurtosis D	3.10±0.67	4.06±1.3	0.044	0.75[0.55,0.95]	0.53	0.88
ADC	skew D	0.01±0.37	0.49±0.77	0.049	0.74[0.50,0.99]	0.58	0.88
	mean ADC	1.91±0.34	1.52±0.37	0.022	0.78[0.56,1.0]	0.63	0.88
	median ADC	1.90±0.36	1.53±0.43	0.038	0.76[0.52,1.0]	0.84	0.45
Multiparametric					0.95[0.87,1.0]	0.89	0.88
ccRCC vs other SRM		CC (19)	Other(17)				
IVIM	mean D	1.88±0.38	1.57±0.43	0.044	0.66[0.46,0.87]	0.79	0.67
	median D	1.89±0.41	1.55±0.43	0.044	0.66[0.46,0.86]	0.79	0.60
Multiparametric					0.70[0.50,0.90]	0.84	0.60
Grade > 1 vs Grade 1		Grade > 1 (17)	Grade 1(10)				
IVIM	mean D	1.64±0.49	1.96±0.24	0.031	0.75[0.56,0.95]	0.90	0.71
	median D	1.62±0.49	1.98±0.27	0.027	0.76[0.57,0.94]	0.90	0.59
	skew D	0.3±0.6	-0.12±0.40	0.035	0.75[0.55,0.95]	0.70	0.76
ADC	mean ADC	1.67±0.42	2.02±0.17	0.018	0.78[0.59,0.96]	0.90	0.65
	median ADC	1.65±0.46	2.02±0.17	0.027	0.76[0.57,0.95]	0.90	0.65
T1	mean T1	1335±326	1709±530	0.014	0.79[0.58,1.0]	0.70	0.82
	median T1	1264±345	1621±514	0.020	0.77[0.56,0.99]	0.60	0.82
Multiparametric					0.85[0.71,1.0]	0.70	0.82

Table 1. Sequence-by-sequence statistically significant features with mean±stdev and Mann-Whitney p-value. The logistic regression AUC with sensitivity and specificity at the Youden J statistic cutoff is shown for each individual feature in the three rightmost columns. Diffusion coefficients [10^{-3} mm²/s].

Table 1

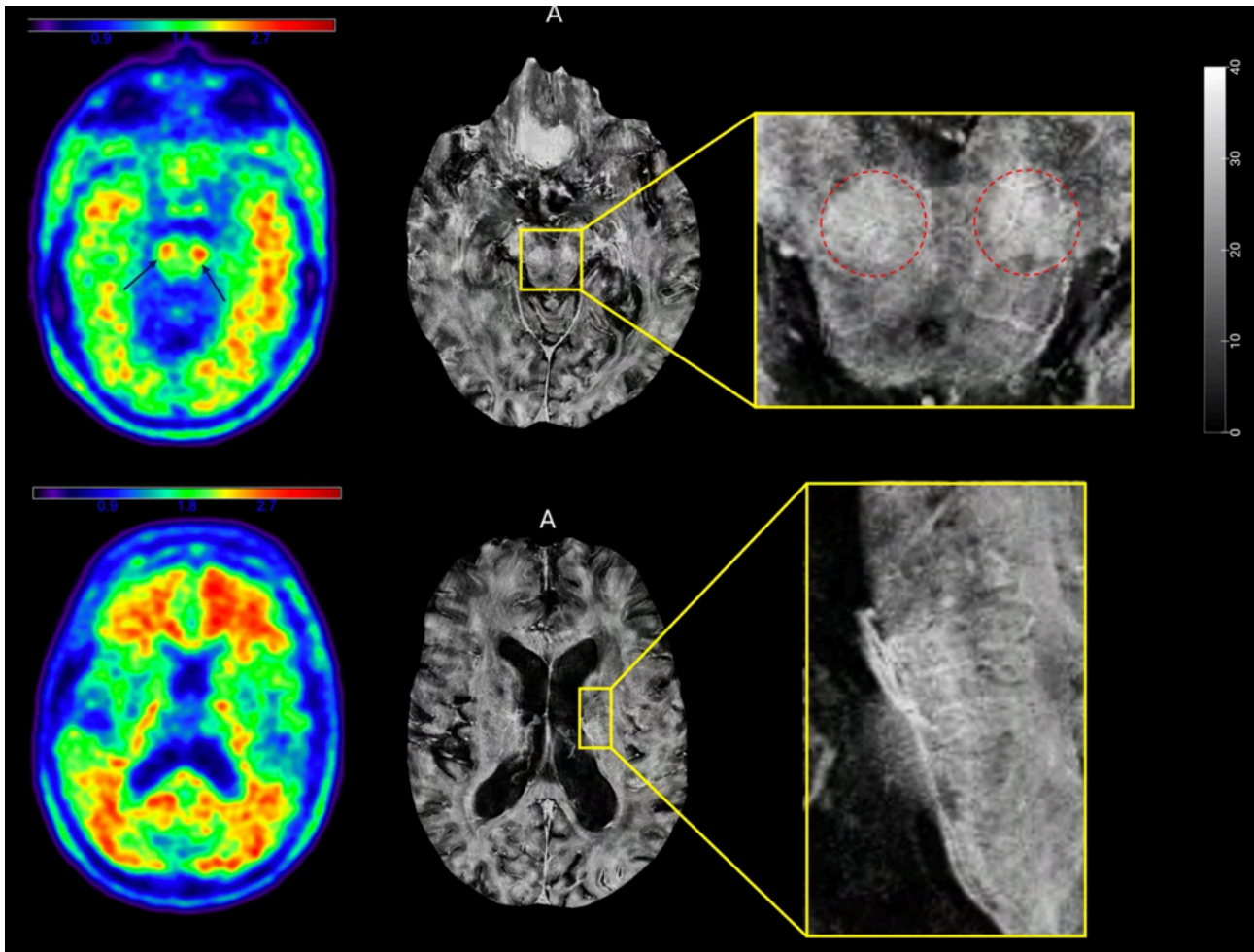
Optimized 7-Tesla QSM reconstruction: Clinical feasibility

Felisha Ma¹, Pinar Ozbay², Akbar Alipour¹

¹Icahn School of Medicine at Mount Sinai,

²Bogazici University Institute of Biomedical Engineering

Alzheimer's disease (AD) is a progressive neurological disorder predominantly characterized by the abnormal accumulation of beta-amyloid ($A\beta$) plaques. $A\beta$ can be detected using Positron Emission Tomography (PET) imaging or high spatial resolution MRI that allows for the in-vivo visualization and quantification of $A\beta$ plaques in the brain. Detection of $A\beta$ plaques with MRI has been associated with paramagnetic iron deposition near these plaques. Conversely, proteins such as $A\beta$ plaques show diamagnetic properties due to their high concentration of paired electrons. When deposits are comprised of both $A\beta$ and iron, these substances exert opposing effects on the overall magnetic susceptibility. Ultra-high field MRI at 7 Tesla (7T) provides a higher sensitivity, and thus better signal-to-noise ratio and MRI contrast than 3T or 1.5T. In this study, we leveraged the high sensitivity of 7T MRI to measure the diamagnetic susceptibility of $A\beta$ aggregated in the brain of AD patients using separated quantitative susceptibility mapping (QSM). In-vivo MRI experiment was performed in AD/MCI (N=4) individuals aged 65-80 years. Scanning was conducted on a 7T MRI scanner (Magnetom, Siemens Healthcare, Erlangen, Germany) using 1Tx/32Rx Nova head coil. To calculate QSM, a 3D high-resolution spoiled gradient echo (GRE) sequence was used (voxels size=0.3x0.3x1.5 mm³, TR/TE = 32/10 ms, and flip angle = 12°). QSM images were reconstructed using the Morphology-Enabled Dipole Inversion (MEDI) algorithm with CSF referencing. We separated magnetic sources in QSM into paramagnetic and diamagnetic sources using an algorithm developed by Sisman et al. The estimated susceptibility values of negative sources in a set of enhancing Ab plaque were correlated against Ab PET distribution. In the figure, the negative QSM (brighter regions) and $A\beta$ PET images reveal a noteworthy correlation, with higher negative susceptibility values in the red nucleus displaying a strong association with $A\beta$ levels in AD patients. A moderate correlation was observed in the proventricular white matter. However, in regions with a higher $A\beta$ burden, a substantial correlation between $A\beta$ and negative QSM was not observed. This study represents the first implementation of separated QSM at 7T in living AD patients. Our key finding revealed a strong correlation between higher $A\beta$ levels in the red nucleus and elevated negative susceptibility values. Importantly, this study demonstrates the clinical feasibility of using the separated-source QSM technique. The findings presented in this study underscore the potential of the 7T separated-source QSM methodology as an alternative tool to detect $A\beta$ imaging in AD patients.



$A\beta$ PET and negative QSM images of an Alzheimer's disease (AD) patient showing higher $A\beta$ and negative susceptibility values (brighter regions) in red nucleus and moderate correlation between $A\beta$ and negative susceptibility in proventricular white matter.

Exploring in vivo T cell imaging in atherosclerosis

Shequouia A. Nauta MD^{1,2,3}, Anna Ranzenigo PhD^{1,2,3}, Trea St. Hillaire BSc^{1,2,3}, Martin Umali BSc^{1,2,3}, Abraham J.P. Teunissen PhD^{1,2,3,4}, Mohammad Rashidian PhD⁵, Mandy M.T. van Leent MD, PhD^{1,2,3}

¹BioMedical Engineering and Imaging Institute, Icahn School of Medicine at Mount Sinai, New York, NY, USA.

²Department of Diagnostic, Molecular and Interventional Radiology, Icahn School of Medicine at Mount Sinai, New York, NY, USA.

³Cardiovascular Research Institute, Icahn School of Medicine at Mount Sinai, New York, NY, USA.

⁴Icahn Genomics Institute, Icahn School of Medicine at Mount Sinai, New York, NY, USA.

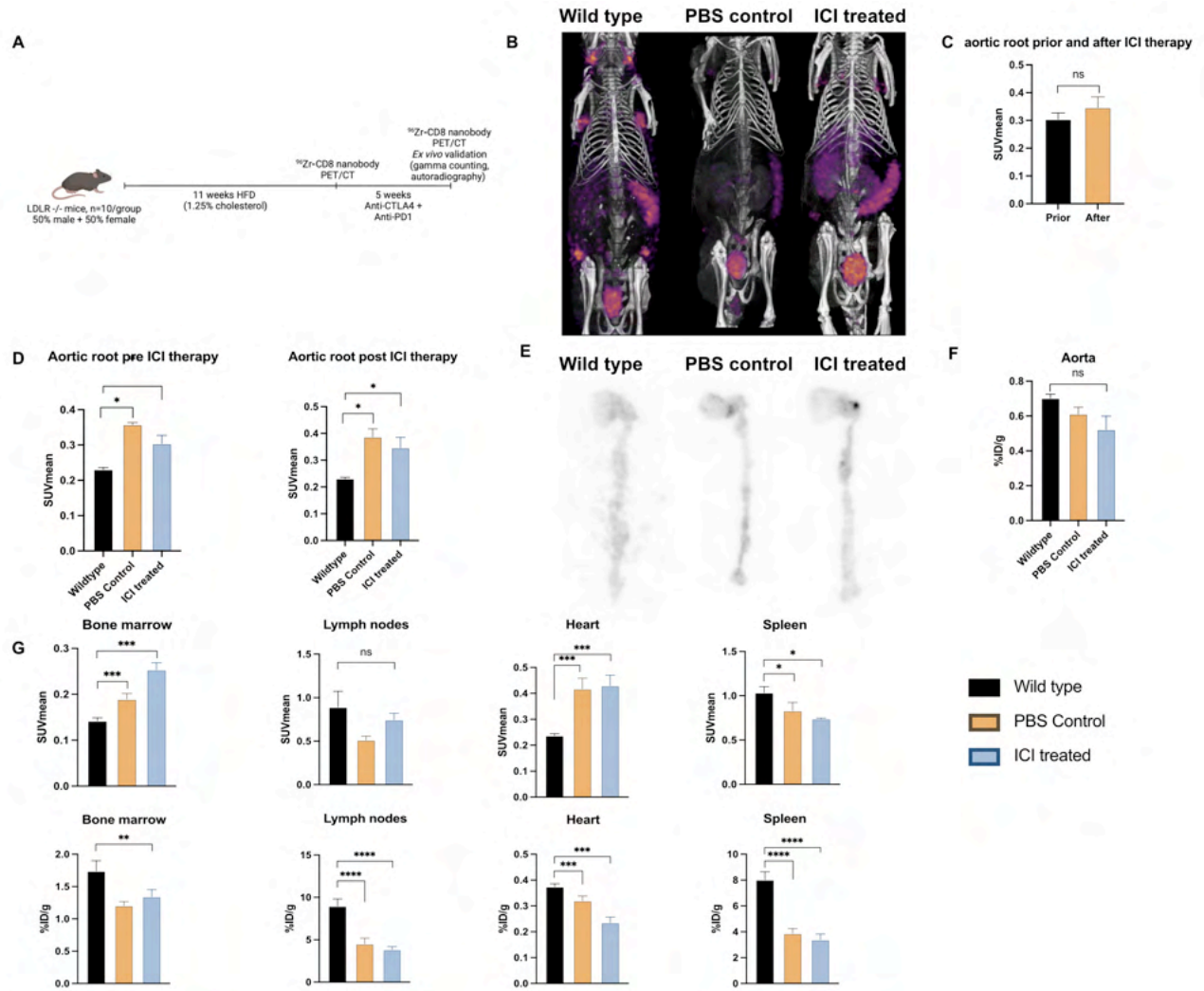
⁵Dana-Farber Cancer Institute, Harvard Medical School, Boston, MA, USA.

Introduction: Immune checkpoint inhibitors (ICI) are commonly used in cancer treatment. They target certain protein receptors such as CTLA-4 and PD-1, which downregulate T cell response. By removing the block on T cell activation, they can stimulate antitumor immune responses. However, ICI therapy is commonly associated with adverse inflammatory effects, such as myocarditis. Some research suggest that immunotherapy might also aggravate atherosclerotic CVD. A recent study has shown that short time blocking CTLA-4 and PD-1 induces infiltration of CD8+ T cells in the arterial wall and drives plaque progression in atherosclerotic Ldlr^{-/-} mice. Here, we used a nanobody-based radiotracers targeting CD8 to noninvasively study cytotoxic T cell dynamics in atherosclerosis-prone mice treated with ICI.

Methods: Ldlr^{-/-} mice (10 male, 10 female) were fed a high cholesterol (1.25%) diet for 11 weeks, followed by 4 weeks of ICI treatment (200 μ g of an anti CTLA-4 and anti PD-1 antibody, 2x/week, i.p.) or PBS. Both groups were compared to healthy C57BL/6 mice. Prior and after ICI or PBS treatment, mice were injected intravenously with ~200 μ Ci 89Zr-labeled CD8-specific nanobodies. 24 hours later, mice underwent positron emission tomography (PET) with contrast-enhanced computed tomography (CT; Nanoscan, Mediso). 89Zr-CD8 nanobody uptake in the aortic root was determined by calculating the SUVmean. Imaging results were validated by ex vivo radioactivity counting and autoradiography of the aorta.

Results: PET/CT imaging showed that 89Zr-CD8 primarily accumulated in the bone marrow, lymph nodes, kidneys and spleen (Fig 1B). In Ldlr^{-/-} mice, increased 89Zr-CD8 signal was observed in the aortic root (SUV wild-type versus Ldlr^{-/-} mice, 0.23 versus 0.37, P<0.05) (Fig 1C-D). Autoradiography analysis of the ^{89}Zr -tracer uptake in mouse aortas showed a stronger signal in roots of Ldlr^{-/-} mice (Fig 1E). Gamma counting data revealed that there was less uptake in the spleen and bone marrow of Ldlr^{-/-} mice versus the wildtype control (Fig 1F-G). Differences between the PBS control and treated groups were not significant.

Conclusion: Our findings demonstrate that 89Zr-CD8 could potentially be used to assess CD8 T-cell dynamics atherosclerotic plaques. However, it seemed not sensitive enough to determine differences prior versus post-ICI treatment. Lower CD8 T-cell signal in the hematopoietic organs in Ldlr^{-/-} mice could be explained by the myeloid bias in atherosclerotic mice. Future studies are needed for validation of the results. Currently, similar studies to assess 89Zr-CD8 are being performed in human subjects.



Analysis of CD8 T cell dynamics in mice using ⁸⁹Zr-CD8 PET tracer

Short-term Sirolimus Treatment Increases Cerebral Blood Flow in Asymptomatic APOE4 Females Determined by 3T MRI

Caitlin M. Neher¹, Oleksandr Khagai², Jessica Overschmidt³, Joanne Cassani³, Xin Xing⁴, Abeoseh Flemister³, Stefan J. Green⁵, Mehmet Kurt¹, David Beversdorf³, Feng Xu⁶, John W. Grinstead⁷, Priti Balchandani², Talissa A. Altes³, Ai-Ling Lin³

¹University of Washington, Seattle, WA, USA

²Icahn School of Medicine at Mount Sinai, New York, NY

³University of Missouri, Columbia, MO, USA

⁴University of Kentucky, Lexington, KY, USA

⁵Rush University, Chicago, IL, USA

⁶Johns Hopkins University, Baltimore, MD, USA

⁷Siemens Healthineers, Columbia, MO, USA

Background: Apolipoprotein $\epsilon 4$ allele (APOE4) is the strongest genetic risk factor for late-onset Alzheimer's disease (AD) with females having higher risk than males. Compared with non-carriers, cognitively normal, middle-aged APOE4 carriers have lower cerebral blood flow (CBF) decades before clinical symptoms appear. Early intervention to protect CBF would be critical for APOE4 carriers to mitigate AD progression. We have shown in APOE4 mice that Rapamycin (a.k.a. Sirolimus), a FDA-approved mTOR-inhibitor, can restore CBF. Here, in the first human study, our goal is to determine whether the findings translate to human APOE4 carriers by measuring CBF with MRI.

Method: The study was performed at the University of Missouri. Low dose Sirolimus (1 mg/day) was given for 4 weeks to two middle-aged, cognitively normal APOE4 females (45-65 yrs; MOCA>28). APOE status was determined by oral swabs. 3T MRI-based pseudo-continuous arterial spin-labeled (PCASL, 1.7x1.7x4mm resolution) images were acquired at four time-points: baseline (pre-treatment), 2nd and 4th week into treatment, and washout (2 weeks post-treatment). PCASL data was processed with FSL BASIL toolbox and regionally analyzed using FreeSurfer segmentation of T1-weighted images.

Results: Average values of CBF (ml/100g/min) increased in all areas of investigation. When compared to baseline values, we observed an average $34.8 \pm 2.1\%$ increase in washout CBF in the cortex across subjects (Fig. 1). Within the cortex, there was an average increase of 41.5 ± 8.9 , 28.2 ± 6.2 , 37.4 ± 1.7 , and $33.1 \pm 0.3\%$ in the frontal, parietal, temporal and occipital lobes, respectively. White matter CBF showed a similar trend, increasing by $33.7 \pm 4.9\%$ across subjects from baseline to washout (Fig. 1). Smaller AD-associated regions were evaluated and also showed CBF improvement: the entorhinal cortex showed a $25.1 \pm 4.3\%$ increase, while the hippocampus and amygdala showed a 21.4 ± 1.1 and $23.6 \pm 9.8\%$ increase, respectively (Fig. 1). No side effects were observed, and no changes in blood glucose and HbA1c levels were found in the participants.

Conclusion: Short-term Sirolimus treatment can effectively increase CBF for asymptomatic APOE4 females, who have the highest risk for AD. Future work will include APOE4 males, increase the sample size and compare CBF with non-carriers (e.g., APOE3/APOE2). Restoration of CBF may pave a way to mitigate or prevent AD developments for APOE4 carriers.

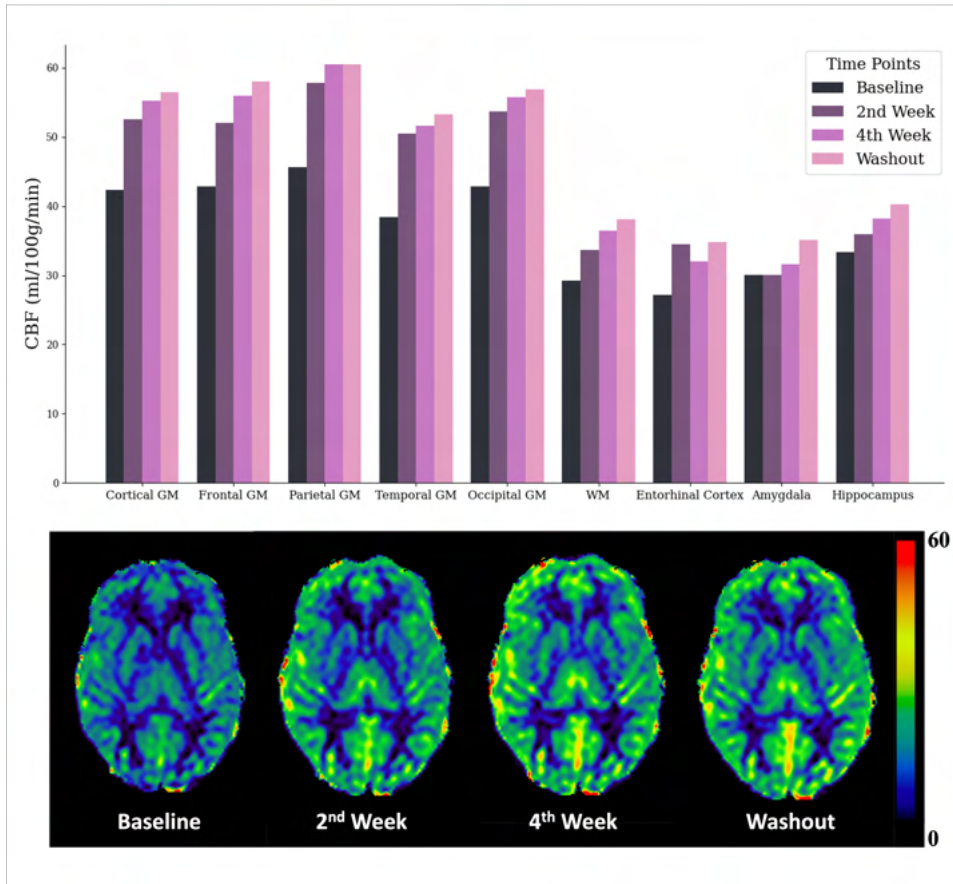


Figure 1. Longitudinal results shown: Subject 1 CBF (ml/100g/min) changes across masked regions (top); Subject 1 axially sliced perfusion (ml/100g/min) maps, co-registered and brain extracted (bottom).

Functional Connectivity of the Locus Coeruleus with Bilateral Insula is associated with increased Anxious Arousal in Anxiety Disorder and PTSD

Philipp T. Neukam¹, Sarah C. Boukezzi¹, Yael Jacob¹, Yolanda I. Whitaker¹, Priti Balchandani², Laurel S. Morris¹, James W. Murrough¹

¹ Depression and Anxiety Center for Discovery and Treatment, Department of Psychiatry, Icahn School of Medicine at Mount Sinai, New York, NY, USA

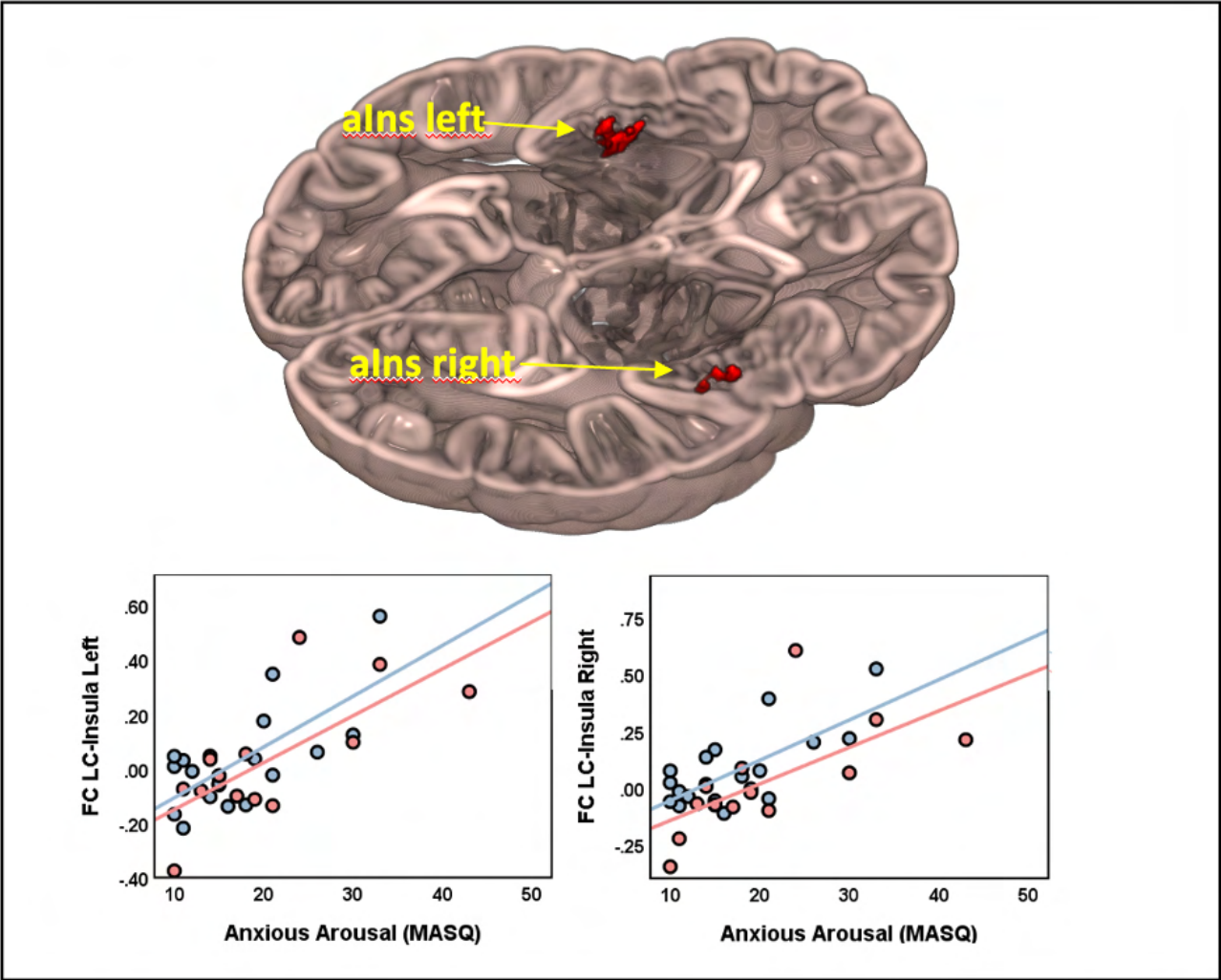
² BioMedical Engineering and Imaging Institute, Icahn School of Medicine at Mount Sinai, New York, NY, USA

Background: Anxiety and stress related disorders are among the most prevalent neuropsychiatric conditions in the United States, with pathological anxiety symptoms such as anxious arousal and fear being core features. Research in animal models suggests that increased tonic activation of locus coeruleus (LC), a brainstem nucleus primarily responsible for the synthesis of norepinephrine in the brain, together with other brain regions is related to anxiety related behaviors. The aim of this study was to use ultra high field 7-Tesla imaging and seed-based resting-state functional connectivity (RSFC) from the LC to the whole brain and relate the connectivity parameters to anxious arousal, a core feature of pathological anxiety and PTSD.

Methods: The available data set scanned at BMEII consisted of patients with anxiety-related disorders (N=20), PTSD (N=13), and Health Controls (N=27). Individual LC masks were created from a brainstem ROI with 400 μm^3 resolution using an in-house developed unsupervised Gaussian mixture model machine learning algorithm for segmentation. Additionally, 10 minutes of resting-state data were collected with 1.5 mm³ (16 subjects with 2.5 mm³) resolution and preprocessed using multi-echo independent component analysis. The LC masks were then coregistered to EPI space and voxel wise Fisher-Z correlation coefficients from the LC mask to the whole brain were computed in the context of a seed-based RSFC analysis. Anxious arousal was collected with the Mood and Anxiety Symptom Questionnaire. Correlations were conducted to investigate relationships between the NM content in the LC and clinical symptoms. A one-sample t-test was conducted on the group level on the correlation maps that included anxious arousal, gender and age as predictors.

Results: The analysis revealed significant bilateral clusters RSFC of the LC with the insula (left: -42 4 -9, k = 215, p <0.001 k(FWE corr.); right: 43 5 -4, k = 86, p <.05 k(FWE corr.)) that positively correlated with anxious arousal (left insula r = 0.557, p <.001, right insula r = 0.438, p = 0.011) in anxiety and PTSD patients. There was no difference, however, between the anxiety and PTSD group for both insula regions (all p >.60).

Conclusion: This is the first study using 7T imaging to show that the strength of the functional coupling between the LC, a core region implicated in anxiety, and the insula, a region that has been suggested to represent anxiety sensitivity and individuals having high anxiety sensitivity may be susceptible to anxiety disorders.



LC to whole brain functional connectivity demonstrating significant positive correlations with anxious arousal in bilateral anterior insula as measured with the Mood and Anxiety Symptom Questionnaire

Automated diagnosability review of liver confidence map overlaid elastograms via deep learning

Heriberto A. Nieves-Vazquez*¹, Efe Ozkaya PhD*^{2,3}, Waiman Meinhold PhD⁴, Octavia Bane PhD*^{2,3}, Jun Ueda PhD⁴, Bachir Taouli MD MHA^{2,3}

¹Department of Biomedical Engineering, Georgia Institute of Technology, Atlanta, GA, USA

²BioMedical Engineering and Imaging Institute, Icahn School of Medicine Mount Sinai, New York, NY, USA

³Department of Diagnostic, Molecular and Interventional Radiology, Icahn School of Medicine at Mount Sinai, New York, NY, USA

⁴School of Mechanical Engineering, Georgia Institute of Technology, Atlanta, GA, USA *H.A.N and E.O. contributed equally to this work.

Introduction: Several factors can contribute to the failure of liver Magnetic Resonance Elastography (MRE) acquisition, including motion artifacts, inadequate wave propagation, insufficient signal-to-noise ratio, patient-related factors, or image reconstruction errors. Liver MRE image outputs must be visually inspected to identify imaging artifacts that signify acquisition failure. This initial study employs deep learning (DL) to automate the classification of liver MRE image quality for streamlining the MRE image review process.

Materials and Methods: A dataset was curated from 914 confidence map overlaid elastogram (CMOE) slices from 149 MRE exams in 90 patients (age: 52.8 ± 14.1 years, M/F: 51/39) who had undergone 2D liver MRE at a vibration frequency of 60 Hz using a Resoundant system. Exams were completed with a 2D spin-echo echo-planar imaging (SE-EPI) sequence acquired at either 1.5T (n=51) or 3T (n=25) and with a 2D gradient-echo (GRE) sequence acquired at either 1.5T (n=13) or 3T (n=1). Two independent observers examined the confidence map overlaid elastograms for liver stiffness measurement and assigned a quality score (non-diagnostic or diagnostic). A Resnet50 DL architecture was modified to accommodate grayscale CMOE slices as input and binary quality classification. The architecture was trained using an 8-fold stratified cross-validation comprising 800 slices with the remaining 114 images used as a consistent test dataset. Cohen's Kappa coefficient was computed to assess the interobserver agreement between the two observers and the agreement between the model's outputted predictions and Observer 1. Accuracy, precision, and recall metrics are reported.

Results: The interobserver agreement was near-perfect (Kappa 0.896 [95% CI: 0.870-0.922]). Test accuracies ranging from 0.649 to 0.842 with an average of 0.749 were achieved during the DL cross-validation. Agreement between Observer 1 and the DL predictions during the cross-validation ranged from slight to substantial (Kappa 0.206 to 0.661).

Conclusions: Our initial study demonstrated a moderate performance in DL-based diagnostic quality classification of liver elastograms, presenting a benchmark for additional studies. Improvement in performance is needed in future work prior to implementation in the clinical workflow.

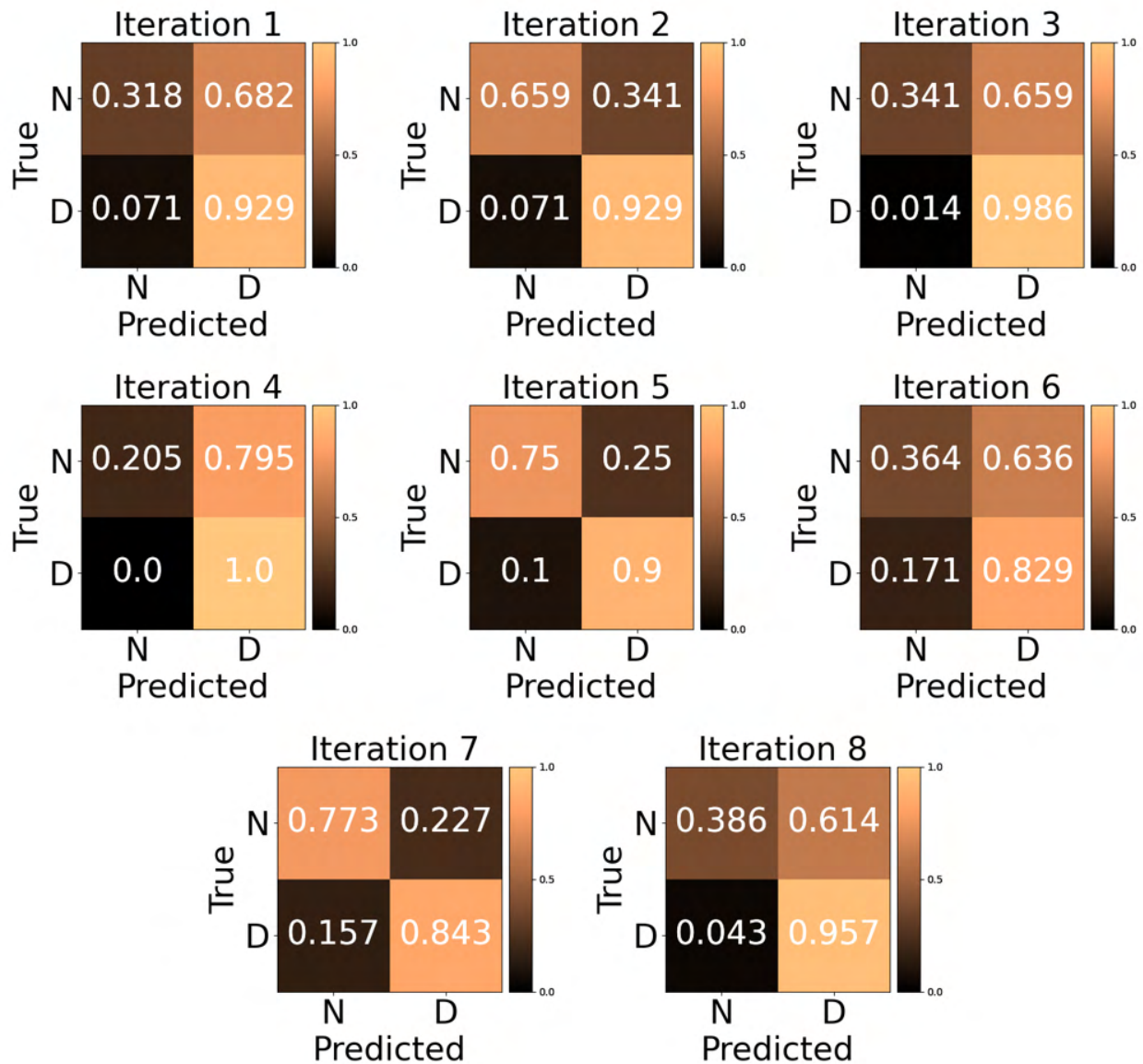


Figure: Confusion matrices of each iteration of the cross-validation, where (N) signifies non-diagnostic image quality and (D) signifies diagnostic image quality, were generated for the test dataset consisting of 114 slices.

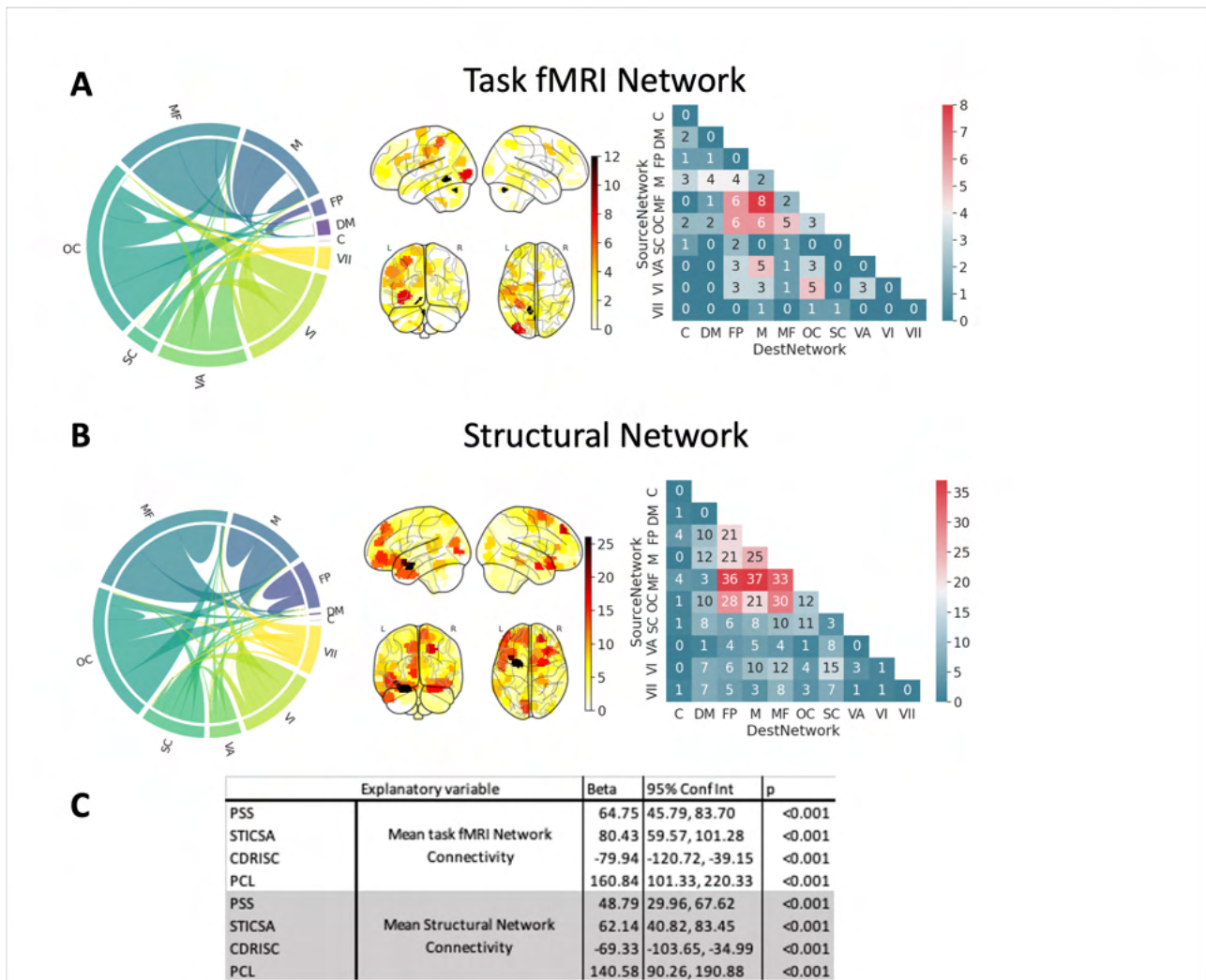


Figure 1 - Task based functional network (A) and structural network (B) which discriminate PTSD and controls. First column is a network level chord plot, second column shows which brain regions are most involved in the network, third column shows a heatmap of connections by network. C = Cerebellum. DM = Default Mode, FP = Frontal Parietal, M = Motor, MF = Medial Frontal, OC = Other Cortical, SC = Subcortical, VA = Visual Association, VI = Visual 1, VII = Visual 2. (C) Associations between functional and structural connectivity estimates and mental health questionnaires, adjusting for age and sex.

Design of a Single Walled Carbon Nanotube-Based Nanosensor for the Inflammatory Cytokine TNF-alpha

Syeda Rahman¹, Ryan Williams¹

¹The City College of New York

Introduction: Single-walled carbon nanotubes (SWCNT) have gained considerable attention for serving as building blocks for biosensors due to their unique optical properties. Semiconducting SWCNTs are fluorescent in the near-infrared range (NIR, 900-1600 nm) due to their optical band-gap between valence and conduction band.¹ Different structures of SWCNT, called chiralities, exhibit unique absorbance and emission bands. Optical nanosensors are advantageous over electrochemical biosensors because of their biocompatibility, photostability and potential for continuous monitoring of analytes. Due to its high surface to volume ratio, SWCNT sensors are very sensitive to their local chemical environment.² We are designing highly specific aptamer-based nanosensors that fluoresce in the NIR region to detect disease biomarkers such as inflammatory cytokines. Aptamers are short DNA sequences that act as a recognition unit for the analyte. TNF-alpha is a proinflammatory cytokine involved in cell signaling, apoptosis, necrosis, resistance to infection and cancer. It plays a critical regulatory role in dysregulated immune responses in degenerative diseases.² We designed a TNF-alpha aptamer based SWCNT sensor that responds to the addition of TNF-alpha protein by changes in fluorescence intensity.

Materials and Methods: HiPCO- SWCNT (NanoIntegris Technologies) were sonicated in a 1:2 ratio with a TNF-alpha specific aptamer to solubilize and functionalize the nanotubes. The resulting suspension was ultracentrifuged to remove impurities and aggregates. The top 75% of the that was filtered through a 100kDa Amicon centrifugal filter to remove excess DNA. Then, the nanosensors were characterized with a UV-Visible absorption spectrophotometer. To test the sensor's response, 250 nM TNF-alpha protein was added to 0.5 mg/L SWCNT-aptamer in 1X PBS. For 3 hours following antigen addition, repeated NIR fluorescence measurements were taken with a NIR spectrophotometer (Applied NanoFluorescence; Texas, USA.) at an excitation wavelength of 638 nm. We took fluorescence spectra before adding the protein indicated as (-1 min) and immediately after adding the protein (0 min) followed by continuous time points. All chiralities were analyzed for center wavelength shift and fluorescence intensity changes to determine any interaction between the nanosensor and the protein.

Results: We found that the fluorescence intensity of the SWCNT decreases over time with addition of 250 nM TNF-alpha protein in PBS. The intensity after exposure to TNF-alpha protein dropped 50% from the initial timepoint.

Conclusions: Aptamer-based SWCNT nanosensors hold great promise for the future of point of care devices, early detection of specific biomarkers and other sensing applications. Our future directions include testing SWCNT in conditioned media to detect proteins of interest.

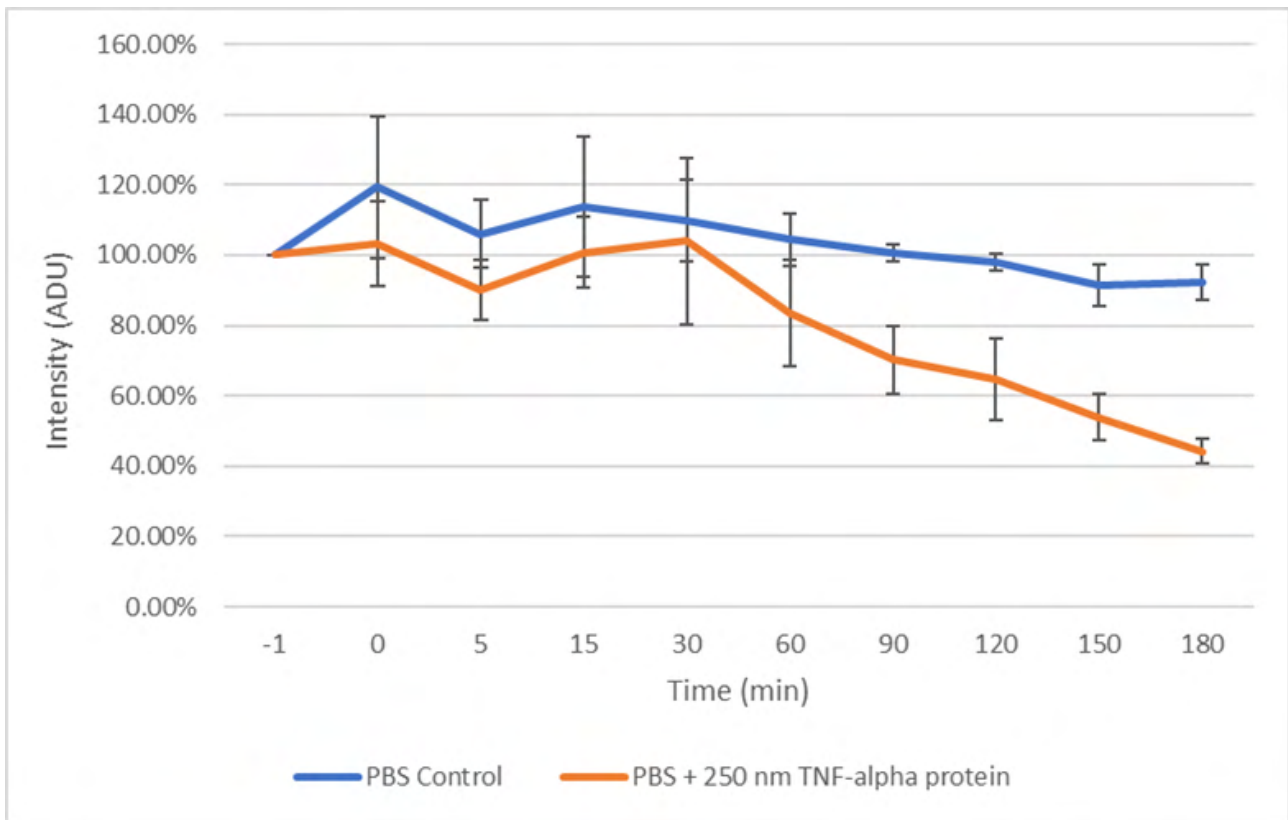


Figure 1.(7,5) Peak Normalized Intensity

Monitoring lipid nanoparticles' biodistribution

Anna Ranzenigo¹, Judit Morla Folch¹, William Wang¹, Martin Umali¹, Trea St. Hillaire¹, Maria Giulia Davighi¹, Vedran Peric², Shequoia Nauta¹, Jazz Munitz¹, Zahi A. Fayad¹, Willem J. M. Mulder², Mandy M. T. van Leent¹, Abraham J. P. Teunissen¹

¹Biomolecular Engineering and Imaging Institute, Icahn School of Medicine at Mount Sinai, New York, NY, USA.

²Department of Nephrology, Radboud Institute for Molecular Life Sciences, Radboud University Medical Center, Nijmegen, The Netherlands.

RNA therapeutics enable regulating protein synthesis *in vivo*. However, RNA's poor *in vivo* stability requires delivery methods that prevent RNA degradation. Lipid nanoparticles (LNPs) have attracted considerable attention for their ability to efficiently employ RNA to treat a broad range of diseases. The recent U.S. Food and Drug Administration (FDA) approval of RNA-loaded LNP vaccines for the prevention of COVID-19 demonstrates the clinical potential of this technology. LNPs are formed by microfluidically mixing nucleic acids and various lipids, which self-assemble to form the desired LNP. Typical LNP formulations comprise an ionizable lipid that non-covalently binds to RNA, a helper phospholipid (i.e., 1,2-distearoyl-sn-glycero-3-phosphocholine (DSPC)) and cholesterol to adjust the fluidity, and a polyethylene glycol (PEG)-lipid to improve colloidal stability. Although LNPs are becoming widely used, little is known about their *in vivo* stability and the biodistribution and degradation of their constituents. Here, we report on our progress in studying LNP biodistribution by PET imaging. We functionalized different LNP's components with deferoxamine (DFO) to facilitate their radiolabeling with ⁸⁹Zr, either prior or after LNP formulation. We first ⁸⁹Zr-labeled siRNA and formulated LNPs with two different lengths of lipid (C14 and C18) of the PEG-lipid. We injected the radiolabeled LNPs in mice and compared their *in vivo* behavior. LNPs are prepared by microfluidics. siRNA loading was quantified by RiboGreen assay. PEG-lipid and siRNA were functionalized with DFO through a multi-step synthesis optimized in our lab. The LNP's biodistribution and pharmacokinetics were evaluated *in vivo* by intravenously injecting C57BL/6 female mice with the selected radiolabeled compound. To determine the *in vivo* half-life of ⁸⁹Zr-LNPs blood was drawn at 1, 5, 15, and 30 min and 1, 2, 4, 17, 24, and 48 hours after injection. The biodistribution was determined through PET-CT imaging at 1, 4, 24 and 96 hours. After each timepoint tissues of interest were harvested, weighed, and gamma-counted using a Wizard2 2480 automatic gamma counter. Values were corrected for decay and expressed as a percentage of the injected dose per gram of tissue (%ID/g). The dissimilar pharmacokinetics and biodistribution of bare siRNA and siRNA loaded into LNPs show that the siRNA stays associated with the nanocarrier *in vivo* and, thereby, efficiently accumulates in the liver and hematopoietic organs (Fig. 1). It's interesting the comparison between the different lengths of PEG-lipid. The different *in vivo* behavior suggests that the different lengths drastically change the circulation of the LNPs.

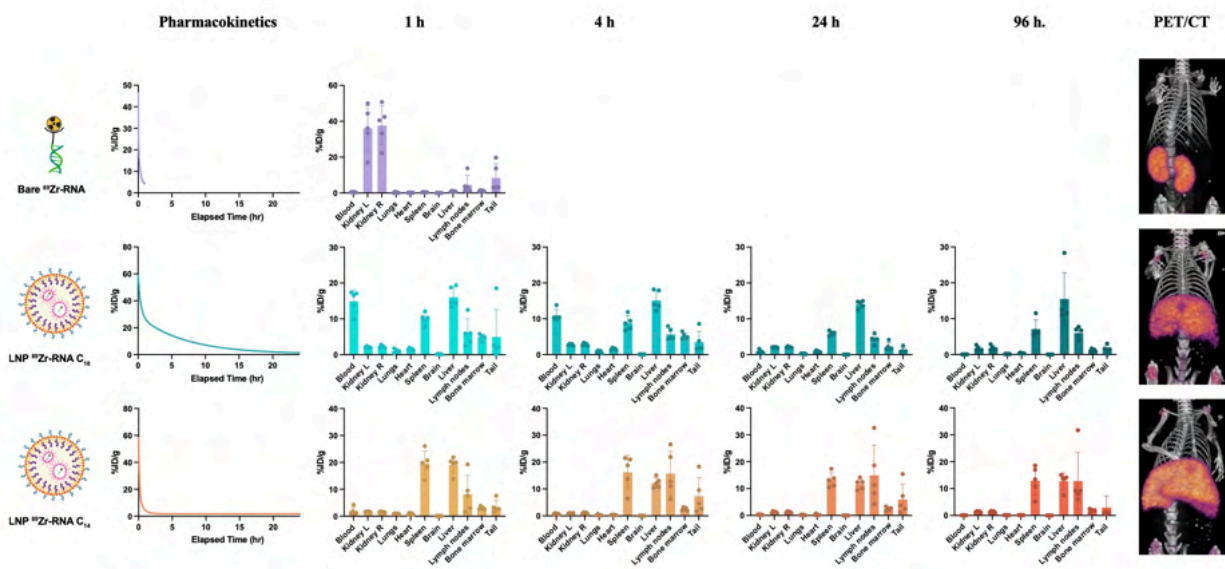


Figure 1: Comparison between bare ^{89}Zr -RNA and ^{89}Zr -RNA loaded into LNPs with two different lengths of lipid (C₁₄ and C₁₈) in the PEG-lipid chain.

Figure 1: Comparison between bare ^{89}Zr -RNA and ^{89}Zr -RNA loaded into LNPs with two different lengths of lipid (C₁₄ and C₁₈) in the PEG-lipid chain.

Disaggregating the social exposome's role in brain development: A study of environmental and contextual factors influencing adolescents' functional connectivity

Vida Rebello¹, Elza Rechtman¹, Stefano Renzetti², Azzurra Invernizzi¹, Megan K. Horton¹

¹ Department of Environmental Medicine and Public Health, Icahn School of Medicine at Mount Sinai, New York, NY, USA ;

¹ Department of Medical and Surgical Specialties, Radiological Sciences and Public Health, University of Brescia, Brescia, Italy

Background: The social exposome encompasses a spectrum of exposures, extending beyond physical and chemical agents to include socioeconomic status, educational opportunities, and neighborhood characteristics. Although the influence of these individual components on brain development is recognized, an exposomic approach to understand the collective impact on brain functional connectivity at rest during adolescence requires further investigation. Three indices capturing the social exposome- child opportunity index (COI), social vulnerability index (SVI) and Area Deprivation index (ADI)- offer a contextual understanding of neighborhood characteristics, as composite measures for specific indicators. Our study aims to first examine associations between the aggregated social exposome indicators and connectivity within the network maintaining ongoing resting brain activity, the default mode network (DMN), in adolescents. Next, we disaggregate these indices into their individual indicators to assess the indicators most impacting DMN connectivity. This approach contributes to a nuanced understanding of the social exposome's role in brain development and identifies indicators that may inform intervention strategies.

Methods: We utilized data from the Adolescent Brain Cognitive Development (ABCD) Study (n= 6332; ages 9-11 years; 48.9% female). Baseline resting-state functional magnetic resonance imaging (rs-fMRI), and demographics were collected. DMN estimates were derived using the Gordon parcellation atlas. Baseline residential addresses provided geocoded estimates for indicators across three indices, redundant indicators across indices were excluded leaving a total of 40 individual factors: COI (29), SVI (6), and ADI (5). Associations between the social exposome and DMN connectivity were quantified using weighted quantile sum (WQS) regression adjusting for sex, age, MRI manufacturer, handedness, and site, including a penalization term for the estimate of the weights and setting bootstrap samples and repeated holdout validation at 30 iterations (# of iterations will be increased in subsequent analysis).

Results: The aggregate social exposome was positively associated with DMN connectivity (b= 0.003; 95% CI [0.002, 0.004]). Primary indicators (Fig. 1) included fewer uncleaned Superfund sites nearby (w: mean estimated weight = 0.16), followed by a higher proportion of two-parent households (w= 0.06) and higher percentage of housing with complete plumbing (w= 0.05).

Conclusion: Understanding actionable items that may inform targeted interventions can contribute to improved long-term health prospects for children. Our exposomic approach leveraged WQS allows us to examine the overall impact of social factors on children's brain development, while identifying which individual factors are most impactful. These findings may inform resource allocation in children's health, reinforcing that actionable measures often depend more on resource distribution than on evidence gaps.

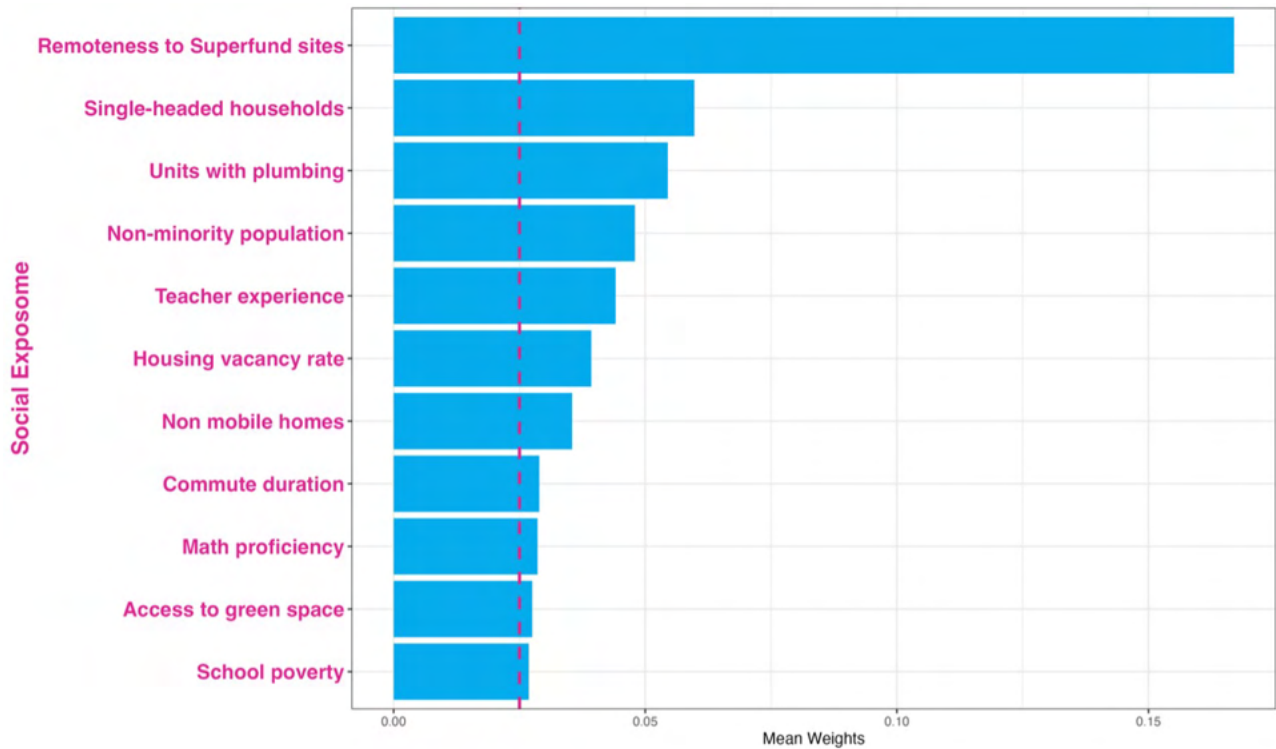


Figure 1. Associations between the WQS social exposome indicators and DMN connectivity among the 6332 adolescents included in the current study. Results from the WQS regression models for DMN connectivity, using 30 repeated holdouts and adjusting for sex, age, MRI manufacturer, handedness, and site. The dotted line represents the threshold from the equi-weighted index (i.e., $1/c$), where c is the number of components in the mixture. Bar plot shows the mean estimated WQS weights for indicators above the threshold.

AI-Enabled Left Atrial Volumetry in Coronary Calcium Scans (AI-CAC) Predicts Atrial Fibrillation as Early as One Year, Improves CHARGE-AF, and Outperforms NT-proBNP: The Multi-Ethnic Study of Atherosclerosis

Morteza Naghavi¹, David Yankelevitz², Anthony P. Reeves³, Matthew J. Budoff⁴, Dong Li⁴, Kyle Atlas¹, Chenyu Zhang¹, Thomas L. Atlas⁵, Seth Lirette¹, Jakob Wasserthal⁶, Sion K. Roy⁴, Claudia Henschke², Nathan D. Wong⁷, Christopher Defilippi⁸, Susan R. Heckbert⁹, Philip Greenland¹⁰.

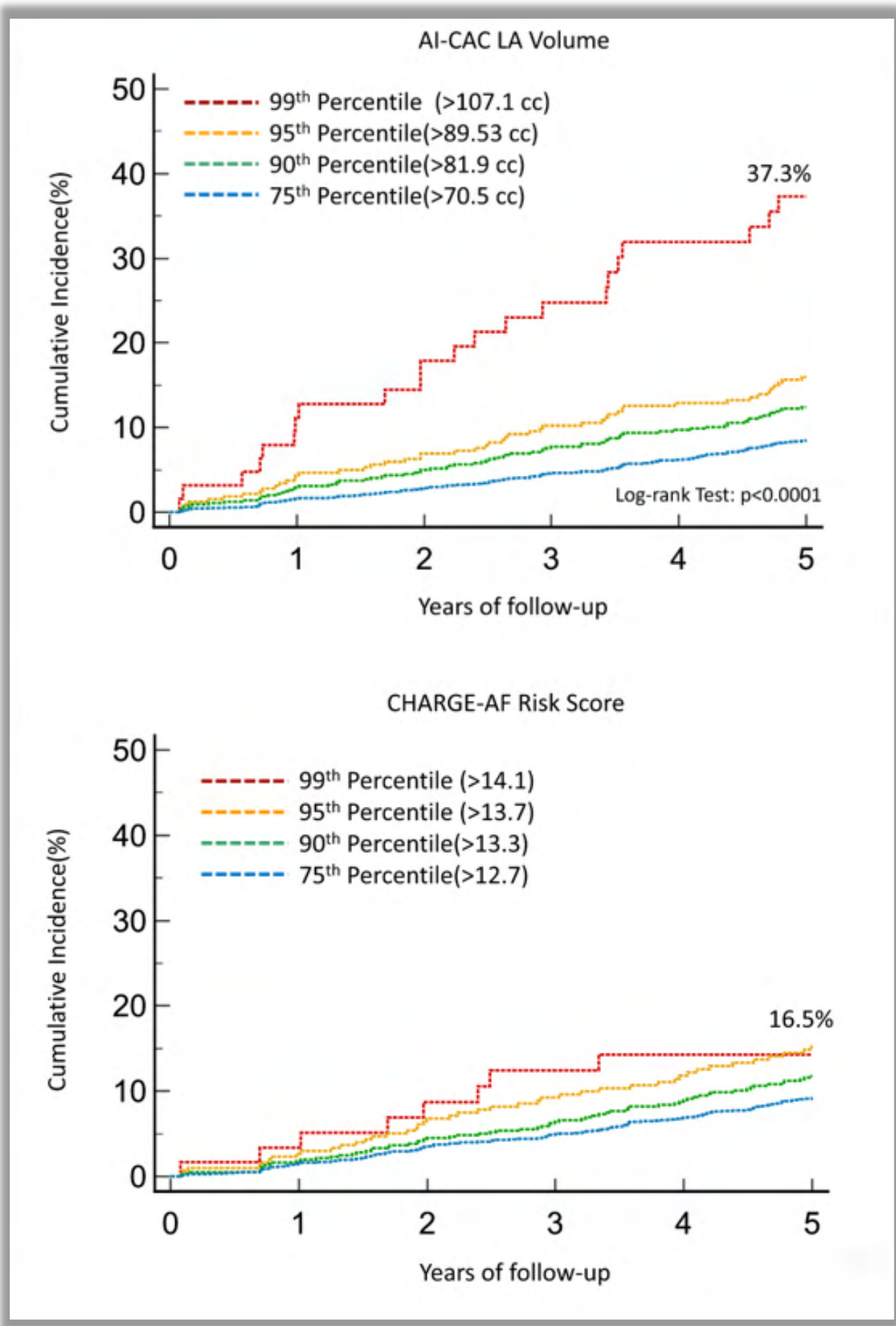
¹HeartLung.AI, Houston, TX, ²Mount Sinai Hospital, New York, NY ³Department of Computer Engineering, Cornell University, Ithaca, NY
⁴The Lundquist Institute, Torrance, CA ⁵Tustin Teleradiology, Tustin, CA ⁶Universität Basel, Basel, Switzerland ⁷Heart Disease Prevention Program, Division of Cardiology, University of California Irvine, CA ⁸Inova Heart and Vascular Institute, Falls Church, VA
⁹University of Washington, Seattle, WA ¹⁰Northwestern University, Evanston, IL

Background: Coronary artery calcium (CAC) scans contain actionable information beyond CAC scores that is not currently reported.

Methods: We have applied artificial intelligence-enabled automated cardiac chambers volumetry to CAC scans (AI-CAC) to 5535 asymptomatic individuals (52.2% women, ages 45-84) that were previously obtained for CAC scoring in the baseline examination (2000-2002) of the Multi-Ethnic Study of Atherosclerosis (MESA). AI-CAC took on average 21 seconds per CAC scan. We used the 5-year outcomes data for incident atrial fibrillation (AF) and assessed discrimination using the time-dependent area under the curve (AUC) of AI-CAC LA volume with known predictors of AF, the CHARGE-AF Risk Score and NT-proBNP (BNP). The mean follow-up time to an AF event was 2.9±1.4 years.

Results: At 1,2,3,4, and 5 years follow-up 36, 77, 123, 182, and 236 cases of AF were identified, respectively. The AUC for AI-CAC LA volume was significantly higher than CHARGE-AF for Years 1, 2, and 3 (0.836 vs. 0.742, 0.842 vs. 0.807, and 0.811 vs. 0.785, respectively, all p<0.05), but similar for Years 4 and 5, and significantly higher than BNP at Years 1-5 (all p<0.01), but not for combined CHARGE-AF and BNP at any year. AI-CAC LA significantly improved the continuous Net Reclassification Index for prediction of AF over years 1-5 when added to CHARGE-AF Risk Score (0.60, 0.28, 0.32, 0.19, 0.24), and BNP (0.68, 0.44, 0.42, 0.30, 0.37) (all p<0.01).

Conclusion: AI-CAC LA volume enabled prediction of AF as early as one year and significantly improved on risk classification of CHARGE-AF Risk Score and BNP.



Cumulative Incidence of Atrial Fibrillation (AF) in the Top Quartile of AI-CAC Left Atrial (LA) Volume vs. CHARGE-AF Score over 5 years of follow-up.

AI-Enabled Cardiac Chambers Volumetry in Coronary Calcium Scans (AI-CAC) Predicts Heart Failure and Outperforms NT-proBNP: The Multi-Ethnic Study of Atherosclerosis

Morteza Naghavi, ^a, Anthony Reeves, ^b, Matthew Budoff, ^c, Dong Li, ^c, Kyle Atlas, ^a, Chenyu Zhang, ^a, Thomas Atlas, ^d, Sion K. Roy, ^c, Claudia Henschke, ^e, Nathan D. Wong, ^f, Christopher Defilippi, ^g, Daniel Levy, ^h, David Yankelevitz, ^e,

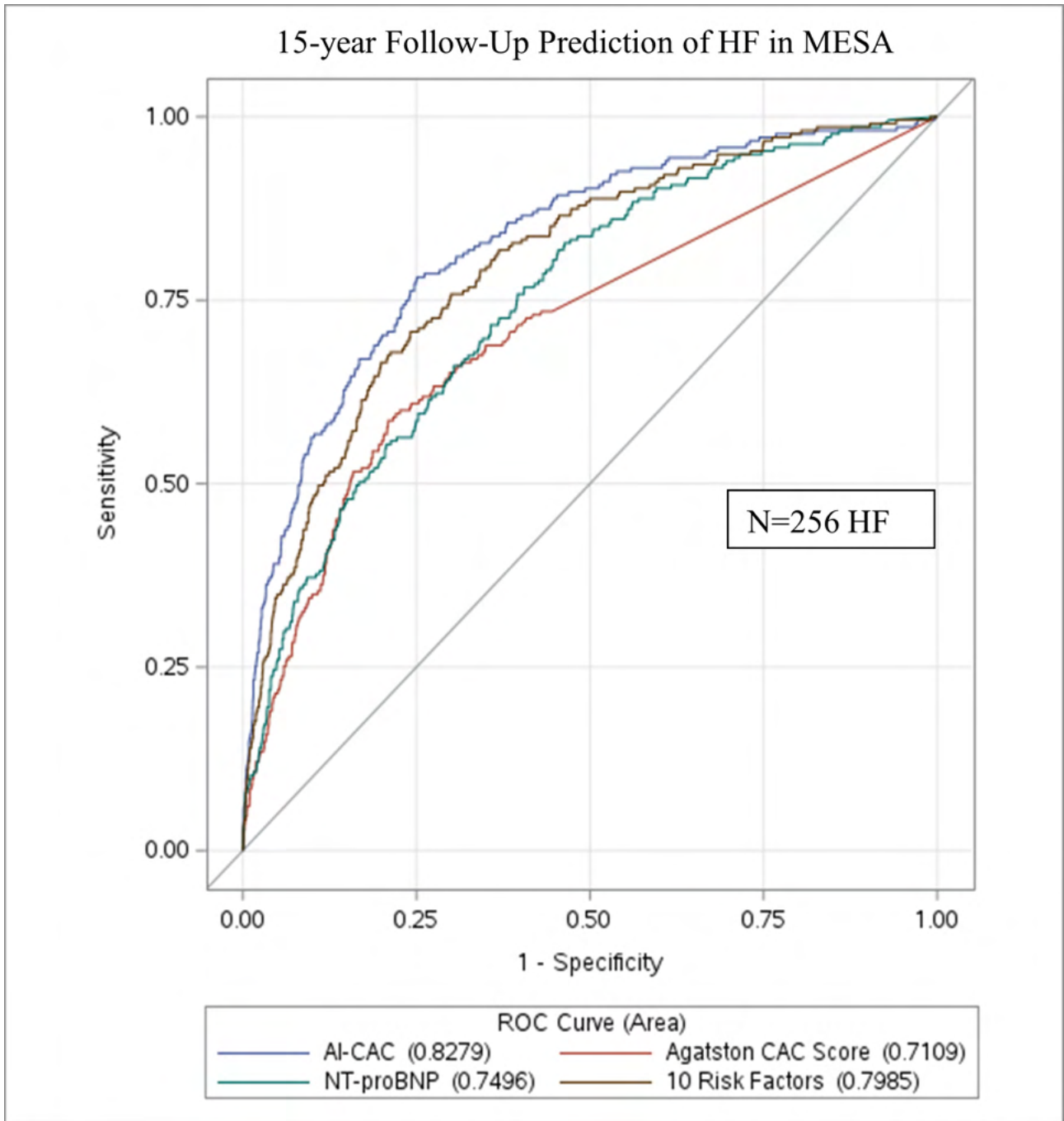
^a. HeartLung.AI, Houston, TX ^b. Department of Computer Engineering, Cornell University, Ithaca, NY ^c. The Lundquist Institute, Torrance, CA ^d. Tustin Teleradiology, Tustin, CA ^e. Mount Sinai Hospital, New York, NY ^f. Heart Disease Prevention Program, Division of Cardiology, University of California Irvine, CA ^g. Inova Heart and Vascular Institute, Falls Church, VA ^h. National Institutes of Health, Bethesda, Maryland

Introduction: Coronary artery calcium (CAC) scans contain useful information beyond the Agatston CAC score that is not currently reported. We recently reported that artificial intelligence (AI)-enabled cardiac chambers volumetry in CAC scans (AI-CAC) predicted incident atrial fibrillation in the Multi-Ethnic Study of Atherosclerosis (MESA). In this study, we investigated the performance of AI-CAC for prediction of incident heart failure (HF) and compared it with 10 known clinical risk factors, NT-proBNP, and the Agatston CAC score.

Methods: We applied AI-CAC to 5750 CAC scans of asymptomatic individuals (52% women, White 40%, Black 26%, Hispanic 22% Chinese 12%) free of known cardiovascular disease at the MESA baseline examination (2000-2002). We used the 15-year outcomes data and compared the time-dependent area under the curve (AUC) of AI-CAC versus NT-proBNP, Agatston score, and 10 known clinical risk factors (age, gender, diabetes, current smoking, hypertension medication, systolic and diastolic blood pressure, LDL, HDL, total cholesterol, and hs-CRP) for predicting incident HF over 15 years.

Results: Over 15 years of follow-up, 256 HF events accrued. The AUC for predicting HF with AI-CAC (0.826) was significantly higher than NT-proBNP (0.742) and Agatston score (0.712) ($p < 0.0001$), and comparable to clinical risk factors (0.818, $p = 0.4141$). AI-CAC category-free Net Reclassification Index (NRI) significantly improved on clinical risk factors (0.32), NT-proBNP (0.46), and Agatston score (0.71) for HF prediction at 15 years ($p < 0.0001$).

Conclusion: AI-CAC significantly outperformed NT-proBNP and the Agatston CAC score, and significantly improved the AUC and category-free NRI of clinical risk factors for incident HF prediction.



Comparing Receiver Operating Curve (ROC) Area under Curve (AUC) between Artificial Intelligence enabled Cardiac Chamber Volumetry (AI-CAC) vs NT-proBNP, Agatston CAC Score, and Clinical risk factors over 15 years.

Coronary Artery Calcium Scans Powered by Artificial Intelligence (AI-CAC) Predicts Atrial Fibrillation and Stroke Comparably to Cardiac Magnetic Resonance Imaging: The Multi-Ethnic Study of Atherosclerosis (MESA)

Morteza Naghavi,^a Anthony P. Reeves,^b Kyle Atlas,^a Chenyu Zhang,^a Dong Li,^c Thomas Atlas,^d Claudia Henschke,^e Nathan D. Wong,^f Sion K. Roy,^c Matthew J. Budoff,^c David Yankelevitz,^e

^a. HeartLung.AI, 2450 Holcombe, Houston, TX, 77021 ^b. Department of Electrical and Computer Engineering, Cornell University, 616 Thurston Ave. Ithaca, NY 14853 ^c. The Lundquist Institute, 1124 W Carson St, Torrance, CA 90502 ^d. Tustin Teleradiology, 13422 Newport Ave Suite I, Tustin, CA 92780 ^e. Mount Sinai Hospital, 1468 Madison Ave, New York, NY 10029 ^f. Heart Disease Prevention Program, Division of Cardiology, University of California, Irvine, CA

Background: AI-CAC provides more actionable information than the Agatston coronary artery calcium (CAC) score. We have recently shown in the Multi-Ethnic Study of Atherosclerosis (MESA) that AI-CAC automated left atrial (LA) volumetry enabled prediction of atrial fibrillation (AF) as early as one year. In this study we evaluated the performance of AI-CAC LA volumetry versus LA measured by human experts using cardiac magnetic resonance imaging (CMRI) for predicting AF and stroke, and compared them with CHARGE-AF risk score, Agatston score, and NT-proBNP.

Methods: We used 15-year outcomes data from 3552 asymptomatic individuals (52.2% women, age 61.7±10.2 years) who underwent both CAC scans and CMRI in the MESA baseline examination. CMRI LA volume was previously measured by human experts. Data on BNP, CHARGE-AF risk score and the Agatston score were obtained from MESA. Discrimination was assessed using the time-dependent area under the curve (AUC).

Results: Over 15 years follow-up, 562 cases of AF and 140 cases of stroke accrued. The AUC for AI-CAC versus CMRI for AF and stroke were not significantly different (0.802 vs. 0.798 and 0.762 vs. 0.751 respectively, p=0.60). AI-CAC significantly improved the continuous Net Reclassification Index (NRI) for prediction of AF and stroke when added to CHARGE-AF risk score (0.28, 0.21), NT-proBNP (0.43, 0.37), and Agatston score (0.69, 0.41) respectively (p for all<0.0001).

Conclusion: AI-CAC automated LA volumetry and CMRI LA volume measured by human experts similarly predicted incident AF and stroke over 15 years. Further studies to investigate the clinical utility of AI-CAC for AF and stroke prediction are warranted.

Case Example 1

Female

Age: 57

CAC Score: 0

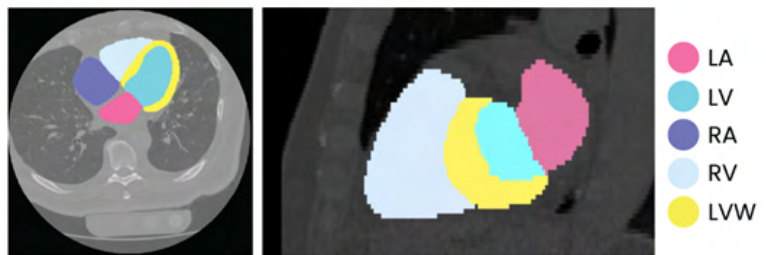
10-Year ASCVD Risk: 1.4%

Cardiothoracic Ratio: 0.5

LA Volume: 84.6 cc

Female cohort LA Volume: 55.8±14.1

This case developed Afib



Case Example 2

Female

Age: 60

CAC: 0

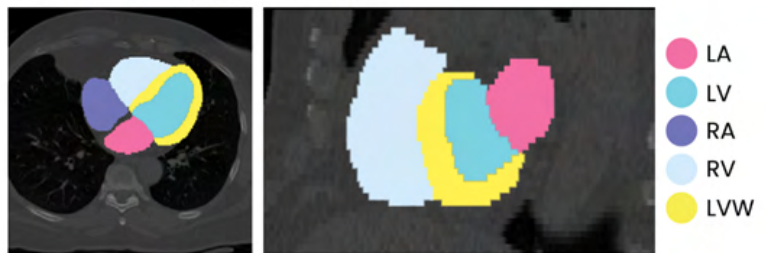
10-year ASCVD Risk: 4.1%

Cardiothoracic Ratio: 0.49

LA Volume: 76.2 cc

Female cohort LA Volume: 55.8±14.1

This case developed Afib and stroke.



Examples of AI-CAC detection of high-risk individuals with enlarged left atrium (LA) in coronary artery calcium (CAC) scans with calcium score of zero who subsequently experienced adverse events.

Automated Left Ventricular Volumetry using Artificial Intelligence in Coronary Calcium Scans (AI-CAC) Predicts Heart Failure Comparably to Cardiac MRI and Outperforms NT-proBNP: The Multi-Ethnic Study of Atherosclerosis (MESA)

Morteza Naghavi,^a Anthony Reeves,^b Kyle Atlas,^a Dong Li,^c Chenyu Zhang,^a Thomas Atlas,^d Sion K. Roy,^c Matthew Budoff,^c Claudia Henschke,^e David Yankelevitz,^e Nathan D. Wong,^f.

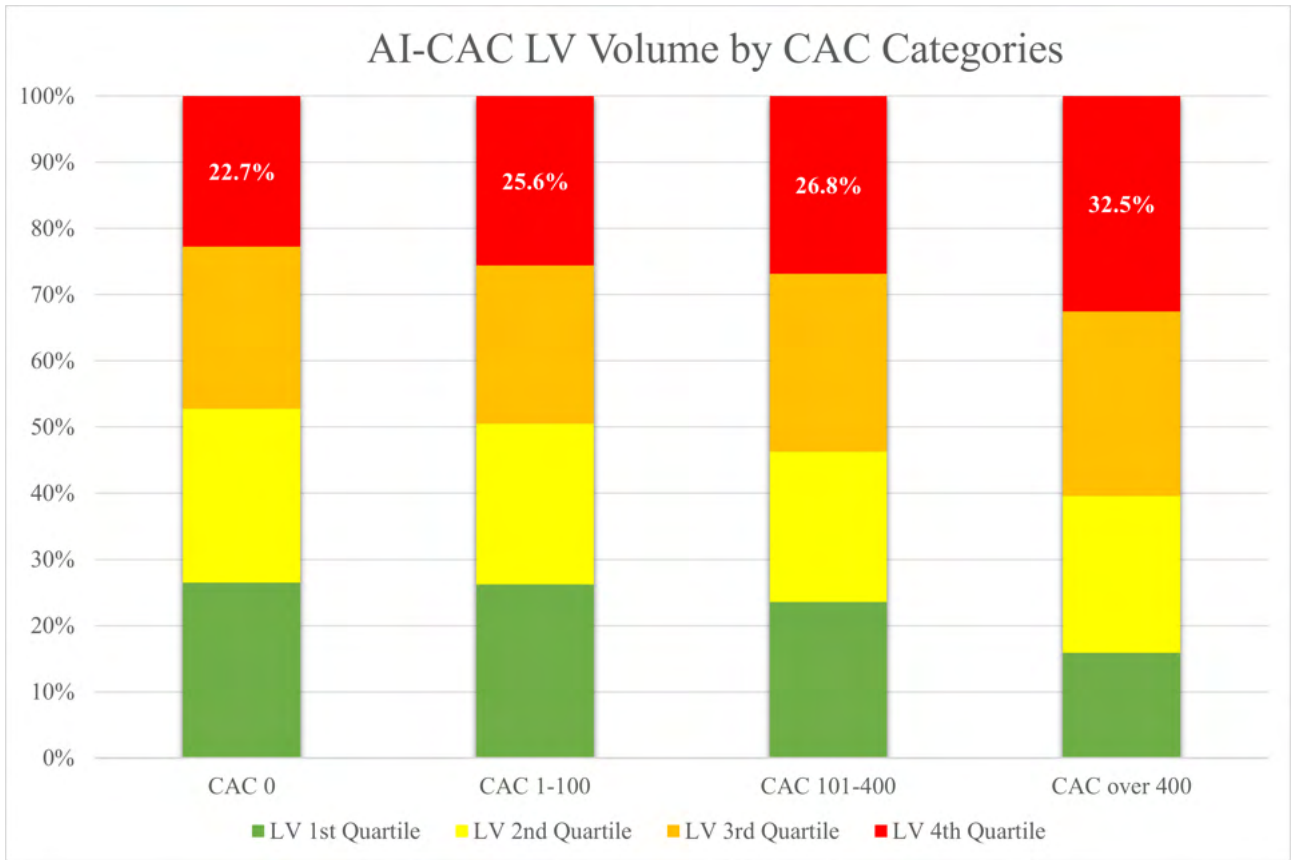
^a. HeartLung.AI, Houston, TX ^b. Department of Computer Engineering, Cornell University, Ithaca, NY ^c. The Lundquist Institute, Torrance, CA ^d. Tustin Teleradiology, Tustin, CA ^e. Mount Sinai Hospital, New York, NY ^f. Heart Disease Prevention Program, Division of Cardiology, University of California, Irvine, CA

Introduction: Artificial intelligence-powered coronary artery calcium scan (AI-CAC) provides more actionable information than currently reported. In this study we compared left ventricular (LV) volume measured by AI-CAC versus cardiac magnetic resonance imaging (CMR) and NT-proBNP for predicting heart failure (HF). Additionally, we compared AI-CAC vs. NT-proBNP for detection of left ventricular hypertrophy (LVH) defined by CMR.

Methods: We used 15-year outcomes data for incident heart failure (HF) from 3078 asymptomatic MESA participants (52.3% women, age 62.2±10.3 years) who underwent both CAC scans and CMR at the baseline examination. Data on CMR semi-manual LV volume, NT-proBNP, and Agatston CAC score were obtained from MESA. Discrimination was assessed using the time-dependent area under the curve (AUC) for incident HF.

Results: Over 15 years of follow up, 133 cases of HF were diagnosed. The AUC for AI-CAC (0.789) and CMR (0.793) were not significantly different ($p=0.67$) but were significantly higher than NT-proBNP (0.719) and Agatston score (0.664) ($p<.0001$) for prediction of incident HF. AI-CAC and CMR significantly improved the continuous Net Reclassification Index of NT-proBNP (0.37) and Agatston score (0.45) for HF prediction ($p<0.001$ for all). The AUC for AI-CAC vs. NT-proBNP for LVH was 0.871 vs. 0.600 for males and 0.854 vs. 0.600 for females.

Conclusion: In MESA, AI-CAC automated LV volumetry and CMR semi-automated LV volumetry equally predicted incident HF over 15 years and outperformed NT-proBNP. AI-CAC significantly outperformed NT-proBNP for detection of LVH. Both AI-CAC and CMR significantly improved on NT-proBNP and Agatston CAC score for predicting incident HF.



AI-CAC Left Ventricle (LV) Volume Quartiles by Agatston Coronary Artery Calcium (CAC) Score Categories

Opportunistic Artificial Intelligence-based Detection of Osteoporosis and Osteopenia Using Thoracic Vertebral Bone Mineral Density Measurements in Coronary Artery Calcium Scans

Kyle Atlas,¹, Chenyu Zhang,¹, Amirhossein Jaberzadeh,¹, Juan Montoya,¹, Isabel De Oliveira,¹, Venkat Sanjay Manubolu,¹, Marlon Montes,¹, Song Shou Mao,¹, Thomas Atlas,², Dong Li,³, Claudia Henschke,⁴, David Yankelevitz,⁴, Anthony P. Reeves,⁵, Matthew Budoff,¹, Morteza Naghavi,¹

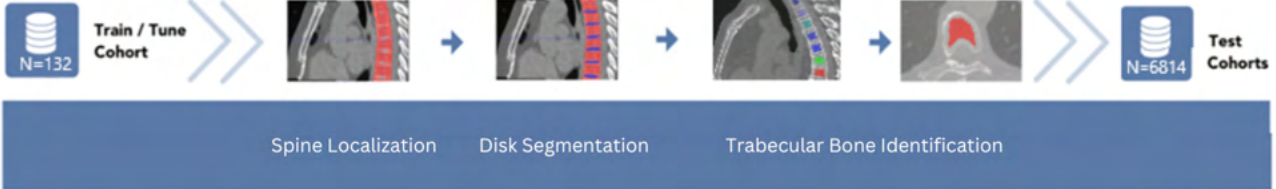
¹ HeartLung Technologies, Torrance, CA, USA, ² Tustin Teleradiology, Tustin, CA, USA, ³ Emory University, Atlanta, GA, USA, ⁴ Mount Sinai Hospital, New York, NY, USA, ⁵ Cornell University, Ithaca, NY, USA.

Introduction: Previously we reported a manual method of measuring thoracic vertebral bone mineral density (BMD) using quantitative computed tomography (QCT) in non-contrast cardiac CT scans used for coronary artery calcium (CAC) scoring. In this report, we present validation studies of an artificial intelligence (AI) based automated bone mineral density (AutoBMD) measurement that recently received FDA approval as an opportunistic add-on to CAC scans.

Methods: A deep learning model was trained to detect vertebral bodies. Subsequently signal processing techniques were developed to detect discs and trabecular components of the vertebral body. The model was trained using 132 CAC scans comprising 7649 slices. To validate AutoBMD, we used all 6814 cases of manual BMD measurements previously reported from CAC scans in the Multi-Ethnic Study of Atherosclerosis (MESA).

Results: Mean±SD for AutoBMD and manual BMD were 166.3 ± 48.0 g/cm³ and 163.0 ± 46.7 g/cm³ respectively ($p=0.23$). MESA cases were 47% male and 53% female with age 60 ± 9.1 . Human experts vs. AutoBMD reported 23% vs. 21% for osteoporosis, and 32% vs. 34% for osteopenia ($p=0.7$). A strong correlation was found between AutoBMD and manual measurements ($R=0.97$, $p<0.0001$). AutoBMD averaged 15 seconds per report vs. 5.5 minutes for manual measurements ($p<0.0001$).

Conclusion: AutoBMD is an FDA approved AI-enabled opportunistic tool that reports BMD with Z-score and T-score, and accurately detects osteoporosis and osteopenia in CAC scans. No extra cost of scanning and no extra radiation to patients, plus the high prevalence of asymptomatic osteoporosis, make AutoBMD a valuable add-on to CAC scans.



Patient Name: Doe, Jane

ID: 9008
Date of Exam: 2/16/2023
Date of Birth: 1/1/1953
Gender: Female

Your Clinic's Logo Here



Hounsfield Unit (HU)

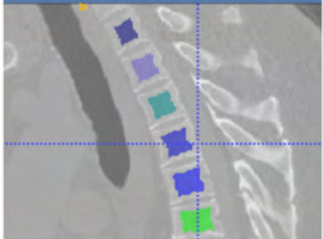
A quantitative scale for describing radiodensity.

Vertebra1	114.6
Vertebra2	100.1
Vertebra3	102.7
Mean HU	105.8

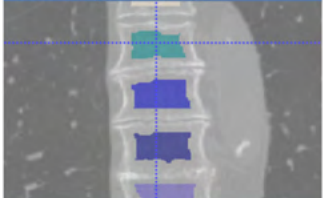
BMD (mg/cc)

Mean BMD	106
Z-score	-2
T-score	-3.2

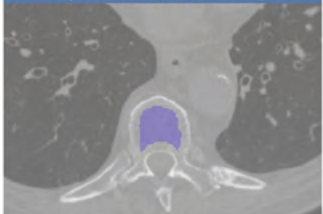
Sagittal (side view)



Coronal (front view)

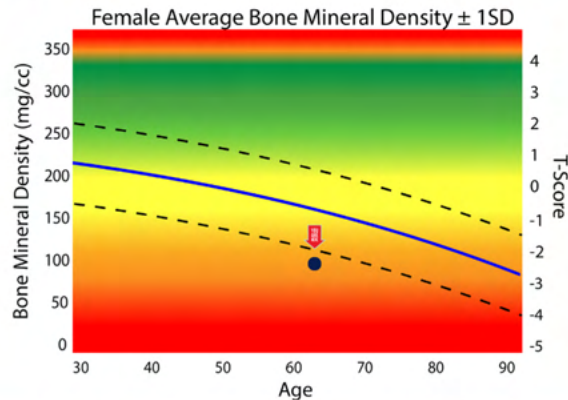


Axial (cross sectional view)



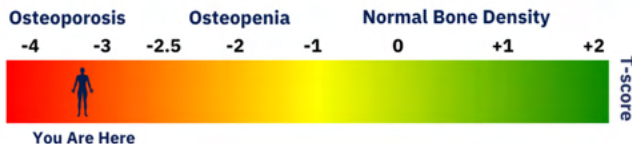
Your Z-score: -2.0

Z-score compares your bone density to average values for a person of your same age and gender.



Your T-score: -3.2

T-score is your bone density compared with what is normally expected in a healthy adult of your sex. *Your T-Score of -3.2 indicates you likely have osteoporosis (severe bone loss).*



Recommendations

All patients should ensure an adequate intake of dietary calcium and vitamin D. The National Osteoporosis Foundation recommends adults under age 50 need 1,000 mg of calcium and 400-800 IU of vitamin D daily. Adults 50 and over need 1,200 mg of calcium and 800-1,000 IU of vitamin D daily. **Based on your BMD results, you have osteoporosis and should seek follow up care with your physician.**

Follow up

People with diagnosed cases of osteoporosis or at high risk for fracture should have regular BMD tests. For patients eligible for Medicare, routine testing is allowed once every 2 years. For more information visit www.AutoBMD.ai.

Electronically signed by: Thomas Atlas, MD 1

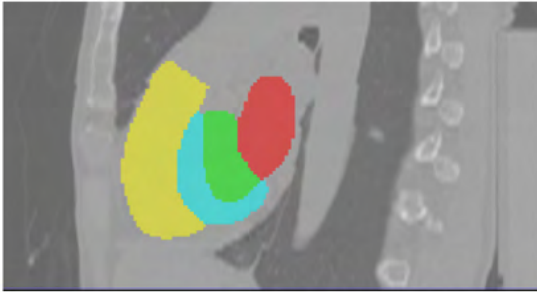
AI-enabled Automated Cardiac Chambers Volumetry in Non-contrast ECG-gated Cardiac Scans Vs. Non-contrast Non-gated Lung Scans

Anthony P. Reeves, PhD¹, Kyle Atlas, BS², Chenyu Zhang, MS², Matthew Budoff, MD³, Claudia Henschke, MD⁴, David Yankelevitz, MD⁴, Edward Callahan, MD², Morteza Naghavi, MD².

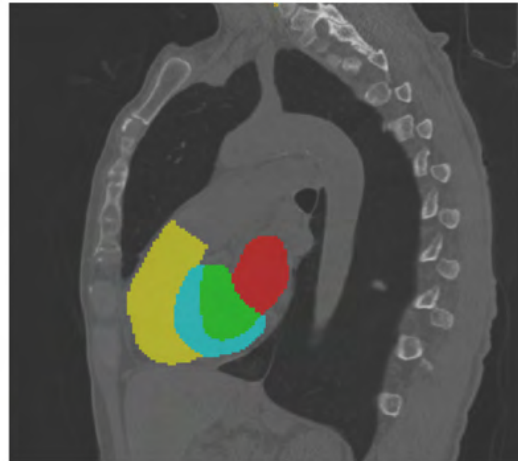
¹. Cornell University, Ithaca, NY, USA, ². HeartLung Technologies, Torrance, CA, USA, ³. The Lundquist Institute, Torrance, CA, USA, ⁴. Mount Sinai Hospital, New York, NY, USA.

Introduction: We have developed an AI-enabled automated volume measurement of cardiac chambers (AutoChamber) that works on ECG-gated coronary artery calcium scans and correlates well with contrast enhanced coronary CT angiography scans. We have recently reported that increased left atrial volume measured by AutoChamber is a strong predictor of new onset atrial fibrillation (Afib) in asymptomatic individuals of Multi-Ethnic Study of Atherosclerosis (MESA). In this study, we compare the volumetry results in ECG-gated CAC scans with those of non-gated full-chest lung cancer screening scans in the same individuals. **Methods:** We have studied 169 cases of paired ECG-gated cardiac CT scans and non-gated lung scans. Mean±SD for age was 62±10 with 52% female. All cases were asymptomatic and were scanned for preventive health assessment. AutoChamber was run on all cases by an independent operator who was not involved in data analysis. P value was calculated using a two-tailed test of significance with $\alpha=0.05$. **Results:** AutoChamber in cardiac scans vs lung scans reported volume (Mean±SD) for left atrium (LA) as 67.2 and 70.1, left ventricle (LV) 102.8 and 105.5 right atrium (RA) 81.9 and 85.7 right ventricle (RV) 140.7 and 134.2 left ventricular wall (LVW) 113.0 and 109.7 respectively (P <0.0001). Correlations between cardiac and lung scans for each cardiac chamber: LA (R = 0.92), LV (R = 0.93), RA (R = 0.91), RV (R = 0.92), and left ventricular wall (LVW) R = 0.95. **Conclusions:** AutoChamber volumetry results are similar in ECG-gated cardiac scans vs non-gated full-chest lung scans. This AI-enabled automated tool is promising as it can provide added value to patients undergoing coronary calcium and lung cancer screening scans flagging enlarged cardiac chambers at risk of Afib and heart failure.

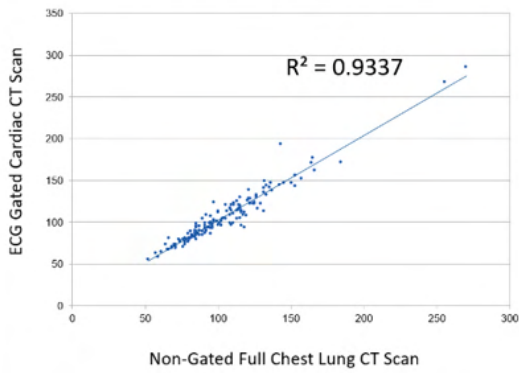
ECG-Gated Cardiac CT Scan



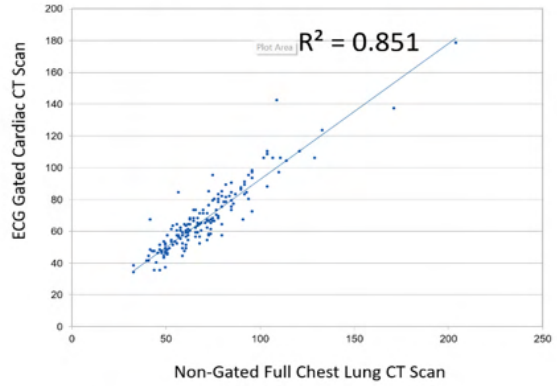
Non-Gated Full-Chest Lung CT scan



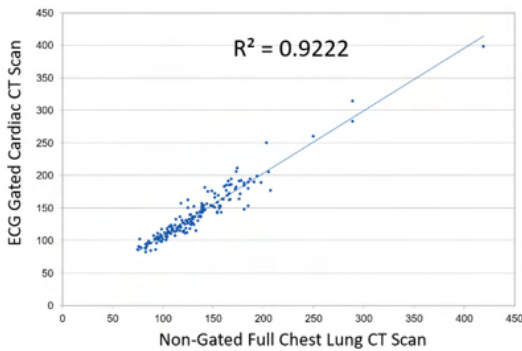
AutoChamber LV Volume



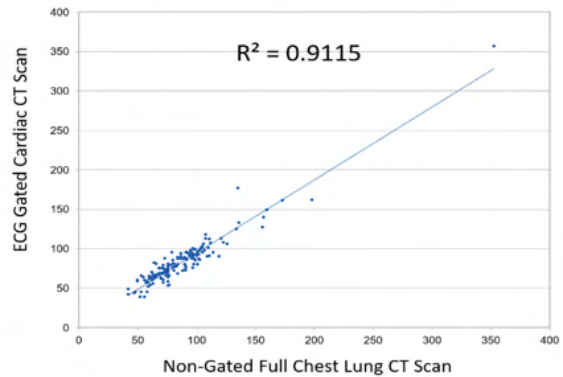
AutoChamber LA Volume



AutoChamber RV Volume



AutoChamber RA Volume



Correlations between Automated Cardiac Chambers Volumetry in Non-contrast ECG-gated Cardiac Scans Vs. Non-contrast Non-gated Lung Scans

Distribution Of Microvascular Endothelial Function In Different Clinical And Non-clinical Settings In The United States And China

Leila Messahli ¹; Yasamin Naghavi ²; Ahmed Gul ²; Maha Gul ²; Ruoyu Zhuang ²; Albert Yen ¹; Hirofumi Tanaka ³; Ralph Metcalfe ²; Stanley Kleis ²; Morteza Naghavi ⁴

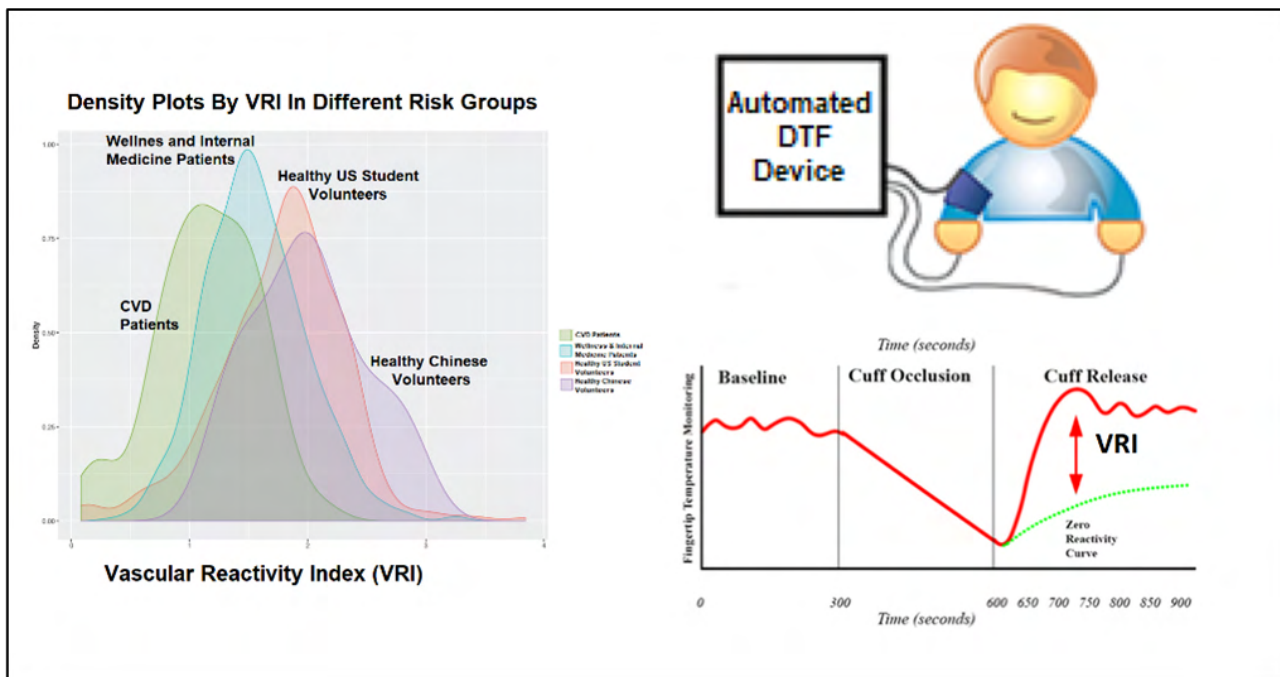
¹: Endothelix, Houston, TX; ²: University of Houston, Houston, TX; ³: University of Texas Austin, Austin, TX; ⁴: American Heart Technologies, Houston, TX;

Background: Despite the fact that microvascular (endothelial) dysfunction is associated with various diseases from cardiovascular to kidney, lung, liver, and other medical conditions, it has not been extensively studied in various clinical and non-clinical settings as blood pressure has. Digital Thermal Flowmetry (DTF) of microvascular endothelial function is a new and automated technique based on monitoring fingertip temperature fall and rebound during reactive hyperemia. Here we report distributions of microvascular function across (1) CVD patients, (2) wellness and internal medicine clinics, (3) college students, and (4) community-based healthy volunteers in China.

Methods: A total of 7,907 endothelial function test results were collected from various settings. Blood pressure and heart rate were measured before the tests. The tests were conducted using FDA-approved automated VENDYS devices (Endothelix Inc., Palo Alto, CA). Adjusted maximum temperature rebound was reported as Vascular Reactivity Index (VRI) and compared across different settings.

Results: VRI in CVD patients, wellness and internal medicine clinics, college students, and Chinese volunteers were (1.25±0.34) (1.53±0.5) (1.86±0.5) (1.95±0.44.) respectively P<0.01. Age was weakly correlated with VRI with the equation age=-0.01 VRI+2.01 (r=0.17 p<0.001)

Conclusions: To our knowledge, this is the largest database of finger-based endothelial function testing. VRI showed distinct distributions across various clinical and non-clinical settings with CVD patients exhibiting the lowest and Chinese healthy volunteers the highest values. The VRI trend mimics the statistically expected risk trend with CVD patients having the highest and Chinese healthy volunteers having the lowest CVD events risk.



On the right a schematic illustration of VENDYS Digital Thermal Monitoring of Endothelial Function is shown. On the left, the density plot of VRI (Vascular Reactivity Index) across different populations from high CVD risk to low CVD risk.

Opportunistic AI-enabled Automated Bone Mineral Density Measurements In Lung Cancer Screening And Coronary Calcium Scoring CT Scans Are Equivalent

Chenyu Zhang,¹ Kyle Atlas,¹ Amirhossein Jaberzadeh,¹ Juan Montoya,¹ Isabel De Oliveira,¹ Venkat Sanjay Manubolu,¹ Marlon Montes,¹ Thomas Atlas,² Song Shou Mao,³ Dong Li,³ Claudia Henschke,⁴ David Yankelevitz,⁴ Anthony P. Reeves,⁵ Matthew Budoff,³ Morteza Naghavi,¹.

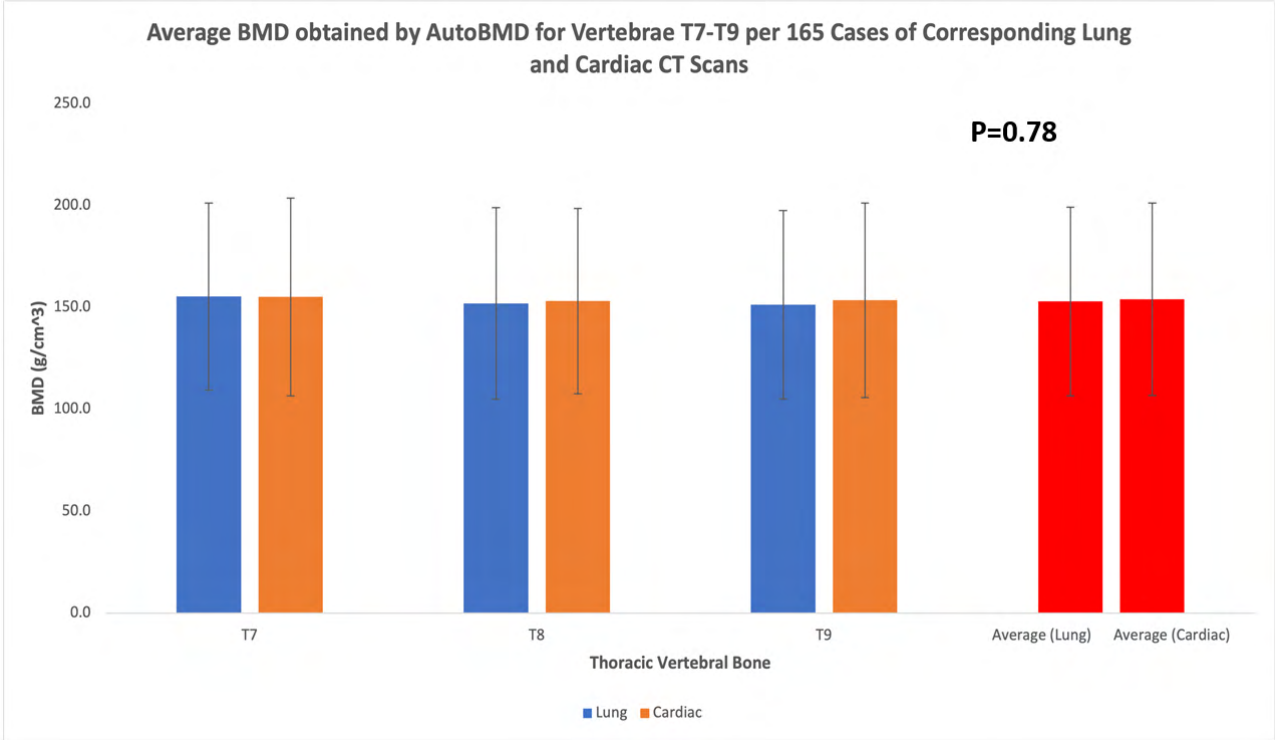
¹ HeartLung Technologies, Torrance, CA, USA, ² Tustin Teleradiology, Tustin, CA, USA, ³The Lundquist Institute, Torrance, CA, USA ⁴ Mount Sinai Hospital, New York, NY, USA, ⁵ Cornell University, Ithaca, NY, USA.

Introduction: We previously reported a novel manual method for measuring bone mineral density (BMD) in coronary artery calcium (CAC) scans and validated our method against Dual X-Ray Absorptiometry (DEXA). Furthermore, we have developed and validated an artificial intelligence (AI) based automated BMD (AutoBMD) measurement as an opportunistic add-on to CAC scans that recently received FDA approval. In this report, we present evidence of equivalency between AutoBMD measurements in cardiac vs lung CT scans.

Methods: AI models were trained using 132 cases with 7649 (3mm) slices for CAC, and 37 cases with 21918 (0.5mm) slices for lung scans. To validate AutoBMD across both cardiac and lung scans against manual measurements, we used only one reference set comprising 991 cases of BMD measured manually on CAC scans from the Harbor UCLA Lundquist Institute. We then used 165 additional cases who underwent both cardiac and lung scans on the same day.

Results: Mean±SD for age was 69 ± 9.4 years with 52.4% male. AutoBMD in lung and cardiac scans, and manual BMD in cardiac scans were 153.7 ± 43.9 , 155.1 ± 44.4 , and 163.6 ± 45.3 g/cm³, respectively (p=0.09). Bland-Altman agreement analysis between AutoBMD lung and cardiac scans resulted in 1.37 g/cm³ mean differences. Pearson correlation coefficient between lung and cardiac AutoBMD was $R^2 = 0.95$ (p <0.0001).

Conclusion: Opportunistic BMD measurements using AutoBMD in CAC and lung cancer screening scans is promising and yields similar results. No extra radiation plus the high prevalence of asymptomatic osteoporosis makes AutoBMD an ideal screening tool for osteopenia and osteoporosis in CT scans done for other reasons.



Average BMD in T7-T9 in 165 corresponding heart and chest CT scans by AutoBMD.

AI-enabled Cardiac Chambers Volumetry in Non-Contrast Cardiac CT scans Detects HFrEF vs. HFpEF

Emily Jaalouk¹, Sanjay Manubolu¹, Song Shou Mao¹, Kyle Atlas², Chenyu Zhang², Anthony Reeves³, Matthew Budoff¹, Morteza Naghavi¹.

¹. The Lundquist Institute, Torrance, CA ². HeartLung.AI, Houston, TX ³. Cornell University, Ithaca, NY

Introduction: We have developed an AI-enabled automated volumetry of cardiac chambers (AutoChamber) that works both on non-contrast and contrast-enhanced cardiac CT scans used for coronary artery calcium (CAC) score and coronary CT angiography (CCTA), as well as lung cancer screening CT scans. We have previously reported the agreement between AutoChamber measurements in CAC vs. CCTA, CAC vs lung scans, and cardiac MRI measurements. Here we report echocardiography-based ejection fraction (EF) data showing the ability of AutoChamber in distinguishing heart failure with reduced ejection fraction (HFrEF) versus heart failure with preserved ejection fraction (HFpEF).

Methods: Data from 75 patients who underwent both cardiac CT scan and echocardiography at Harbor UCLA medical center were obtained. AutoChamber was applied to all cases and reported estimated volume for left atrium (LA), left ventricle (LV), right atrium (RA), and right ventricle (RV). Body surface area (BSA) was calculated to create LV volume index (LVVI) by dividing LV volume by BSA. This allows for a more accurate assessment of the size of the left ventricle relative to the size of the individual. BSA for male and female were 1.59 ± 0.3 and 1.29 ± 0.2 . To create echocardiography LV volume (E-LVVI) and AutoChamber LV volume (A-LVVI). HFrEF and HFpEF were defined as $EF < 40\%$ and $EF > 50\%$ respectively.

Results: Average EF was 57.5 ± 7.0 in males and in females 59.7 ± 8.1 respectively. AutoChamber volume for HFpEF vs HFrEF were LA ($84.8+35.3$ vs $113.2+32.8$ $p=0.002$), LV ($109.9+36.7$ vs $170.7+65.9$ $p=0.0007$), RA ($97.5+58.3$ vs $117.2+51.1$ $p=0.18$), RV ($135.6+52.1$ vs $176.2+70.8$ $p=0.008$), LVW ($116.1+39.1$ vs $170.6+56.9$ $p=0.0005$). Density plots below show a clear distinction between HFpEF and HFrEF and comparable results.

Conclusion: AI-enabled automated cardiac chambers volumetry can correlate well with echocardiography based LVVI and detects HFrEF vs HFpEF. Further studies are needed to evaluate the ability of AutoChamber for prospective detection of patients at risk of HFrEF vs HFpEF.

Hybrid 18F-FDG PET/MRI Predicts Adverse Clinical Outcomes in Cardiac Sarcoidosis

Philip M. Robson¹, Maria Giovanna Trivier^{1,2}, Vittoria Vergani³, Gina LaRocca², Angelica M. Romero-Daza^{4,4}, Ronan Abgral⁵, Ana Devesa¹, Levi-Dan Azoulay⁶, Nicolas A. Karakatsanis⁷, Aditya Parikh², Christia Panagiota², Anna Palmisano⁸, Louis DePalo⁹, Helena L. Chang¹⁰, Joseph H. Rothstein¹⁰, Rima A Fayad¹, Marc A. Miller², Valentin Fuster², Jagat Narula², Marc R. Dweck¹¹, Adam Morgenthau⁹, Adam Jacobi¹², Maria Padilla⁹, Jason C. Kovacic¹³, Zahi Fayad¹

¹ BioMedical Engineering and Imaging Institute, Icahn School of Medicine at Mount Sinai, New York, NY ² Department of Medicine (Cardiology), Icahn School of Medicine at Mount Sinai, New York, NY ³ School of Biomedical Engineering and Imaging Sciences, King's College London, London, UK ⁴ Department of Cardiology, Hospital La Luz - Quirón Salud, Madrid, Spain ⁵ Department of Nuclear Medicine, University Hospital of Brest, European University of Brittany, EA3878 GETBO, Brest, France ⁶ Sorbonne Université, INSERM, CNRS, Laboratoire d'Imagerie Biomédicale (LIB), Paris, France ⁷ Division of Radiopharmaceutical Sciences, Department of Radiology, Weill Cornell Medical College, New York, NY ⁸ Experimental Imaging Center, Department of Radiology, IRCCS San Raffaele Scientific Institute, Milan, Italy ⁹ Division of Pulmonary, Critical Care and Sleep Medicine, Icahn School of Medicine at Mount Sinai, New York, NY ¹⁰ International Center for Health Outcomes and Innovation Research, Department of Population Health Science and Policy, Icahn School of Medicine at Mount Sinai, New York, NY ¹¹ British Heart Foundation Centre for Cardiovascular Science, University of Edinburgh, Edinburgh, UK ¹² Department of Radiology, Icahn School of Medicine at Mount Sinai, New York, NY ¹³ Victor Chang Cardiac Research Institute, Darlinghurst, Australia and; St Vincent's Clinical School, University of NSW, Australia

Introduction: Both 18F-FDG PET and cardiac MR are utilized in the assessment of cardiac sarcoidosis and have shown value in prognostication. They provide complementary evidence of active inflammation and current injury (fibrosis), respectively. In this study we sought to evaluate the benefit of combining the assessment of active inflammation via 18F-FDG PET and cardiac fibrosis via late gadolinium enhancement MRI for the prediction of clinical adverse events in cardiac sarcoidosis.

Methods: Patients with suspicion of cardiac sarcoidosis were enrolled to undergo hybrid 18F-FDG PET/MRI imaging. Cardiac MRI included late gadolinium enhanced (LGE) imaging. Images were assessed semi-quantitatively and assigned to be MR(+) if LGE was observed, and PET(+) if FDG uptake was observed. Further evaluation assigned image-based positivity if %LGE was >5.7% (MR(+)>5.7%) and if FDG uptake was focal (PET(+))FOCAL). Patients were grouped into categories based on combined MR and PET image-based findings. The occurrence of clinical events was assessed by review of the Electronic Medical Record at the end of the study. The primary clinical endpoint was occurrence of any of: cardiac arrest, ventricular tachycardia (VT), or implantation of a cardioverter defibrillator (ICD) for secondary prevention. The secondary endpoint also included heart failure (HF) or heart block. The association between clinical endpoints and hybrid imaging classifications was compared with odds ratios and multivariable logistic regression.

Results: 148 patients were enrolled, with final chart review after a median follow up of 5.5 years. Eighteen/28 patients met the primary/secondary clinical endpoints. Positivity on both modalities based on hybrid PET/MRI imaging results showed the strongest association with the primary clinical endpoint. MR>5.7%(+)PET(+))FOCAL compared to all other categories showed an unadjusted odds ratio (OR) for meeting the primary endpoint of 9.2; 95% CI 3.0-28.7; p=0.0001, which remained significant after adjusting for age, sex, weight, left ventricular ejection fraction, prior corticosteroid or immune suppressant therapy (OR 9.3, 95% CI 2.0-44.0, p=0.005) - see Figure 1. Hybrid assessment was more predictive of outcome compared to either modality alone: For MR(+)>5.7% vs. MR(-)>5.7% (unadjusted [adjusted] OR 3.6 [2.9], 95% CI 1.3-10.0 [0.6-13.5], p 0.02 [0.2]), and for PET(+))FOCAL vs. PET(-) (unadjusted [adjusted] OR 5.8 [5.2], 95% CI 1.5-21.9 [1.2-22.6], p 0.01 [0.03]).

Conclusions: Utilizing both 18F-FDG PET and cardiac MRI provides an image-based assessment that is more strongly associated with adverse clinical outcomes and should be considered preferentially over either modality alone in the assessment and management of cardiac sarcoidosis.

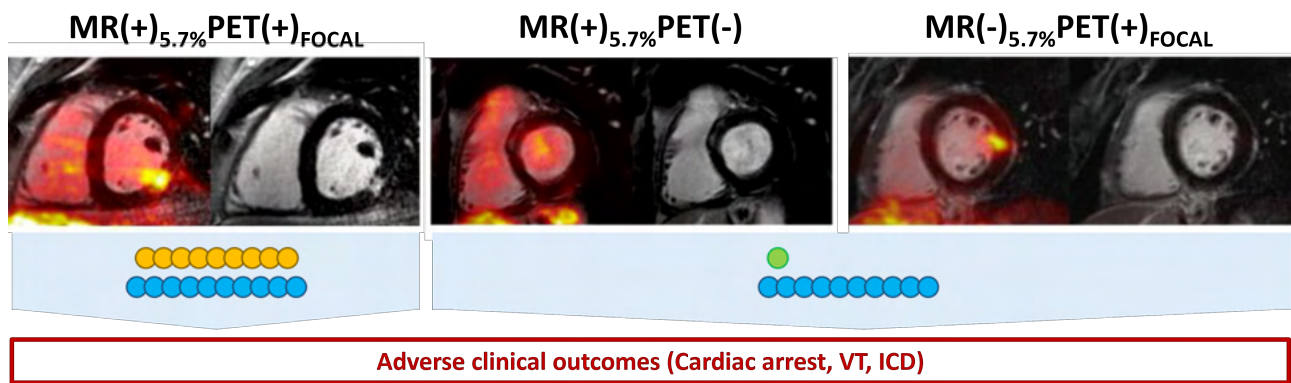


Figure 1: Fused 18F-FDG PET/MRI images showing categories with FDG uptake (PET(+)) and late gadolinium enhancement (MR(+)). Positivity on both modalities conferred more than 9-fold higher odds of progressing to adverse clinical outcome.

PET/MRI imaging of mitral valve prolapse

Maria Giovanna Trivieri MD PhD^{1,2,3}, Marc A. Miller MDd, Philip M. Robson PhDa,c, Dimosthenis Pandis, MDe, Ana Claudia Costa, MDe, Busra Cangut, MDc, Renata Pyzik, MSa, Rachel Pake, Aileen Leonardo, RNa, Ana Devesa, MDa, Dario Colliia, PhD, Stamatios Lerakis, MDb, Wenli Zhaob, Steve Liao, MDb, Vivek Reddy, MDd, Seunghee Kim-Schulze, PhDf, Samantha Sartori, PhDb, David Adams, MDe, Zahi A. Fayad, PhDa,b,c

¹BioMedical Engineering and Imaging Institute, ²Cardiovascular Institute, ³Diagnostic, Molecular and Interventional Radiology, dHelmshley Electrophysiology Center, eCardiovascular Surgery, fImmunology and Immunotherapy, Icahn School of Medicine at Mount Sinai, New York, NY

Mitral valve prolapse (MVP), identified in 1-3% of the general population, is the most common cardiac valvular abnormality, with complications that include heart failure, ventricular arrhythmias and sudden cardiac death (SCD). While there have been multiple features identified as markers of increased risk, left ventricular replacement fibrosis appears to be a consistent finding in Arrhythmic MVP. Late gadolinium enhancement (LGE) by cardiac magnetic resonance imaging (MRI) is considered the most sensitive and specific modality for assessing the presence and distribution of replacement fibrosis and it has been strongly associated with increased incidence of arrhythmic events in patients with MVP. Using 18F-fluorodeoxyglucose (FDG) uptake on hybrid Positron Emission Tomography (PET)/MRI to detect myocardial inflammation, preliminary investigations from our group suggest that these fibrotic changes may be preceded by a chronic inflammatory phase and that inflammation and scarring may be part of a continuum of ventricular transformation and directly associated with arrhythmia development and complexity. In this presentation we discuss the rationale and design of a new study that will characterize the relationship between intensity and pattern of 18F-fluorodeoxyglucose (FDG) uptake on hybrid PET/MRI, arrhythmia burden, severity of MVP, and mitral regurgitation (MR). The study will establish the inflammatory origin of the 18F-FDG signature, by validating 18F-FDG signals against 68Ga-DOTATATE, a more specific marker for inflammation, and against histology of myocardial biopsy tissue. The study will also relate the 18F-FDG and arrhythmic signature with long term development of arrhythmia in a longitudinal study. This study may lead to more accurate imaging guided patient management and have the potential to significantly influence current guideline recommendations for risk stratification assessment, medical therapy, and timing for surgical intervention in patients with MVP at risk of malignant arrhythmia and SCD.

NIH/NHLBI R01 HL166720. Principal Investigators: Maria Trivieri, MD, PhD, Marc Miller, MD, David Adams, MD, Zahi Fayad, PhD

Multimodal Profiling Of Stress-induced Immune Reprogramming in Cardiovascular Participants

David O'Connor¹, Renata Pyzik¹, Philip M. Robson¹, Mandy van Leent¹, Maria Giovanna Trivieri¹, James Murrrough¹, Lisa Shin², Audrey Kaufmann¹, Heli Patel¹, Johnny Ng¹, Aislinn Diaz¹, Erin Hanlon³, Ahmed Tawakol³, Zahi Fayad¹.

¹Icahn School of Medicine at Mount Sinai,

²Tufts University,

³Massachusetts General Hospital

Chronic psychosocial stress is a pervasive component of the human experience, carrying an attributable cardiovascular disease (CVD) risk that is on par with smoking or cardiometabolic disease (CMD). While a “heart-brain connection” has long been postulated, the mechanisms underlying stress’s deleterious effects on the cardiovascular system are largely under-investigated. Previous studies using combined positron emission tomography and magnetic resonance imaging (PET/MRI) have demonstrated links between severe, acute psychosocial stress and altered neural, immune, and cardiovascular functions in post-traumatic stress disorder (PTSD) patients with low CVD risk. These landmark findings uncovered a stress-associated neuro-immune-cardiovascular axis, which has now been validated by several other groups and proven to be a pervasive promoter of cardiovascular diseases. Our previous work also observed strong links between stress-associated neural activity (SNA) and several CMD components and showed that genetics and lifestyle factors can modulate the relationship between stress and CVD. However, critical knowledge gaps remain. In this presentation, we discuss the rationale and design of a new study aiming to provide a better understanding of how stress-induced disruptions in neural networks lead to immune system dysregulation, CMD and atherosclerosis. The study also aims to investigate the mechanisms by which genetic and lifestyle factors impact the neuro-immune-cardiovascular axis. This study also aims to investigate these processes in individuals at higher risk for cardiovascular disease, the same population that would stand to gain the most from insights on how best to modulate this system to improve cardiovascular health.

NIH/NHLBI PO1 HL131478. Principal Investigator: Zahi Fayad, PhD

Aptamers as Recognition Probes for Detection of Interleukin-6 with Fluorescent Single-Walled Carbon Nanotubes

Amelia K. Ryan¹, Ryan M. Williams¹

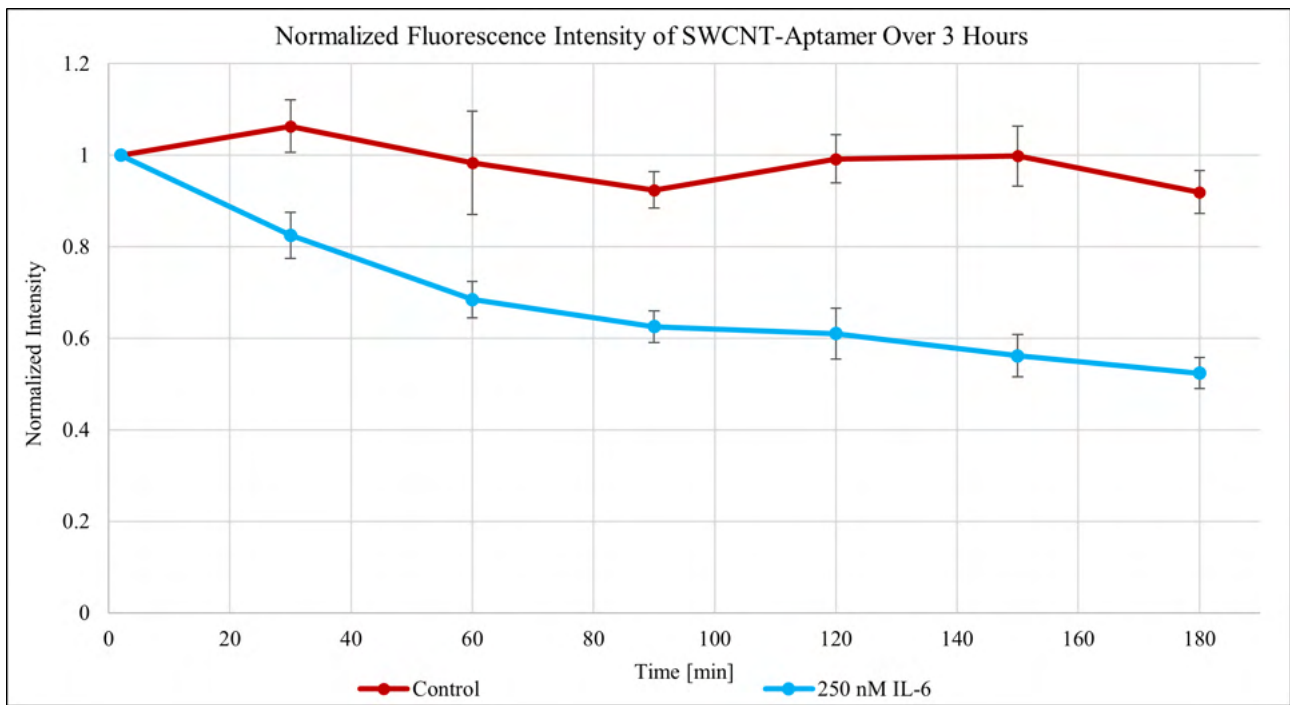
¹The City College of New York

Introduction: Interleukin-6 (IL-6) plays a critical role in the pathogenesis and progression of neurodegenerative diseases, autoimmune diseases, cancer, and other inflammatory conditions. As a diagnostic biomarker, efficient and accessible detection of IL-6 is of clinical interest. Single-walled carbon nanotubes (SWCNT) are versatile fluorescent materials that can be functionalized to detect a variety of targets. In rational nanosensor design, recognition probes with known affinity for the intended target - such as antibodies or DNA aptamers - are utilized. Aptamers may hold advantages over antibodies due to their small size, flexible structures, and low cost. Our objective is to develop an aptamer-based SWCNT sensor to rapidly detect IL-6 with high sensitivity and specificity.

Materials and Methods: Five DNA sequences were tested in this work. SWCNT-DNA suspensions were prepared via sonication and subsequent ultracentrifugation. The resulting nanosensor suspensions were characterized with a UV-visible absorption spectrophotometer. Varying concentrations of IL-6 protein from 0.1 to 400 nM were added to nanosensors in vitro. Fluorescence spectra were acquired with a NIR spectrophotometer following the addition of IL-6. Spectra were analyzed with custom MATLAB code and two-tailed t-test.

Results: Of the DNA sequences tested, a 31-nt aptamer showed the greatest response to IL-6 protein - 55% quenching of SWCNT fluorescence (Fig. 1). This DNA sequence was chosen as the main candidate for further testing. The resulting nanosensor demonstrated detection of IL-6 at concentrations as low as 10 nM. With increasing concentration of IL-6, the nanosensor showed a more dramatic reduction in fluorescence intensity, with 40% quenching in response to 400 nM of IL-6. Nanosensors showed a decrease in fluorescence intensity within seconds of IL-6 addition, indicating a near-immediate response.

Conclusions: In this work, we have developed an easily assembled novel nanosensor for rapid detection of IL-6 based on SWCNT and an analyte-specific aptamer. After screening multiple SWCNT-DNA constructs, we identified the sequence that provided the highest sensitivity to IL-6. Aptamer-functionalized SWCNT showed sensitivity and specificity for IL-6 in vitro. Fluorescence modulation of SWCNT was dependent on IL-6 concentration, with a limit of detection at 10 nM. Future work with this nanosensor may include deployment in cell culture models or in vivo. Rapid, inexpensive, noninvasive detection of IL-6 as an inflammatory disease biomarker holds promise for early diagnosis, observation of disease progression, and evaluation of response to therapy.



Fluorescence modulation of SWCNT-Aptamer in response to IL-6

Ex Vivo MRI and Neuropathology for Investigation of Traumatic Brain Injury

Alan C Seifert¹, Rebecca Folkerth², Bradley N Delman³, Emma Thorn⁴, Holly Carrington², Ariel Pruyser², John Crary⁴, Kristen Dams-O'Connor²

¹Biomedical Engineering and Imaging Institute, Department of Radiology, Graduate School of Biomedical Sciences, Icahn School of Medicine at Mount Sinai

²Brain Injury Research Center, Department of Rehabilitation and Human Performance, Icahn School of Medicine at Mount Sinai

³Department of Radiology, Biomedical Engineering and Imaging Institute, Icahn School of Medicine at Mount Sinai

⁴Neuropathology Brain Bank and Research Core, Icahn School of Medicine at Mount Sinai

Introduction: MRI and histology are complementary components of a multimodal autopsy. The major benefit of including a strong MRI component in post-mortem investigation of human brain tissue is that ex vivo MRI can serve as a bridge between the detailed mechanistic information available by neuropathology and imaging-based biomarkers that can be implemented in vivo in future work. In this work, we present an example case drawn from an ongoing radiology-pathology correlation study of the late effects of traumatic brain injury.

Methods: A whole brain specimen was extracted from a donor with a history of traumatic brain injury. The specimen was fixed by immersion in formalin for >1 month, degassed, then packaged into a custom-built imaging vessel. The specimen was immobilized and the container was filled with a 1H-free susceptibility-matching fluid (Fluorinert) and sealed. The specimen was scanned at 3 Tesla (Skyra, Siemens) using a 20-channel head/neck coil. The protocol included FLAIR (0.63mm isotropic, TR/TI/TE=4800/1650/291ms, 2.3hr), susceptibility-weighted imaging (0.63mm isotropic, TR/TE1/TE2=29.00/20.00/24.88ms, 55min), and multi-echo GRE (ME-GRE) (0.39mm isotropic, TR/TE1/TE2/TE3/TE4=28.0/2.95/ 8.80/14.60/20.40ms, FA= 45°/25°/10°, 2hr each). ME-GRE images were combined by root-sum-of-squares, and T1, T2*, and apparent proton density (S0) maps were fitted. MR images were read by a neuroradiologist and findings of suspected pathology were marked. Suspected pathology was sectioned at brain cutting, and stained slides were produced. MR images and slides were interpreted at a consensus conference.

Results: Findings in this case included: (1) a focal hypointensity on anatomical and susceptibility-weighted imaging in the superior frontal gyrus associated with a punctate rust-colored lesion on gross examination, and clumps of brown iron breakdown pigment accompanied by vacuolization, neuronal loss, and gliosis on microscopy. This finding, illustrated in Figure 1, is consistent with an old contusion. Other findings included (2) diffuse white matter hyperintensity with sparing of U-fibers on anatomical MRI, associated with pallor and atrophy on gross examination and Luxol fast blue-stained histology; (3) Atrophy, myelin loss, and glial scar in the splenium of the corpus callosum; (4) a lacune in the genu of the right internal capsule; and (5) hippocampal sclerosis.

Discussion: The combination of ex vivo MRI and neuropathology by a multi-disciplinary team is more powerful than the results produced by the two approaches in isolation. Image-guided sectioning improves the sensitivity of neuropathology by identifying lesions for sectioning that would likely be missed otherwise, and the detailed mechanistic information provided by neuropathology enhances the interpretation of imaging findings.

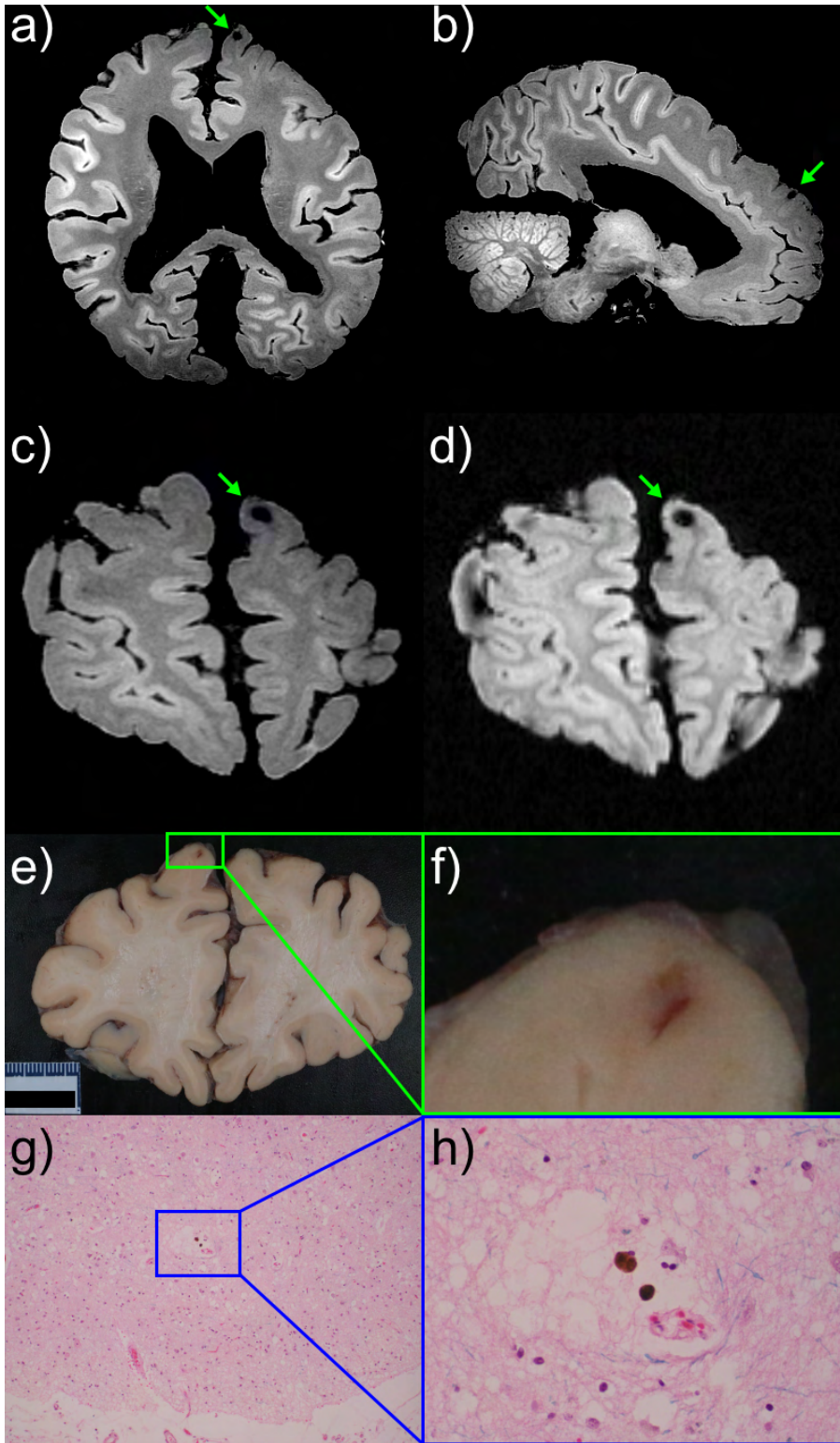


Figure 1: Three-plane ME-GRE (a-c) and coronal SWI (d), gross photography (e,f), and H&E histology (g,h) of an old contusion.

White Matter Integrity Predicts Recovery Response Time of Deep Brain Stimulation for Depression

Ha Neul Song¹, Helen S. Mayberg¹, Ki Sueng Choi¹

¹Nash Family Center for Advanced Circuit Therapeutics, Icahn School of Medicine at Mount Sinai, New York, NY 10019.

Deep brain stimulation (DBS) targeting the subcallosal cingulate cortex (SCC) has proven effective for treatment-resistant depression (TRD), across a set of consecutive cohorts. SCC is structurally connected with other brain regions via white matter (WM) bundles, and stimulation of all connections is crucial for DBS clinical outcomes. Despite consistent SCC targeting, which aims to maximize the activation of critical WM bundles, variability persists in the recovery response time across patients, potentially linked to baseline variations in brain abnormalities. This study explores the status of WM integrity (approximated using diffusion MRI) and their longitudinal changes in the critical WM activation pathways. We assessed the time to reach a stable response (TSR, more than 50% improvement of HDRS17 in two consecutive weeks) in 33 TRD patients receiving SCC-DBS. Preoperative and longitudinal MRI data were acquired on a 3T scanner with 2 mm isotropic resolution and 60 directions, including five b0 and two opposite phase encoding directions for distortion correction. The study examined the relationship between TSR and baseline fractional anisotropy (FA) of targeted WM bundles (cingulum bundle, forceps minor, subcortical junction, and uncinata fasciculus). Pearson correlation between TSR and FA along each WM bundle's trajectory was conducted, selecting the area with the maximum r value. Selected FA values in WM bundles served as features for linear regression predicting TSR. In the same areas, longitudinal FA changes at 1, 3, and 6 months post-operation were analyzed to compare fast and slow responders. Our findings reveal a significant negative correlation between TSR and FA in bilateral midcingulate cortex, bilateral forceps minor, and left uncinata fasciculus adjacent to left hippocampus and left insula. A linear model of FA successfully predicted TSR, with the left midcingulate cortex emerging as the strongest predictor among critical WM bundles. Moreover, post-hoc analysis found that the magnitude of FA increases in these regions over 6 months was associated with a faster response. Slow response was associated with FA values in cingulum bundles and forceps minor that did not change or decreased over the same period. These findings suggest that WM abnormalities in critical WM bundles undergo repair with chronic SCC-DBS suggesting that DBS may facilitate neuroplasticity changes in selective activated WM pathways. This study sheds light on both sources of individual variability in SCC-DBS response time, as well as a potential mechanism mediating DBS antidepressant response.

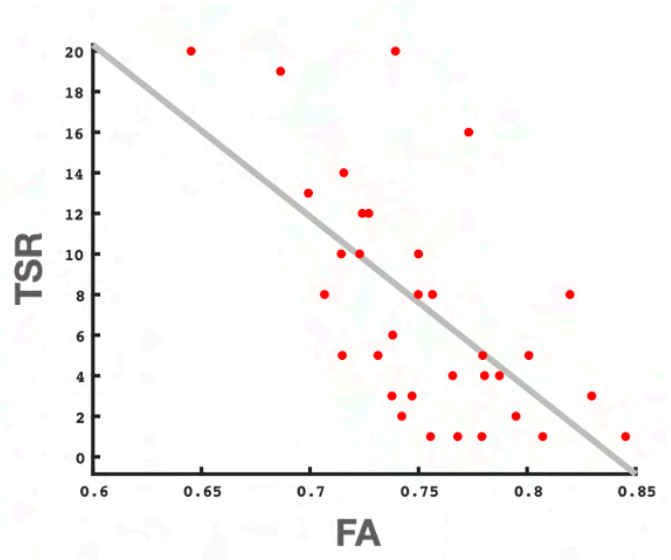
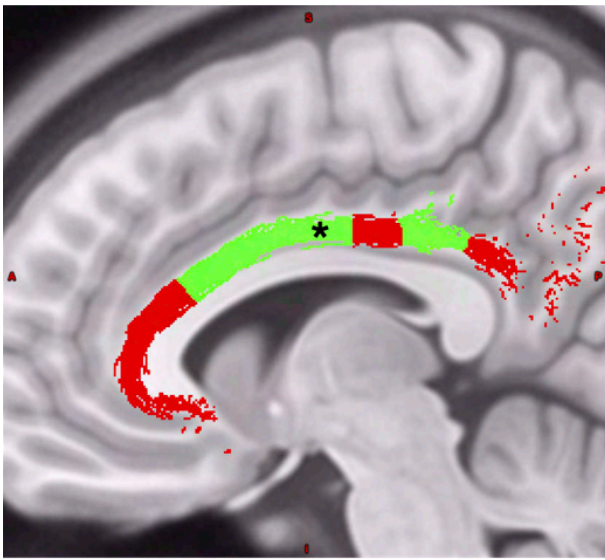


Figure 1. The relationship between TSR and FA in the left cingulum bundle (red in left). Green regions indicate significant correlation between them (the highest r value on a black asterisk). Right scatter plots show individual values of TSR and FA ($r = -0.64$, $p < 0.001$).

Exploring ENTPD3 as a target for beta cell mass imaging by PET

Trea St. Hillaire^{1,2}, Anna Ranzenigo^{1,2}, Sheqouia Nauta^{1,2}, Martin Umali^{1,2}, Abraham Teunissen^{1,2}, Don Scott³, James A. Duty⁴, Andrew Stewart⁵, Mandy van Leent^{1,2}

¹BioMedical Engineering and Imaging Institute, Icahn School of Medicine at Mount Sinai

²Cardiovascular Research Institute, Icahn School of Medicine at Mount Sinai

³Department of Diagnostic, Molecular and Interventional Radiology, Icahn School of Medicine at Mount Sinai, New York, NY, USA.

⁴Center for Therapeutic Antibody Development, Icahn School of Medicine at Mount Sinai ⁵Diabetes, Obesity and Metabolism Institute, Icahn School of Medicine at Mount Sinai

Introduction: Beta cells play a critical role in the pathogenesis of type 1 and type 2 diabetes, marked by beta cell's loss and impairment. Imaging approaches capable of distinguishing between beta cell loss and functionality, is important to understanding diabetes pathophysiology and gauging beta cell mass. Unfortunately, there are no tools available to evaluate beta cell mass in vivo without a highly specific beta marker. Currently, research delves into imaging tools using target biomolecules to effectively assess beta cell mass, with particular emphasis on the promising target, ENTPD3. Previous studies have validated the high specificity of ENTPD3 for beta cells. Here, we aimed to evaluate ENTPD3 as a target for in vivo PET imaging of beta cell mass.

Methods: We radiolabeled ENTPD3 Mab5E10 by conjugating it with chelator Desferrioxamine B (DFO) and incubating this with ⁸⁹Zr. Female Rag-/- mice underwent transplant surgery, wherein a thousand human islets from five distinct donors were transplanted under the capsule of their left kidney (Panel A). Within four to eight weeks post-surgery, these mice received tail vein injections, 150 μ Ci, of 5E10 ENTPD3 antibodies or 2B3 isotype control. Subsequently, the mice underwent PET/CT imaging 72 hours post-injection, then were sacrificed to facilitate gamma counting of organs to detect radioactivity. Furthermore, autoradiography was conducted on the kidneys.

Results: Our product exhibited high radiochemical purity, demonstrated by radioactive thin layer chromatography (TLC), which revealed no unbound ⁸⁹Zr, achieving a radiochemical yield of 73% (Panel B). Gamma counting results indicated significant accumulation of the antibody in the spleen and liver (Panel C). At the 72-hour mark there was a large amount of antibody in the circulation, which is expected of antibodies. There was greater accumulation in the left kidney, the site of islet transplant, compared to the right kidney (Panel D). After removing the graft, a comparison between the left kidney and the graft reveals a higher accumulation of the radiotracer in the graft, suggesting binding to the beta cells (Panel E). Additionally, autoradiography revealed radioactivity accumulation on the transplant site, which was not observed on the isotype control, indicating specific binding of the antibody to the islet graft (Panel F).

Conclusion: We have shown human islet grafts can be detected with ENTPD3 in vivo. The development of a radiotracer with properties suited for in vivo imaging (for example, faster clearance from circulation) are next steps in developing imaging methods to measure beta cell mass in humans.

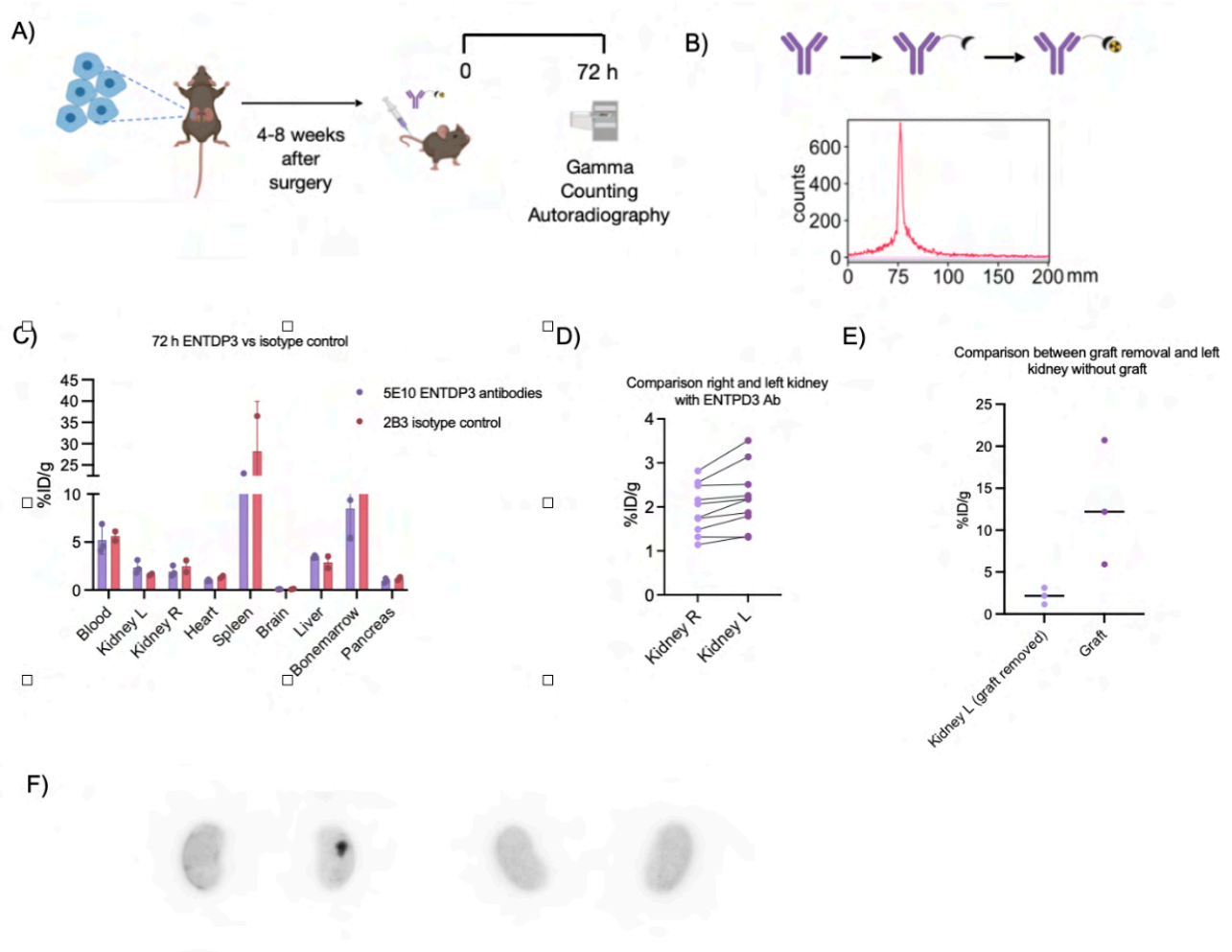


Figure 1. (A) Schematic outline of experiment. Human islets were transplanted under the capsule of the mice left kidney, followed by intravenous administration of the ^{89}Zr -labeled ENTPD3 radiotracer prior to conducting gamma counting and autoradiography. (B) Radio TLC of complete binding to ^{89}Zr . (C) Gamma counting of tissues with ^{89}Zr -labeled ENTPD3 at 72 hours post administration. (D) Gamma counting of the right and left mice kidney after ^{89}Zr -labeled ENTPD3 injection at 72 hours post administration. (E) Comparison of %ID/g of kidney once human islets graft were removed versus %ID/g of human islets graft alone. (F) Autoradiography of Rag^{-/-} mice right and left kidney with human islets located under the capsule of the left kidney ENTPD3 (left) and isotype (right).

Characterizing daily physical activity patterns in endometriosis with unsupervised learning via functional mixture models

Bryan Tricoche¹, Ipek Ensari, PhD¹

¹Icahn School of Medicine at Mount Sinai, Icahn School of Medicine at Mount Sinai

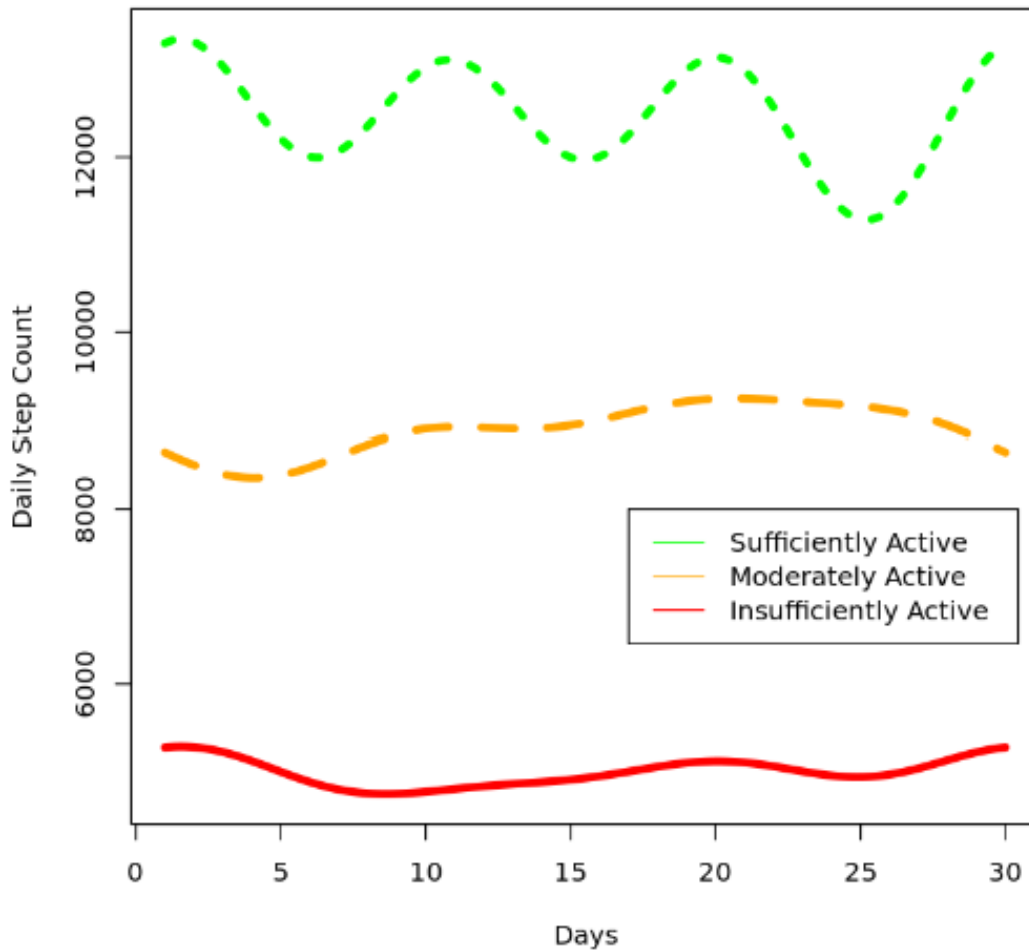
Introduction: Regular physical activity (PA) is associated with many health benefits and lower risk of non-communicable diseases. For chronic diseases associated with reduced PA due to physical impairment, characterization of the temporal and between-individual variations in PA is particularly valuable for identifying individuals at risk and designing interventions. One such condition is endometriosis, an inflammatory disease characterized by uterine tissue adhesions resulting in chronic pelvic pain that severely impairs quality of life. We herein investigate latent profiles (i.e., clusters) of daily PA trajectories among individuals with endometriosis via functional mixture models (FMMs). In contrast to aggregating multiple data points per person, FMMs use entire data curves as the unit of analysis, thus allowing consideration of the temporal trends in the PA data. This approach can yield potentially important information that can inform meaningful differences among clusters.

Methods: The sample included 149 adults with an endometriosis diagnosis enrolled into the NIH All of Us Research Program and provided step count data from FitBit wrist-worn trackers. For analysis of habitual PA patterns, we included 30 consecutive days of data from each individual, allowing up to 5 days of missingness, yielding 4,378 total days for analysis. Each participant's data were smoothed using a Fourier-transform to create the functional data matrix and fit the FMMs. The optimal number of clusters was determined using the Bayesian information criterion (BIC).

Results: The best-fitting model identified 3 clusters (K) based on the 30-day PA distribution (BIC = -10253.86). PA trajectories for the clusters are provided in Figure 1. Cluster 1 was characterized by a steady curve with the least variability over the 30-day period and a mean of 4,972 daily steps (SD=2540.4), indicating overall physical inactivity. Cluster 2 was characterized by larger variations across the days and 8,857 average daily steps (SD=3602.4), indicating moderate activity levels. Cluster 3 was associated with the highest variability in both PA patterns and daily step counts (Mean=12,595; SD=5338.3).

Discussion: This study provides the first accelerometry-based analysis of habitual PA trajectories among individuals with endometriosis. We report distinct profiles that further fit the categories of insufficiently active, moderately active, and sufficiently active based on the PA guidelines. These findings suggest that this heterogeneous patient population can benefit from improving PA in a personalized approach that considers the individual and environmental factors for delivering the ideal intervention at the right time.

Average Smoothed Curves of Daily Steps Data by Cluster



PA trajectories for the 3 model-estimated clusters. Each line represents the cluster-level average of the Fourier-transformed smooths for the person-level days of steps data (N1=68, N2=15, N3=66). Cluster 1 (red) demonstrates insufficient PA levels, Cluster 2 (orange) demonstrates moderate PA levels, and Cluster 3 (green) demonstrates adequate PA levels based on PA guidelines for adults.

Patient-specific tissue engineering model of an inherited cardiomyopathy: an in vitro platform for personalized medicine.

Katherine Jankowski¹, Serena Chang¹, Francesca Stillitano², Kevin D. Costa¹, Irene C. Turnbull¹.

¹Cardiovascular Research Institute, Icahn School of Medicine at Mount Sinai, New York, NY, USA.

²Department of Cardiology, University Medical Center Utrecht, Utrecht, The Netherlands.

Introduction: Heterozygous deletion of arginine 14 (R14del) is a mutation of the phospholamban gene (PLN) associated with dilated and arrhythmogenic cardiomyopathy. With no available cure, the development of representative disease models is critical for mechanistic and therapeutic studies. Objective: To demonstrate the application of patient-derived human engineered cardiac tissue (hECT) as a disease model of PLN-R14del cardiomyopathy.

Methods: We employed human induced pluripotent stem cells (iPSCs) from (a) patients with clinical cardiomyopathy who are PLN-R14del carriers, and from (b) healthy family members without the mutation (non-carriers). We used cardiomyocytes derived from each of these iPSC lines to fabricate patient-specific carrier hECTs, and healthy non-carrier hECTs. For tissue fabrication, one million iPSC-derived cardiomyocytes were combined with a Collagen/Matrigel mixture and dispensed into a custom mold with integrated force sensor end-posts, where they were maintained in culture at 37 °C and 5% CO₂ (Figure 1a). To evaluate hECT contractile function, real-time optical tracking of post deflection was used to calculate twitch force with and without electrical field stimulation (Figure 1b).

Results: Under spontaneous beating conditions, carrier hECTs displayed significantly higher beat rate variability and lower contractile force, with slower maximum rates of contraction and relaxation, compared to non-carrier hECTs (Figure 1c). During 1-Hz electrical pacing, this pattern remained, where carrier hECTs displayed decreased contractility compared to non-carrier hECTs, including a trend towards longer relaxation time in carrier hECTs. Findings were confirmed using hECTs created with iPSC lines from two different families, under pacing frequencies from 0.5 to 3.0 Hz, and analysis time points from 1 to 4 weeks.

Conclusion: The hECTs from carrier cell lines recapitulated abnormal cardiac contractile function characteristic of PLN-R14del patients. These hECT models are being used to study disease mechanisms of PLN-R14del cardiomyopathy; they also hold potential in personalized medicine to test candidate therapeutic interventions in patient-specific hECTs.

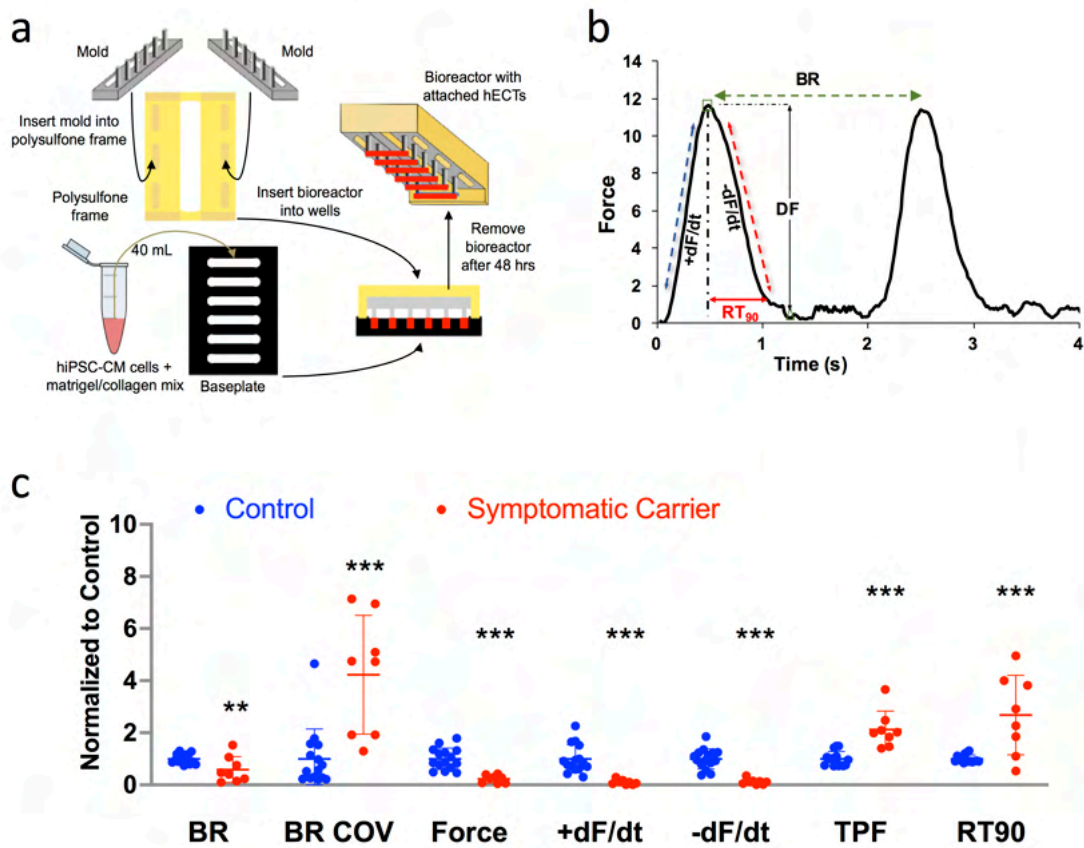


Figure 1. a) Schematic of hECT fabrication using custom bioreactor (Turnbull IC, et al. Methods Mol Biol. 2018). b) Schematic of contractility parameters of developed force (DF), maximum rates of contraction (+dF/dt) and relaxation (-dF/dt); time to peak force (TPF) and time to relaxation 90 (RT90), beat rate (BR) = [time between peaks]⁻¹. c) Contractility parameters under spontaneous conditions for non-carrier (control) hECTs and carrier (symptomatic) hECTs. Values normalized to control. Intrinsic beat variability measured as coefficient of variation (COV). Dot plots show individual data with mean ± SD. *p<0.05, **p<0.01, ***p<0.001; by Student's t-test.

Mesoscale Lipid Nanoparticle Formulation for Targeted Delivery of Nucleic Acids to Renal Proximal Tubule Epithelium

Anastasiia Vasylaki¹, Ryan Williams¹

¹Department of Biomedical Engineering, The City College of New York

Introduction: Nanoparticles in the mesoscale size range (300 - 400 nm) have been demonstrated to selectively target the kidneys, particularly proximal tubular epithelial cells. This drug delivery platform can potentially improve the efficacy of kidney therapeutics through increased accumulation at the disease site, as well as reduced adverse effects. However, mesoscale nanoparticle kidney targeting has only been shown with polymeric carriers thus far. The aim of this study was to develop a lipid-based mesoscale nanoparticle formulation, that can later be applied for targeted delivery of nucleic acids for kidney disease treatment.

Materials and Methods: Nanoprecipitation method was used to formulate mesoscale lipid nanoparticles (MLNP) with siRNA cargo. MLNP composition included an ionizable lipid, a phospholipid, cholesterol, and a PEGylated lipid. Nanoparticle size was optimized through modifications of the formulation composition and process parameters. Dynamic light scattering was used to characterize the MLNP size and polydispersity index, while electrophoretic light scattering was used for zeta potential. siRNA encapsulation efficiency was measured using a fluorescence-based RNA-quantitation assay. The MLNP cytotoxicity has been tested using the MTT assay.

Results: To produce siRNA-loaded lipid nanoparticles in the mesoscale size range, five different formulation modifications have been tested (Fig. 1). All of the modifications led to an increase in the nanoparticle size; however, MLNP larger than 300 nm have been produced through a combination of increased total lipid concentration, modification of lipid molar ratio, increased ion concentration, and modification of mixing parameters. To achieve the stable PEGylation required for kidney targeting, the MLNP lipid composition has also been optimized. The MTT assay has shown that the viability of renal epithelial cells is unaffected by treatment with MLNP formulations containing IL-6 siRNA and non-targeting siRNA. Hence, the developed formulation has no cytotoxic effect on renal epithelial cells and can be used for further studies.

Conclusions: In the current work, we have developed a mesoscale lipid nanoparticle formulation that has been optimized for targeted nucleic acid delivery to the proximal tubular epithelial cells. MLNPs have shown preliminary indications of safety, and their efficacy in delivery of nucleic acids to renal cells will be investigated in further in vitro and in vivo studies.

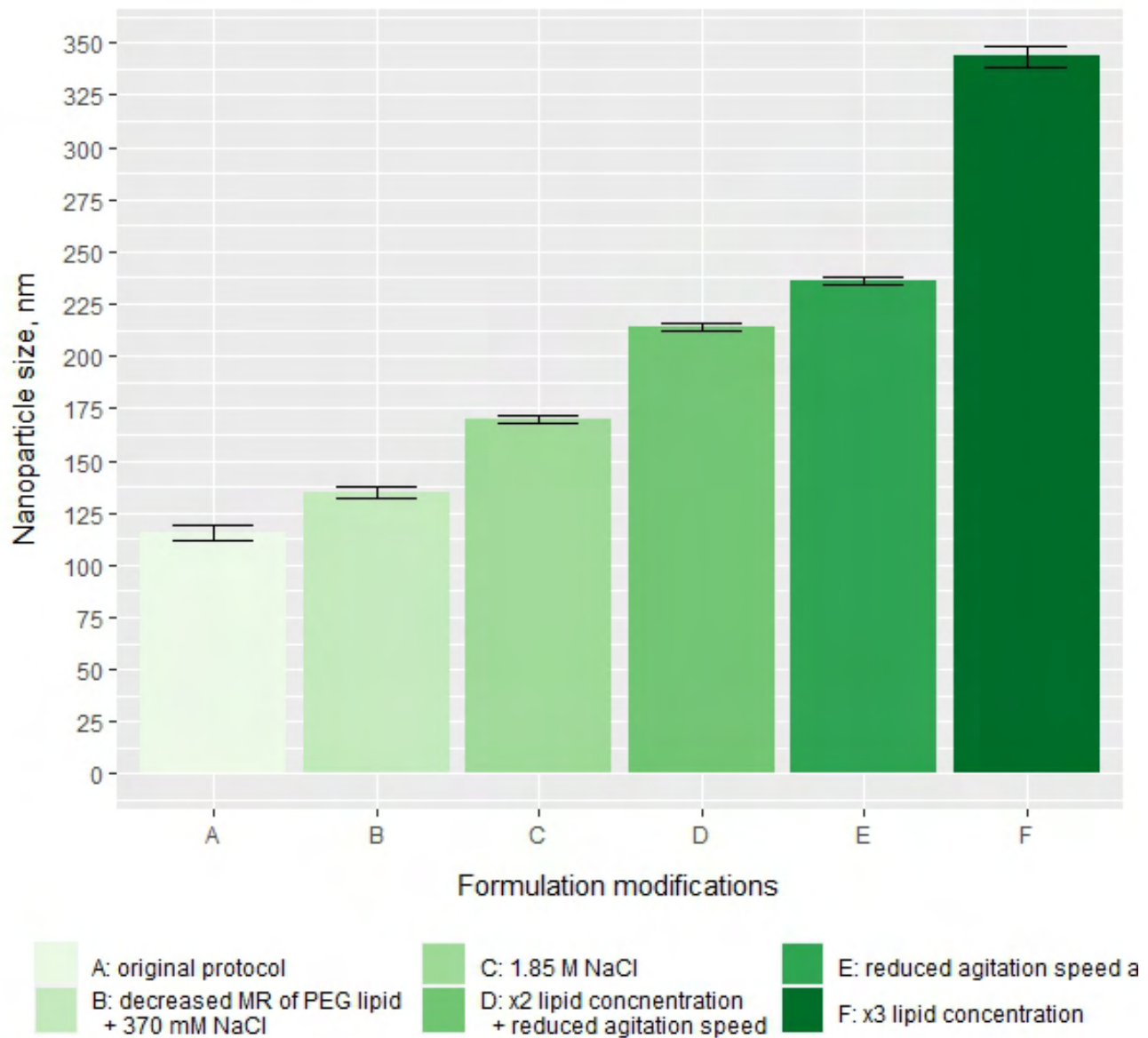


Figure 1. Lipid nanoparticle size as a result of various formulation modifications.

Detection and characterization of perivascular spaces using high-resolution T2-weight 7T MRI and automatic segmentation

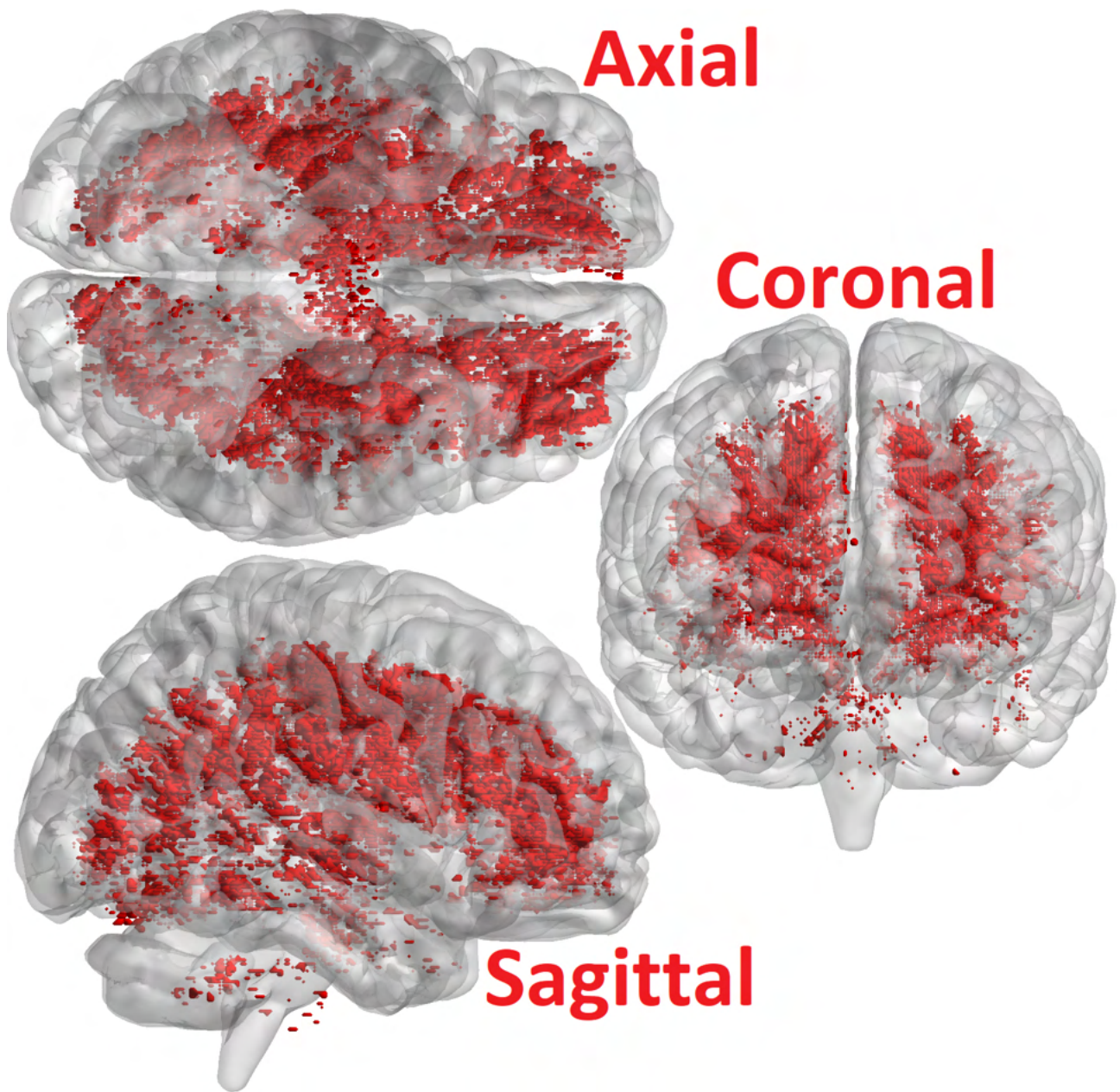
Gaurav Verma¹, Oleksandr Khagai¹, Mackenzie Langan¹, Mariana Figueiro², Bradley N. Delman¹, Priti Balchandani¹)

¹Biomedical Engineering and Imaging Institute, Icahn School of Medicine at Mount Sinai, New York, NY, USA

²Population Health Science, Icahn School of Medicine at Mount Sinai, New York, NY, USA

³Neuroradiology, Icahn School of Medicine at Mount Sinai, New York, NY, USA

Perivascular spaces are cerebrospinal fluid filled spaces within white matter that appear as hyperintense regions against a dark white matter background under t2-weighted MRI. The higher SNR achievable at ultrahigh field (7T or more) may enable higher spatial resolution and overall better visualization of these spaces. More numerous or enlarged PVSs may be implicated in a variety of neurocognitive disorders like mild cognitive impairment (MCI), dementia or the neurological effects of COVID-19. It is hypothesized that more numerous or larger PVSs may be indicative of disruptions in the brain's glymphatic clearance mechanisms. Manual segmentation of PVSs in ultrahigh field MRI is a cumbersome process due to their large number, small size and subtle appearance. To that end, we have developed and previously demonstrated an algorithm for detection of PVSs called PVS semi-automated segmentation (PVSSAS). Methods Four patients with mild cognitive impairment (MCI) and five healthy controls of a comparable age were scanned using high-resolution T2-weighted MRI at 7T. Scan parameters included: TE/TR = 59/9250 ms, 512x512, 62 slices of 2.0 mm thickness with 0.2 mm slice gap, FOV = 200 x 169 mm², GRAPPA factor = 2, total scan time, 6:49 minutes. After interpolation, final voxel size was 0.2 x 0.2 x 2.0 mm³. The scanning plane was oriented coronal-oblique perpendicular to the long axis of the hippocampus, with coverage spanning whole brain. A white matter mask was generated in native space using the statistical parametric mapping (SPM12) software in Matlab. The original T2 TSE data and white matter mask were processed using the PVSSAS algorithm previously published by this research group. PVSSAS uses a Frangi filter to detect ellipsoid regions of hyperintensity against the white matter background. Regions with average white matter intensity one standard deviation above the white matter background were segmented fully automatically in the whole-brain dataset. Segmented PVSs were analyzed using the regionprops3 algorithm within Matlab and quantitative metrics were obtained including total count (PVSCount), median volume (PVSMedVol), Total PVS Volume (PVSTotalVol), median long axis length (PVSMedLongAxis), short axis (PVSMedShortAxis) and median diameter (PVSMedEquiD). Results/Discussion PVS Statistics MCI HC PVSCount 2528 2640 PVSMedVol 28 27 PVSTotalVol 493 430 PVSMedEquiD 3.8 3.7 PVSMedLongAxis 9.6 9.3 PVSMedShortAxis 4.9 4.9 Initial results from this pilot cohort showed no major differences in PVS count between healthy controls and MCI patients. However, trends of higher PVS median volume and size were observed among the MCI patients, resulting in a larger total volume occupied by PVS.



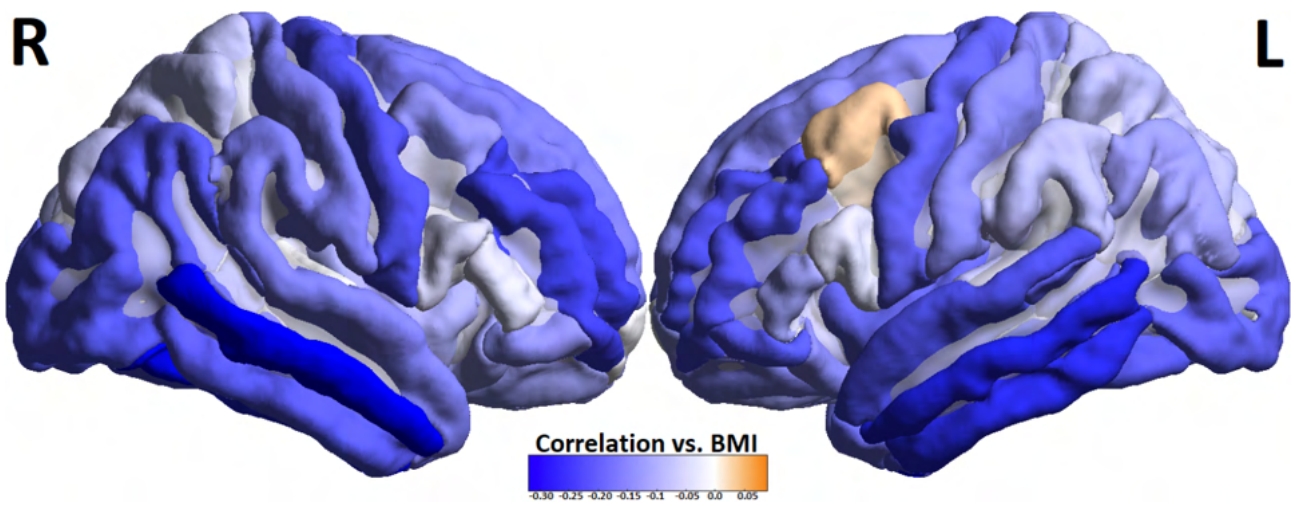
Axial, coronal and sagittal three-dimensional projections showing distribution of perivascular spaces as segmented by the PVSSAS algorithm in an older adult.

Correlation of cortical gray / white matter ratio and body mass index (BMI) in a cohort of healthy controls and major depression patients scanned with 7T T1-weighted MRI

Gaurav Verma, Claudia Kirsch, James Murrugh. Priti Balchandani

1) BMEII, and 2) Psychiatry, Icahn School of MEicine at Mouns Sinai

Introduction From 2000 to 2020, prevalence of obesity in the US grew from 30.5% to 41.9%, making it among the most costly diseases in the country. Obesity may be a risk factor for a number of other diseases including heart disease and cognitive impairments. Major depression carries a lifetime risk of around 12% making it one of the most common mental disorders. Both diseases are risk factors for each other, and common anti-depressant treatments such as selective serotonin reuptake inhibitors (SSRIs) or monamine oxidase inhibitors (MAOIs) carry increased risk for weight gain as a side effect. High resolution magnetic resonance (MRI) at ultrahigh field (7T or more) may help to better characterize the effects of MDD and obesity on brain physiology and morphology. This study investigated the relationship between brain gray and white matter ratios and body mass index (BMI) in the presence and absence of major depressive disorder. **Methods** We assessed T1-weighted MPRAGE imaging from forty-four MDD patients (17F/27M, 37.6±11.6 years) and forty-seven healthy controls (20F/27M, 36.4±10.7 years). Patients were screened against substance abuse and were not undergoing antidepressant treatment at the time of the study. Scan parameters included: TE/TR=3.62/6000ms, field-of-view=224x168 mm³, array size=320x240x240, voxel size=0.7mm³ isotropic, 7:26min. BMI was calculated as weight in kilograms and the square of height in meters. All scans were acquired with a Siemens 7T MAGNETOM whole-body MRI scanner and a 32-channel receive, single channel transmit Nova head coil. The acquired images were automatically segmented using the FreeSurfer 6.0 algorithm, which parcellated the cortex into 34 regions of interest (ROIs) per hemisphere for a total of 68 total regions. Three whole-brain ratios were also obtained consisting of total gray matter / white matter ratio (G/W), white matter / supratentorial volume (W/ST) and gray matter / brain segmentation volume (G/BS). Pearson partial correlation was performed between BMI and each of the 68 cortical ROIs and three whole-brain metrics. Both complete correlations and partial correlations adjusting for age as a covariate were performed. **Results/Discussion** BMI was found to be significantly negatively correlated with G/W and G/BS ratios, and significantly positively correlated with W/ST ratio when evaluated among healthy controls and the combined control and MDD patient cohort. These correlations were not significant when evaluated among the MDD patient cohort alone. Table 1 shows rho and p-values for the three whole-brain comparisons for all subjects, MDD-only cohort and healthy control cohort. All three of the whole-brain metrics tested showed significant correlation with BMI with and without



3D renderings of left and right hemisphere showing correlation between Gray/White matter ratio and BMI. Blue colors indicate negative correlations and are present across nearly all cortical brain regions.

Strategies for motion- and breathing-robust estimation of fMRI intrinsic neural timescales

Andrew Goldberg¹, Isabella Rosario¹, Jonathan Power², Guillermo Horga^{1,3}, and Kenneth Wengler⁴

¹New York State Psychiatric Institute, New York, NY, USA

²Department of Psychiatry, Weill Cornell Medicine, New York, NY USA

³Department of Psychiatry, Columbia University, New York, NY USA

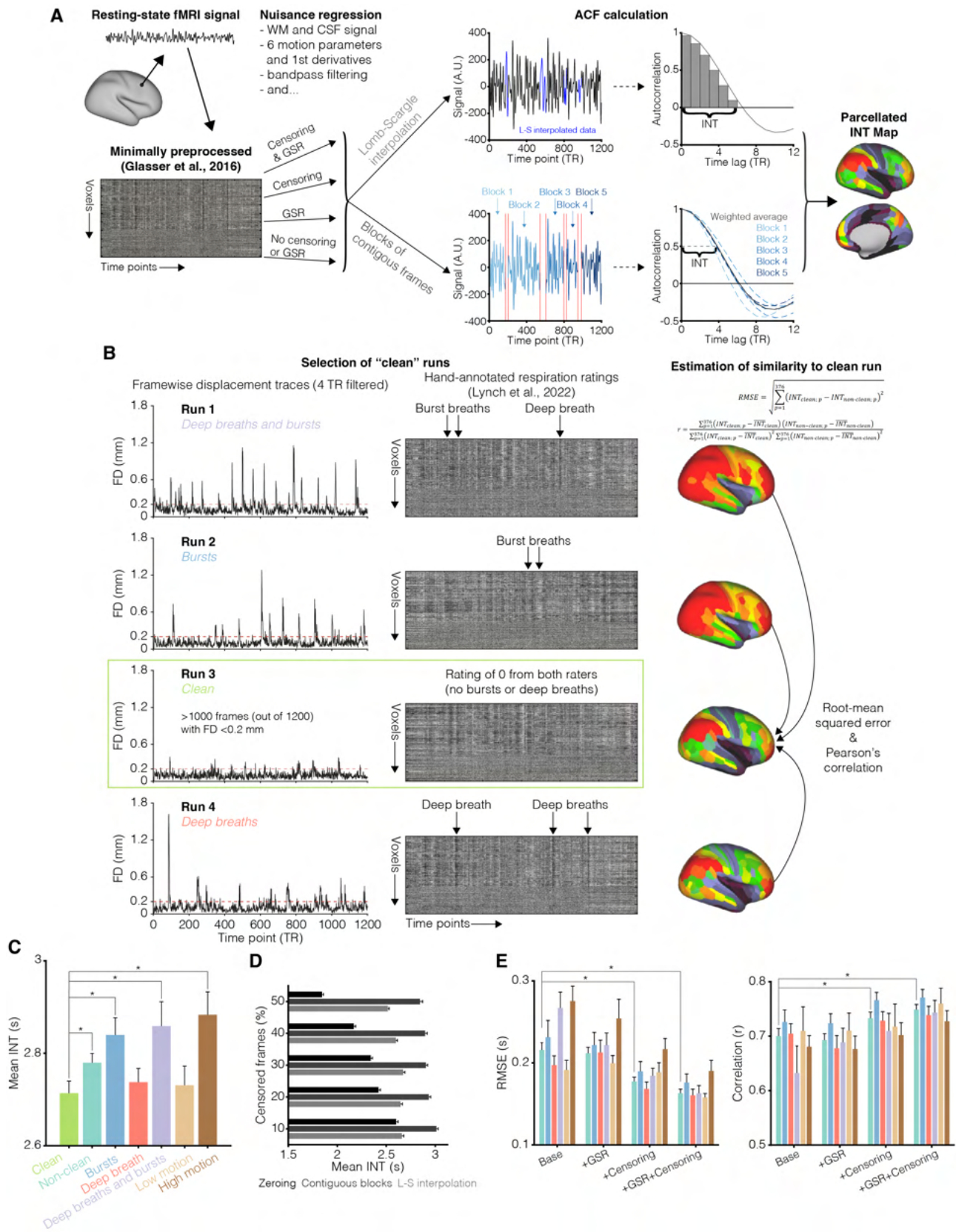
⁴: Department of Psychiatry, Department of Radiology, BioMedical Engineering and Imaging Institute (BMEII), Icahn School of Medicine at Mount Sinai, New York, NY USA

Introduction: Intrinsic neural timescale (INT) is a resting-state fMRI (rs-fMRI) measure reflective of the time window of neural integration within a brain region. Despite its relevance to neuropsychiatric disorders, physiological artifacts, which can impinge on the validity of fMRI findings, have not been systematically considered in INT estimation. Two such artifacts, head motion and respiration, pose serious issues in rs-fMRI studies. Here, we analyzed how two preprocessing strategies involving these artifacts, frame censoring and global signal regression (GSR), affect INT estimation.

Materials and Methods: We used a subset of the HCP Young Adult dataset with runs annotated for breathing patterns (Lynch et al., 2020) and at least one "clean" run that was free from head motion (frame displacement < 0.2 mm for > 1000/1200 frames) and breathing artifacts. The subset of analyzed data comprised these "clean" runs and other "non-clean" runs from the same participants (n = 46). All data were preprocessed using the HCP minimal preprocessing pipeline and nuisance regression was performed with standard regressors. Nuisance regression also included: 1) frame censoring and GSR; 2) only frame censoring; 3) only GSR; or 4) neither. We evaluated the ability of frame censoring and GSR to correct for artifacts by comparing non-clean runs to their respective clean run within a subject; we investigated the impact of frame censoring on INT estimation using synthetic frame censoring; and we determined the ability of post-hoc correction methods to correct for frame-censoring-induced errors.

Results: Non-clean runs had increased INT across the brain compared to their respective clean runs (t157=3.72, pFDR=0.0017). The amount of error in INT between non-clean and clean runs correlated with head motion (t111=4.10, pFDR<0.0001). Together, these results illustrate that physiological artifacts bias INT estimation. There was a relationship between the amount of synthetically censored frames and both the mean INT (t688=-10.48, pFDR<0.0001) and mean error (t688=16.02, pFDR<0.0001), suggesting that frame censoring itself biases INT estimation. GSR and frame censoring improved the similarity between INT maps in non-clean runs and their respective clean runs (t448=-7.14, pFDR<0.0001). Next, we determined whether the bias introduced by frame censoring could be corrected in post-hoc correction models. In the synthetically frame-censored data, post-hoc correction reduced estimation error (t135=-4.16, pFDR=0.0002). In the non-clean runs, post-hoc correction reduced also reduced estimation error (t176=-3.15, pFDR=0.0116).

Conclusions: Overall, these results simultaneously reflect the utility of frame censoring and GSR in minimizing physiological artifacts, as well as the importance of accounting for potential confounds in INT estimation.



A: Overview of preprocessing approach and intrinsic neural timescale (INT) estimation. B: Overview of selection of "clean" and "non-clean" runs and estimation of similarity between them. C: Physiological artifacts bias INT estimation. D: Synthetic frame censoring demonstrates that frame censoring itself biases INT estimation. E: Frame censoring and global signal regression improve similarity between INT maps estimated from non-clean and clean runs.

Using sleep quality and 7T MRI to explore structural differences in the Locus Coeruleus in those with PTSD and pathological anxiety

Yolanda I. Whitaker, B.S.^{1,4}, Philipp T. Neukam, PhD.^{1,4}, Korey Kam, PhD.^{1,2,4}, Priti Balchandani^{1,2,3,4,5}, PhD., James Murrough, MD, PhD.^{1,2,4}, Laurel S. Morris, PhD.^{1,2,4}.

¹Mount Sinai Hospital,

²Icahn School of Medicine at Mount Sinai;

³Biomedical Engineering and Imaging Institute,

⁴Department of Psychiatry,

⁵Department of Radiology.

Background: Sleep disturbances are common among patients with post-traumatic stress disorder (PTSD) and pathological anxiety. Research has found that brainstem structures involved in sleep/wake regulation are hypothesized to contribute to the development of PTSD and pathological anxiety. One of these brain structures includes the Locus Coeruleus (LC); this is because the LC is a major regulator of norepinephrine (NE) in the brain and extends projections throughout the CNS, controlling bodily arousal states as well as sleep-wake cycles. Recently, researchers have used ultra-high field 7-T magnetic resonance imaging (MRI) to directly examine the LC in vivo. However, the present study is the first evaluation of structural LC measures in vivo with self-reported sleep quality in individuals with and without anxiety disorders.

Methods: Data used for this study derives from a 7T neuroimaging R01 NIH-funded study at the Depression and Anxiety Center at Mount Sinai. The sample included patients with Anxiety-Related disorders (ANX) (N=40, 77.5% female, mean age=31.3) PTSD (N=22, 68.2% female, mean age=35.5), and Health Controls (N=34, 47.1% female, mean age=34.4). Participants underwent an ultra-high field 7T MRI scan to measure LC volume (normalized by whole brain volume) and LC signal intensity. Masks of the LC were automatically segmented using a gaussian mixture modeling and a supervised masking approach. Clinical symptoms related to sleep were measured by the Pittsburgh Sleep Quality Index (PSQI), a self-report survey that assesses sleep quality and disturbances for 1-month. Pearson's correlations were conducted to investigate relationships between LC functioning and sleep symptoms.

Results: Within the patient group alone (ANX and PTSD patients combined), sleep quality negatively correlated with LC mask volume [$R(44)=-0.299$, $p=0.048$]. However, this correlation was not seen within the HC group. Although not statistically significant, the patient group demonstrated a larger LC volume (mean=0.21) compared to the HC group (mean=0.01).

Conclusion: This finding suggests that an enlarged LC may play a role in diminished sleep quality within clinical populations. Future research on this topic must be conducted to determine the extent to which there are LC alterations in sleep, in those with pathological anxiety and PTSD.

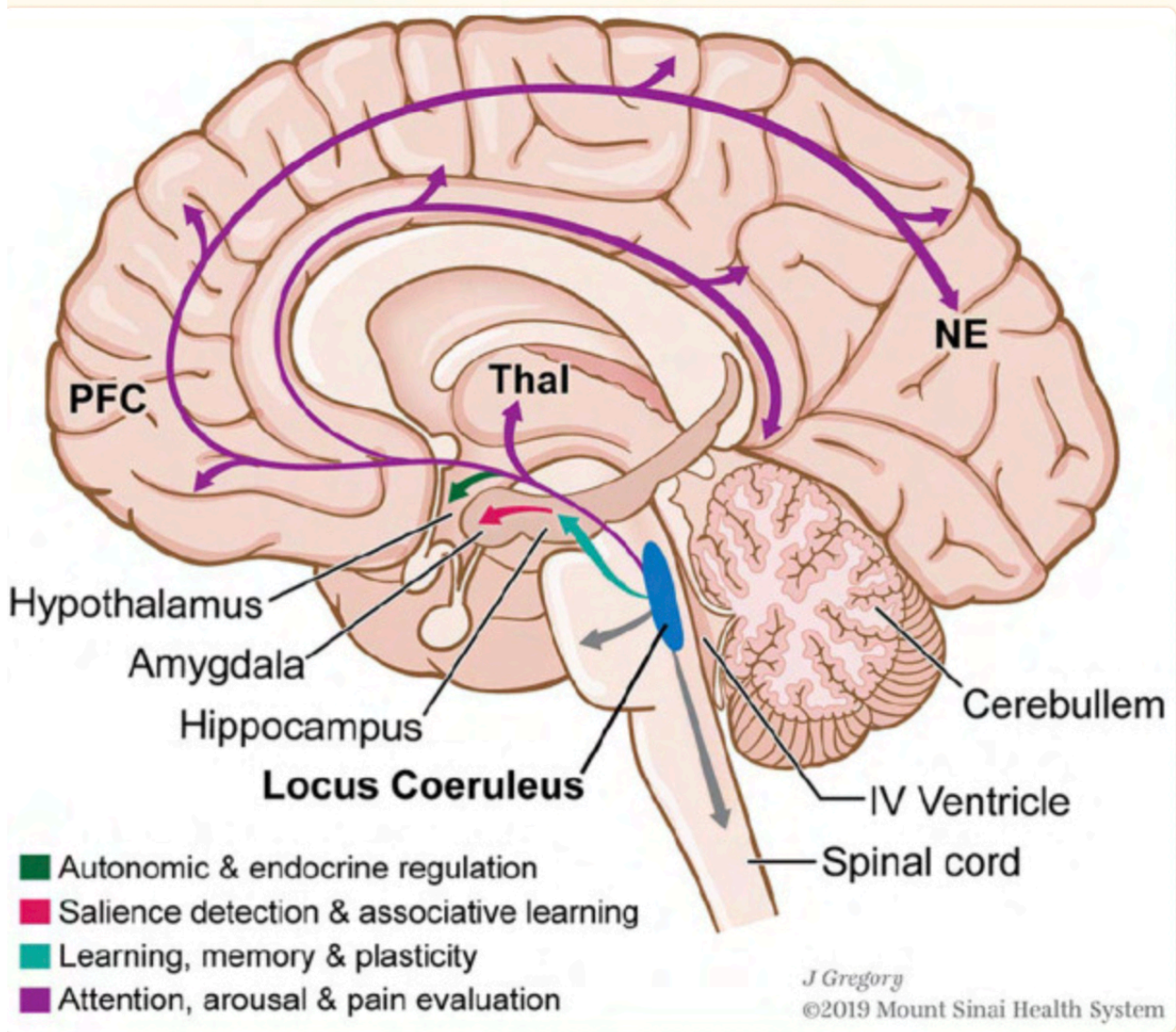


Image of LC Network (Gregory, 2019)

Evaluation of a Novel Self-Sealing Dialysis Port

Jacob M. Wright ¹, Alan I. Benvenisty ², Kenneth R. Nakazawa ², Marina de Cos ¹, Kirk N. Campbell ¹, Eric G. Lima ³, Evren U. Azeloglu ^{1,4}

¹Nephrology, Department of Medicine, Icahn School of Medicine, New York, NY, USA

²Department of Surgery, Icahn School of Medicine, New York, NY, USA

³Mechanical Engineering, The Cooper Union, New York, NY, USA

⁴Pharmacological Sciences, Icahn School of Medicine, New York, NY, USA

Introduction: Complications associated with incorrect cannulation of hemodialytic vascular accesses limit treatment opportunities outside the clinic. To improve quality of life and reduce complications, we developed a novel access port, called Safe Entry Port for AV fistulae (SEAL), that integrates with fistulae, guides cannulation, and uses an internal colinear valve to prevent aneurysms and reduce bleeding.

Methods: SEAL was fabricated using direct metal laser sintering of FDA-approved Ti-6Al-4V with silver-doped titanium nitride (TiN/Ag) coating (Figure 1A-C). Device properties such as self-sealing capabilities, fatigue testing, and bacterial resistance were assessed. Preclinical performance was evaluated in an adult sheep brachiocephalic arteriovenous fistula model, where SEAL was implanted subdermally on a mature fistula and cannulated biweekly for six weeks. Device integration and host tissue reaction were evaluated using micro-CT.

Results: SEAL is engineered to integrate directly over a fistula via Ti matrix interaction with host tissue, guide cannulation, and stop bleeding via an internal colinear valve using tensile energy of the subcutaneous tissue following needle removal. In vitro testing on a closed-loop circuit demonstrates that the valve operates as expected and can withstand high circulatory pressures after needle withdrawal (Figure 1 D-G). In repeated cannulations of the device during ex vivo simulations with 14G needles, the peak force required to engage the valve recorded in our dialysis fatigue cycling simulation was 160.5 ± 0.02 mN. The device withstood cannulation cycles equivalent to 14 years of dialysis. The colinear valve smoothly opened for continuous flow through the needle guide. Antimicrobial TiN/Ag coating showed significant reduction in bacterial growth (Figure 1 H). In preclinical trials (Figure 1 I-J), no signs of infection or back bleeding were observed during the continuous six-week cannulation period; vascular access was continuous with no resistance or complications.

Conclusion: In summary, SEAL has the potential to change the future of dialysis treatments and improve the quality of life for patients due the reduction of complications and improved access to home hemodialysis.

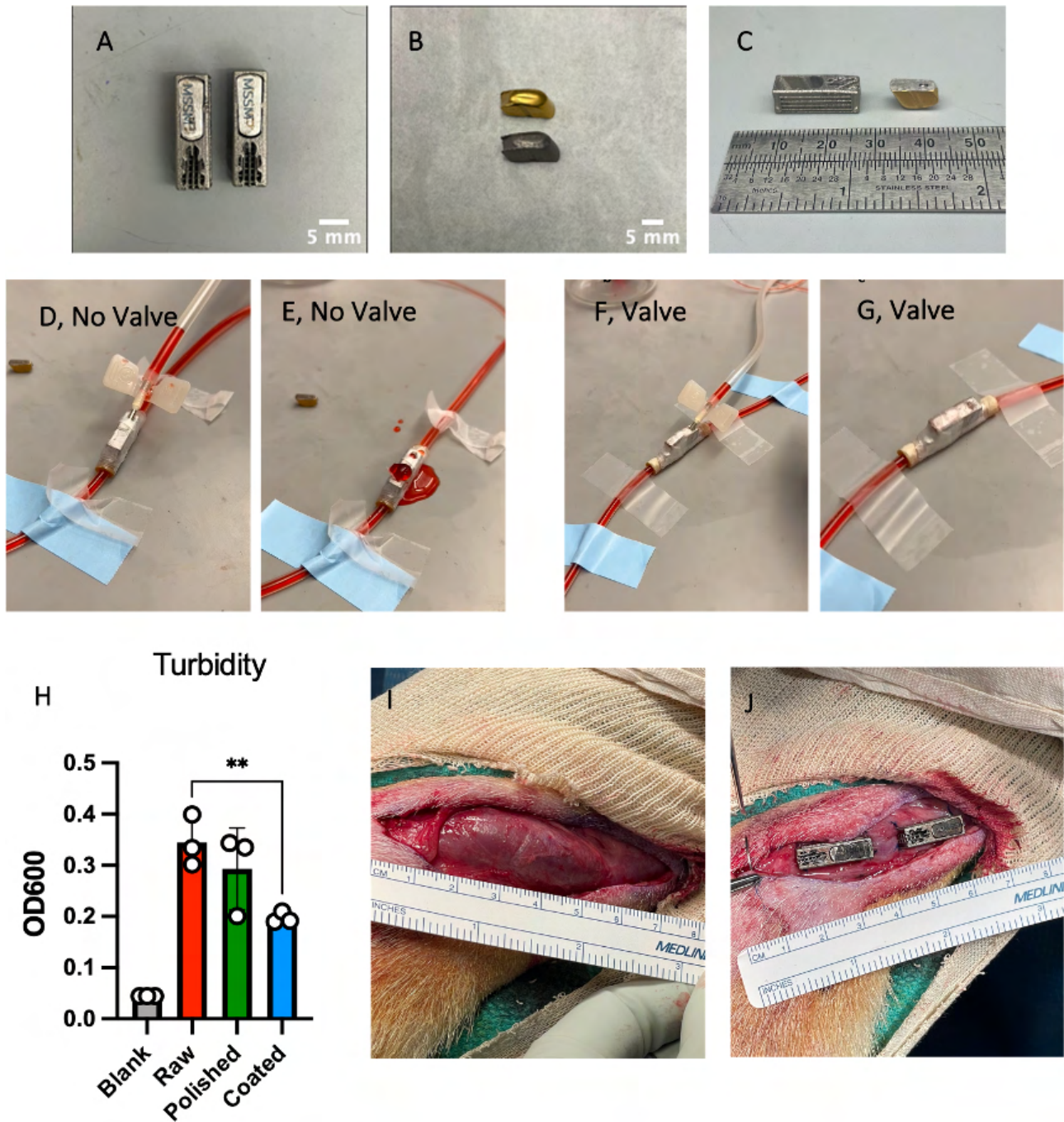


Figure 1: Seal device, valve, raw, TiN/Ag (A, B, C), In vitro simulation of SEAL with no valve scenario (D). Needle removal without valve (E). Valve cannulation (F). Needle removal with valve (G). *S. aureus* bacteria turbidity growth assay of inoculated valves (H). AV fistula matured 12 weeks (I). Implanted SEAL devices (J).

Increased Blood-Brain Barrier Permeability in ME/CFS: An MRI Study

Sheryl Liu ¹, Dengrong Jiang ³, Rodolphe Leforestier ², Hanzhang Lu ³, Benjamin Natelson ⁴, Xiang Xu ²

¹Livingston High School, Livingston, NJ, United States

²BioMedical Engineering and Imaging Institute, Icahn School of Medicine at Mount Sinai, New York, NY, United States

³Department of Radiology, Johns Hopkins University, Baltimore, MD, United States

⁴Department of Neurology, Icahn School of Medicine at Mount Sinai, New York, NY, United States

Introduction: The etiology of Myalgic Encephalomyelitis/Chronic Fatigue Syndrome (ME/CFS) remains elusive. It has been hypothesized that increases in blood-brain barrier (BBB) permeability in patients with ME/CFS lead to many of the symptoms experienced by these patients. A dysfunctional BBB is associated with chronic neuroinflammation and can lead to a sustained illness with chronic relapse recovery cycles. Post-Acute Sequelae of SARS-CoV-2 infection (PASC) patients, many of whom also meet ME/CFS diagnostic criteria, differ primarily in the shorter duration of their illness compared to those with classic non-PASC ME/CFS. Assessing BBB permeability across PASC ME/CFS, classic non-PASC ME/CFS, and healthy individuals could validate this hypothesis and deepen our understanding of ME/CFS pathophysiology. Traditional method for measuring the BBB permeability involves Gadolinium contrast agents. Since these contrast agents are large molecules, they are sensitive to major leakage of BBB, but may not detect subtle changes of BBB permeability. In this study, we utilized water-extraction-with-phase-contrast-arterial-spin-tagging (WEPCAST) MRI to non-invasively measure the BBB permeability to water. In this pilot study we recruited a group of PASC ME/CFS patients, classic ME/CFS patients, and healthy individuals.

Methods: All MRI scans were conducted on a Siemens 3T Skyra scanner with a 32-channel head coil. The WEPCAST MRI technique measures BBB permeability to water by labeling the water molecules in the incoming arteries and, by determining the fraction of the water that remained in the vessel versus those exchanged into the brain tissue at the capillary-tissue interface to determine water extraction fraction (E). The measurement is performed in the superior sagittal sinus (SSS), yielding a whole-brain measure of E. The flux in the 4 major feeding vessels of the brain were measured using phase contrast to estimate global cerebral blood flow (CBF). the BBB permeability index, permeability-surface-area product (PS), was calculated from E and f according to the Renkin-Crone model: $PS = -lnf_0(1 - E) \times f$].

Results: We found that there was no significant difference in E or CBF between the three groups, but the PS was significantly higher in the classic non-PASC ME/CFS group than the PASC ME/CFS or the healthy control groups.

Conclusion: The results provide imaging-based evidence of neuroinflammation associated with ME/CFS.

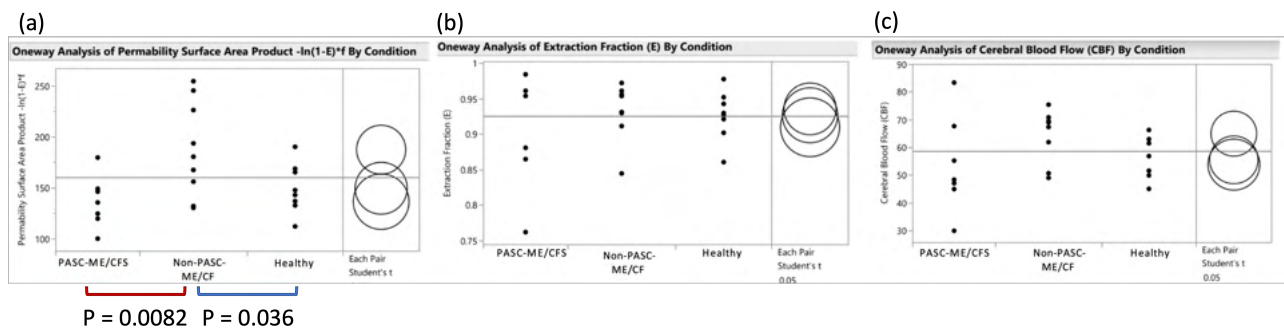


Figure 1. Paired-wise comparisons of permeability surface area product (a), water extraction fraction (b) and CBF (c) between the PASC-ME/CFS group, non-PASC ME/CF group and healthy controls.

Functionalized SWCNT-Aptamer Sensors for Selective Dopamine Detection: Exploring Selectivity and Sensitivity.

Hanan Yafai¹, Ryan M. Williams²

¹ Department of Biomedical Engineering, The City College of New York, New York, NY 10031

² Department of Biomedical Engineering, The City College of New York, New York, NY 10031

Introduction: Neurotransmitters function as critical chemical messengers, facilitating communication among neurons and the nervous system. Precise monitoring of dopamine (DA), a vital neurotransmitter regulating movement, cognition, and emotions, is important for understanding and treating neuropsychiatric disorders linked to dysregulated DA levels. However, existing methods are invasive, time-consuming, and inaccurate. This study investigates single-walled carbon nanotubes (SWCNTs) as building blocks for DA sensors. SWCNT-based nanosensors offer advantages like near-infrared (nIR) fluorescence, photostability, and sensitivity. We explore SWCNT-aptamer sensors, where aptamers (ssDNA molecules obtained through a process known as SELEX) are functionalized around SWCNTs to enhance DA selectivity. Addressing the limitations of traditional methods, SWCNT-Aptamer presents a solution with high spatial and temporal precision.

Methods: For sensor and control preparation, a DA aptamer and (GT)10 control (samples, $n = 6$ for each complex) were prepared by suspending 0.5 mg HiPCO SWCNTs and both DA aptamer and (GT)10 single-stranded in a 2:1 oligonucleotide-to-SWCNT mass ratio in 1X PBS solution. The solution was probe tip sonicated, then ultracentrifuged to remove impurities and residual catalyst ($58,000 \times g$, 1 hr., 4°C) in an Optima MAX-XP. To eliminate unbound DNA, the solution was filtered through a 100 kDa filter. Remaining (GT) 10-SWCNTs were resuspended in 1X PBS. The final solution was characterized by absorbance spectroscopy using a V-730 UV-VIS spectrophotometer to determine concentration. Fluorescence response of DA Aptamer and GT-10-SWCNT sensors to dopamine was analyzed using the NS MiniTracer NIR spectrometer. Fluorescence peaks were assigned to SWCNT chiralities based on literature data. MATLAB was used for pseudo-Voigt model fitting to determine the center wavelength and intensity of the (7,5) E11 chirality peak.

Results: Our findings affirm the efficacy of our sensor in detecting dopamine. The GT10-SWCNT sensor exhibited sensitivity to dopamine, with varying levels. Notably, at time point 0, the Aptamer+dopamine group displayed a higher initial intensity increase (352%), while the GT10+dopamine group exhibited a lower initial intensity (257%). A sustained intensity decrease was observed in both groups over time after the 30-minute mark until reaching baseline.

Conclusions: The DA aptamer group's rapid fluorescence increase upon dopamine binding suggests specific interactions, while limited binding sites or faster dissociation may cause a subsequent intensity decrease. The GT10 sequence, with potentially slower initial binding, allows continuous dopamine interaction, resulting in a more prolonged intensity increase and sustained response. Future steps include assessing the sensor's ability to discriminate against other catecholamines and exploring its performance across wider dopamine concentration ranges.

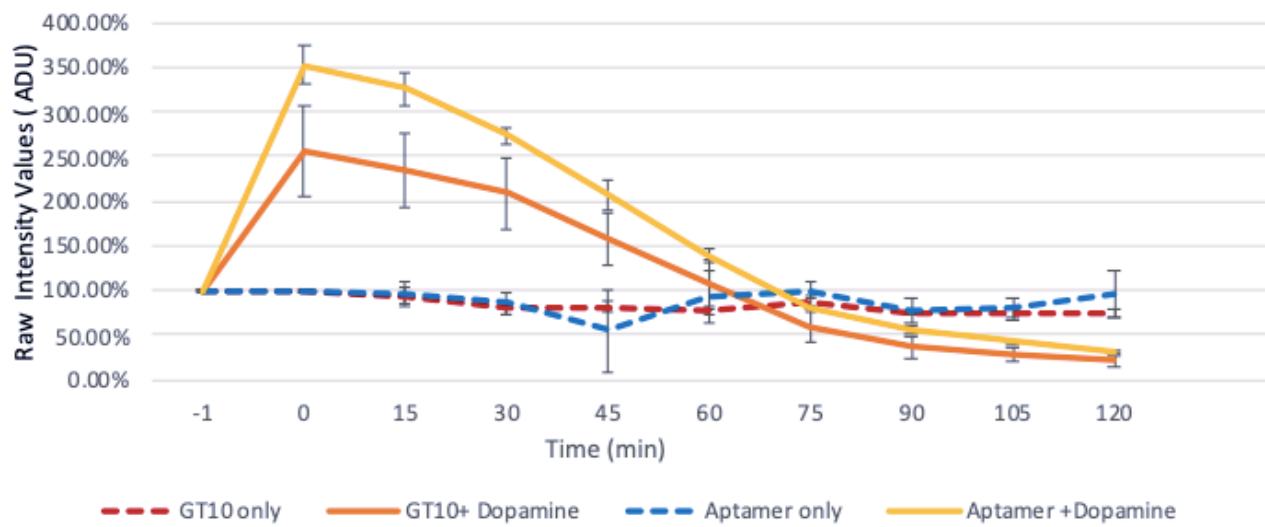


Figure 1. SWCNT (7,5) Normalized Fluorescence Intensity

MRAnnotator: A Multi-Anatomy Deep Learning Model for MRI Segmentation

Alexander Zhou¹, Zelong Liu¹, Andrew Tieu¹, Nikhil Patel¹, Sean Sun², Anthony Yang², Peter Choi², Valentin Fauveau¹, George Soultanidis¹, Mingqian Huang², Amish Doshi², Zahi A. Faya^{1,2}, Timothy Deyer (^{3,4}, Xueyan Mei¹

¹BioMedical Engineering and Imaging Institute, Icahn School of Medicine at Mount Sinai, New York, NY

²Department of Diagnostic, Molecular, and Interventional Radiology, Icahn School of Medicine at Mount Sinai, New York, NY

³East River Medical Imaging, New York, NY

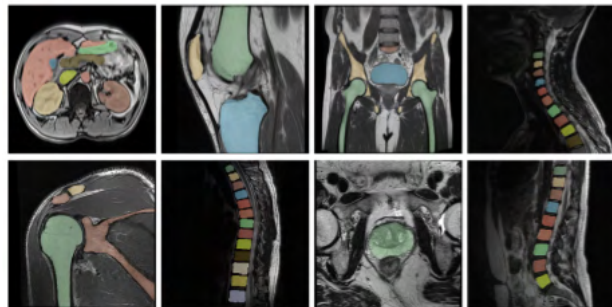
⁴Department of Radiology, Cornell Medicine, New York, NY

Purpose: To develop a deep learning model for multi-anatomy and many-class segmentation of diverse anatomic structures on MRI imaging (MRAnnotator).

Materials and Methods: In this retrospective study, two datasets were curated and annotated for model development and evaluation. An internal dataset of 1022 MRI sequences from various clinical sites within a health system and an external dataset of 264 MRI sequences from an independent imaging center were collected. In both datasets, 49 anatomic structures were annotated as the ground truth. The internal dataset was divided into training, validation, and test sets and used to train and evaluate an nnU-Net model. The external dataset was used to evaluate nnU-Net model generalizability and performance in all classes on independent imaging data. Dice coefficient scores were calculated to evaluate model segmentation performance.

Results: MRAnnotator achieved an overall average Dice score of 0.817 on the internal dataset hold-out test set, and an overall average Dice score of 0.814 on the external dataset.

Conclusion: The developed model achieves robust and generalizable segmentation of 49 anatomic structures on MRI imaging. A future direction is focused on the incorporation of additional anatomic regions and structures into the datasets and model.

Figure 1**Table 1**

Anatomic study	Average internal Dice score	Average external Dice score
Abdomen out-of-phase	0.790	0.783*
Bony pelvis	0.932	0.860
Prostate T1	0.951	0.912
Shoulder PD	0.880	0.937
Knee PD	0.879	0.878
Cervical spine T2	0.855	0.835
Thoracic spine T2	0.728	0.742
Lumbar spine T2	0.803	0.809
Overall average	0.817	0.815

FIGURE: Examples of model segmentations of various structures in diverse anatomic protocols: abdomen, knee, pelvis, cervical spine, shoulder, thoracic spine, prostate, and lumbar spine. TABLE: MRAnnotator model performance on internal and external test datasets, measured by Dice score. Scores by anatomic study are averaged across the contained anatomic structures, while the overall average is across all 49 structures for the internal dataset and 47 structures for the external dataset.

Development of a Next Gen 9.4 T Magnetic Resonance System for Translational Neuroscience

Wasif Zia^{*1}, Alexandre R. Franco¹, J. Thomas Vaughan Jr.^{1,2}

¹Nathan S Kline Institute, ²Columbia University

Nathan S. Kline Institute, Columbia University, and General Electric (GE) are working together to build a powerful MRI scanner with National Science Foundation funding award # 2117823, which is currently in year 3. New York state is building a special facility for it and upgrading their animal facility, human experiment room and a sleeping lab is envisaged as well. The scanner will be a shared resource in the Tristate area and fifty research groups along the East Coast. The scanner will have a magnetic field strength of 9.4 T. This particular field strength allows direct comparison with many pre-clinical scanners being used around the world and is coupled with high performance gradients from GE with a field strength and slew rates of 140 mT/m and 810 T/m/s, respectively, for unprecedented performance. Figure shows the magnet awaiting installation in mid-2025. Currently, we are developing a 36-tray shim tube assembly based on magnet-gradient interaction (MGI) simulations to nest the high-performance gradient set and rigidly secure it into the 65 cm bore magnet with axial stops in the service end. The service end will also have a water manifold and wire guides where each wire will carry ~900 A. The patient bed is a cantilever design without a conventional bridge to isolate the subject from vibrations. With this system, we will acquire in vivo images and spectra from humans, NHPs, and smaller laboratory animals to facilitate comparative and translational studies on a single scanner. Targeted specifications include: 1) in-plane spatial resolution for brain structural imaging of 50 microns, 2) maximal temporal resolution of functional MR imaging (fMRI) measured connectivity events of less than 100ms, 3) maximal spatial resolution of fMRI of 100s of microns, and 4) high resolution spectroscopic measurement of metabolites and neurotransmitters in human brain comparable to values heretofore achievable only in small rodent models in high resolution systems of the same or higher field strengths. To achieve the latter, we are also developing an ultra-high field laboratory to fabricate our own RF coils including detunable Transverse Electromagnetic (TEM) coil and use the concept of B1 shimming. To manage the issue of B0 inhomogeneity we plan higher order shims to be integrated with our TEM coil. Our objective is to develop a state-of-the-art MRI system and development hub unprecedented human MR capability at 9.4 T.



Fig. 1: 9.4T, 65cm bore magnet received at local warehouse. Alexandre Franco (L) and Thomas Vaughan (R) provide scale.

Selected for Innovation Station

mercure - A flexible open-source platform for deploying AI models into clinical practice

James O'Callaghan^{1,2}, Roy Wiggins^{1,2}, Amanpreet Singh Saimbhi^{1,2}, Kai Tobias Block¹

¹Center for Biomedical Imaging, Department of Radiology, NYU Grossman School of Medicine

²Center for Advanced Imaging Innovation and Research, Department of Radiology, NYU Grossman School of Medicine

Introduction: There has been tremendous excitement about the use of AI for radiology applications in recent years, which has inspired many research groups to develop models for tasks such as automated disease detection, image preprocessing, and radiomics. However, despite widespread enthusiasm, real-world clinical adoption of AI-supported algorithms remains limited. Barriers to clinical translation include strict requirements for algorithm performance as well as infrastructure challenges for seamless integration into radiology IT systems. To address these issues, tools are required to enable algorithm developers to test and evaluate AI models in clinical environments. Here, we present an open-source solution called "mercure" that provides everything needed for deploying AI prototypes into routine workflows.

Materials and Methods: mercure can be installed on any server running the Ubuntu operating system. It provides a DICOM listener to receive studies from imaging devices, PACS/VNAs, or workstations. A web-based user interface is provided for easy configuration of the data flow via "Rules", "Modules", and "Targets". Rules specify how incoming study data are filtered and processed by a module (or chain of modules), and to which targets (DICOM, DICOMweb, local folder, S3, or XNAT) the results will be dispatched. Notifications can be configured to provide alerts on events such as process completion or errors. Comprehensive logs and audit trails can be reviewed in the web interface. Processing modules are Docker containers with a simple data-exchange interface that perform operations or calculations on received images. Algorithms can be written in any language (e.g., Python, C++, or MATLAB) so that AI models developed using frameworks such as MONAI, PyTorch, or TensorFlow can be easily integrated and deployed as modules. Installation in mercure can be done manually or via automatic download from Dockerhub - providing a convenient mechanism for distribution and sharing of modules with collaborators.

Results: The software, including all source code and installation scripts, is provided through a public GitHub repository. Documentation and tutorials can be found at the project homepage <https://mercure-imaging.org>, which also provides access to a library with example processing modules. The library also contains various utility modules, such as for DICOM anonymization or BIDS/NIfTI conversion.

Conclusions: mercure offers a simple and flexible solution for automating DICOM processing tasks. The user-friendly web-based interface and Docker-based module architecture enable developers to deploy AI models into the clinical workflow with minimal effort. mercure is provided as open-source software and can be used for free without usage restrictions.

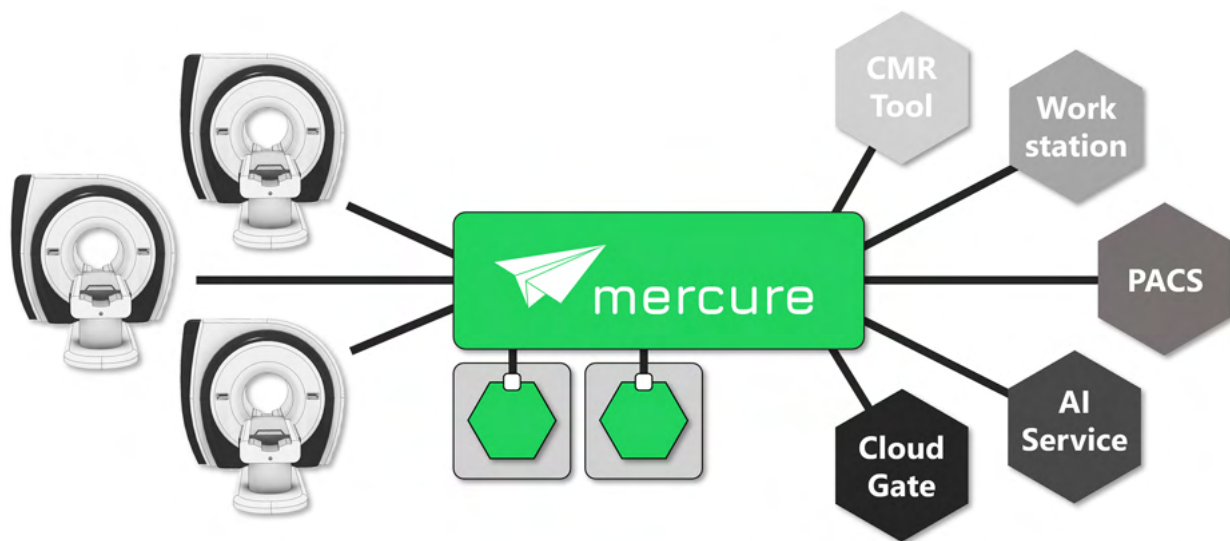


Figure 1: The open-source mercure software can be installed on-premise on any Linux server. Studies can be routed from imaging devices, such as MRI or CT scanners, or can be sent from a PACS/VNA. Processing steps can be implemented as Docker containers. Results can be dispatched to different destinations depending on the triggered processing rules.

Creating an open-source low-field MRI scanner in just one week - Experience from the MRI4ALL hackathon

Kai Tobias Block², Leeor Alon^{1,2}

¹Center for Biomedical Imaging, Department of Radiology, NYU Grossman School of Medicine

²Center for Advanced Imaging Innovation and Research, Department of Radiology, NYU Grossman School of Medicine

Introduction: Until recently, only a few companies possessed the expertise to build magnetic resonance imaging (MRI) systems, which resulted in restricted access to MRI scanners and development tools. In the last years, however, novel low-field MRI designs have been introduced that eliminate the need for superconducting magnets and extensive engineering resources. Motivated by this progress, our center organized a hackathon in October 2023 to tackle the challenge of creating a working low-field MRI system in just one week. Here, we share details about the construction of the scanner and present the developed open-source resources, which aim to provide broader access to MRI technology.

Materials and Methods: In preparation for the hackathon, software was developed using the Magpylib and Pymoo libraries to calculate the optimal placement of 990 N40UH permanent magnets into a Hallbach array. The arrangement was transferred into CAD software and used to design ring-shaped holders for the magnets. A shell for the magnet as well as nestable inserts were designed, including the holder for a cooling system, three holders for gradient coils, holders for shim magnets, and an insert for the RF coil. Wire patterns for the gradient coils were calculated using the CoilGen package and imprinted into the gradient inserts. Components were 3D-printed using polycarbonate. During the event, 52 participants worked in 4 teams to assemble the scanner. Polarities of the magnets were determined, ring-formers were populated, and the 12 magnet rings were fastened together with brass bolts. To evaluate homogeneity, a field-mapping robot was created using Arduino-controlled step motors and a Hall probe. Measured field maps were used to calculate the placement of shim magnets. Gradient coils were built by bending enameled copper wire and glueing it into the imprints of the 3D-printed holders. A solenoid RF coil was built and tuned to 1.83 MHz. A Red Pitaya 122-16 SDR board was connected to a GPA-FHDO gradient amplifier and loaded with the MaRCoS firmware to control the scanner. Console software for configuring scans and viewing acquired images was programmed in Python using PyQt5, PyPulseq, and additional support libraries.

Results: Figure 1 shows the constructed scanner, named Zeugmatron Z1. After resolving multiple technical problems, MRI signals were successfully received, and the scanner started producing first images. Developed code and resources have been published at <https://mri4all.org>.

Conclusions: Our hackathon showed that building low-field MRI scanners is possible with limited resources and can enable more researchers to engage in the advancement of medical imaging.

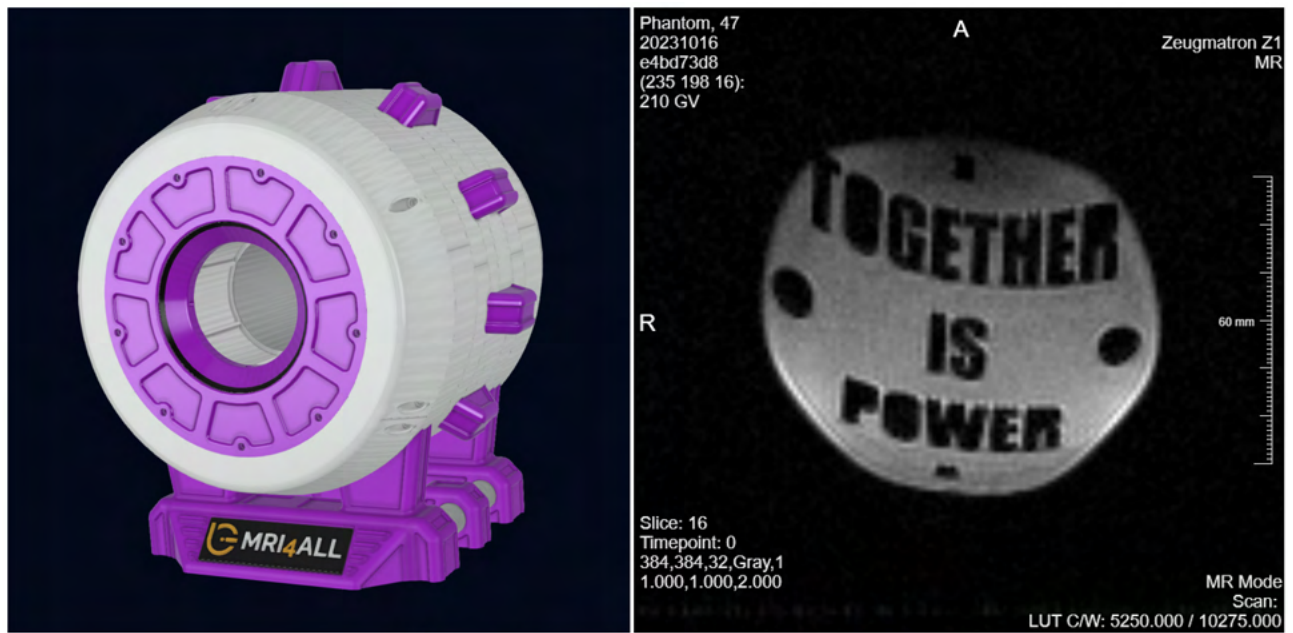


Figure 1: (Top left) CAD model of the MRI scanner with a field strength of 0.043 Tesla, created by a Halbach array made from 990 N40UH magnets. (Top right) MR image of a test phantom acquired with the scanner using a 3D SE sequence. (Bottom) The hackathon attendees with the assembled Zeugmatron Z1 scanner.

Optimizing Remote Vital Sign Alarms in Healthcare at Home: Insights from Alarm Simulations Using Real-world Data.

Nicole Zahradka PhD¹, Brian Hylton², Matt Wilkes MD, PhD¹

¹Clinical Research, Current Health from Best Buy Health, Boston, MA, 02108, USA.

²Customer Growth, Current Health from Best Buy Health, Boston, MA, 02108, USA.

Introduction: The significance of continuous vital sign monitoring for early detection and intervention in preventing adverse events is heightened during healthcare at home. The integration of wearables for continuous monitoring increases assessment frequency but may pose challenges with information overload for clinicians. Despite its importance, there is limited evidence on optimal alarm recommendations for home-based healthcare programs. This study aims to assess the impact of alarm settings on alarms using a simulated approach with real-world patient data collected remotely in a clinical setting.

Methods: Vital signs were continuously measured using the Current Health (CH) platform in 76 patients admitted to healthcare at home programs (Figure 1). Alarm settings were evaluated through a simulated system representing the physiological track and trigger component of the CH platform employing various alarm parameters (Python Software Foundation. Python Language Reference, version 3.8). Three vital sign alarm rulesets (A1, A2, A3) were tested, each with four aggregation windows (AW5 = 5 min, AW15 = 15 min, AW1 = 1 h, AW4 = 4 h). To compare the effects of alarm settings, the patient's length of stay was divided into 4-h assessment windows similar to the assessment frequency on a general medical/surgical ward. A positive alarm window (WAP) was an assessment window with at least one alarm trigger. Patient and alarm rates were defined as the percentage of patients with at least one WAP and average WAP per patient per day, respectively. Alarm metrics were compared between alarm rulesets and aggregation windows. Analyses were performed using GraphPad Prism 9 Version 9.3.1. (GraphPad Software, San Diego, CA, USA).

Results: The study demonstrated that the alarm ruleset influenced alarm metrics, with different rulesets triggering alarms at varying rates (Table 1). The A2 ruleset, utilizing individual vital sign rules, triggered alarms most frequently, resulting in increased patient and alarm rates. Conversely, the A3 ruleset, incorporating multiple vital signs with logic-based rules, triggered alarms less often with decreased patient and alarm rates across all aggregation windows. Increased aggregation windows were associated with decreased alarms, patient rates, and alarm rates for all rulesets.

Conclusion: As healthcare transitions into home-based settings, the study emphasizes the importance of evaluating standard tools, practices, and clinical interpretation in this new environment. The findings underscore the need for customization, suggesting that vital sign thresholds within the normal range, smaller aggregation windows, and individual vital sign rules are more amenable to modification to enhance specificity and mitigate alarm fatigue.

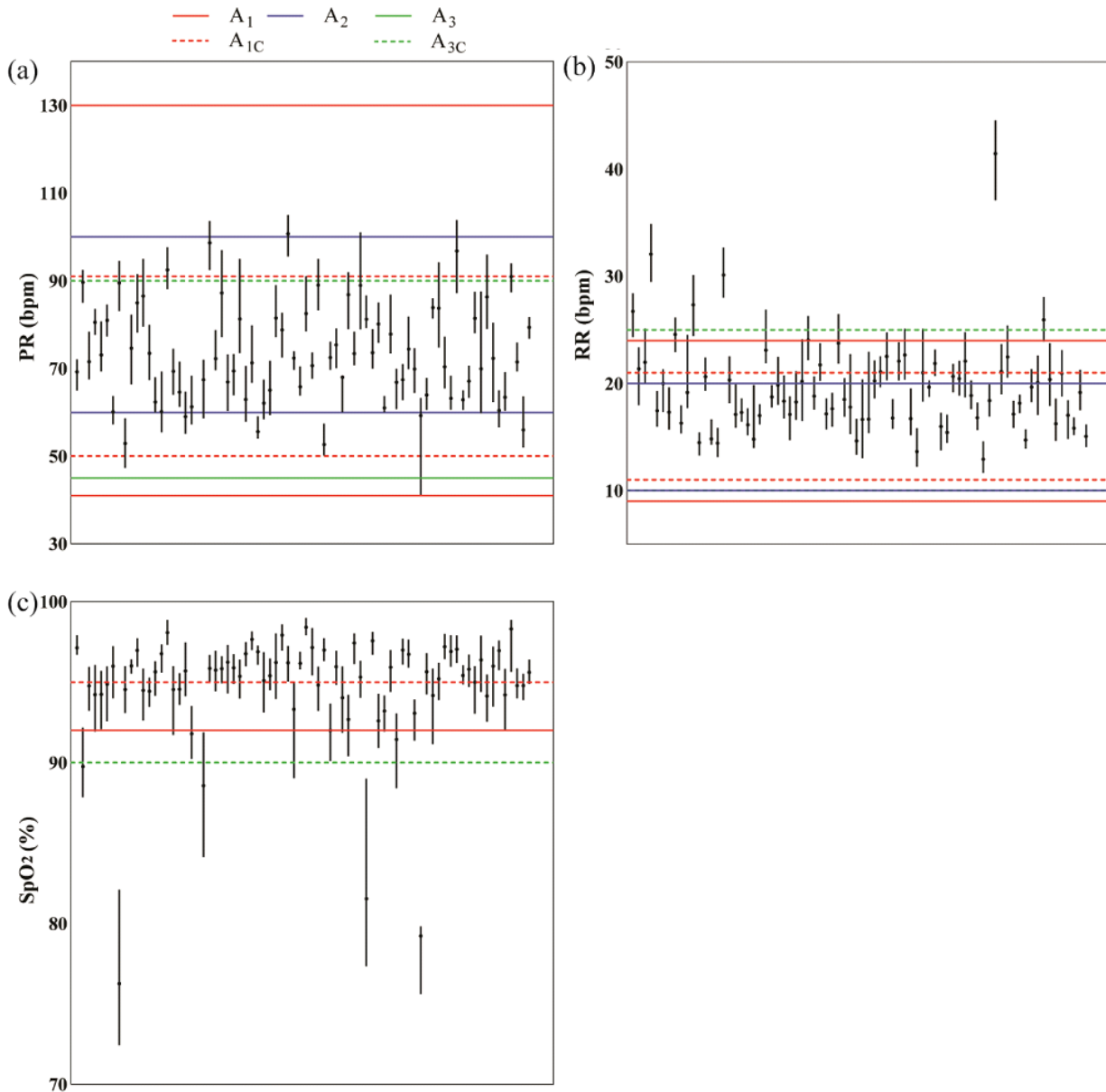


Figure 1. Median (IQR) vital signs for each patient in the healthcare at home dataset. (a) Pulse rate (PR); (b) Respiratory rate (RR); (c) Oxygen saturation (SpO₂). The horizontal lines indicate the threshold values set for each alarm ruleset. Solid horizontal lines are thresholds used in single vital sign rules: A₁ (purple), A₂ (cyan), A₃ (magenta). Dashed horizontal lines are thresholds used in logic-based rules: A_{1C} (cyan), A_{3C} (blue).

Table 1. Alarm metrics.

Ruleset	A ₁				A ₂				A ₃			
	AW ₅	AW ₁₅	AW ₁	AW ₄	AW ₅	AW ₁₅	AW ₁	AW ₄	AW ₅	AW ₁₅	AW ₁	AW ₄
Aggregation Window												
W _{AP}	2251	1759	1195	791	3113	2855	2467	2121	942	626	356	200
Patient Rate (%)	100	96.1	76.3	65.8	100	100	98.7	93.4	80.3	65.8	48.7	32.9
Alarm Rate	3.2	2.5	1.7	1.1	4.4	4	3.5	3	1.3	0.9	0.5	0.3

Figure 1. Median (IQR) vital signs for each patient in the healthcare at home dataset. (a) Pulse rate (PR); (b) Respiratory rate (RR); (c) Oxygen saturation (SpO₂). The horizontal lines indicate the threshold values set for each alarm ruleset. Solid horizontal lines are thresholds used in single vital sign rules: A₁ (purple), A₂ (cyan), A₃ (magenta). Dashed horizontal lines are thresholds used in logic-based rules: A_{1C} (cyan), A_{3C} (blue). Table 1. Alarm metrics.

Development of a reversibly detachable modular electronic interface for a thin wireless health monitoring patch system

Ashok Chhetry¹, Maggie Nedbalek², Yun Soung Kim¹

¹Biomedical Engineering and Imaging Institute, Icahn School of Medicine at Mount Sinai

²Biomedical Engineering, Columbia University

Introduction: Recent interest in developing comfortable, long-term wearable health monitoring patches has led to innovations combining soft silicone elastomers, stretchable nanomembrane electrodes, and a compact electronic module on fabric. These smart silicone-based patches offer high-quality biopotential signal acquisition without skin-irritating adhesives or gels. We've shown the effectiveness of a hyperelastic elastomer-coated fabric for biopotential monitoring, noting its high signal quality and ease of use at home. However, improvements are needed: replacing the patch requires significant effort and resources, and while gold electrodes lack scalability, using spin-coated Ag/AgCl electrodes could enhance scalability and signal stability. To address these issues, we've designed an updated patch that allows easy detachment of the electronic module using spring-loaded pogo pins and magnetic locking mechanisms, streamlining replacement and improving functionality (Fig. 1).

Materials and Methods: The patch layer uses a breathable fabric (9907T, 3M) coated with Silbione (RTV 4420, Elkem) and is embedded with Ag/AgCl stretchable electrodes. Electrodes are prepared by spin coating (3000 rpm for 60 s) electrically conductive Ag/AgCl ink (126-49, Creative Materials) diluted by xylene (0.91 w/w%) onto a polyimide/glass substrate. Coated ink is cured at 150°C for 30 minutes at ambient pressure. Cured electrodes are patterned using a femtosecond laser (LS-Lab, LASEA) and are transfer-printed to Silbione. A flexible custom copper-polyimide is used to electrically connect the electrodes to the wireless module. An elastomeric reinforcement piece embedded with magnets and flat disc contacts is attached to the connector. The wireless module contains electronics for Bluetooth communication, front-end amplification, and power management, and is encased in an elastomeric enclosure, which contains magnets and pogo pins. Protruding design features are built into the pair of elastomeric pieces to guide attachment and prevent sliding.

Results: Spin-coated and laser-patterned Ag/AgCl electrodes exhibited excellent electrical property with resistance $<3 \Omega$ from two furthest points (Fig. 2). Molded silicone locking provided good fitment for flat disc contacts, magnets, and pogo pins (Fig. 3). Custom flexible connector affixed to the locking mechanism served as an efficient wire while being compliant to maintain device's overall flexibility.

Conclusions: Preliminary results show the detachable interface based on magnets, pogo-enabled electrical contacts, and the locking feature built into molded rubber pieces is a suitable approach that transform single-use patch sensors to a versatile modular patch system. With further refinement in the locking interface and validation in free-living scenarios, the described system could enable unique studies requiring multi-parametric longitudinal health data at reduced system costs and user burden.

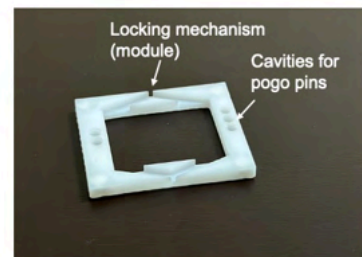
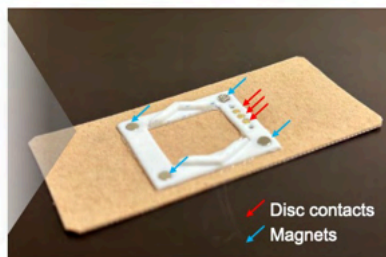
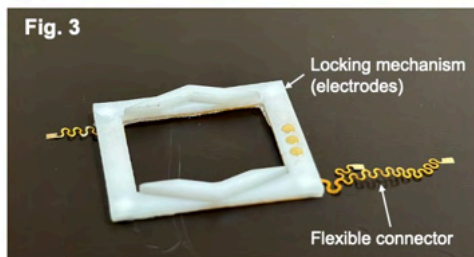
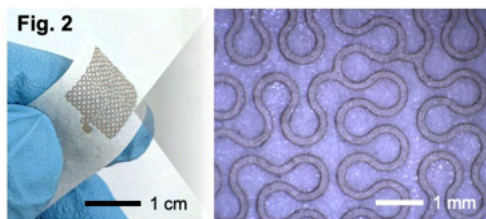
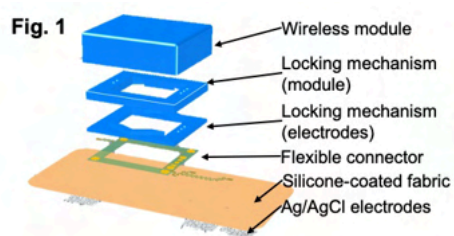


Fig. 1. Blow-up rendering with a description for each of the key structural component. Fig. 2. A photograph (left) and a microscope view (right) of a laser-patterned Ag/AgCl electrode. Fig. 3. Assembly of the flexible connector and electrode-side locking mechanism (left). Fully integrated patch layer embedded with magnets and flat disc contacts (center). Photograph of the locking mechanism integrated into the wireless module (right).

A Novel Subdural Hematoma Evacuation Device For Subdural Hemorrhage Treatment

Isabella Morgan^{1,2}, Joseph Borrello^{1,2}, Turner S. Baker^{1,2}, Iden Kurtaliaj^{1,2}, Benjamin Rapoport^{1,2}

¹Sinai BioDesign, Department of Neurosurgery, Mount Sinai Hospital, New York, USA

²Department of Neurosurgery, Mount Sinai Hospital, New York, USA

Introduction: Subdural hemorrhage (SDH), bleeding between the dura and the brain surface, is a common and debilitating condition that can result in severe neurologic impairment and death. With an aging population, SDH is one of the most common neurosurgical operations with over 160k cases per year in the US and Europe, and is expected to become the most common reason for brain surgery by 2025^{1,2}. Current evacuation methods are either too invasive or not effective for removing hematomas, and lead to high recurrence and mortality rates^{3,4,5,6}. To address this need we developed a neuroendoscopic device for SDH treatment. In addition, we designed two specialized phantom models for its validation. The first model is used to assess the device's efficacy in evacuating hematomas, and the second model is used to evaluate its navigation and visualization capabilities.

Materials and Methods: **Device Design:** The evacuation device was designed using Fusion360 and 3D printed in Formlabs Durable V2 using the Formlabs Form 3 printer. **Evacuation:** To assess evacuation, an SDH model of the subdural space was developed, comprising brain, blood, dura, skull, and skin tissue analogs. **Navigation:** To assess navigation, a blood-free model with clinically relevant SDH cavities was developed. The model has two components: a base and an interchangeable top with three different heights to create different hematoma cavities. 17 touch-points are placed across the simulated brain surface to simulate areas that surgeons need to navigate endoscopically. **Device Testing:** Two neurosurgeons completed a SDH evacuation with the evacuation model and three neurosurgeons tested the device on the navigation functionality model.

Results: **Evacuation Efficiency:** One neurosurgeon achieved a 91% evacuation percentage in 6:55 minutes, and the other a 70% evacuation percentage in 3:30 minutes. **Navigation Accuracy:** Surgeons conducted navigation tests with depths of hematoma cavities of 15 mm, 20 mm, and 25 mm, and completed these assessments in average times of 310 seconds, 287 seconds, and 330 seconds, respectively. Surgeons accurately reached at least 88% of all touch points.

Conclusions: We have demonstrated the evacuation efficiency and navigation precision of our device through two innovative phantom tests, establishing the neuroendoscopic approach as a promising method for treating subdural hematoma (SDH). Future research will focus on refining the device's design to ensure it is clinically relevant and compatible with existing standard procedures.

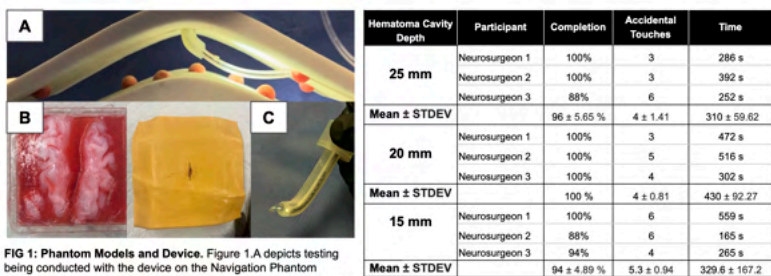


FIG 1: Phantom Models and Device. Figure 1.A depicts testing being conducted with the device on the Navigation Phantom Model. Figure 1.B depicts the evacuation phantom model, with and without the "skull cap" and "scalp". Figure 1.C depicts the neuroendoscopic subdural hematoma evacuation device.

Hematoma Cavity Depth	Participant	Completion	Accidental Touches	Time
25 mm	Neurosurgeon 1	100%	3	286 s
	Neurosurgeon 2	100%	3	392 s
	Neurosurgeon 3	88%	6	252 s
Mean ± STDEV		96 ± 5.65 %	4 ± 1.41	310 ± 59.62
20 mm	Neurosurgeon 1	100%	3	472 s
	Neurosurgeon 2	100%	5	516 s
	Neurosurgeon 3	100%	4	302 s
Mean ± STDEV		100 %	4 ± 0.81	430 ± 92.27
15 mm	Neurosurgeon 1	100%	6	559 s
	Neurosurgeon 2	88%	6	165 s
	Neurosurgeon 3	94%	4	265 s
Mean ± STDEV		94 ± 4.89 %	5.3 ± 0.94	329.6 ± 167.2

Table 1: Navigation Testing Data. Testing performed by three neurosurgeons depicting completion percentage, accidental touches and procedural time on the three hematoma cavities.

FIG 1: Phantom Models and Device. Figure 1.A depicts testing being conducted with the device on the Navigation Phantom Model. Figure 1.B depicts the evacuation phantom model, with and without the "skull cap" and "scalp". Figure 1.C depicts the neuroendoscopic subdural hematoma evacuation device. Table 1: Navigation Testing Data. Testing performed by three neurosurgeons depicting completion percentage, accidental touches and procedural time on the three hematoma cavities.

Consumer-mediated RWD generation for Precision Medicine Research

Dan Park, Vik Kheterpal, Ed Ramos

CareEvolution, CareEvolution, Scripps Digital Trials Center/CareEvolution

Just in the first few weeks of 2024, the medical community has witnessed the emergence of therapies and medicines poised to redefine patient care and treatment paradigms. Innovations such as GLP-1 agonists, novel pain management solutions, and CRISPR gene therapies, highlight the rapid pace of medical advancement and underscore the essential need for personalized medicine and precision medicine research. Such research is crucial for knowledge discovery - not only in understanding the broad impacts of these innovations but also in ensuring they are effectively integrated into patient care, maximizing their benefits across diverse populations. Over the last decade, we've observed significant initiatives emphasizing the importance of detailed, patient-centric data collection, spanning genomics, environmental factors, and lifestyle choices. This evolution towards a more personalized healthcare model necessitates an infrastructure that supports the efficient collection and analysis of real-world data, enabling researchers to tailor healthcare solutions to individual needs. We will explore the pivotal technical components and strategies that underpin the secure and patient-centered collection of health data, focusing on interoperability, security, and patient engagement. Through examples, such as the PROGRESS study and other research initiatives that utilize digital tools for data collection, we aim to illustrate the transformative potential of technology in improving clinical outcomes and patient care. These case studies will demonstrate how collaboration and technological innovation are essential for advancing precision medicine and enhancing our understanding of how to effectively deploy new treatments. Our aim is to illuminate the role of digital innovation in enhancing medical research and patient care - and celebrate the collective achievements of the research community and the technological advancements that facilitate this progress, emphasizing the collaborative effort required to navigate the complexities of modern healthcare and push the boundaries of precision medicine.

Enabling studies with multi-modal, deep data capture

Enrolling 1,000 participants—500 people with type 2 diabetes, and 500 without—to understand individual level glycemic response.

HbA1c



genomics



microbiome



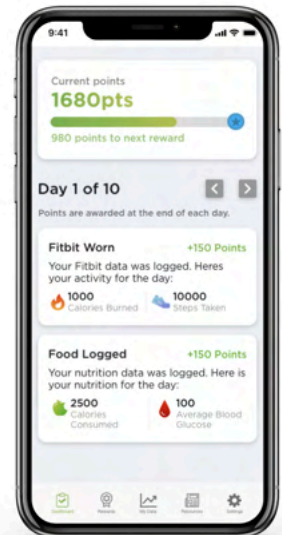
biometrics



nutritional intake



glucose response



 **PROGRESS**

A high-level schematic of the multimodal data capture in PROGRESS

Superfusion Device for Pharmacological Testing in Precision Medicine

Sa'ileen Ahmad^{*1}, Rashida Zannat Akifa^{*1}, Christopher Dyjak^{*1}, Fariha Islam^{*1}, Sebastian Maurice^{*1}, Irene C. Turnbull², A.H. Rezwanuddin Ahmed¹.

* These authors contributed equally to this work.

¹Biomedical Engineering, The City College of New York, CUNY.

²Cardiovascular Research Institute, Icahn School of Medicine at Mount Sinai.

Introduction: Cardiomyocytes are complex muscle cells in the heart that are very sensitive to mechanical and biochemical stimuli, and are prone to contractile dysfunction as well. These dysfunctions lead to major heart problems, including arrhythmia and myocardial infarction. Pharmacological agents and medicines meant to help patients can often instigate such dysfunctions. This may lead to the removal of many beneficial drugs from the market. **Challenge to be Addressed:** We use patient-specific induced pluripotent stem cell-derived cardiomyocytes to test their response to pharmacological stimuli. However, the rapid and transient response to some drugs during electrophysiological testing complicates data collection via traditional pipetting techniques, which are temporally slow compared to the swift cellular reactions the cells undergo. This prevents accurate measurements and disrupts the experiment. To solve this problem, a low-cost superfusion device, rapid and with microliter precision, was developed. Prior arts and current market searches include devices that fulfill many of the parameters needed for this experiment - multi-solution dispensation, microliter precision, affordable cost, small-footprint size, or noise interference - but not all at once.

Material and Methods: Conceptual designs were developed taking inspiration from other devices in addition to our own engineered modifications, and the Pugh method was used to stratify the best approach. Different iterations of the device were refined through feasibility and validation testing, tuning components comprising the fully assembled superfusion prototype.

Results: Our team is still progressively prototyping. Early results indicate that the device can realize the parameters needed for rapid stimulatory experiments on cardiomyocytes. The superfusion device can dispense microliters of fluid within seconds, and can switch to different solutions almost instantaneously (Figure 1). Additionally, the device produces little to no noise or vibration, so as not to interfere with small response signals from contractile cardiomyocytes. Our device is kept at an affordable (<\$600) price for the standard research lab.

Conclusion: Our superfusion device may help in the future with experiments involving cells or microfluidics, and can be useful to any lab that requires rapid and precise dispensation of solutions, beyond the cardiovascular field. For example, this device can be integrated into labs performing experiments in neural tissue; many of these experiments involve the dispensation of neurotransmitters onto tissue samples, and this may be done with our device. This device will definitely find a niche in multiple lab settings that need precise dispensing.

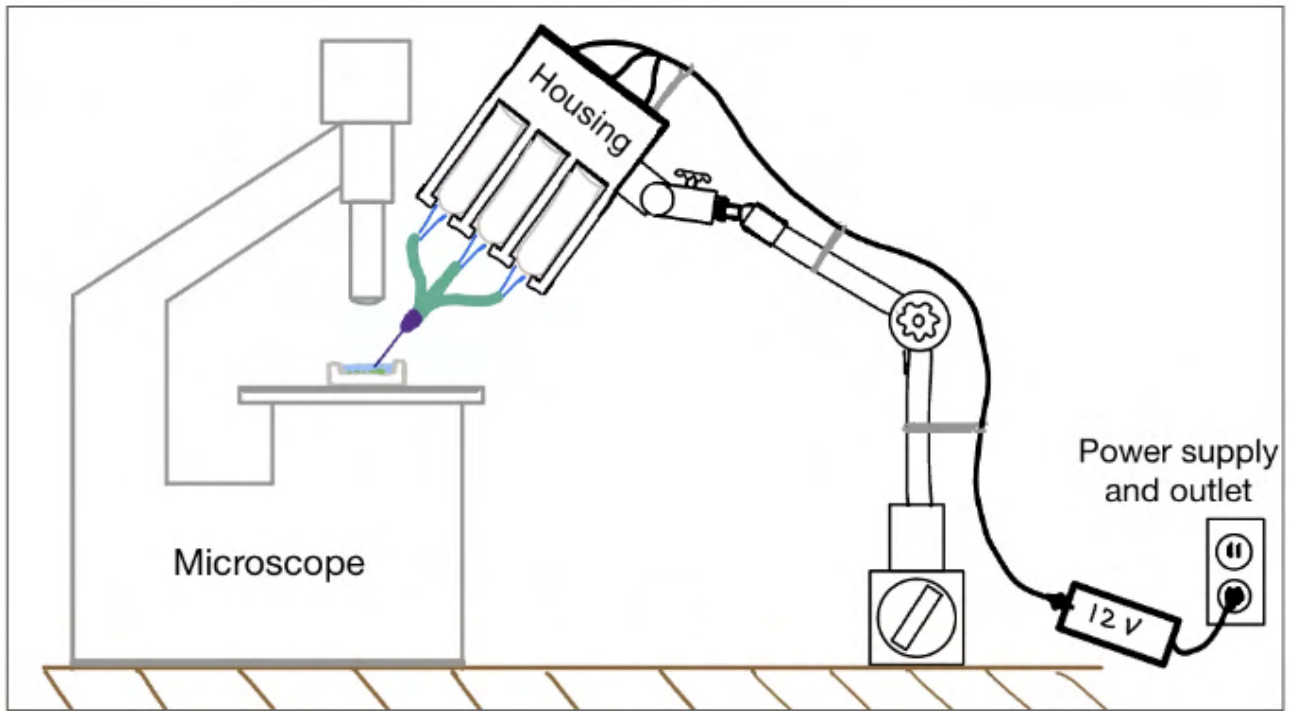


Figure 1. Diagram of prototype of superfusion device. Not to scale.

Sponsors



deepc.ai



Bracco

Bruker Biospin

CareEvolution llc.

SA Instruments Inc.

